

Dissertation zur Erlangung des Doktorgrades
der Fakultät für Chemie und Pharmazie
der Ludwig-Maximilians-Universität München

**Combining Alkaline Earth and Rare
Earth Metals in
Oxonitrido(carbido)silicates as
Luminescent Materials for
Solid-State Lighting**

Lisa Gamperl

aus

Pfaffenhofen an der Ilm, Deutschland

2022

Erklärung

Diese Dissertation wurde im Sinne von §7 der Promotionsordnung vom 28. November 2011 von Herrn Prof. Dr. Wolfgang Schnick betreut.

Eidesstattliche Versicherung

Diese Dissertation wurde eigenständig und ohne unerlaubte Hilfsmittel erarbeitet.

München, den 17.10.2022

.....

Lisa Gamperl

Dissertation eingereicht am:	06.07.2022
1. Gutachter:	Prof. Dr. Wolfgang Schnick
2. Gutachter:	Prof. Dr. Hubert Huppertz
Mündliche Prüfung am:	12.10.2022

für Jessica
für Mama und Papa

Danksagung

Mein größter Dank gilt Herrn Prof. Dr. Wolfgang Schnick für die freundliche Aufnahme in seine Arbeitsgruppe und die Möglichkeit, meine Dissertation über dieses sehr spannende Thema anfertigen zu können. Die hervorragenden Rahmenbedingungen und die Freiheiten sowohl bei der Themenwahl als auch bei der Fülle an zur Verfügung stehenden synthetischen und analytischen Methoden bildeten nicht nur für meine Dissertation die perfekten Voraussetzungen, sondern hat bereits eine Vielzahl hervorragender Doktoren hervorgebracht, in die ich mich jetzt erfreulicherweise einreihen darf. Seit Sie zu Beginn meines Studiums die Grundvorlesung der Anorganischen Chemie gehalten haben, war ich von der Festkörperchemie fasziniert und wusste da bereits, wo ich in meiner akademischen Laufbahn hinmöchte. Mit Ihrer Art, Vorträge und Vorlesungen zu halten, schaffen Sie es immer wieder, Ihre Zuhörer zu faszinieren und für Ihre Forschung zu begeistern. Ich bin Ihnen sehr dankbar, dass ich nicht nur mein Lieblingsthema bearbeiten konnte, sondern dies durch die Kooperation mit Lumileds, die meine Doktorarbeit bereichert hat, noch zu intensivieren.

Ich bedanke mich ganz herzlich bei Herrn Prof. Dr. Hubert Huppertz für die Übernahme des Koreferats meiner Dissertation. Darüber hinaus möchte ich mich bei ihm für die Organisation der Obergurgl-Seminare Festkörperchemie bedanken. Diese Konferenz war vor allem an Anfang meiner Promotion sehr interessant und lehrreich, sowohl um Einblicke in themenrelevante Forschung aus anderen Arbeitskreisen zu erhalten und Ideen für die eigene Forschung zu sammeln als auch die Möglichkeit, zum ersten Mal die eigenen Forschungsergebnisse einem fremden und breiteren Publikum in einer sehr angenehmen Atmosphäre zu präsentieren.

Des Weiteren danke ich Herrn Prof. Dr. Hans-Christian Böttcher, Herrn Prof. Dr. Konstantin Karaghiosoff, Herrn Prof. Dr. Oliver Oeckler und Frau Prof. Dr. Silvija Markic für ihre freundliche Bereitschaft zur Teilnahme an der Prüfungskommission meines Rigorosums.

Besonderer Dank gilt allen Beteiligten der Kooperation mit Lumileds: Herrn Dr. Peter J. Schmidt, Herrn Dr. Niels Van der Veen, Herrn Volker Weiler und vor allem Herrn Dr. Philipp Strobel. Ich danke Euch für die freundschaftliche Zusammenarbeit und die ausgezeichnete Unterstützung in Sachen Lumineszenzmessungen aller Art, Interpretation der Ergebnisse, Diskussionen und Anregungen bei den Meetings und Input bei meinen Manuskripten, was zusammengenommen nicht nur zu meinem Verständnis der Materie beigetragen, sondern auch die Qualität der Manuskripte angehoben hat.

Außerdem möchte ich mich bei meinen weiteren Kooperationspartnern bedanken. Zuerst bei meinem ehemaligen Praktikanten Herrn Georg Krach, der mich ganz am Anfang meiner

Promotion begleitet hat, was auch direkt zu meiner ersten Publikation führte. Herrn Dr. Otto E. O. Zeman und Herrn Dr. Thomas Bräuniger danke ich für die Hilfsbereitschaft und Unterstützung in Sachen NMR-Auswertung und -Interpretation. Zuletzt möchte ich Herrn Dr. Lukas Neudert, Herrn Peter Schultz, Frau Dr. Dajana Durach und Herrn Prof. Dr. Oliver Oeckler meinen herzlichen Dank im Zusammenhang mit elektronenmikroskopischen Untersuchungen und Synchrotronmessungen aussprechen. Insbesondere Herr Prof. Dr. Oliver Oeckler muss dabei für seine großartige Hilfe bei und interessanten Austausch über diverse kristallographische Fragestellungen hervorgehoben werden.

Bei Frau Olga Lorenz, Herrn Wolfgang Wünschheim, Herrn Dr. Dieter Rau und Herrn Thomas Miller bedanke ich mich für die Unterstützung in allen geräte- und computertechnischen, organisatorischen und sicherheitsrelevanten Bereichen. Ganz besonders möchte ich mich bei Herrn Wolfgang Wünschheim für die unzähligen Male an Hilfe bedanken, wenn mal wieder das Kühlwasser an den Hochfrequenzöfen gestreikt hat. Obwohl uns das fast zur Verzweiflung gebracht hätte, konnte ich mich doch jedes Mal wieder auf Deine schnelle und anstandslose Unterstützung verlassen. Ohne Dich wäre meine praktische Arbeit nicht möglich gewesen.

Herrn Dr. Steffen Schmidt und Herrn Dr. Markus Döblinger sei für die Einweisung an das Rasterelektronenmikroskop und darüber hinaus für die Hilfestellung bei kleineren Problemen gedankt. Herrn Christian Minke danke ich für NMR-Messungen und für die Hilfe bei Fragen zum Rasterelektronenmikroskop. Herrn Dr. Peter Mayer danke ich für die Einkristall-Messungen.

Meinem Vorgänger Herrn Dr. Christian Maak danke ich ganz herzlich für die Aufnahme in den Arbeitskreis und die Einführung in die Thematik. Danke, dass Du mir Dein umfangreiches Wissen vermittelt und mir mit Rat und Tat bei allen möglichen Fragen zu Seite gestanden hast.

Bei Herrn Dr. Sebastian Wendl, Herrn Tobias Giffthaler und Herrn Reinhard Pritzl bedanke ich mich herzlich für die vielen konstruktiven, inspirierenden und ermutigenden Gespräche über allerlei fachliche Fragestellungen. Danke, dass ich immer auf Euch zukommen konnte und ihr immer ein offenes Ohr und gute Ideen für mich hattet. Insbesondere Herrn Tobias Giffthaler danke ich vielmals für seine Zeit und Beantwortung aller Fragen sowie seine anstandslose Hilfsbereitschaft und bereichernden Anmerkungen zu meinen Manuskripten. Danke an Herrn Reinhard Pritzl für die vielen gemeinsamen Projekte und den ständigen Austausch nicht nur bei fachlichen Angelegenheiten.

Meinen Arbeitskollegen und Freunden Herrn Dr. Sebastian Wendl, Herrn Tobias Giffthaler, Herrn Reinhard Pritzl, Frau Sophia Wandelt und Herrn Florian Engelsberger danke ich für

deren Hilfsbereitschaft, die tolle Zeit in der Kaffeeküche und bei der Mittagspause, die Ablenkung vom Laboralltag und die vielen lustigen Stunden innerhalb und außerhalb des Labors.

Des Weiteren danke ich meinen aktuellen und ehemaligen Laborkollegen aus D2.107, Herrn Dr. Mathias Mallmann, Herrn Dr. Peter Wagatha, Herrn Dr. Jonas Häusler, Herrn Dr. Niklas Cordes, Frau Dr. Claudia Lermer, Frau Dr. Kerstin Gotschling, Herrn Dr. Stefan Rudel, Herrn Florian Engelsberger, Herrn Thanh Chau und Frau Mirjam Zipkat für die schöne Zeit und die angenehme Arbeitsatmosphäre.

Ich möchte mich noch bei den bisher nicht genannten Mitgliedern der Arbeitskreise Schnick, Hoch, Johrendt und Lotsch, die mich während meiner Promotion unterstützt haben, bedanken.

Zu guter Letzt gilt mein allergrößter Dank meiner Familie, insbesondere Jessica und meiner Mama Josefine. Danke, dass ihr stets an mich geglaubt und mich auf meinem langen Weg begleitet und immer unterstützt habt!

Es ist nicht genug, zu wissen - man muss es auch anwenden.

Es ist nicht genug zu wollen - man muss es auch tun.

Johann Wolfgang von Goethe

Table of Contents

1	Introduction.....	1
1.1	Present Challenges in the Field of Energy Savings	1
1.2	LEDs as the Illumination Technology of the Future	5
1.3	Basic Principles of Solid-State Luminescence	9
1.4	Structural Chemistry of (Oxo)nitridosilicates	13
1.5	Scope of this Thesis	19
1.6	References	19
2	Synthesis of $RE_{6-x}Ca_{1.5x}Si_{11}N_{20}O$ ($RE = Yb, Lu; x \approx 2.2$) with $Lu_{6-x}Ca_{1.5x}Si_{11}N_{20}O:Ce^{3+}$ Offering Interesting Spectral Properties for Yellow-Emitting Phosphors in 1pcLEDs.....	25
2.1	Introduction.....	26
2.2	Results and Discussion	27
2.2.1	Synthesis and Chemical Analysis.....	27
2.2.2	Crystal Structure Determination and Description	29
2.2.3	UV/Vis Spectroscopy.....	34
2.2.4	Luminescence	36
2.3	Conclusion.....	40
2.4	Experimental Part	41
2.4.1	Synthesis	41
2.4.2	Electron Microscopy	41
2.4.3	Single-Crystal X-ray Diffraction	41
2.4.4	Powder X-ray Diffraction.....	42
2.4.5	Fourier Transform Infrared (FTIR) Spectroscopy.....	42
2.4.6	UV/Vis Spectroscopy.....	42
2.4.7	Luminescence	42
2.5	Acknowledgements.....	43
2.6	References	43

3	Missing Member in the $M^{\text{II}}M^{\text{III}}\text{Si}_4\text{N}_7$ Compound Class: Carbothermal Reduction and Nitridation Synthesis Revealing Substitution of N by C and O in $\text{CaLu}[\text{Si}_4\text{N}_{7-2x}\text{C}_x\text{O}_x]:\text{Eu}^{2+}/\text{Ce}^{3+}$ ($x \approx 0.3$).....	47
3.1	Introduction	48
3.2	Results and Discussion.....	49
3.2.1	Synthesis and Chemical Analysis	49
3.2.2	Structure Description	51
3.2.3	NMR Spectroscopy.....	53
3.2.4	UV/Vis Reflectance Spectroscopy	55
3.2.5	Luminescence	56
3.3	Conclusion	60
3.4	Experimental Part	61
3.4.1	Synthesis.....	61
3.4.2	Powder X-ray Diffraction.....	61
3.4.3	CHNS Analysis.....	62
3.4.4	Scanning Electron Microscopy (SEM) and Energy-dispersive X-ray Spectroscopy (EDX).....	62
3.4.5	Transmission Electron Microscopy (TEM)	62
3.4.6	Solid-state NMR spectroscopy	62
3.4.7	UV/Vis Spectroscopy.....	62
3.4.8	Luminescence	62
3.5	Acknowledgements	63
3.6	References	63
4	Synthesis and Luminescence Properties of Amber Emitting $\text{La}_7\text{Sr}[\text{Si}_{10}\text{N}_{19}\text{O}_3]:\text{Eu}^{2+}$ and Syntheses of the Substitutional Variants $\text{RE}_{8-x}\text{AE}_x[\text{Si}_{10}\text{N}_{20-x}\text{O}_{2+x}]:\text{Eu}^{2+}$ with $\text{RE} = \text{La}, \text{Ce}; \text{AE} = \text{Ca}, \text{Sr}, \text{Ba}; 0 \leq x \leq 2$	67
4.1	Introduction	68
4.2	Results and Discussion.....	69
4.2.1	Synthesis and Chemical Analysis	69
4.2.2	Crystal Structure Elucidation.....	71
4.2.3	Structure Description	73

4.2.4	UV/Vis Reflectance Spectroscopy	75
4.2.5	Luminescence	75
4.3	Conclusion.....	79
4.4	Experimental Part	80
4.4.1	Synthesis.....	80
4.4.2	Single-Crystal X-ray Diffraction	80
4.4.3	Powder X-ray Diffraction	81
4.4.4	Scanning Electron Microscopy (SEM) and Energy-dispersive X-ray Spectroscopy (EDX).....	81
4.4.5	UV/Vis Spectroscopy	81
4.4.6	Luminescence	82
4.5	Acknowledgements.....	82
4.6	References	82
5	State-of-the-Art Complex Structure Elucidation and Luminescence Properties of Strontium and Barium Lanthanum Oxonitridosilicate Oxides.....	87
5.1	Structure Elucidation of Complex Endotaxially Intergrown Barium Lanthanum Oxonitridosilicate Oxides by Combination of Microfocused Synchrotron Radiation and Transmission Electron Microscopy	87
5.1.1	Introduction.....	88
5.1.2	Results and Discussion.....	89
5.1.3	Conclusion.....	103
5.1.4	Experimental Part.....	104
5.1.5	Acknowledgements.....	106
5.1.6	References	106
5.2	Unpublished Results.....	111
5.2.1	Introduction.....	111
5.2.2	Results and Discussion.....	111
5.2.3	Conclusion.....	116
5.2.4	Experimental Part.....	117
5.2.5	Acknowledgements.....	119

5.2.6	References.....	119
6	Conclusion and Outlook	121
7	Summary	129
7.1	Synthesis of $RE_{6-x}Ca_{1.5x}Si_{11}N_{20}O$ ($RE = Yb, Lu; x \approx 2.2$) with $Lu_{6-x}Ca_{1.5x}Si_{11}N_{20}O:Ce^{3+}$ Offering Interesting Spectral Properties for Yellow-Emitting Phosphors in 1pcLEDs	129
7.2	Missing Member in the $M^II M^III Si_4 N_7$ Compound Class: Carbothermal Reduction and Nitridation Synthesis Revealing Substitution of N by C and O in $CaLu[Si_4 N_{7-2x} C_x O_x]:Eu^{2+}/Ce^{3+}$ ($x \approx 0.3$)	130
7.3	Synthesis and Luminescence Properties of Amber Emitting $La_7 Sr[Si_{10} N_{19} O_3]:Eu^{2+}$ and Syntheses of the Substitutional Variants $RE_{8-x} AE_x [Si_{10} N_{20-x} O_{2+x}]:Eu^{2+}$ with $RE = La, Ce; AE = Ca, Sr, Ba; 0 \leq x \leq 2$	131
7.4	Structure Elucidation of Complex Endotaxially Intergrown Lanthanum Barium Oxonitridosilicate Oxides by Combination of Microfocused Synchrotron Radiation and Transmission Electron Microscopy	132
8	Appendix.....	133
A.	Supporting Information for Chapter 2	133
	References	143
B.	Supporting Information for Chapter 3	145
	Reference	149
C.	Supporting Information for Chapter 4	151
	References	177
D.	Supporting Information for Chapter 5	179
	References	219
9	Publications.....	221
9.1	List of Publications	221
9.1.1	Synthesis of $RE_{6-x}Ca_{1.5x}Si_{11}N_{20}O$ ($RE = Yb, Lu; x \approx 2.2$) with $Lu_{6-x}Ca_{1.5x}Si_{11}N_{20}O:Ce^{3+}$ Offering Interesting Spectral Properties for Yellow-Emitting Phosphors in 1pcLEDs.....	221
9.1.2	Missing Member in the $M^II M^III Si_4 N_7$ Compound Class: Carbothermal Reduction and Nitridation Synthesis Revealing Substitution of N by C and O in $CaLu[Si_4 N_{7-2x} C_x O_x]:Eu^{2+}/Ce^{3+}$ ($x \approx 0.3$).....	221

9.1.3	Synthesis and Luminescence Properties of Amber Emitting $\text{La}_7\text{Sr}[\text{Si}_{10}\text{N}_{19}\text{O}_3]:\text{Eu}^{2+}$ and Syntheses of the Substitutional Variants $\text{RE}_{8-x}\text{AE}_x[\text{Si}_{10}\text{N}_{20-x}\text{O}_{2+x}]:\text{Eu}^{2+}$ with $\text{RE} = \text{La}, \text{Ce}$; $\text{AE} = \text{Ca}, \text{Sr}, \text{Ba}$; $0 \leq x \leq 2$	222
9.1.4	Structure Elucidation of Complex Endotaxially Intergrown Lanthanum Barium Oxonitridosilicate Oxides by Combination of Microfocused Synchrotron Radiation and Transmission Electron Microscopy	222
9.2	Conference Contributions	225
9.3	Deposited Crystallographic Data.....	227

1 Introduction

1.1 Present Challenges in the Field of Energy Savings

Climate change is the single greatest threat to a sustainable future but, at the same time, addressing the climate challenge presents a golden opportunity to promote prosperity, security, and a brighter future for all.

Ban Ki-Moon, 8th Secretary-General of the United Nations (2007–2016)

The CO₂ content of the atmosphere, and thus also the climate, has repeatedly undergone major changes in the course of Earth's history. Beginning with the industrial revolution in the mid-1800s and the associated use of fossil fuels such as coal, oil and natural gas, CO₂ concentrations have risen far above the natural range of variation over the past 800,000 years. Since the first measurement in 1958, the CO₂ concentration of the atmosphere was around 316 ppm but in 2020, the annual average concentration of CO₂ in Earth's atmosphere was 414 ppm and in March 2021, it reached a new high of 417 ppm (Figure 1.1a). This represents an increase of nearly 50% over the level before industrialization, whereby the increase has been particularly steep over the past three decades. The CO₂ concentration is thus much higher than at any time in the past 800,000 - probably even three million years. The series of measurements was the first to show the connection between burning of fossil raw materials and the concentration of the greenhouse gas CO₂.^[1, 2]

Directly associated with the steep rise in concentration of the greenhouse gas CO₂ in the atmosphere is the increase in global temperature recorded since the beginning of industrialization (Figure 1.1b), which causes an additional greenhouse effect, the so-called anthropogenic greenhouse effect. Earth's surface has already warmed by more than 1.2 °C on global average compared to pre-industrial times. According to the available paleoclimatic data, such a temperature level has never occurred during the past 2,000 years and very likely never during the current warm period, the Holocene, which began just under 12,000 years ago - i.e., never in the course of modern human history. A wide range of research has ruled out natural causes for the current, very steep rise in temperature since the beginning of industrialization. It can only be explained by man-made amplification of the greenhouse effect, which leads not only to global warming, but also to many other serious consequences. Extreme weather events like heat waves, droughts, heavy rainfall, and strong tropical storms are becoming more frequent and more intense and thus lead to increased mortality, melting

of ice, rising of sea levels by several meters, increased spread of diseases and threaten the supply of resources such as water and agricultural products and food.^[1, 2]

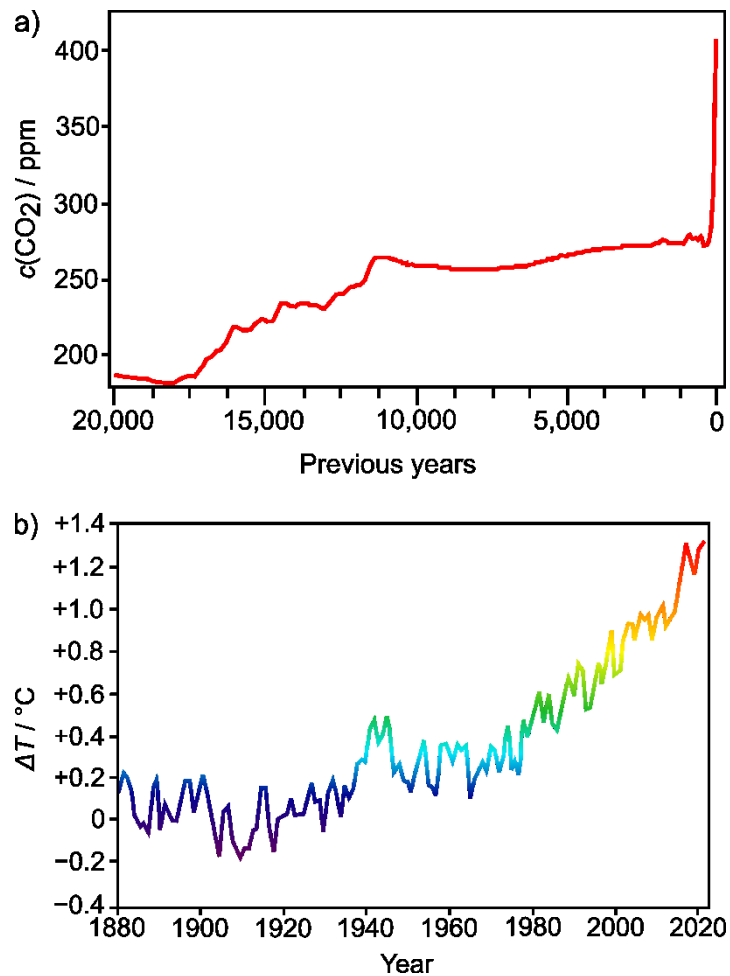


Figure 1.1. (a) CO₂ concentration in the atmosphere over the past 20,000 years. (b) Global mean temperature deviation with respect to the annual average in the time period from 1881 to 1910.^[1]

Some elements of the climate system have critical thresholds that, when exceeded, result in severe and sometimes unstoppable and irreversible changes.^[1, 2] Therefore, the international community committed itself to limiting global warming in a range between 1.5 °C and well below 2 °C with the Paris Climate Agreement concluded in 2015.^[3]

Of the CO₂ emissions released by industrialized civilizations from 2009 to 2018, 86% came from the combustion of fossil fuels for energy production.^[1, 2] According to the United States (U.S.) Energy Information Administration Annual Energy Outlook from 2018, the United States of America (USA) accounted for a total energy consumption of 96.8 quads (quadrillion British thermal units, approx. $2.8 \cdot 10^4$ TWh) of primary energy in 2017. Thereof, approx. 38% were consumed for electricity usage. An estimation by the U.S. Department of Energy (DOE) Solid-State Lighting (SSL) Program concluded that the lighting sector consumed approx. 6

quads (approx. 1,758.4 TWh) of energy and accounted for 6% of total energy or 16% of the total electricity consumed in the U.S. in 2017, respectively.^[4] For comparison, the U.S. energy consumption solely caused by lighting equals about half of the total primary energy consumption in Germany in 2017, which was approx. 13,523 PJ or approx. 3,756 TWh.^[5] This shows that the lighting sector has a very high and promising potential to reduce energy consumption and thus the emission of significant amounts of climate-damaging CO₂.

The hitherto high energy consumption and high CO₂ emissions of the lighting sector were mainly caused by the use of incandescent light bulbs. Their widespread application was based on covering the whole visible spectrum leading to very good color rendering and a warm-white color temperature, but the main drawback is their very poor energy balance with less than 5% of the consumed energy being irradiated as visible light but more than 95% lost through emission in the infrared spectral range and therefore heat production (see also Figure 1.9). The correlated color temperature (CCT) is an important feature of light sources used especially for indoor lighting and is defined as the temperature of an ideal blackbody radiator whose apparent color is most similar to that of the light source and is subdivided into e.g. warm (2500–4000 K) and cold (5000–7500 K) white light sources.^[6, 7] The color rendering index (CRI) indicates the light quality and is a measure of a light source's capability to replicate colors compared to sunlight, whose CRI is defined as 100, at the same CCT.^[8] Incandescent light bulbs also reach a CRI value of 100, whereby colors are perfectly reproduced analogous to sunlight.^[6, 7] A crucial factor defining a light source's energy efficiency is the luminous efficacy, which is the total amount of visible light emitted by a light source and defined as the ratio of produced luminous flux to electrical input power. The luminous flux is weighted by the sensitivity of the human eye to various wavelengths, which has its maximum at 555 nm and thereby, the theoretically achievable maximum luminous efficacy is 683 lm·W⁻¹.^[6, 9] Incandescent light bulbs only achieve approx. 15 lm·W⁻¹.^[10] This led the European Union (EU) in 2009 to decide to gradually phase out conventional incandescent bulbs to aim a reduction of primary energy use by 20% by 2020.^[11, 12] Compact fluorescent lamps could not establish themselves as successors of incandescent light bulbs, because despite a higher energy efficacy of up to 100 lm·W⁻¹, color rendering was low (CRI 80–90) and toxic mercury was used, which additionally makes disposal problematic.^[8, 10]

A new illumination generation based on SSL was boosted by the utilization of white phosphor-converted light-emitting diodes (pcLEDs) because of high energy efficiency, environmental friendliness due to absence of toxic elements, long lifetime, dimmability, immediate switch on, low size and weight.^[7, 11] Nowadays, LED appliances can reach efficacies of approx. 200 lm·W⁻¹, with the practical limit for pcLED packages being 255 lm·W⁻¹.^[6, 9] Therefore, it is important to adjust emission profiles to the eye sensitivity

curve to obtain maximum efficiency, which is expected to reach $240 \text{ lm}\cdot\text{W}^{-1}$ by 2025.^[6, 10] According to the DOE SSL Program lighting market model, the energy consumption of the lighting sector without LEDs is projected to grow from approx. 6 quads (approx. 1,758.4 TWh) in 2015 up to approx. 6.7 quads (approx. 1,963.6 TWh) in 2035. Nevertheless, a reduction of 75% in energy consumption, which is equal to 5.1 quads (approx. 1,494.7 TWh), can be achieved if the goals for LED efficacy are met (Figure 1.2).^[13]

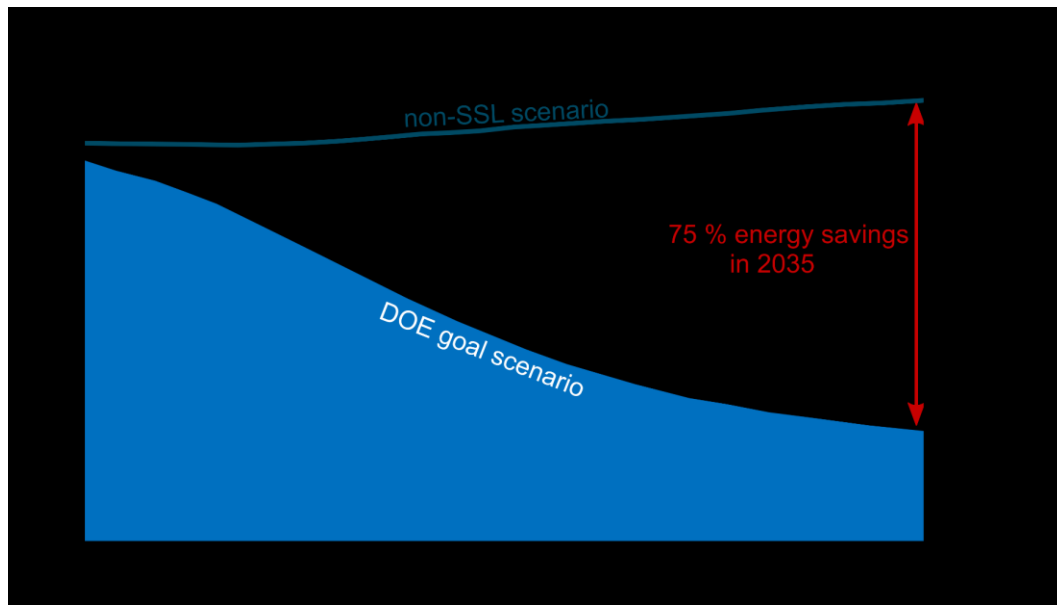


Figure 1.2. Forecast of the U.S. lighting-based energy consumption from 2015 to 2035 in a non-LED scenario compared to the energy consumption if the goals of the DOE SSL Program lighting market model are reached.^[13]

LED lighting sales are expected to expand from approx. 3% in 2013 to about 84% in 2030 due to improving cost competitiveness, recently issued efficiency standards and regulatory changes.^[14] A recent analysis by McKinsey forecasts a global market share of LEDs in general lighting to be about 45% in 2016 and almost 70% in 2020, leading to a market volume of approx. 64 billion €. ^[15] However, current state-of-the-art LEDs still need to be improved in many areas such as packaging, engineering, lighting quality, energy consumption. Through synthesis and development of new phosphors with to specific requirements modified emission properties, LEDs can be widely applied not only in general indoor and outdoor lighting, but e.g. also in the automotive sector, as backlighting in liquid crystal displays (LCD), or for horticultural lighting.^[4, 9, 13, 14]

1.2 LEDs as the Illumination Technology of the Future

A LED is a semiconductor appliance which emits light upon an electric current. It is composed of a p-n-junction formed by contacting a p-type and an n-type semiconductor. A p-type semiconductor results upon doping, i.e., targeted introduction of impurities leading to an increased charge carrier concentration, a semiconductor with an element with a lower number of electrons, also called holes located in the valence band. Therefore, doping with an element exhibiting more electrons, which are located in the conduction band, results in an n-type semiconductor.^[16-18] At the contact point of a p-type and an n-type semiconductor, electrons and holes recombine leading to an region free of charge carriers, the so-called depletion region (Figure 1.3a).^[19]

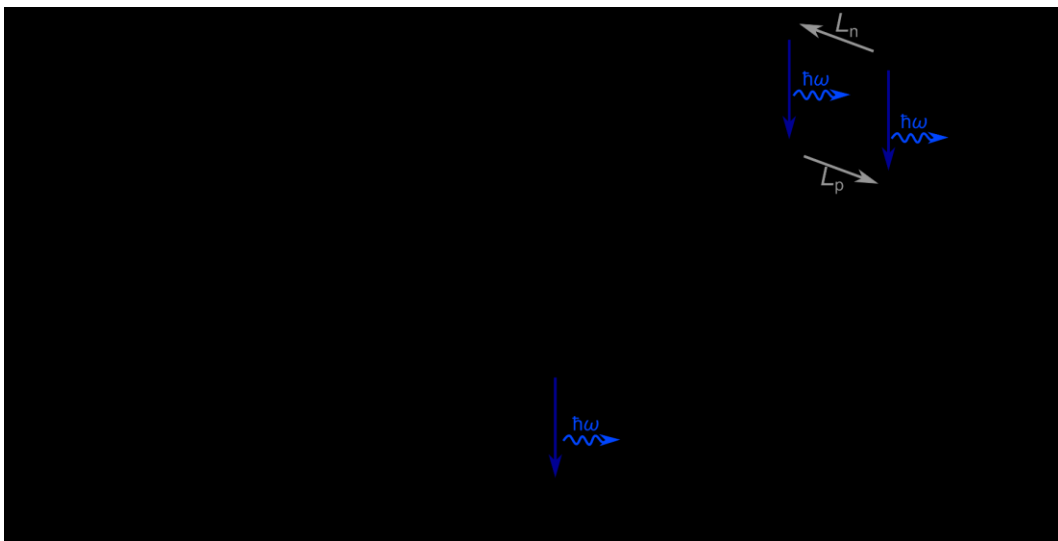


Figure 1.3. (a) Unbiased p-n-homojunction. Black dots as electrons, black circles as holes. W_D : thickness of the depletion region. (b) p-n-homojunction under forward bias. L_n and L_p with gray arrows: carrier diffusion length before recombination. Dark blue vertical arrows: electron-hole-recombination under emission of a photon (lighter blue $h\omega$) with emission color corresponding to E_g . (c) p-n-heterojunction under forward bias. W_{DH} : thickness of the double heterostructure active region. The charge carriers are confined by the barriers of the heterojunction.^[19]

By applying an electrical voltage that allows natural current flow, which is called forward bias, electrons and holes recombine at the p-n-junction leading to the emission of photons whose energy corresponds to the energetic separation of valence and conduction band, called band gap (E_g , Figure 1.3b). Therefore, LEDs always emit monochromatic light with a discrete energy and thus wavelength. The different types of semiconductors being elemental (e.g., Si or Ge) and compound semiconductors, denoted by the element group of which the semiconductor is made of, e.g., II-VI for ZnS or III-V for GaAs and GaN. When n- and p-type regions consist of the same semiconductor, the p-n-junction is named homojunction.^[16-18]

A so called double heterostructure is formed by combining two large band gap semiconductors with a small band gap semiconductor termed active region (Figure 1.3c). The charge carriers are restricted to the active region by the large band gap barrier. Since the thickness of the active region is much smaller than the diffusion length of the charge carriers, these have a much higher concentration compared to homojunctions, increasing the radiative recombination rate (Figure 1.3c).^[19]

Light generation in inorganic materials of LEDs is based on a phenomenon called electroluminescence, which was first described by *Round* in 1907 based on the glow of carborundum (SiC), a IV-IV compound semiconductor, crystals upon application of an electrical current.^[20] In 1927, *Losev* wrote the first publication on the emission of silicon carbide diodes and published the first paper on the LED.^[21-23] He also found that the light generation was based on a cold electronic discharge and could be very quickly turned on and off.^[19] In the difficult years during and after World War II, no one seized the chance to disseminate his expertise or to pursue the capability of his findings, so his much-deserved standing as one of the pioneering individuals of physics and engineering in the 20th century was never recognized.^[21] Therefore, it took multiple years for further developments in the field of LEDs. LED research was revived in the 1950s by the discovery of III-V semiconductors, which were previously unknown since this compound class does not appear naturally.^[19] In 1962, *Holonyak* and *Bevacqua* developed the first visible-light LED with GaAsP as a red emitting component.^[24] *Grimmeiss* and *Scholz* reported in 1964 on green emitting GaPN LEDs.^[25] Blue LEDs were fabricated in 1969 based on SiC, but due to its indirect band gap, power-conversion efficiencies were very low.^[19] *Craford et al.* reported on GaAsP based orange, yellow and green emitting LEDs in 1971 and 1972, thus most of the visible spectrum could be covered by LEDs.^[26, 27] The intensive exploration, variety of accessible colors and low costs through mass production led to the rapid commercialization of LEDs, which however were primarily used in niche areas like indicator lights in telephones or operator panels due to low efficiencies and restricted current densities leading to low brightness so that they could not be used for general lighting applications. Moreover, efficient blue emission remained a challenge since no appropriate large and direct band gap semiconductors with adequate quality were available then.^[28] GaN was considered for blue LEDs due to its large and direct band gap ($E_g = 3.4$ eV) and in 1968, *Maruska et al.* prepared the first single crystal films of GaN by halide vapor phase epitaxy (HVPE).^[29, 30] Those film showed intrinsic n-type conductivity while it was challenging to prepare GaN exhibiting p-type conductivity upon doping with Zn or Mg due to inferior crystal quality and impurity contamination.^[29] Finally, *Pankove et al.* reported on the first GaN based, green emitting prototype LED in 1971.^[31] However, samples prepared by HVPE suffer from severe contamination with oxygen or hydrogen which impedes practical applications.

The breakthrough of GaN based appliances started with the implementation of the metal-organic chemical vapor deposition (MOCVD) process in 1971, which led to the exclusion of contaminations.^[29, 32] This method was adapted by *Akasaki* and *Amano* to synthesize the first high-quality device-grade GaN layer in 1986.^[33] However, the challenge of conductivity with p-doped GaN still remained. Mg and Zn can be introduced into GaN during the MOCVD process, but they form hydride complexes due to H-containing starting materials.^[28] In 1988, *Amano et al.* discovered enhanced luminescence of Zn-doped GaN, denoted as GaN:Zn, prepared by MOCVD after annealing the samples with an electron beam in a scanning electron microscope (SEM).^[34] *Akasaki et al.* also reported on low resistant p-type GaN:Mg samples prepared by low energy electron beam irradiation (LEEBI) in a SEM.^[35] The underlying mechanism can be explained by generation of free electrons and holes due to excitation by the electron beam, which leads to breaking of acceptor-H bonds and releasing H₂.^[36] An easier way to decompose those complexes was found by *Nakamura* in 1992 through thermal annealing of those GaN films.^[37] Due to the band gap of GaN being 3.4 eV, emission should be located in the UV region, but remaining deeper lying acceptor-H levels lead to the observed blue emission. To achieve true blue emitting LEDs, the band gap of GaN has to be lowered by the introduction of e.g. In, which allows defined tuning the band gap and thus emission wavelength from 2.0 to 3.4 eV by varying the In content.^[29] *Nakamura et al.* reported on the first high quality Ga_{1-x}In_xN films leading to true blue and green emitting LEDs.^[29, 38] Eventually, *Amano*, *Akasaki* and *Nakamura* developed the key appliance structure which enabled true blue emission from nitride semiconductors.^[29] For these achievements, *Amano*, *Akasaki* and *Nakamura* were awarded the 2014 Nobel Prize in Physics "for the invention of efficient blue light-emitting diodes which has enabled bright and energy-saving white light sources".^[39] Since then, device architecture have further been optimized implementing the double heterostructure design (Figure 1.4).^[28]

As mentioned above, LEDs emit solely monochromatic light. However, for most applications and especially general lighting, white light is required, which can be achieved by additive color mixing in several approaches. First, multiple LED chips emitting different wavelengths like blue, yellow-green, and red can be combined. Despite tunability, this assemble has multiple drawbacks such as higher costs and complexity or low color rendering due to the narrow-emitted wavelengths. Furthermore, LEDs differ in their respective working lifetimes, which leads to dissimilar aging of the LEDs and a shift of the respective color points. Another problem of these arrays is the deficiency of LEDs with efficient green emission, to which the human eye is very responsive. This is called "green gap" and limits the luminous efficacy of such devices.^[6, 7, 28]

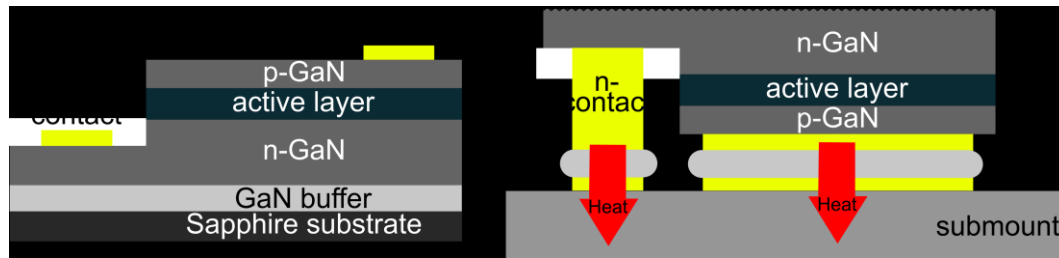


Figure 1.4. Ga_{1-x}In_xN chip designs. (a) Scheme of the first blue emitting Ga_{1-x}In_xN LED. The buffer layer accounts for lattice mismatches between the sapphire substrate and the n-GaN layer for improving the structural quality of the films.^[29] (b) Scheme of a state-of-the-art, thin-film, flip-chip LED. The improved heat dissipation, which is necessary due to ohmic resistance, allows higher current densities and therefore higher light output. The surface of the n-GaN layer is roughened to increase the light extraction efficiency. The active layer consists in both cases of a Ga_{1-x}In_xN double heterostructure.^[28]

Therefore, another design based on a blue emitting primary LED combined with a light conversion element, especially inorganic phosphors was implemented. The phosphors partly absorb the blue light, down-convert the energy and emit light with lower energy, i.e., longer wavelength, and thus are called phosphor-converted LEDs (pcLEDs). There are three main architectures of this approach (Figure 1.5): combining a blue primary LED with a yellow emitting phosphor (1pcLED), yellow-green and orange-red phosphors (2pcLEDs) or full-conversion by near-UV (nUV) emitting LEDs with blue, yellow-green and orange-red phosphors (RGB-pcLED).^[6, 7] The first commercialized white 1pcLEDs used broadband yellow emitting $Y_{3-x}Gd_xAl_{5-y}Ga_yO_{12}:Ce^{3+}$ (YAG:Ce³⁺) excited by a blue Ga_{1-x}In_xN primary LED, but its application is limited to the automotive section due to a high CCT and low CRI upon lacking red spectral portions.^[40, 41] This can be improved by adding one or more red emitting phosphors leading to the most common and relevant 2pcLED approach, which results in higher CRI and lower CCT, thus making these LEDs suitable for illumination-grade lighting applications.^[42-47] The CRI can further be improved by RGB-pcLEDs due to coverage of the whole visible spectrum but efficiency may suffer due to the nUV-LED and repetitive conversion of energy by the sequence of green-yellow and finally orange-red emission.^[6]

LEDs offer many advantages compared to incandescent bulbs like a simple design, higher cost effectiveness, great versatility in different application areas given by the controllability of spectral properties like emitted wavelength, CCT or CRI due to the combination of different phosphors, and technical aspects such as accessible form factors and, most important, higher energy efficiency. This is particularly very important in order to achieve the goals mentioned at the beginning of this thesis in order to reduce the emissions of greenhouse gases and thus minimizing climate change and its damaging consequences. However, further improvements have still to be achieved to meet the goals.

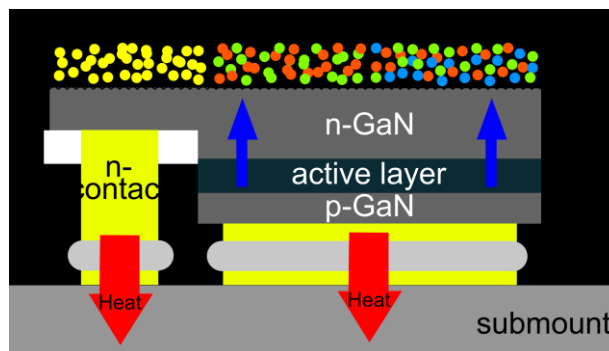


Figure 1.5. Schematic pcLED chip designs based on a state-of-the-art, thin-film, flip-chip LED emitting blue or nUV light, which excites the different phosphors and leads to white light upon additive color mixing.^[28]

1.3 Basic Principles of Solid-State Luminescence

The term luminescence was first introduced in 1888 by *Wiedemann* and describes light phenomena that are not caused by temperature contrary to the case with incandescent bulbs.^[48] It can be further divided into the type of excitation (e.g., photoluminescence due to electromagnetic radiation, electroluminescence upon an electric voltage or chemiluminescence resulting from the energy of a chemical reaction) and form of emission (e.g., fast and spin-allowed ($\Delta S = 0$) fluorescence or slow and spin-forbidden ($\Delta S = 1$) phosphorescence). In the following, we refer to the most common term luminescence. A luminescent solid material, which transforms one of these energy forms into electromagnetic radiation, is called phosphor.^[49] To obtain luminescence from a phosphor, point defects have to be introduced into an optical transparent material called host. This can be achieved by the accurate incorporation, i.e., doping, of activator ions with energy levels that can be populated by excitation onto cation sites with similar size and charge in the host lattice.^[50, 51] These energy levels are energetically located within the band gap of the host material and lead to new absorption and emission bands. Only few elements are optically active with suitable energy levels and can be incorporated into host structures. Transition metal ions and especially rare earth ions like Eu^{2+} and Ce^{3+} fulfill these conditions.^[6, 16, 52, 53]

The steps involved in the luminescence process of an activator ion can be illustrated by a configurational coordinate diagram, which plots the potential energy of the activator ions ground ($4f$) and excited ($5d$) states against the configuration coordinate r (Figure 1.6).

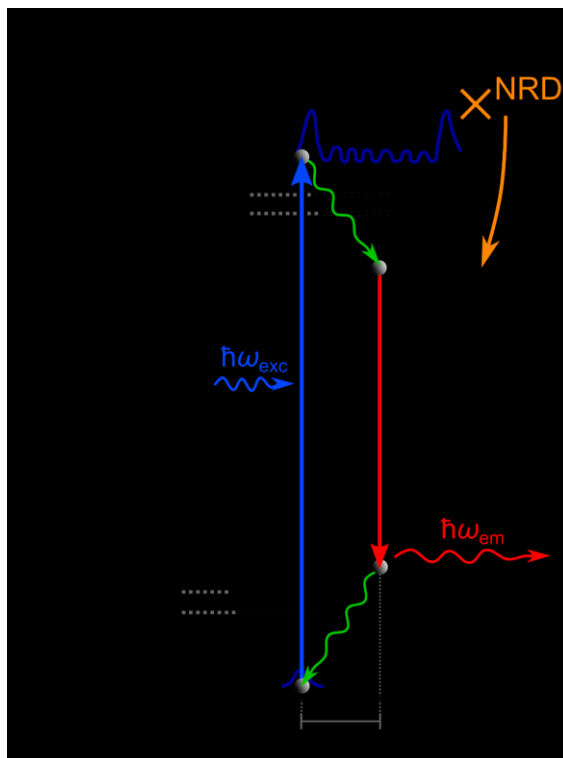


Figure 1.6. Configuration-coordination diagram of an activator ion with broadband emission. Absorption of a photon ($\hbar\omega_{\text{exc}}$) leads to excitation of an electron (gray sphere) from the ground to the excited state (blue arrow). After vibrational relaxation into the electronically excited state (green arrow), the electron returns to vibrationally excited states in the electronic ground state upon emission of a photon with lower energy ($\hbar\omega_{\text{em}}$, red arrow) and finally, returns to the vibrational ground state after vibrational relaxation (green arrow). Black horizontal lines indicate vibrational states with energetic separation $\hbar\omega_{\text{g}}$ or $\hbar\omega_{\text{e}}$ in the ground and excited state, respectively. Vertical arrows represent electronic transitions, which occur much more rapidly than vibrational interactions. Wave functions, which can be explained by a harmonic oscillator, are exemplarily shown for the vibrational ground and an excited state in dark blue. Nonradiative decay (NRD, orange arrow) upon thermal excitation of an excited electron leads to a return to the ground state without the emission of a photon. r_{g} and r_{e} denote the activator-ligand distances in the ground and excited states, respectively, and Δr the distance shift caused by different (often weaker) activator-ligand distances following excitation. Only the transitions with maximum intensity are shown.^[54-56]

First, an electron is excited from the energetic ground state to a vibrationally and electronically excited state upon absorption of a high energetic photon, which is emitted by the blue primary LED in a pcLED device. Then, the electron relaxes nonradiative, i.e., without emission of a photon due to very fast relaxation rates, to the vibrational ground level by transferring the excess energy to the surrounding lattice in form of lattice vibrations. From there, the electron returns spontaneously to a vibrationally excited state in the electronic

ground state upon emission of a photon followed by a fast relaxation to the vibrational ground state. Due to the vibrational relaxation processes, the emitted photon has a lower energy than the absorbed photon and therefore, the emitted wavelength is red-shifted, i.e., down converted or, since the processes take place in the phosphor, phosphor-converted. In principle, the vibrational motion in this system acts like a harmonic oscillator with ω being the frequency of the oscillator. At absolute zero temperature, only the lowest vibrational levels are occupied, whereas higher temperatures lead to the occupation of higher vibrational levels. The highest probability of finding the system in the vibrational ground state ($\hbar\omega = 0$) is at r_g or r_e , whereas the probability of finding the system being in vibrationally excited states ($\hbar\omega > 0$) is at the edges of the parabola ($r \neq r_g$ or r_e), independent of the system being in the electronic ground or excited state (see dark blue wave functions in Figure 1.6). Therefore, excitation occurs from the vibrational ground state at r_g , where the wave function has its maximum value, and the transition ends at the edge of the parabola of the excited state, since the vibrational excited states have their maximum values and thus highest probability there. This resembles the maximum of the absorption band. However, it is also possible, even though less probable, for transitions to occur from $r \neq r_g$ or to not the edges of the excited parabola, which results in the observable width of the absorption band. Hence, the band widths increase with higher Δr values. The same applies for the emission process. The energetic difference between the maxima of the absorption and emission bands is called Stokes shift, which is higher for larger values of Δr and thus larger optical band widths. The Stokes shift can be calculated by Equation 1.1,^[49]

$$E_{\text{Stokes}} = 2S \times \hbar\omega \quad (1.1)$$

whereby the Huang-Rhys coupling constant S is proportional to $(\Delta r)^2$ and is a measure for the strength of the electron-phonon coupling and thus depends on the rigidity of the host structure, with high rigidity corresponding to small S values. A large Δr results in more possible transitions and thus, broader bands. As described above, ω corresponds to phonon frequencies and depends on the atomic weight of the atoms in the host structure, whereby atoms with large molar masses correspond to small ω values and therefore, a small Stokes shift.^[49, 54] It can be seen from these considerations, that narrow band emission is associated with rigid host structures incorporating atoms with high molar masses. The configurational coordinate diagram additionally illustrates the temperature-dependent quenching of luminescence in a simple way. A nonradiative decay, i.e., radiation-free return along the branches of the parabola to the ground state solely through vibrational relaxation, is possible when an excited electron is further excited to the intersection of the two parabolas. The activation energy required for this additional excitation can be supplied by higher temperatures, i.e. thermal activation.^[54]

As already briefly indicated, the electronic processes in the activator ion cannot be considered independently of the host lattice. The electronic configuration of e.g., Eu^{2+} is $[\text{Xe}]4f^7$ or $5s^25p^65d^04f^7$, respectively, and therefore, the electronic transitions take place between the occupied $4f^7(^8S_{7/2})$ ground state and the unoccupied $5d$ levels, leading to the $4f^6(^7F_0)5d^1$ excited state (Figure 1.7).

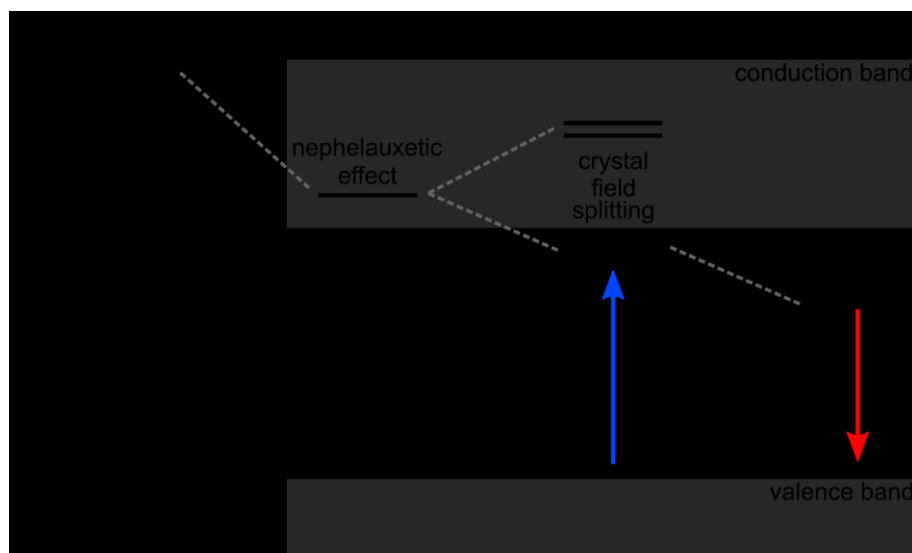


Figure 1.7. Schematic illustration of the influence of local structure and environment on the $5d$ levels of rare earth activator ions in a host lattice compared to the free ion. Energetic difference between conduction and valence band corresponds to the band gap.^[6, 52, 57]

The $4f$ states are energetically deeper lying and shielded by the outer $5s^2$ and $5p^6$ orbitals, so that they are nearly unaffected by the ligands of the host material, which is in contrast to the outer lying and strongly by the host affected $5d$ levels.^[16] Since the $4f \rightarrow 5d$ transitions are parity- and spin-allowed, absorption and emission bands are broad and intense.^[16, 49, 53] There are three major impacts of the host lattice on the energetic position of the $5d$ levels compared to the free ion, whose emission for Eu^{2+} is located in the UV region ($\lambda_{\text{em}} \approx 295 \text{ nm}/33,856 \text{ cm}^{-1}$).^[58] First, the nephelauxetic effect, also known as cloud-expanding effect or centroid shift, is a measure for the covalency of the activator-ligand bond. The higher the covalency, the higher is the overlap between activator and ligand orbitals and therefore, the electron repulsion decreases due to greater electron delocalization resulting in a lowering of orbital energies compared to the free non-coordinated ion.^[16, 49] Second, the crystal field splitting refers to the splitting of previously degenerate $5d$ orbitals and affects the absorption band of the activator ion. The degree of this splitting depends on the coordination geometry and symmetry, coordination number, activator-ligand bond lengths and coordinating anion with its size and charge. Splitting of the previously degenerate $5d$ orbitals leads to partly energetically lowered $5d$ levels and therefore, the absorption and $4f \rightarrow 5d$

transition is red-shifted.^[7, 16, 49] Finally, the aforementioned Stokes shift, which describes the energetic difference between absorption and emission band maxima, influences the emission and depends on the rigidity of the host lattice. After excitation of an electron into the vibrationally excited $5d$ levels, some of this energy is transferred to the host lattice as nonradiative relaxation into the vibrational ground state of the electronically excited state before the radiative return to the ground state. Due to the nonradiative energy dissipation, the emission occurs at lower energy than excitation, leading to a red shift. A small Stokes shift, i.e., small Δr , is desired for reaching high luminescence because it avoids too strong overlap between the absorption and emission bands and therefore, very broad bands, which would otherwise result in reabsorption of emitted light by the emitting activator ion, and strong thermal quenching.^[16, 49]

It can be seen from the previous considerations that the energetic positions of the $5d$ levels and thus the emission properties like spectral position and shape of the emission band are highly sensitive to the local surrounding of the activator ion. This offers a high potential for tuning specific emission properties for the desired applications by variations in the crystal structure of the host material.

1.4 Structural Chemistry of (Oxo)nitridosilicates

In the previous chapter, it was shown that the emission properties of the activator ion strongly depend on the host material, which has to meet several requirements to be considered for usage in applied phosphors. The host is required to exhibit a large band gap ($E_g \geq 4$ eV), so that it is optically transparent and activator ions absorption and emission processes can take place. Furthermore, this ensures that the energetic separation between the $5d$ levels of the activator ion and the conduction band of the host is large enough to avoid unwanted energy loss due to thermal activation of the excited electron into the conduction band, which is then withdrawn from the luminescence process resulting in low quantum efficiencies.^[59] Additionally, an ideal host material should offer high thermal and chemical stability against thermal degradation and hydrolysis or oxidation for long-time stability.^[55] A compound class, which fulfills all of the mentioned requirements and is therefore very well suited as host materials, are (oxo)nitridosilicates. However, nitridosilicates do not occur naturally due to the presence of oxygen and the higher stability of oxides. The only exception from this is $\text{Si}_2\text{N}_2\text{O}$, which is usually of meteoritic origin.^[60] This shows that the synthesis of nitridosilicates is more complex compared to oxosilicates, which can be explained by dissimilar physical and chemical properties of oxygen and nitrogen. O_2 contains a double bond with a binding enthalpy of $\Delta H = 498 \text{ kJ}\cdot\text{mol}^{-1}$, a high electron affinity of elemental oxygen ($E_{\text{EA}} = -1.46$ eV), so that it can easily be reduced to O^{2-} , and in the case of naturally occurring triplet oxygen exhibits two unpaired electrons (diradical), which in summary makes oxygen highly reactive.

N_2 in contrast contains a much more stable triple bond with a much higher binding enthalpy of $\Delta H = 945 \text{ kJ}\cdot\text{mol}^{-1}$, a positive electron affinity of elemental nitrogen ($E_{EA} = 0.07 \text{ eV}$), which makes reduction to N^{3-} difficult, and only paired electrons. Therefore, N_2 is highly unreactive at ambient temperature, which is why nitrogen is often used as inert gas to protect sensitive substances from contact with oxygen and why nitridosilicates require harsher synthesis conditions.^[61] Nevertheless, the advantage offered by nitridosilicates, despite challenging synthesis conditions, is the significantly extended structural diversity compared to silicates. Oxo- and nitridosilicates are built from condensed $[\text{SiO}_4]$ or $[\text{SiN}_4]$ tetrahedra. While oxygen can only bind to silicon in a terminal (oxygen bond to one silicon is denoted as $O^{[1]}$) or single-bridging ($O^{[2]}$) manner and solely through common corners, nitrogen occurs additionally threefold- ($N^{[3]}$) and fourfold-bridging ($N^{[4]}$), both corner and edge linked. This leads to a higher achievable degree of condensation, which gives the molar ratio of tetrahedra centers to corners, i.e., $\kappa = n(\text{Si})/n(\text{N},\text{O})$. The lowest value $\kappa = 1/4$ corresponds to isolated $[\text{SiO}_4]$ or $[\text{SiN}_4]$ tetrahedra, while the binary species SiO_2 and Si_3N_4 reach the maximum values of $\kappa = 1/2$ and $\kappa = 3/4$ limited by electrostatics.^[60, 62] The condensed tetrahedra build up rings, chains, layers or networks, whose voids can be filled by metal ions like alkaline earth or rare earth ions for charge compensation and stability. This all leads to a considerably advanced structural variety of nitridosilicates.^[60] Combining different cations with diverse valence states facilitate the formation of various crystal structures. These ions can be substituted by similar sized and charged activator ions like Eu^{2+} or Ce^{3+} to create phosphors. As a result, (oxo)nitridosilicates are not only suitable as host materials, but also offer numerous possibilities for tuning luminescence properties to adapt for the desired applications due to the large chemical and structural variety.^[6, 16, 52]

As depicted in the previous chapter, the distinct luminescence properties of the activator ions are influenced by the nephelauxetic effect, crystal field splitting and Stokes shift. The nephelauxetic effect depends on the nature of the ligands. Nitrogen offers a smaller electronegativity compared to oxygen ($\chi_{\text{Pauling}}(\text{N}) = 3.04$, $\chi_{\text{Pauling}}(\text{O}) = 3.44$), which results in a higher covalency of the activator-ligand bond and thus an energetic decrease of the $5d$ levels. Going from nitrogen to carbon, which offers an even higher electronegativity ($\chi_{\text{Pauling}}(\text{C}) = 2.55$), the covalency of the activator-ligand bond is further increased.^[6, 16, 63] Additionally, the higher charge of nitrogen, shorter activator-ligand bond lengths and pronounced variety of structural possibilities and thus local structures surrounding the activator ions results in a larger crystal field splitting and a further lowering of the $5d$ states compared to oxygen. Moreover, the structural benefits like higher degree of condensation improve structural rigidity, which is necessary for a small Stokes shift resulting in narrow-band emission, lower thermal quenching, and higher efficiency. All those effects combined lead to a red-shift of absorption and emission bands, which enables the efficient absorption

of nUV or blue light, e.g., from a blue $\text{Ga}_{1-x}\text{In}_x\text{N}$ primary LED, and allows for emission covering the whole visible spectrum.^[6, 16]

The structural variability of (oxo)nitridosilicates allows for tuning the emission properties and adapting to the desired application. Not only the substitution of oxygen by nitrogen leads to a shift in the emission band but also variation of cation sizes due to different alkaline earth or rare earth ions. Upon doping, Eu^{2+} occupies preferably alkaline earth ion sites like Sr^{2+} , which determines the coordination sphere and thus the crystal field splitting. Substitution of Sr^{2+} by a larger cation like Ba^{2+} leads to sites with larger metal-ligand distance and therefore, a smaller crystal field splitting resulting in a blue-shifted emission.^[52, 58] Spectral tuning of phosphors is a perennial subject of both scientific and technical importance because it allows to understand structure-property relations and provide recommendations on designing and developing phosphors with adjustable emission colors and spectral properties along with improved luminescence efficiency and thermal stability to optimize the phosphors for practical applications.^[52]

The trend of adapting emission properties through atomic substitutions can be seen by the evolution of pcLEDs. One of the first phosphors relevant for application was yellow emitting $\text{Y}_{3-x}\text{Gd}_x\text{Al}_{5-y}\text{Ga}_y\text{O}_{12}:\text{Ce}^{3+}$ (YAG: Ce^{3+}), which was used in 1pcLEDs due to its broadband emission. This broad emission originates from the spin- and parity-allowed $5d^1 \rightarrow 4f^1$ transition of Ce^{3+} , whereby the $4f^1$ ground state is split into two levels $^2F_{5/2}$ and $^2F_{7/2}$ separated by approx. 2000 cm^{-1} due to spin-orbit coupling, resulting in a double-band shape.^[49] The observed broadband yellow emission is suitable for generation white light in combination with a blue emitting $\text{Ga}_{1-x}\text{In}_x\text{N}$ primary LED. However, the emission band does not cover the red spectral region which leads to cool-white light with a high CCT but low CRI and therefore, limits possible application fields to e.g., the automotive sector (Figure 1.8).^[40, 41, 64]

Phosphors for application in residential lighting require lower CCT but higher CRI values, for which deep red-emitting phosphors are responsible. This can be achieved by the implementation of nitrides leading to red-emitting phosphors. Industrial relevant orange-red emitting phosphors used in 2pcLEDs are $(\text{Ba},\text{Sr})_2\text{Si}_5\text{N}_8:\text{Eu}^{2+}$ ($\lambda_{\text{em}} \approx 590\text{--}625 \text{ nm}$, full width at half-maximum (*fwhm*) $\approx 2050\text{--}2600 \text{ cm}^{-1}$) and $(\text{Sr},\text{Ca})\text{AlSiN}_3:\text{Eu}^{2+}$ ($\lambda_{\text{em}} \approx 610\text{--}660 \text{ nm}$, *fwhm* $\approx 2100\text{--}2500 \text{ cm}^{-1}$), whose advantages are tunability, high thermal and chemical stability, high efficiencies and color rendition.^[43-47, 66] However, due to their rather broad emission bands, they emit in the deep and infrared (IR) spectral range ($\lambda > 650 \text{ nm}$), which cannot be perceived by the human eye and leads to energy losses and consequently, low energy efficiencies.

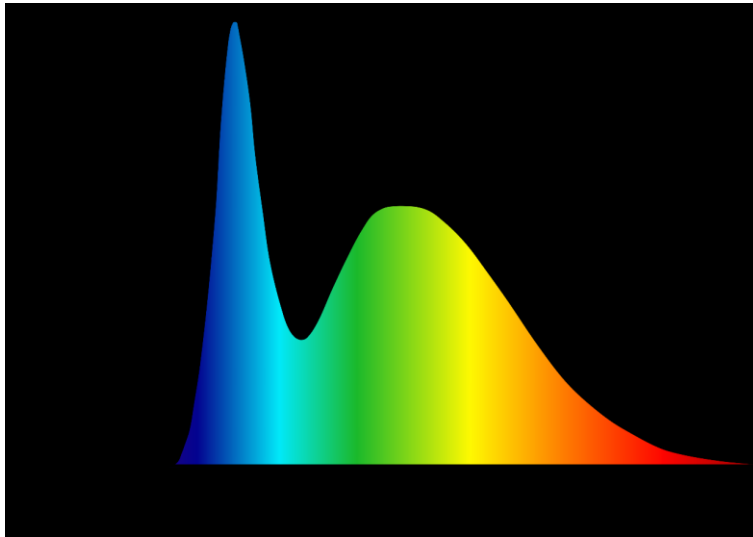


Figure 1.8. Emission spectrum of a white light emitting 1pcLED consisting of a blue $\text{Ga}_{1-x}\text{In}_x\text{N}$ primary LED ($\lambda_{\text{em}} = 460 \text{ nm}$, $\text{fwhm} = 30 \text{ nm}$) and $\text{YAG}:\text{Ce}^{3+}$ ($\lambda_{\text{em}} = 555 \text{ nm}$, $\text{fwhm} = 160 \text{ nm}$) as the phosphor.^[65]

This phenomenon is commonly known as IR spill-over.^[28, 42, 45, 47, 66-69] Therefore, efficient narrow-band red-emitting phosphors are highly desired since they lower IR spill-over and increase efficiencies (Figure 1.9).

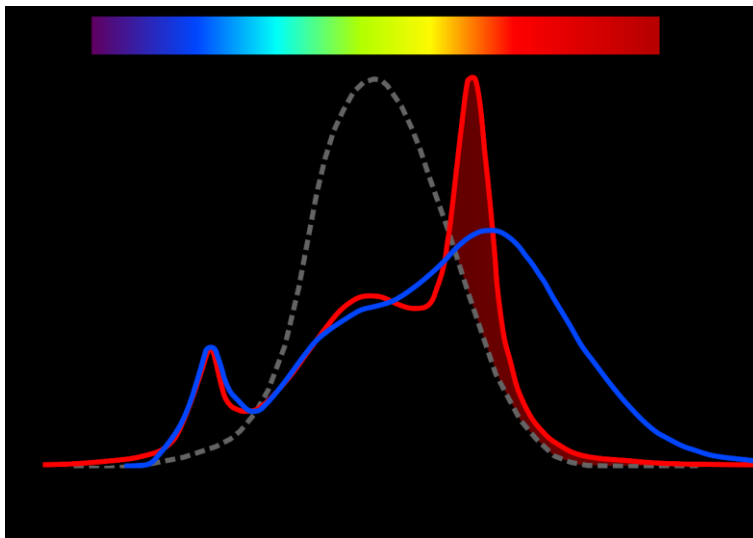


Figure 1.9. Comparison of the wavelength dependent emission spectra of various lighting technologies. Black curve: emission of an incandescent light bulbs with high emission in the IR region ($\lambda > 740 \text{ nm}$). Blue curve: state-of-the-art high CRI LED (3000 K, CRI 90). Red curve: demonstrated spectrum of a high CRI pcLED using a narrow-red phosphor ($\text{fwhm} = 30 \text{ nm}$). Gray dotted line: eye sensitive curve ($\lambda_{\text{max}} = 555 \text{ nm}$). Insert: visible spectrum with corresponding color perception. Red area: low photopic sensitivity but improved color rendition.^[7, 68-70]

Auspicious contenders for efficient and narrow-band red-emitting phosphors are $\text{Sr}[\text{LiAl}_3\text{N}_4]:\text{Eu}^{2+}$ (SLA, $\lambda_{\text{em}} = 650 \text{ nm}$, $\text{fwhm} = 50 \text{ nm}/1180 \text{ cm}^{-1}$, Figure 1.10),

Sr[Li₂Al₂O₂N₂]:Eu²⁺ (SALON, $\lambda_{em} = 614 \text{ nm}$, $fwhm = 48 \text{ nm}/1286 \text{ cm}^{-1}$) and Sr[Mg₃SiN₄]:Eu²⁺ (SMS), which is up to now the most narrow orange-red emitting Eu²⁺-doped nitride phosphor ($\lambda_{em} = 615 \text{ nm}$, $fwhm = 43 \text{ nm}/1170 \text{ cm}^{-1}$).^[71-73]

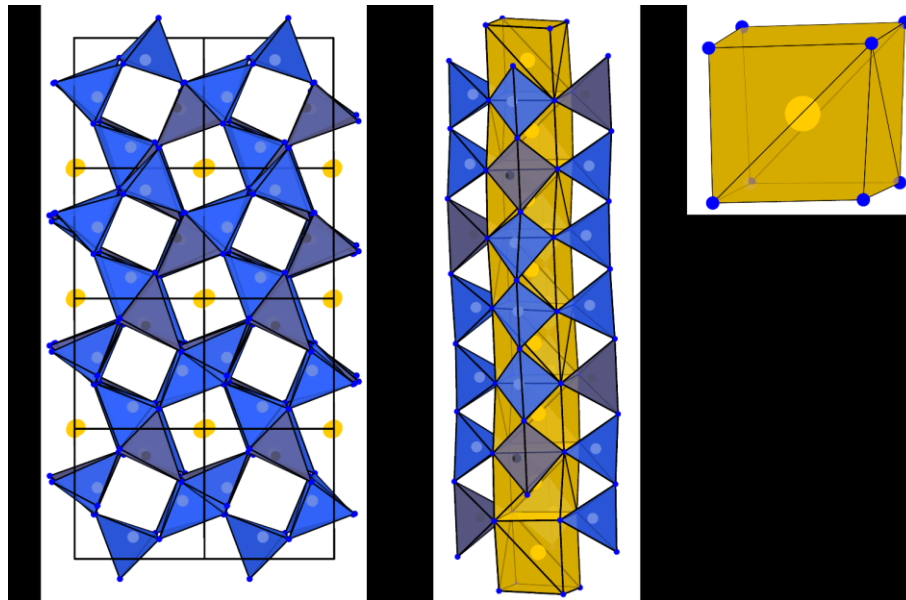


Figure 1.10. Crystal structure of Sr[LiAl₃N₄]. (a) 2×2×2 structure viewed along [011]. (b) Stack of cuboid-like [SrN₈] polyhedra linked via common faces with coordination by [AlN₄] and [LiN₄] tetrahedra. (c) Detailed view of a cuboid-like [SrN₈] polyhedron. Sr in yellow, [AlN₄] as light blue tetrahedra, [LiN₄] as dark blue tetrahedra, [SrN₈] as yellow polyhedra.^[71]

They crystallize in the highly symmetric UCr₄C₄ or therefrom derived structure types and have structural characteristics such as a highly condensed anionic network, cation ordering, and highly symmetric crystallographic activator sites with roughly equal activator-ligand distances in common, which are advantageous for narrow-band emitting phosphors. SLA was shown to increase luminous efficacy of a prototype pcLED by 14% compared to commercially available high CRI LED using (Ba,Sr)₂Si₅N₈:Eu²⁺ or (Sr,Ca)AlSiN₃:Eu²⁺.^[71] Nevertheless, SLA suffers from moisture sensitivity, which hinders practical application without additional stabilization.^[52] SALON is a good example for a blue-shifted emission upon incorporation of oxygen, but does not meet the required narrow-band emission of 30 nm.^[9, 69] Although SMS is the narrowest orange-red emitting Eu²⁺-doped nitride phosphor, it cannot be used for practical application due to its small band gap resulting in high thermal quenching.^[73]

Research is not only focused on narrow red-emitting phosphors for improving CRI and efficiency, but is also focused on narrow-band green-emitting phosphors (e.g. Ba₂LiSi₇AlN₁₂:Eu²⁺: $\lambda_{em} = 515 \text{ nm}$, $fwhm = 61 \text{ nm}/2280 \text{ cm}^{-1}$; Ba[Li₂(Al₂Si₂)N₆]:Eu²⁺:

$\lambda_{em} = 532 \text{ nm}$, $fwhm = 57 \text{ nm}/1962 \text{ cm}^{-1}$) for improving backlighting in liquid crystal displays due to the high wavelength-sensitivity of the human eye located in the green spectral region.^[71, 74-76] Furthermore, today's research tends towards enlarged application of RGB-pcLEDs for improved efficiency and to precisely match and stabilize color points, for which narrow blue-emitting phosphors (e.g. $\text{Sr}_{0.25}\text{Ba}_{0.75}\text{Si}_2\text{O}_2\text{N}_2:\text{Eu}^{2+}$: $\lambda_{em} = 472 \text{ nm}$, $fwhm = 37 \text{ nm}$) are necessary.^[77, 78]

Although a lot of research has previously been done, it is still essential to further modify known phosphors as well as explore previously unknown structures and compound classes for the development of new efficient, narrow-band emitting phosphors with enhanced luminescent properties relevant for applications. This can be achieved by the substitution of alkaline earth (*AE*) and rare earth (*RE*) ions, anionic substitution (N, O, C) or substitution of chemical units like *AEO* by *REN* and vice versa, possibly leading to new structural motifs and surroundings for the activator ions.^[52] Oxonitridosilicates have already proven themselves as suitable host materials. Alkaline earth ions are necessary to provide the sites suitable for occupation by Eu^{2+} upon doping. Rare earth ions are not only providing sites dopable with Ce^{3+} but also improve structural stability due to their higher charge and can positively influence the Stokes shift since their small size but high atomic weight increase rigidity and diminish phonon frequencies. This confirms that alkaline and rare earth oxonitrido(carbido)silicates are very fascinating compound classes due to their impressive structural possibilities, chemical and physical stability, suitability as phosphor materials and modifiability of luminescence properties. To synthesize this promising compounds, new strategies have to be explored. The latest and advanced methods providing high-resolution data are essential for the precise elucidation of rather complex crystal structures, which was not possible in the past. Extensive investigations of luminescence properties or band structures are essential to completely understand the effects of varying *RE* and *AE* on band structures, band gap size and the position of Eu^{2+} *5d* levels and hence, allow improving and possibly tuning luminescence properties. Such data facilitate more accurate declarations about structure-property relations and may specify how to optimally adapt phosphors to the required applications and in terms of energy efficiency.

In the current context of climate change and its dramatic consequences, a significant reduction of energy consumption or avoidance of energy loss is urgently necessary to reduce CO_2 emission and therefore, help to meet the goals of the Paris Climate Agreement.

1.5 Scope of this Thesis

This thesis is focused on the explorative synthesis and characterization of novel phosphors based on Eu^{2+} - or Ce^{3+} -doped oxonitrido(carbido)silicates with variation of alkaline earth and rare earth metal ions through high-temperature reactions using different synthesis routes. The crystal structures of the presented multinary compounds were solved and refined based on the latest state-of-the-art crystallographic techniques like powder and single-crystal diffraction with X-ray or microfocused synchrotron radiation and transmission or scanning electron microscopy (TEM and SEM). Moreover, the optical properties were thoroughly investigated using UV/Vis and luminescence measurements. Previously unknown crystal structures are desired upon implementation of multiple cations and anions with different chemical properties like valence states or bonding characteristics. This combination enables the charge neutral substitution of *REN* by *AEO* and vice versa, which leads to certain phase widths and slightly different surroundings of the activator ions and therefore, allows for tunability of the luminescence characteristics adapting them to match with the desired requirements for applications as down-conversion materials in solid-state lighting.

1.6 References

- [1] Deutsche Meteorologische Gesellschaft Deutsches Klima-Konsortium, Deutscher Wetterdienst, Extremwetterkongress Hamburg, Helmholtz-Klima-Initiative, klimafakten.de, *Was wir heute übers Klima wissen - Basisfakten zum Klimawandel, die in der Wissenschaft unumstritten sind*, **2021**.
- [2] Deutsche Akademie der Naturforscher Leopoldina e. V., *Klimawandel: Ursachen, Folgen und Handlungsmöglichkeiten*, **2021**.
- [3] United Nations Climate Change Conference, *Paris Agreement*, **2015**.
- [4] C. Elliott, M. Yamada, J. Penning, S. Schober, K. Lee, *Energy Savings Forecast of Solid-State Lighting in General Illumination Applications*, U.S. Department of Energy, Office of Energy Efficiency and Renewable Energy, Building Technologies Office, Washington, D.C., **2019**.
- [5] Bundesministerium für Wirtschaft und Klimaschutz, *Gesamtausgabe der Energiedaten – Datensammlung des BMWK*, **2022**, <https://www.bmwk.de/Redaktion/DE/Artikel/Energie/energiedaten-gesamtausgabe.html>, visited on April 19th, 2022.
- [6] A. Kitai, *Materials for Solid State Lighting and Displays*, John Wiley and Sons, West Sussex, **2017**.
- [7] N. C. George, K. A. Denault, R. Seshadri, *Annu. Rev. Mater. Res.* **2013**, 43, 481–501.
- [8] J. McKittrick, L. E. Shea-Rohwer, *J. Am. Ceram. Soc.* **2014**, 97, 1327–1352.

- [9] M. Pattison, M. Hansen, N. Bardsley, C. Elliott, K. Lee, L. Pattison, J. Tsao, *2019 Lighting R&D Opportunities*, U.S. Department of Energy, Office of Energy Efficiency and Renewable Energy, Building Technologies Office, Washington, D.C., **2020**.
- [10] *Solid-State Lighting R&D Plan*, U.S. Department of Energy, Office of Energy Efficiency and Renewable Energy, Building Technologies Office, Washington, D.C., **2016**.
- [11] C. Feldmann, *Z. Anorg. Allg. Chem.* **2012**, 638, 2169–2171.
- [12] European Commission, *FAQ: phasing out conventional incandescent bulbs*, **2009**, https://ec.europa.eu/commission/presscorner/detail/en/MEMO_09_368, visited on April 19th, 2022.
- [13] J. Penning, K. Stober, V. Taylor, M. Yamada, *Energy Savings Forecast of Solid-State Lighting in General Illumination Applications*, U.S. Department of Energy, Office of Energy Efficiency and Renewable Energy, Building Technologies Office, Washington, D.C., **2016**.
- [14] *Energy Savings Forecast of Solid-State Lighting in General Illumination Applications*, U.S. Department of Energy, Office of Energy Efficiency and Renewable Energy, Building Technologies Office, Washington, D.C., **2014**.
- [15] McKinsey & Company, *Lighting the way: Perspectives on the global lighting market (2nd edition)*, **2012**, https://www.mckinsey.com/~media/mckinsey/dotcom/client_service/automotive%20and%20assembly/lighting_the_way_perspectives_on_global_lighting_market_2012.ashx, visited on April 19th, 2022.
- [16] R.-J. Xie, Y. Q. Li, N. Hirosaki, H. Yamamoto, *Nitride Phosphors and Solid-State Lighting*, Taylor & Francis, Boca Raton, **2011**.
- [17] J. P. Colinge, C. A. Colinge, *Physics of Semiconductor Devices*, Springer, Boston, **2005**.
- [18] M. Born, T. Jüstel, *Chem. Unserer Zeit* **2006**, 40, 294–305.
- [19] E. F. Schubert, *Light-Emitting Diodes (2nd edition)*, Cambridge University Press, Cambridge, **2006**.
- [20] H. J. Round, *Electr. World* **1907**, 19, 309–310.
- [21] N. Zheludov, *Nat. Photonics* **2007**, 1, 189–192.
- [22] O. V. Losev, *Telegrafiya i Telefoniya bez Provodov (transl. Wireless Telegraphy and Telephony)* **1927**, 44, 485–494.
- [23] O. V. Losev, *Lond. Edinb. Dublin Philos. Mag. J. Sci.* **1928**, 6, 1024–1044.
- [24] N. Holonyak, S. F. Bevacqua, *Appl. Phys. Lett.* **1962**, 1, 82–83.
- [25] H. G. Grimmeiss, H. Scholz, *Phys. Lett.* **1964**, 8, 233–235.
- [26] W. O. Groves, A. H. Herzog, M. G. Craford, *Appl. Phys. Lett.* **1971**, 19, 184–186.
- [27] M. G. Craford, R. W. Shaw, A. H. Herzog, W. O. Groves, *J. Appl. Phys.* **1972**, 43, 4075–4083.

- [28] P. Pust, P. J. Schmidt, W. Schnick, *Nat. Mater.* **2015**, *14*, 454–458.
- [29] H. P. Maruska, W. C. Rhines, *Solid-State Electron.* **2015**, *111*, 32–41.
- [30] H. P. Maruska, J. J. Tietjen, *Appl. Phys. Lett.* **1969**, *15*, 327–329.
- [31] J. I. Pankove, E. A. Miller, J. E. Berkeyheiser, *RCA Rev.* **1971**, *32*, 383–392.
- [32] H. M. Manasevit, F. M. Erdmann, W. I. Simpson, *J. Electrochem. Soc.* **1971**, *118*, 1864–1868.
- [33] H. Amano, N. Sawaki, I. Akasaki, Y. Toyoda, *Appl. Phys. Lett.* **1986**, *48*, 353–355.
- [34] H. Amano, I. Akasaki, T. Kozawa, K. Hiramatsu, N. Sawaki, K. Ikeda, Y. Ishii, *J. Lumin.* **1988**, *40–41*, 121–122.
- [35] H. Amano, M. Kito, K. Hiramatsu, I. Akasaki, *Jpn. J. Appl. Phys.* **1989**, *28*, L2112–L2114.
- [36] J. A. Van Vechten, J. D. Zook, R. D. Horning, B. Goldenberg, *Jpn. J. Appl. Phys.* **1992**, *31*, 3662–3663.
- [37] S. Nakamura, T. Mukai, M. Senoh, N. Iwasa, *Jpn. J. Appl. Phys.* **1992**, *31*, L139–L142.
- [38] S. Nakamura, T. Mukai, *Jpn. J. Appl. Phys.* **1992**, *31*, L1457–L1459.
- [39] J. Heber, *Nat. Phys.* **2014**, *10*, 791.
- [40] G. Blasse, A. Brill, *Appl. Phys. Lett.* **1967**, *11*, 53–55.
- [41] Z. Xia, A. Meijerink, *Chem. Soc. Rev.* **2017**, *46*, 275–299.
- [42] J. L. Leaño Jr., M.-H. Fang, R.-S. Liu, *ECS J. Solid State Sci. Technol.* **2018**, *7*, R3111–R3133.
- [43] R. Mueller-Mach, G. Mueller, M. R. Krames, H. A. Höpfe, F. Stadler, W. Schnick, T. Jüstel, P. Schmidt, *Phys. Status Solidi A* **2005**, *202*, 1727–1732.
- [44] M. Krames, G. O. Mueller, R. Mueller-Mach, H. Bechtel, P. J. Schmidt, *PCT Int. Appl.* **2010**, WO2010131133A1.
- [45] K. Uheda, N. Hirosaki, Y. Yamamoto, A. Naito, T. Nakajima, H. Yamamoto, *Electrochem. Solid-State Lett.* **2006**, *9*, H22–H25.
- [46] K. Uheda, N. Hirosaki, H. Yamamoto, *Phys. Status Solidi A* **2006**, *203*, 2712–2717.
- [47] H. A. Höpfe, H. Lutz, P. Morys, W. Schnick, A. Seilmeyer, *J. Phys. Chem. Solids* **2000**, *61*, 2001–2006.
- [48] E. Wiedemann, *Ann. Phys.* **1888**, *270*, 446–463.
- [49] G. Blasse, B. C. Grabmaier, *Luminescent Materials*, Springer, Berlin, Heidelberg, **1994**.
- [50] R. C. Ropp, *Luminescence and the Solid State (2nd edition)*, Elsevier, Warren, **2004**.
- [51] T. Jüstel, H. Nikol, C. Ronda, *Angew. Chem. Int. Ed.* **1998**, *37*, 3084–3103; *Angew. Chem.* **1998**, *110*, 3250–3271.
- [52] L. Wang, R.-J. Xie, T. Suehiro, T. Takeda, N. Hirosaki, *Chem. Rev.* **2018**, *118*, 1951–2009.

- [53] H. A. Höppe, *Angew. Chem. Int. Ed.* **2009**, 48, 3572–3582; *Angew. Chem.* **2009**, 121, 3626–3636.
- [54] G. Blasse, A. Bril, *Philips Tech. Rev.* **1970**, 31, 304–332.
- [55] S. Shionoya, W. M. Yen, *Phosphor Handbook (2nd edition)*, CRC Press, New York, **1998**.
- [56] C. R. Ronda, *Luminescence - From Theory to Applications*, Wiley-VCH, Weinheim, **2007**.
- [57] R. Shafei, D. Maganas, P. J. Strobel, P. J. Schmidt, W. Schnick, F. Neese, *J. Am. Chem. Soc.* **2022**, 144, 8038–8053.
- [58] P. Dorenbos, *J. Lumin.* **2003**, 104, 239–260.
- [59] T. M. Tolhurst, P. Strobel, P. J. Schmidt, W. Schnick, A. Moewes, *Chem. Mater.* **2017**, 29, 7976–7983.
- [60] M. Zeuner, S. Pagano, W. Schnick, *Angew. Chem. Int. Ed.* **2011**, 50, 7754–7775; *Angew. Chem.* **2011**, 123, 7898–7920.
- [61] A. F. Holleman, E. Wiberg, N. Wiberg, *Lehrbuch der anorganischen Chemie (102. Auflage)*, de Gruyter, Berlin, Boston, **2008**.
- [62] S. D. Kloß, W. Schnick, *Angew. Chem. Int. Ed.* **2019**, 58, 7933–7944; *Angew. Chem.* **2019**, 131, 8015–8027.
- [63] L. R. Murphy, T. L. Meek, A. L. Allred, L. C. Allen, *J. Phys. Chem. A* **2000**, 104, 5867–5871.
- [64] Z. Chen, Q. Zhang, Y. Li, H. Wang, R.-J. Xie, *J. Alloys Compd.* **2017**, 715, 184–191.
- [65] K. Bando, K. Sakano, Y. Noguchi, Y. Shimizu, *J. Light Visual Environ.* **1998**, 22, 2–5.
- [66] H. Watanabe, N. Kijima, *J. Alloys Compd.* **2009**, 475, 434–439.
- [67] T. Schlieper, W. Milius, W. Schnick, *Z. Anorg. Allg. Chem.* **1995**, 621, 1380–1384.
- [68] *Initial Benchmarks and Long-Term Performance of Narrow-Band Red Emitters Used in SSL Devices*, U.S. Department of Energy, Office of Energy Efficiency and Renewable Energy, Building Technologies Office, Washington, D.C., **2020**.
- [69] Lumileds Holding B. V., *Narrow Red Phosphor Technology*, **2016**.
- [70] *Long-Term Performance of Narrow-Band Red Emitters Used in SSL Devices*, U.S. Department of Energy, Office of Energy Efficiency and Renewable Energy, Building Technologies Office, Washington, D.C., **2021**.
- [71] P. Pust, V. Weiler, C. Hecht, A. Tücks, A. S. Wochnik, A.-K. Henß, D. Wiechert, C. Scheu, P. J. Schmidt, W. Schnick, *Nat. Mater.* **2014**, 13, 891–896.
- [72] G. J. Hoerder, M. Seibald, D. Baumann, T. Schröder, S. Peschke, P. C. Schmid, T. Tyborski, P. Pust, I. Stoll, M. Bergler, C. Patzig, S. Reißaus, M. Krause, L. Berthold, T. Höche, D. Johrendt, H. Huppertz, *Nat. Commun.* **2019**, 10, 1824–1832.

- [73] S. Schmiechen, H. Schneider, P. Wagatha, C. Hecht, P. J. Schmidt, W. Schnick, *Chem. Mater.* **2014**, *26*, 2712–2719.
- [74] P. Strobel, S. Schmiechen, M. Siegert, A. Tücks, P. J. Schmidt, W. Schnick, *Chem. Mater.* **2015**, *27*, 6109–6115.
- [75] M. Zhao, H. Liao, L. Ning, Q. Zhang, Q. Liu, Z. Xia, *Adv. Mater.* **2018**, *30*, 1802489–1802495.
- [76] T. Takeda, N. Hirosaki, S. Funahshi, R.-J. Xie, *Chem. Mater.* **2015**, *27*, 5892–5898.
- [77] P. Strobel, C. Maak, V. Weiler, P. J. Schmidt, W. Schnick, *Angew. Chem. Int. Ed.* **2018**, *57*, 8739–8743; *Angew. Chem.* **2018**, *130*, 8875–8879.
- [78] M. Seibald, T. Rosenthal, O. Oeckler, F. Fahrnbauer, A. Tücks, P. J. Schmidt, W. Schnick, *Chem. Eur. J.* **2012**, *18*, 13446–13452.

2 Synthesis of $RE_{6-x}Ca_{1.5x}Si_{11}N_{20}O$ ($RE = Yb, Lu; x \approx 2.2$) with $Lu_{6-x}Ca_{1.5x}Si_{11}N_{20}O:Ce^{3+}$ Offering Interesting Spectral Properties for Yellow-Emitting Phosphors in 1pcLEDs

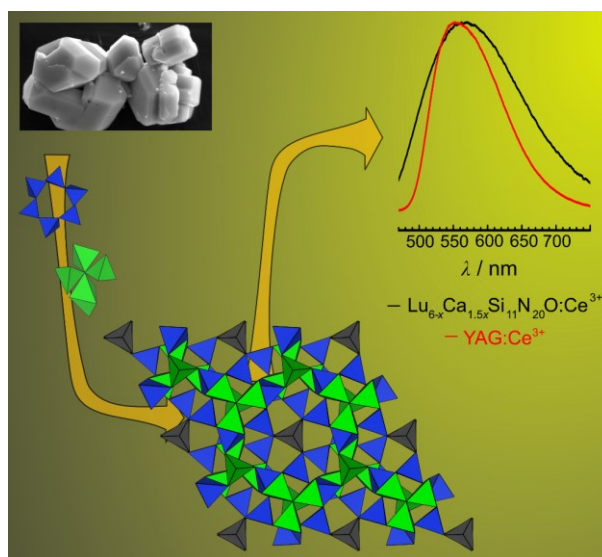
Published in: *Eur. J. Inorg. Chem.* **2019**, 47, 4985–4993

Authors: Lisa Gamperl, Georg Krach, Peter J. Schmidt, and Wolfgang Schnick

DOI: 10.1002/ejic.201901206

Copyright © 2019 Wiley-VCH Verlag GmbH & Co. KGaA

chemistry-europe.onlinelibrary.wiley.com/doi/10.1002/ejic.201901206



Abstract. The oxonitridosilicates $RE_{6-x}Ca_{1.5x}Si_{11}N_{20}O$ ($RE = Yb, Lu; x \approx 2.2$) were synthesized starting from REF_3 , RE_2O_3 , CaH_2 , and “ $Si(NH)_2$ ” in a radiofrequency furnace at 1600 or 1400 °C, respectively. The crystal structure was solved and refined from single-crystal X-ray diffraction data of dark red $Yb_{6-x}Ca_{1.5x}Si_{11}N_{20}O$ crystals in the trigonal space group $P31c$ (no. 159) with $a = 9.8281(10)$, $c = 10.5968(13)$ Å and $Z = 2$. The structure represents a filled variant of the $Er_6Si_{11}N_{20}O$ structure type, in which the charge difference caused by substitution of trivalent Yb^{3+} with bivalent Ca^{2+} is balanced by occupation of an additional third cation site. Synthesis of $Lu_{6-x}Ca_{1.5x}Si_{11}N_{20}O:Ce^{3+}$ resulted in a yellow powder with yellow luminescence. Powder X-ray data were analyzed by Rietveld refinement based on the crystal data obtained from $Yb_{6-x}Ca_{1.5x}Si_{11}N_{20}O$. The Ce^{3+} -doped compound exhibits a broad emission ($fwhm \approx 168$ nm/ 5100 cm^{-1}) with a maximum at $\lambda_{em} \approx 565$ nm. The emission extends more in the red spectral range compared to $YAG:Ce^{3+}$, thus making it an interesting phosphor for warm-white single phosphor converted light emitting diodes (1pcLED) with an improved color rendering index.

2.1 Introduction

According to the U.S. Department of Energy Solid-State Lighting Program, light-emitting diodes (LEDs) are revolutionizing the lighting market and offer new opportunities in the field of illumination design and energy efficiency. The energy savings of LED white-light sources will reduce the U.S. lighting energy consumption by nearly one-half in 2030 and about 75% by 2035 compared to conventional white-light sources. LEDs, that had their breakthrough with “*the invention of efficient blue light-emitting diodes which has enabled bright and energy-saving white light sources*” based on $Ga_{1-x}In_xN$ by Akasaki, Amano and Nakamura, have surpassed many conventional lighting technologies (i.e. incandescent, halogen, fluorescent and high-intensity discharge) in terms of energy efficiency, lifetime and color quality.^[1,2] However, ongoing research in the field of phosphor-converted LEDs (pcLEDs) is indispensable to realize the forecasts. Commonly used state-of-the-art white light single phosphor converted light emitting diodes (1pcLEDs) are based on $Y_{3-x}Gd_xAl_{5-y}Ga_yO_{12}:Ce^{3+}$ (YAG:Ce³⁺), a broadband, yellow emitting phosphor ($\lambda_{em} = 530\text{--}560\text{ nm}$).^[3-6] A drawback of the YAG:Ce³⁺ phosphor is its limitation to cool-white light applications (correlated color temperature CCT = 4000–8000 K, color rendering index CRI < 75) due to the lack of red spectral components. To achieve a natural color perception for illumination-grade lighting applications, higher CRI values are strongly sought-after.^[3,7] Improvements can be accomplished by either adding red emitting phosphors such as $Sr_xCa_{1-x}AlSiN_3:Eu^{2+}$, $Ba_2Si_5N_8:Eu^{2+}$ or $Sr[LiAlN_3]:Eu^{2+}$ in 2pcLED or by developing new phosphors with a red-shifted emission compared to YAG:Ce³⁺ in a 1pcLED approach.^[8-10] Nitridoaluminates and nitridosilicates with their highly condensed structures have turned out to be promising host materials with excellent thermal and chemical stability. Their predominantly covalent activator-nitrogen bonds shift the photoluminescence to emission into the red spectral range (nephelauxetic effect), which leads to lower, i.e. warmer color temperatures as it is requested for warm-white LEDs.^[11-13] This makes Ce³⁺-doped nitridosilicates highly promising phosphors for application in warm-white 1pcLEDs. Examples for such recently developed phosphors are $(La,Ca)_3Si_6N_{11}:Ce^{3+}$, $La_3BaSi_5N_9O_2:Ce^{3+}$, $CaAlSiN_3:Ce^{3+}$ and $SrAlSi_4N_7:Ce^{3+}$.^[14-17] In general, Ce³⁺ phosphors are more suited than Eu²⁺ phosphors for applications where high luminance is important.^[18] New Ce³⁺ phosphors are especially needed for high intensity light sources with superior color rendering quality. In this contribution, we report on the synthesis of $Yb_{6-x}Ca_{1.5x}Si_{11}N_{20}O$ and $Lu_{6-x}Ca_{1.5x}Si_{11}N_{20}O$ ($x \approx 2.2$). $Lu_{6-x}Ca_{1.5x}Si_{11}N_{20}O:Ce^{3+}$ shows an interesting luminescence spectrum compared to YAG:Ce³⁺, which makes it a potential new phosphor for warm-white 1pcLEDs for illumination-grade lighting applications.

2.2 Results and Discussion

2.2.1 Synthesis and Chemical Analysis

The synthesis described in the Experimental Section led to CaF_2 as a side product, which can be easily removed by washing with conc. HNO_3 , conc. HCl , H_2O and ethanol. Due to the formation of CaF_2 , an excess of CaH_2 had to be used. Dark red crystals (Figure A1) with a size up to $200\ \mu\text{m}$ were obtained. EDX data (Table A1) showed that Ca is present in all investigated crystals. The averaged determined atomic ratios ($\text{Yb}:\text{Ca}:\text{Si}:\text{N}:\text{O} = 11:7:28:51:4$) agree well within the limits of accuracy with the theoretical values calculated from the sum formula obtained by single-crystal X-ray diffraction data ($\text{Yb}:\text{Ca}:\text{Si}:\text{N}:\text{O} = 10:8:28:51:3$). However, the obtained atomic ratios of Yb and Ca slightly differ in each single measurement, which indicates that the Yb:Ca ratio is moderately variable. This leads to the assumption that the sum formula can be best described with the variable x , leading to $\text{Yb}_{6-x}\text{Ca}_{1.5x}\text{Si}_{11}\text{N}_{20}\text{O}$ ($x \approx 2.2$) as a more accurate description of the entire sample stoichiometry. For determination of the composition of the whole sample, PXRD data were refined with the Rietveld method based on single-crystal X-ray diffraction data. The refinement shows that the syntheses led to phase pure $\text{Yb}_{6-x}\text{Ca}_{1.5x}\text{Si}_{11}\text{N}_{20}\text{O}$ ($x \approx 2.2$, Figure 2.1, Table A2).

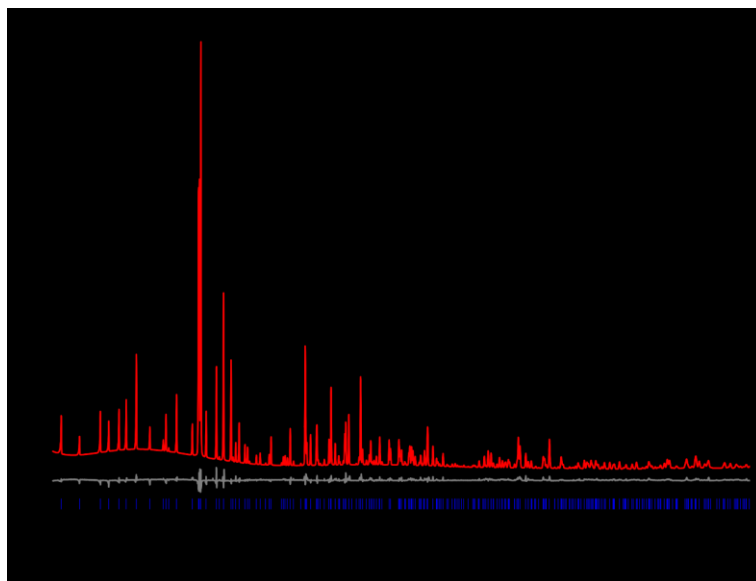


Figure 2.1. Rietveld refinement of PXRD data collected from an $\text{Yb}_{6-x}\text{Ca}_{1.5x}\text{Si}_{11}\text{N}_{20}\text{O}$ ($x \approx 2.2$) powder sample with experimental data (black line, $\text{Cu-K}\alpha_1$ radiation, $\lambda = 1.54056\ \text{\AA}$), calculated pattern (red line), difference profile (gray line) and positions of Bragg reflections (blue bars).

Minor differences in the reflection intensities may be due to slightly variable Yb:Ca ratios on the three cation sites with mixed occupancy. Absence of N-H vibration bands in the FTIR spectrum (Figure A2) show that there are no N-H groups. Synthesis of $\text{Lu}_{6-x}\text{Ca}_{1.5x}\text{Si}_{11}\text{N}_{20}\text{O}:\text{Eu}^{2+}$ led to a pinkish powder with orange-red luminescence under

2 Synthesis of $RE_{6-x}Ca_{1.5x}Si_{11}N_{20}O$ ($RE = Yb, Lu; x \approx 2.2$) with $Lu_{6-x}Ca_{1.5x}Si_{11}N_{20}O:Ce^{3+}$ Offering Interesting Spectral Properties for Yellow-Emitting Phosphors in 1pcLEDs

irradiation with blue light, whereas Ce^{3+} doping resulted in a yellow powder with yellow luminescence. The morphology of the sample shows small crystallites with a size up to 10 μm (Figure A3). The averaged values obtained from EDX measurements (Table A3) of a nondoped sample ($Lu:Ca:Si:N:O:F = 8:7:26:51:7:1$) are comparable to the values measured on $Yb_{6-x}Ca_{1.5x}Si_{11}N_{20}O$ ($x \approx 2.2$) indicating that the previously obtained sum formula is also applicable. The O value is slightly increased presumably due to superficially bound O. Despite washing of the samples, a small residue of CaF_2 is still left which can be analyzed by detection of fluorine. The synthesis of $Lu_{6-x}Ca_{1.5x}Si_{11}N_{20}O$ did not yield single crystals. Therefore, the single-crystal X-ray diffraction data of $Yb_{6-x}Ca_{1.5x}Si_{11}N_{20}O$ ($x \approx 2.2$) were modified and applied for Rietveld refinement of a washed, nondoped sample, which shows no CaF_2 side phase although minor amounts of fluorine were detected by EDX measurements (Figure 2.2, Table A4).

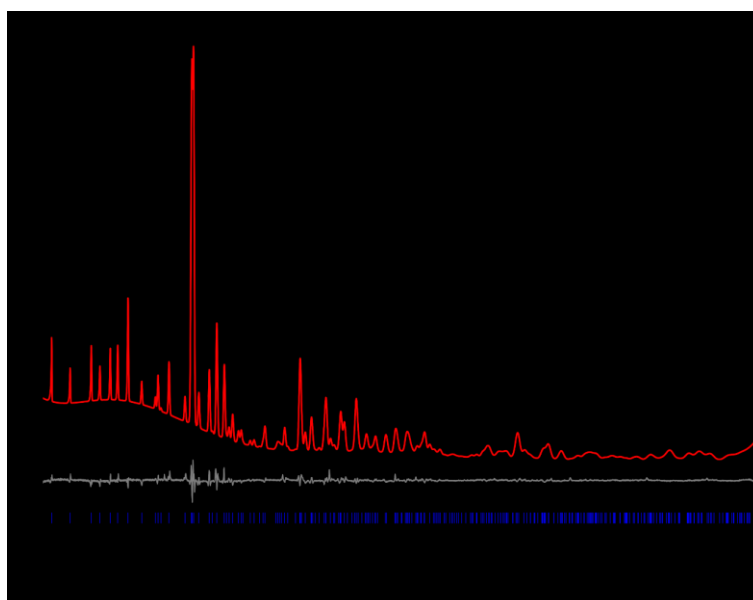


Figure 2.2. Rietveld refinement of PXR data collected from a $Lu_{6-x}Ca_{1.5x}Si_{11}N_{20}O$ sample with experimental data (black line, $Cu-K\alpha_1$ radiation, $\lambda = 1.54056 \text{ \AA}$), calculated pattern (red line), difference profile (gray line) and positions of Bragg reflections (blue bars).

Due to the good accordance of the Rietveld and EDX data compared to $Yb_{6-x}Ca_{1.5x}Si_{11}N_{20}O$ ($x \approx 2.2$), the sum formula $Lu_{6-x}Ca_{1.5x}Si_{11}N_{20}O$ with the same crystal structure can be assumed. Reflection intensity differences are again caused by small differences in the Lu:Ca ratio distributed over the entire sample.

2.2.2 Crystal Structure Determination and Description

The crystal structure of $\text{Yb}_{6-x}\text{Ca}_{1.5x}\text{Si}_{11}\text{N}_{20}\text{O}$ ($x \approx 2.2$) was solved and refined from single-crystal X-ray diffraction data in the trigonal space group $P31c$ (no. 159), in which all atoms were refined with anisotropic displacement parameters. The crystallographic data of the refinement are summarized in Table 2.1.

Table 2.1. Crystallographic Data of the single-crystal structure determination of $\text{Yb}_{6-x}\text{Ca}_{1.5x}\text{Si}_{11}\text{N}_{20}\text{O}$ ($x \approx 2.2$)

Formula	$\text{Yb}_{3.79}\text{Ca}_{3.22}\text{Si}_{11}\text{N}_{20}\text{O}$
formula mass / $\text{g}\cdot\text{mol}^{-1}$	1389.00
crystal system	trigonal
space group	$P31c$ (no. 159)
lattice parameters / Å	$a =$ 9.8281(10)
	$c =$ 10.5968(13)
$V / \text{Å}^3$	886.4(2)
Z	2
X-ray density / $\text{g}\cdot\text{cm}^{-3}$	5.208
abs. coefficient / $\mu\cdot\text{mm}^{-1}$	21.515
absorption correction	Multiscan ^[19]
T / K	293(2)
diffractometer	Bruker D8 Venture
radiation	Mo-K α ($\lambda = 0.71073 \text{ Å}$)
$F(000)$	1264
θ range / °	$3.8297 \leq \theta \leq 32.2982$
independent reflections	1776
refined parameters / restraints	128 / 7
Goof (χ^2)	1.030
R_{int}	0.0962
R_{σ}	0.0443
$R1$ (all data / for $I > 2\sigma(I)$)	0.0428 / 0.0418
$wR2$ (all data / for $I > 2\sigma(I)$)	0.1008 / 0.1002
$\Delta\rho_{\text{max}} / \Delta\rho_{\text{min}} / \text{e Å}^{-3}$	1.881 / -2.386

Atomic coordinates, isotropic displacement parameters, site occupancy factors (Table A5) as well as the anisotropic displacement parameters (Table A6) are summarized in the Supporting Information. $\text{Yb}_{6-x}\text{Ca}_{1.5x}\text{Si}_{11}\text{N}_{20}\text{O}$ ($x \approx 2.2$) crystallizes in a filled variant of the $\text{Er}_6\text{Si}_{11}\text{N}_{20}\text{O}$ structure type, first described by *Woike et al.* and subsequently reported with minor differences regarding the occupation of cation sites by *Köllisch et al.*^[20,21] The structure exhibits a three-dimensional network of vertex sharing $[\text{SiN}_4]$ tetrahedra (Figure 2.3), which contains terminal ($\text{N}^{[1]}$), twofold ($\text{N}^{[2]}$), threefold ($\text{N}^{[3]}$) and even fourfold ($\text{N}^{[4]}$) bridging nitrogen atoms.^[20-26, 13] The terminal nitrogen atom in $\text{Er}_6\text{Si}_{11}\text{N}_{20}\text{O}$ was a novel feature in

2 Synthesis of $RE_{6-x}Ca_{1.5x}Si_{11}N_{20}O$ ($RE = Yb, Lu; x \approx 2.2$) with $Lu_{6-x}Ca_{1.5x}Si_{11}N_{20}O:Ce^{3+}$ Offering Interesting Spectral Properties for Yellow-Emitting Phosphors in 1pcLEDs

nitridosilicates.^[20] The most unusual feature of the structure is the simultaneous occurrence of all functionalities $N^{[1]}$ to $N^{[4]}$.^[21]

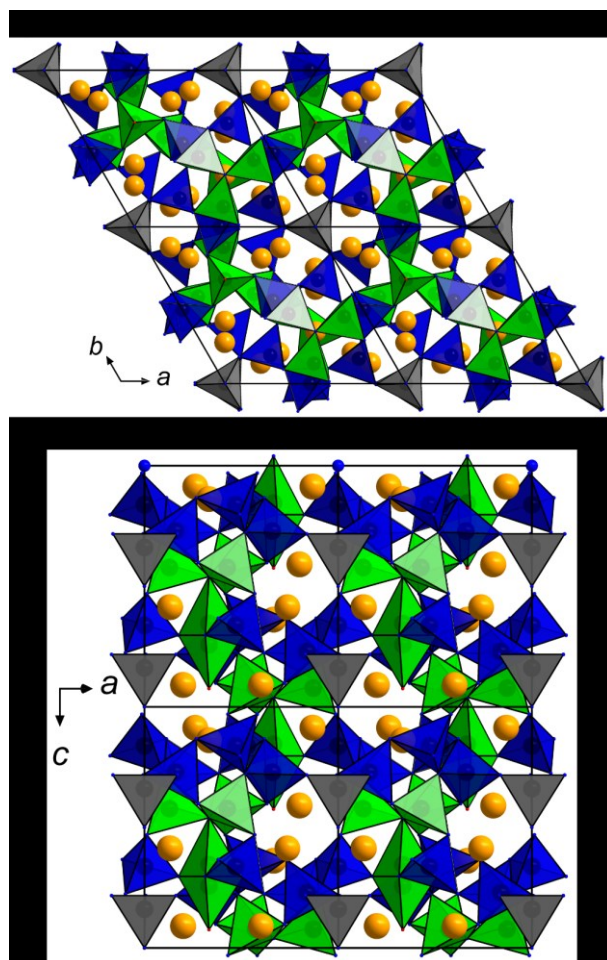


Figure 2.3. Crystal structure of an $Yb_{6-x}Ca_{1.5x}Si_{11}N_{20}O$ ($x \approx 2.2$) $2 \times 2 \times 2$ super cell viewed along (a) [001] and (b) [010]. $[SiN_4]$ tetrahedra in blue, green, and gray, N atoms blue and Yb/Ca atoms orange. Unit cell outline in black.

Condensation of six $[SiN_4]$ tetrahedra leads to the formation of *sechser* rings (Figure 2.4a), which are linked by $[SiN_4]$ tetrahedra to sheets perpendicular to [001].^[27] The connecting tetrahedra contain the terminal nitrogen atoms ($N7$, gray tetrahedra) aligned in the [001] direction. The rings are connected to a star shaped unit containing the fourfold bridging nitrogen atom ($N6^{[4]}$, green tetrahedra, Figure 4b). This unit contains also a Si4/Si5 split position (52%/48%) with Si5 in a $[SiN_3O^{[1]}]$ tetrahedron. In contrast to *Woike et al.* and *Köllisch et al.*, the oxygen site was not refined with a split position but with an enlarged anisotropic displacement parameter along [001], which is oriented in the direction of the columns formed by the *sechser* rings and the star shaped unit. Difference Fourier synthesis ($F_{obs} - F_{calc}$) of the electron density located at the $O1^{[1]}$ site as well as at the $N6^{[4]}$ site, which has also an enlarged anisotropic displacement parameter, does also not indicate a splitting of the electron density at high isosurface levels unlike the Si4/Si5 split position (Figure A4).

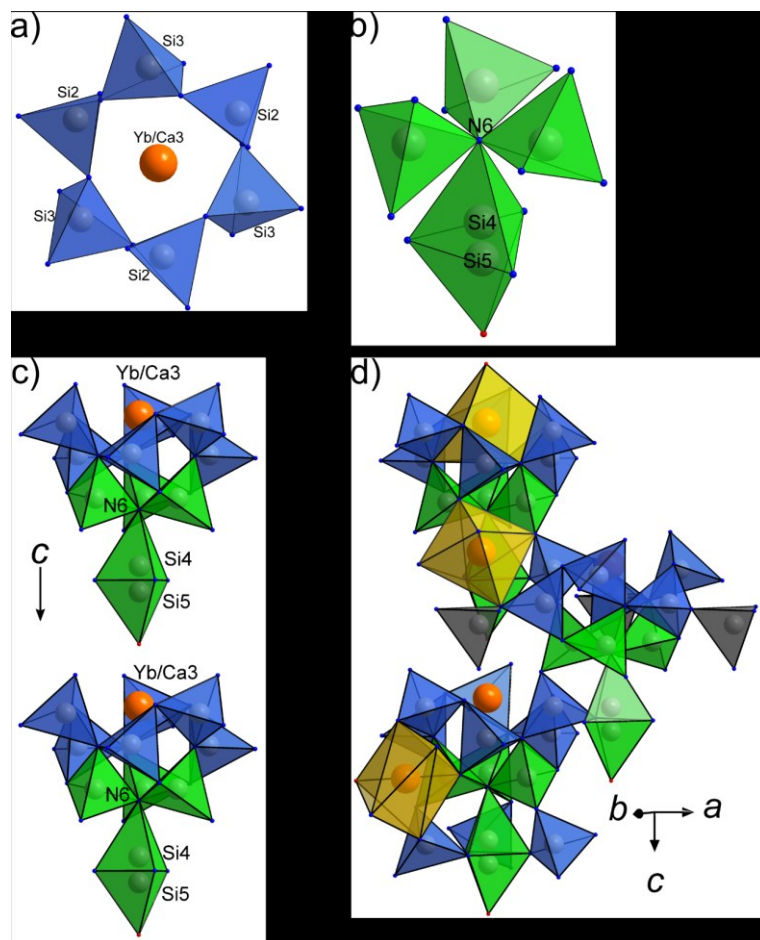


Figure 2.4. (a) Sechser rings of $[\text{SiN}_4]$ tetrahedra (blue) with centered Yb/Ca3 site. (b) Star shaped unit (green $[\text{SiN}_4]$ tetrahedra) containing the fourfold bridging N6 atom and the Si4/Si5 split position. (c) Combinations of ring and star shaped units stacked along $[001]$. (d) Linkage of units in different $[001]$ columns by common corners and via additional tetrahedra (gray) containing the terminal N7 atom. N atoms blue, O atoms red and Yb/Ca atoms orange.

The enlarged anisotropic displacement parameters may be caused by the Si4/Si5 split position. The units combined *via* common $[\text{SiN}_4]$ tetrahedra corners of the ring and star shaped unit with the split position are stacked along the $[001]$ direction (Figure 2.4c). The different so formed columns are shifted against each other in $[001]$ and linked via the star shaped unit of one column to the ring of another column and *vice versa* (Figure 2.4d).

There are three different cation sites with mixed occupancy of Yb and Ca (Figure 2.5). Yb/Ca1 (76%/24%) is coordinated by six nitrogen atoms in a distorted octahedron and Yb/Ca2 (47%/53%) coordinated by five nitrogen and one oxygen atoms forms a distorted trigonal prism. The three cation sites are linked by common edges (Yb/Ca1 to Yb/Ca2 and Yb/Ca2 to Yb/Ca3) or corners (Yb/Ca1 to Yb/Ca3).

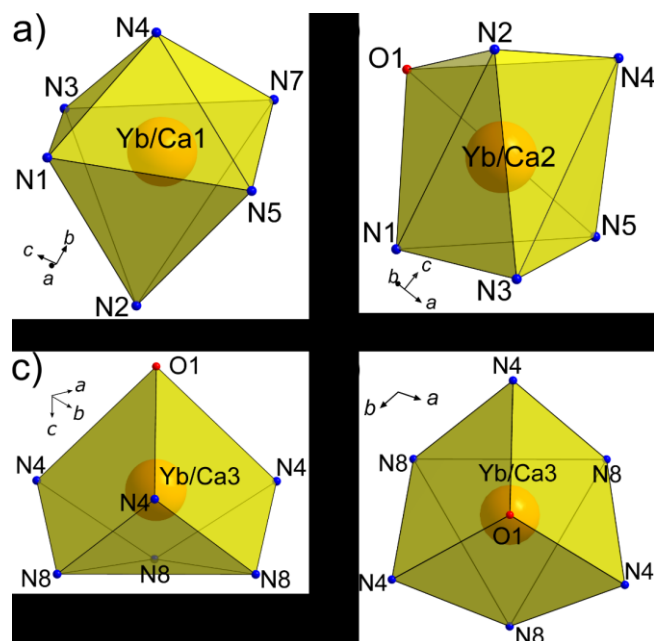


Figure 2.5. Coordination polyhedra of the three cation sites with mixed Yb/Ca occupancy. (a) Yb/Ca1, (b) Yb/Ca2, (c) Yb/Ca3 side view, (d) Yb/Ca3 top view. N atoms blue, O atoms red and Yb/Ca atoms orange.

In contrast to the $Er_6Si_{11}N_{20}O$ structure type,^[20] which exhibits only two cation sites, a third cation site is occupied in $Yb_{6-x}Ca_{1.5x}Si_{11}N_{20}O$ ($x \approx 2.2$) by 9% Yb and 91% Ca in a sevenfold coordination of six nitrogen (N4: 2.547(12) Å, N8: 2.564(10) Å) and one oxygen atom (2.27(3) Å). It can be described by three N4 and three N8 each in a plane twisted against each other forming a zigzag pattern. The coordination sphere is completed by the terminal oxygen atom of the $[SiN_3O]$ tetrahedra, which coordinates Si5 of the Si4/Si5 split position of the star shaped unit connected to the *sechser* ring stacked along [001]. This structural situation but with an under-occupied third cation site located inside the *sechser* rings was also reported by *Köllisch et al.* in contrast to the published structure type.^[20,21] Due to very similar atomic form factors of O^{2-} and N^{3-} , an unequivocal assignment of O and N only by means of X-ray methods is not possible. The explanation of *Woike et al.* for the presence and location of oxygen is only based on structure-chemical arguments like charge balance and its proximity to a potential third cation site occupied by one third in a possible “ $Er_{6.33}Si_{11}N_{21}$ ” structure (Er3–N: 2.37(3) Å), in which oxygen is replaced by nitrogen for charge balance. The oxygen site is split due to the Si4a/Si4b split position and is nearly trigonal planar coordinated by three Er atoms.^[20] In contrast, *Köllisch et al.* argue, that the occupation of the third cation site is necessary to form a tetrahedral coordination of Er for the oxygen atom. Such oxygen centered $[Ln_4O]^{10+}$ ions, which stabilize oxygen atoms that can be considered as not belonging to the silicate anion structure due to the long distance to Si, have already been reported.^[21, 28-30] In the title compound, the third cation site has to be occupied in order to compensate the charges unbalanced by mixed occupancy of the first

two cation sites with divalent and trivalent cations. XRD and EDX data support this assumption. To confirm the assumed anion arrangement, lattice energy (MAPLE)^[31-33] and bond valence sum (BVS)^[34,35] calculations were performed. For MAPLE calculations of $\text{Yb}_{3.79}\text{Ca}_{3.22}\text{Si}_{11}\text{N}_{20}\text{O}$ as well as for “ $\text{Yb}_6\text{Si}_{11}\text{N}_{20}\text{O}$ ” ($\text{Er}_6\text{Si}_{11}\text{N}_{20}\text{O}$ structure type^[21] with Er substituted by Yb) some approximations had to be made (Table A7). The partial MAPLE values calculated for Yb/Ca1–3 are in good agreement with typical MAPLE values for RE^{3+} and Ca^{2+} in nitridosilicates and with the values calculated for “ $\text{Yb}_6\text{Si}_{11}\text{N}_{20}\text{O}$ ”. The Si values are also in good accordance despite the Si split position. Only the value of Si6 is slightly enlarged even compared to “ $\text{Yb}_6\text{Si}_{11}\text{N}_{20}\text{O}$ ”.^[13] The values of the anions are again in good agreement. The (Si6) N_4 tetrahedron contains the terminal nitrogen atom. This site could also be occupied by oxygen, which would explain the high value of Si6 when coordinated only by nitrogen. Substitution of N7 by oxygen (“O7”) leads to more reasonable values, but then more Ca has to be incorporated in the structure for charge balance. However, due to the variable mixed occupancy of the cation sites, it is not possible to determine whether the Ca content is caused by an increased oxygen incorporation. Thus, it cannot be clearly stated that Si6 is only coordinated by nitrogen. Another possibility for charge balance is the incorporation of nitrogen on the former O1 site, which is also terminal (“N11”), but the obtained value is too low for known terminal nitrogen atoms. To further differentiate the occupation of the sites by oxygen and nitrogen, BVS calculations were performed (Table A8). The bond valence sums for N1–N6 as well as for N8 are in good agreement with the assignment of nitrogen. The value of the terminal nitrogen N7 is slightly too low for a nitrogen atom, therefore, as in the MAPLE calculations, N7 was replaced by oxygen (“O7”), whose value deviates slightly from the expected -2 , but it is closer to that of oxygen than the previous value for nitrogen. The substitution affects the BVS values for Yb/Ca1–3 and Si6, which are still reasonable. As explained for the MAPLE calculation, O1 was substituted by nitrogen (“N11”) for charge balance. The obtained value is in the range of the values expected for N and O, respectively, which indicates that both are suitable. MAPLE and BVS calculations agree well with each other, both suggest that oxygen would be more suitable on the N7 site. Incorporation of nitrogen on the former O1 site for charge balance does not solve this problem, so charges could be balanced by Ca. However, the obtained data are insufficient for an unequivocal statement. Since only the boundary conditions were considered, a mixed O/N occupancy is also conceivable. According to Pauling’s second rule,^[36] O should substitute N near the cation site with the higher Ca content to compensate the locally imbalanced charges caused by substitution of Yb^{3+} by Ca^{2+} in a nitrogenous surrounding. It can be assumed that Yb-N pairs are substituted by Ca-O pairs, which are both charge-neutral.^[37] The distribution of Yb and Ca on the different sites seems to depend on the average distances of Yb/Ca to N/O. For Yb/Ca1, the average Yb/Ca1-N distance is about 2.4 Å, Yb/Ca2-N/O about 2.45 Å and

Yb/Ca3-N/O about 2.5 Å. The occupation of the sites is in good agreement with the ionic radii, in which the larger Ca^{2+} occupies preferentially the site with the larger distances.^[31] During the refinement, sum formula constraints were applied in order to achieve charge neutrality by mixed Yb/Ca occupation of the different cation sites. This leads to a sum formula with a slight excess of negative charges, which, however, coincides within the error limits with a charge neutral sum formula. The Si-N distances (1.691(10) – 1.790(7) Å) are in good agreement with the values reported for $Er_6Si_{11}N_{20}O$.^[20,21] The Si5-O1 bond length of 1.92(3) Å is slightly enlarged due to the Si4/Si5 split position. The value is in between the values given in the literature for distances to an oxygen split position. According to *Köllisch et al.*, this represents a transition state between an isolated oxygen atom (i.e. occupancy of Si4) in a $[Ln_4O]^{10+}$ complex and a terminal oxygen atom in a (Si5)N₃O^[1] tetrahedron.^[20,21] The Si4–Si5 distance of the split position is 0.929(17) Å, which is slightly larger than reported, because the absence of an oxygen split position allows the Si atoms to further separate. The Yb/Ca–N distances are in the range of 2.340(9)–2.564(10) Å with slightly shorter Yb/Ca2–O1 and Yb/Ca3–O1 bond length of 2.284(2) and 2.27(3) Å, respectively, which are in also good agreement with the reported values.^[20,21]

Since no single crystals of $Lu_{6-x}Ca_{1.5x}Si_{11}N_{20}O$ ($x \approx 2.2$) were obtained, no independent structural model was elucidated. However, due to similar EDX results and the accordance of the powder diffraction pattern with the $Yb_{6-x}Ca_{1.5x}Si_{11}N_{20}O$ ($x \approx 2.2$) single-crystal data in the Rietveld refinement, it can be assumed that $Lu_{6-x}Ca_{1.5x}Si_{11}N_{20}O$ ($x \approx 2.2$) is isotypic to $Yb_{6-x}Ca_{1.5x}Si_{11}N_{20}O$. As a result of the potential variable occupation of the cation sites, the Lu:Ca ratio may vary.

2.2.3 UV/Vis Spectroscopy

With respect to the red color of the crystals of $Yb_{6-x}Ca_{1.5x}Si_{11}N_{20}O$ ($x \approx 2.2$), a solid-state UV/vis spectrum was recorded to determine the optical band gap. The measured diffuse reflectance spectrum of a powder sample was converted into a pseudo-absorption spectrum using the Kubelka–Munk function $F(R) = (1-R)^2/2R$ with R being the reflectance.^[38] Subsequently, the optical band gap was determined from a Tauc plot, where $h\nu$ is plotted against $(F(R) \cdot h\nu)^{1/n}$ with $n = 1/2$ for a direct allowed transition, by drawing a line tangent at the inflection point.^[39] The optical band gap was estimated to be approx. 1.87 eV (Figure 2.6).

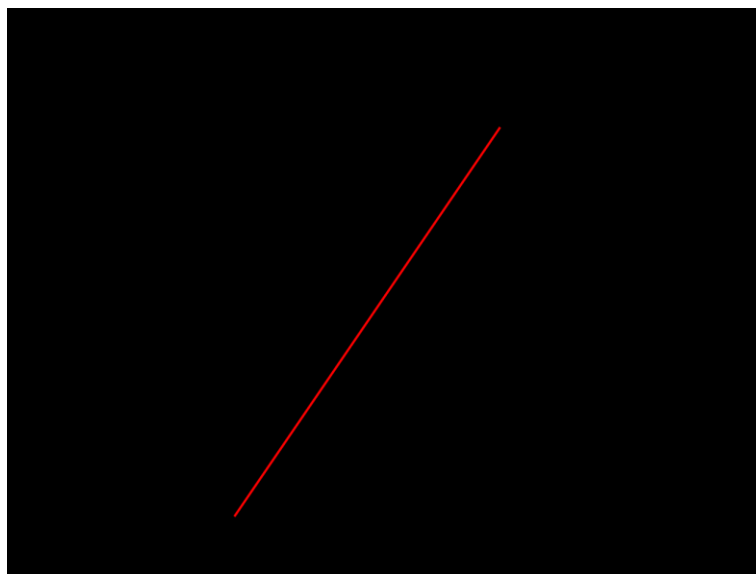


Figure 2.6. Tauc plot ($n = 1/2$) for an $\text{Yb}_{6-x}\text{Ca}_{1.5x}\text{Si}_{11}\text{N}_{20}\text{O}$ ($x \approx 2.2$) powder sample.

The determined optical band gap matches very well with the optical perception of the red crystals. The comparable small band gap of $\text{Yb}_{6-x}\text{Ca}_{1.5x}\text{Si}_{11}\text{N}_{20}\text{O}$ ($x \approx 2.2$) may be caused by the onset of the valence band- Yb^{3+} charge transfer band, which is referred to the transition to the localized $4f^{14}$ ground state of Yb^{2+} .^[40] Due to the low energetic difference, it can be assumed that in the visible range the direct transition will be more likely. The small band gap of $\text{Yb}_{6-x}\text{Ca}_{1.5x}\text{Si}_{11}\text{N}_{20}\text{O}$ ($x \approx 2.2$) may be the reason for the absence of luminescence upon doping with Eu^{2+} or Ce^{3+} because the emitted luminescence will be absorbed by the host material itself. The direct band gap of a nondoped $\text{Lu}_{6-x}\text{Ca}_{1.5x}\text{Si}_{11}\text{N}_{20}\text{O}$ ($x \approx 2.2$) powder sample is approx. 4.5 eV (Figure 2.7).



Figure 2.7. Tauc plot ($n = 1/2$) for a nondoped $\text{Lu}_{6-x}\text{Ca}_{1.5x}\text{Si}_{11}\text{N}_{20}\text{O}$ ($x \approx 2.2$) powder sample.

The band gap corresponds to the valence band-conduction band onset. Here, the direct transition will again probably be more likely due to the low energy difference. The direct band gap makes $Lu_{6-x}Ca_{1.5x}Si_{11}N_{20}O$ ($x \approx 2.2$) a suitable host material for doping, because for pcLED applications wide band gaps ≥ 4 eV are required.

2.2.4 Luminescence

Luminescence properties were obtained from thick bed powder samples of $Lu_{6-x}Ca_{1.5x}Si_{11}N_{20}O:Eu^{2+}$ and $Lu_{6-x}Ca_{1.5x}Si_{11}N_{20}O:Ce^{3+}$ ($x \approx 2.2$). The Eu^{2+} -doped compound shows a reddish luminescence upon irradiation with UV to blue light ($\lambda_{exc} = 440$ nm) and emits at $\lambda_{em} = 618$ nm with a full width at half-maximum (*fwhm*) of 124 nm/3000 cm^{-1} (Figure A6). $Lu_{6-x}Ca_{1.5x}Si_{11}N_{20}O:Ce^{3+}$ ($x \approx 2.2$) shows a more interesting luminescence ($\lambda_{exc} = 440$ nm, Figure 2.8).

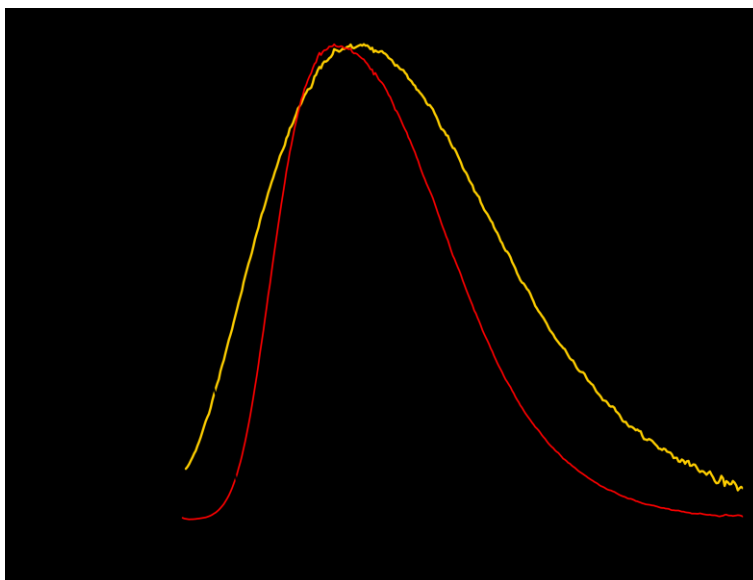


Figure 2.8. Normalized excitation (black) and emission spectra (orange, $\lambda_{exc} = 440$ nm) of $Lu_{6-x}Ca_{1.5x}Si_{11}N_{20}O:Ce^{3+}$ ($x \approx 2.2$) compared to $YAG:Ce^{3+}$ (red).

The emission maximum is positioned at $\lambda_{em} = 565$ nm with a full width at half-maximum (*fwhm*) of 168 nm/5100 cm^{-1} , a quantum efficiency of 22% and color coordinates (CIE 1931, Commission Internationale de l'Éclairage) of $x = 0.436$ and $y = 0.503$ (CIE 1960: $u = 0.214$, $v = 0.370$).^[41] Comparison of the ionic radii indicates that Ce^{3+} (coordination number $CN = 6$: 1.01 Å, $CN = 7$: 1.07 Å) preferably replaces Ca^{2+} ($CN = 6$: 1.00 Å, $CN = 7$: 1.06 Å) rather than Yb^{3+} ($CN = 6$: 0.87 Å, $CN = 7$: 0.93 Å).^[31] The broadband emission, which is typical for Ce^{3+} -doped materials, results from a spin and parity allowed transition from the lowest $5d$ level to the $4f$ ground state split into the two ${}^2F_{5/2}$ and ${}^2F_{7/2}$ levels separated by 2000 cm^{-1} .^[42] In addition, occupation of the asymmetric sites Yb/Ca1/2 (Wyckoff positions 6c with site symmetry 1) and Yb/Ca3 (Wyckoff positions 2b with site symmetry 3) with different activator-N/O distances leads to different crystal field interactions and therefore to multiple doublet

emissions slightly shifted to each other, resulting in a further broadening. The emission spectrum is compared to an industrially optimized $\text{Y}_{3-x}\text{Gd}_x\text{Al}_{5-y}\text{Ga}_y\text{O}_{12}:\text{Ce}^{3+}$ (YAG: Ce^{3+} , Lumileds Phosphor Center Aachen, Lumileds Germany GmbH), which exhibits an emission maximum at $\lambda_{\text{em}} = 552 \text{ nm}$ ($\lambda_{\text{exc}} = 440 \text{ nm}$) with a full width at half-maximum (*fwhm*) of $118 \text{ nm}/3600 \text{ cm}^{-1}$ and a quantum efficiency of 95%. The color coordinates are $x = 0.444$ and $y = 0.537$ ($u = 0.208$, $v = 0.377$). The $\text{Lu}_{6-x}\text{Ca}_{1.5x}\text{Si}_{11}\text{N}_{20}\text{O}:\text{Ce}^{3+}$ ($x \approx 2.2$) luminescence spectrum shows a comparable emission in the yellow region but with an increased emission in the red spectral range. The color point of $\text{Lu}_{6-x}\text{Ca}_{1.5x}\text{Si}_{11}\text{N}_{20}\text{O}:\text{Ce}^{3+}$, which is assigned in the CIE 1960 color space (Figure 2.9), is located nearby YAG: Ce^{3+} in the yellow-orange spectral range.

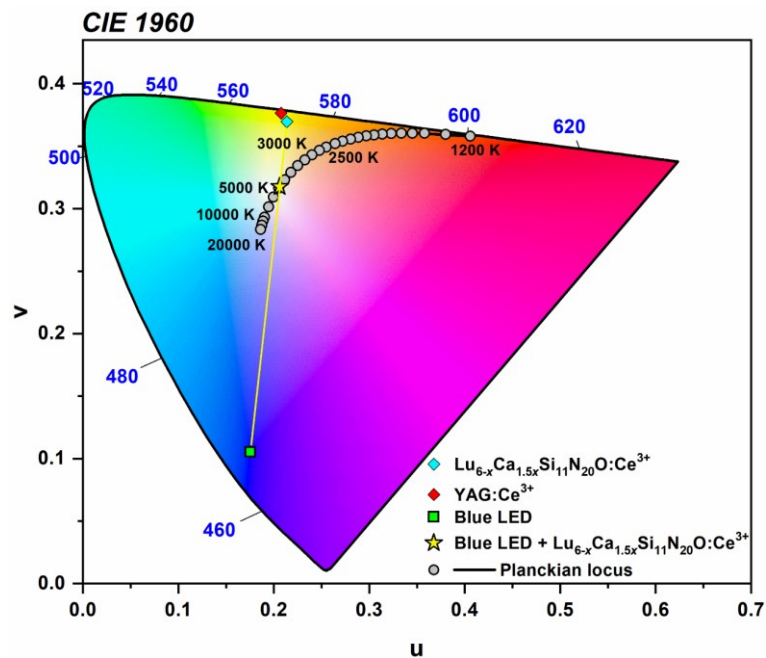


Figure 2.9. CIE 1960 color space with the color points of $\text{Lu}_{6-x}\text{Ca}_{1.5x}\text{Si}_{11}\text{N}_{20}\text{O}:\text{Ce}^{3+}$ ($x \approx 2.2$; turquoise \diamond), YAG: Ce^{3+} (red \diamond) and a blue primary LED (green square) along with an ideal blackbody radiator (Planckian locus, black line with gray squares) at different temperatures (K). Yellow line for determination of the CCT of a theoretical LED based on a blue primary LED and the $\text{Lu}_{6-x}\text{Ca}_{1.5x}\text{Si}_{11}\text{N}_{20}\text{O}:\text{Ce}^{3+}$ phosphor (intersection with Planckian locus indicated with yellow \star).^[41,43]

A theoretical white light 1pcLED based on a blue primary LED ($\lambda_{\text{em}} = 450 \text{ nm}$) combined with the $\text{Lu}_{6-x}\text{Ca}_{1.5x}\text{Si}_{11}\text{N}_{20}\text{O}:\text{Ce}^{3+}$ phosphor would offer a CCT of about 4800 K ($x = 0.352$, $y = 0.361$; $u = 0.212$, $v = 0.327$)^[43]. In comparison, a theoretical YAG: Ce^{3+} based 1pcLED exhibits a CCT of approx. 5300 K ($x = 0.337$, $y = 0.350$; $u = 0.207$, $v = 0.322$). The determined CCT values show that $\text{Lu}_{6-x}\text{Ca}_{1.5x}\text{Si}_{11}\text{N}_{20}\text{O}:\text{Ce}^{3+}$ could offer slightly lower CCT values and could therefore be used in warm-white light applications. However, the main advantage is the increased output in the red spectral range, which could lead to improved CRI compared to a YAG: Ce^{3+} LED. As a main benefit of the title compound, color rendition R_a increases

2 Synthesis of $RE_{6-x}Ca_{1.5x}Si_{11}N_{20}O$ ($RE = Yb, Lu; x \approx 2.2$) with $Lu_{6-x}Ca_{1.5x}Si_{11}N_{20}O:Ce^{3+}$ Offering Interesting Spectral Properties for Yellow-Emitting Phosphors in 1pcLEDs

significantly from 68 to 84 ($R_9 = 29$), a typical value of illumination grade white LEDs. This could make $Lu_{6-x}Ca_{1.5x}Si_{11}N_{20}O:Ce^{3+}$ a potentially better phosphor for applications with a higher color rendering index in warm-white 1pcLED than $YAG:Ce^{3+}$, which leads only to cool, pale white light in combination with a blue emitting $Ga_{1-x}In_xN$ primary LED.

Another yellow phosphor, $Y_{6+(x/3)-y}Ca_{y+(z/2)}Si_{11}N_{20+x-y+z}O_{1-x+y-z}:Ce^{3+}$, which crystallizes analogously to $Lu_{6-x}Ca_{1.5x}Si_{11}N_{20}O$ in the same crystal structure reported by *Woike et al.* with three mixed occupied cation sites, exhibits an emission maximum at $\lambda_{em} = 554$ nm ($\lambda_{exc} = 450$ nm) with *fwhm* of 147 nm. This phosphor was claimed to be used in general white lighting devices requiring high color rendering due to its broad yellow emission.^[44] In comparison to $YAG:Ce^{3+}$, the emission maximum of $Y_{6+(x/3)-y}Ca_{y+(z/2)}Si_{11}N_{20+x-y+z}O_{1-x+y-z}:Ce$ stays almost unchanged but with a broader emission. However, $Lu_{6-x}Ca_{1.5x}Si_{11}N_{20}O:Ce^{3+}$ exhibits a slightly red-shifted emission maximum with an even broader *fwhm* extending in the red spectral range. So it is expected that $Lu_{6-x}Ca_{1.5x}Si_{11}N_{20}O:Ce^{3+}$ offers an even better color rendering than $Y_{6+(x/3)-y}Ca_{y+(z/2)}Si_{11}N_{20+x-y+z}O_{1-x+y-z}:Ce^{3+}$ due to its increased red spectral output.

The quantum efficiency of $Lu_{6-x}Ca_{1.5x}Si_{11}N_{20}O:Ce^{3+}$ with 22% at room temperature is rather low compared to the industrially optimized $YAG:Ce^{3+}$. Based on the quantum efficiency of 22% at room temperature, the quantum efficiency at 6 K can be estimated to about 80% (Figure 2.10).

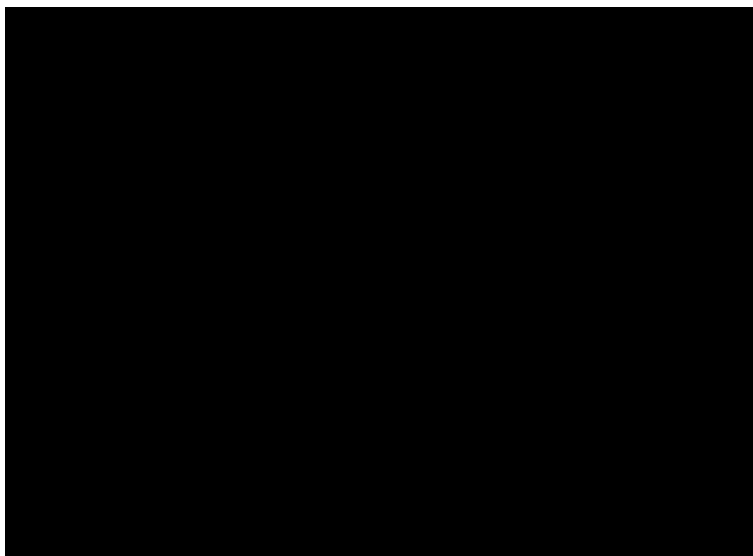


Figure 2.10. Temperature dependent internal quantum efficiencies of $Lu_{6-x}Ca_{1.5x}Si_{11}N_{20}O:Ce^{3+}$ ($x \approx 2.2$).

From thermal quenching investigations it could be expected that the internal quantum efficiency can be increased by about 20% by lowering the excited $4f^05d^1$ state of Ce^{3+} energetically relative to the bottom of the conduction band. Practically, this may be achieved

by partial replacement of Ca^{2+} by heavier alkaline earth elements as being discussed in literature [45].

The influence of the dopant concentrations is investigated by comparison of samples with a nominal dopant content of 0.5, 1, 2 and 4 mol% Ce^{3+} referred to Ca (Figure 2.11, Table A9).

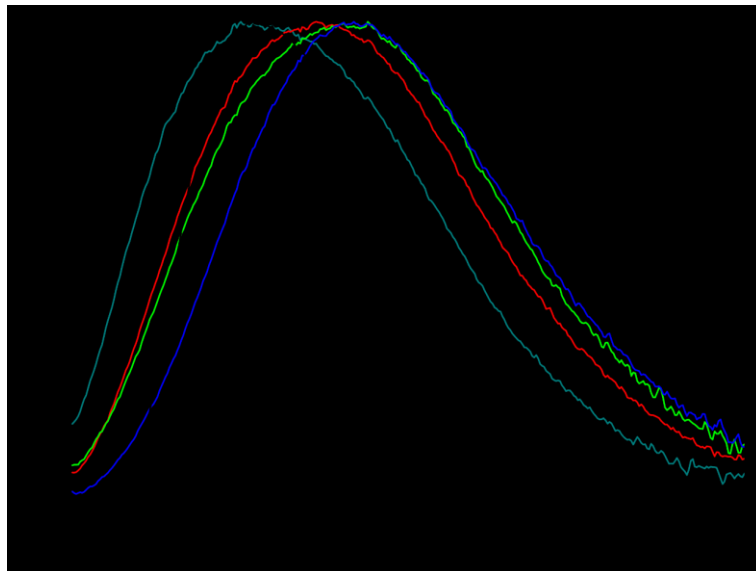


Figure 2.11. Normalized emission spectra ($\lambda_{\text{exc}} = 440 \text{ nm}$) of $\text{Lu}_{6-x}\text{Ca}_{1.5x}\text{Si}_{11}\text{N}_{20}\text{O}:\text{Ce}^{3+}$ ($x \approx 2.2$) with different dopant concentrations of 0.5% (turquoise), 1% (red), 2% (green) and 4% (blue) compared to $\text{YAG}:\text{Ce}^{3+}$ (black).

Increasing the dopant concentration leads to a red-shifted emission while *fwhm* remains largely constant. Phosphors having multiple emission sites can exhibit rather large emission maxima shifts at different doping concentrations because the occupancy of the available activator sites can change significantly depending on the doping concentration and synthesis conditions. Even the quantum efficiency shows no significant or systematic changes and therefore no concentration quenching at the investigated dopant contents (Table A9). There is also no systematic change of the lattice parameters despite increasing the dopant concentration and therefore incorporating a slightly larger cation.

2.3 Conclusion

$Yb_{6-x}Ca_{1.5x}Si_{11}N_{20}O$ and $Lu_{6-x}Ca_{1.5x}Si_{11}N_{20}O$ ($x \approx 2.2$) were synthesized in a solid-state reaction and crystallize in a filled variant of the $Er_6Si_{11}N_{20}O$ structure type. The refinement of the $Yb_{6-x}Ca_{1.5x}Si_{11}N_{20}O$ ($x \approx 2.2$) single-crystal X-ray diffraction data shows that Ca is incorporated by mixed occupancy of the two cation sites known from the $Er_6Si_{11}N_{20}O$ structure type as well as an additional third cation site for charge balance. The results are confirmed by EDX measurements, Rietveld refinements and both MAPLE and BVS calculations. The replacement of Yb/Lu by Ca leads to new structural features and could lead to the incorporation of oxygen in the anionic framework, which could have an influence on the luminescence properties. Furthermore, the third cation site is in contrast to the $Er_6Si_{11}N_{20}O$ structure type reported by *Woike et al.* only occupied if Ca is present. Ce^{3+} presumably occupies the Ca^{2+} sites due to similar radii, therefore the sites preferably occupied by Ce could be identified. However, it was not possible to unequivocally distinguish O and N, thus, neutron diffraction would be necessary as a subject of further research. Rietveld refinement of $Lu_{6-x}Ca_{1.5x}Si_{11}N_{20}O$ ($x \approx 2.2$) was based on the refined single-crystal X-ray diffraction data of $Yb_{6-x}Ca_{1.5x}Si_{11}N_{20}O$ ($x \approx 2.2$), which indicates that both compounds crystallize in the same structure type. The Eu^{2+} -doped compound emits at $\lambda_{em} = 618$ nm with a full width at half-maximum (*fwhm*) of 124 nm/3000 cm^{-1} . $Lu_{6-x}Ca_{1.5x}Si_{11}N_{20}O:Ce^{3+}$ ($x \approx 2.2$) exhibits a more interesting luminescence in the yellow spectral range. With $\lambda_{em} = 565$ nm and *fwhm* of 168 nm/5100 cm^{-1} , the phosphor shows a comparable emission to $Y_{3-x}Gd_xAl_{5-y}Ga_yO_{12}:Ce^{3+}$, which is used in 1pcLED but is limited in application due to its cold-white light upon excitation with a $Ga_{1-x}In_xN$ primary LED. $Lu_{6-x}Ca_{1.5x}Si_{11}N_{20}O:Ce^{3+}$ ($x \approx 2.2$) emits further in the red spectral region, leading to warm-white light, which should offer warmer color temperatures and a higher color rendering index and could therefore be more suited for illumination-grade lighting applications. An $Ga_{1-x}In_xN$ based LED exhibit an excitation wavelength of 435 nm, which makes $Lu_{6-x}Ca_{1.5x}Si_{11}N_{20}O:Ce^{3+}$ ($x \approx 2.2$) suitable for application in LEDs because its excitation wavelength is comparable. Further research is necessary to optimize the quantum efficiency and therefore make $Lu_{6-x}Ca_{1.5x}Si_{11}N_{20}O:Ce^{3+}$ ($x \approx 2.2$) an even more interesting phosphor for modern illumination-grade warm-white lighting applications with increased color rendering index.

2.4 Experimental Part

2.4.1 Synthesis

All synthesis steps were performed in an argon-filled glovebox (Unilab, MBraun, Garching; $O_2 < 1$ ppm; $H_2O < 1$ ppm). For synthesis of $Yb_{6-x}Ca_{1.5x}Si_{11}N_{20}O$, YbF_3 (0.7055 mmol, 162.3 mg; Alfa Aesar, 99.99%), Yb_2O_3 (0.0705 mmol, 27.8 mg; smart elements, 99.99%), CaH_2 (1.6932 mmol, 71.3 mg; Sigma-Aldrich, 99.99%) and Si_3N_4 (0.7760 mmol, 108.9 mg; Ube Industries, SN-E10) were thoroughly ground in an agate mortar and filled into a tungsten crucible, which was then transferred into a water-cooled silica glass reactor of a radiofrequency furnace (type TIG 10/100; Hüttinger Elektronik Freiburg) attached to a Schlenk line. Under purified N_2 -atmosphere, the crucible was heated to 1600 °C in 10 min. The temperature was maintained for 5 h, cooled to 900 °C in 3h and finally quenched to room temperature. Dark red crystals were obtained, which are stable towards air, water, and concentrated mineral acids in repeated washing steps. $Lu_{6-x}Ca_{1.5x}Si_{11}N_{20}O$ was synthesized starting from LuF_3 (0.7017 mmol, 197.4 mg; Sigma-Aldrich, 99.99%), Lu_2O_3 (0.0702 mmol, 27.9 mg; ABCR, 99.9%), CaH_2 (1.6840 mmol, 70.9 mg; Sigma-Aldrich, 99.99%), Si_3N_4 (0.7718 mmol, 108.3 mg; Ube Industries, SN-E10) and with Eu_2O_3 (ABCR, 99.99%) or CeF_3 (Sigma-Aldrich, 99.99%) as dopants. The thoroughly ground starting materials were filled into a tungsten crucible and heated analogously to the Yb compound to a final synthesis temperature of 1400 °C. Eu^{2+} doping yielded a pinkish powder with orange-red luminescence under irradiation with blue light, whereas Ce^{3+} doping resulted in a yellow powder with yellow luminescence. The products are stable towards air, water, and concentrated mineral acids in repeated washing steps.

2.4.2 Electron Microscopy

For investigation of the chemical composition and morphology of all samples a scanning electron microscope (SEM) NanoLab G3 (Helios) equipped with an X-Max 80 SDD detector (Oxford Instruments) for energy dispersive X-ray (EDX) measurements was used. The measurements were performed with an acceleration voltage of 20 kV. A carbon-coating (BAL-TEC MED 020, Bal Tec AG) was applied to prevent electrostatic charging of the samples.

2.4.3 Single-Crystal X-ray Diffraction

A single crystal of $Yb_{6-x}Ca_{1.5x}Si_{11}N_{20}O$ ($x \approx 2.2$) was isolated and fixed on a MicroMount (MiTeGen) with an aperture size of 200 μm . X-ray diffraction data were collected with a Bruker D8 Venture diffractometer with rotating anode (Mo- $K\alpha$ radiation). SADABS was used for absorption correction.^[19] The crystal structure was solved using Direct Methods (SHELXS-97) and refined by least-squares methods (SHELXL-97).^[46-48] Further information of the crystal structure determination can be obtained from the Fachinformationszentrum

Karlsruhe, 76344 Eggenstein-Leopoldshafen, Germany (fax: (+49)-7247-808-666; e-mail: crysdata@fiz-karlsruhe.de) on quoting the depository number CSD-1948717.

2.4.4 Powder X-ray Diffraction

For powder X-ray diffraction (PXRD), the ground samples were sealed into glass capillaries (0.1 mm diameter, wall thickness 0.01 mm; Hilgenberg GmbH, Malsfeld, Germany) and measured on a STOE STADI P diffractometer (Cu- $K\alpha_1$ radiation, $\lambda = 1.5406 \text{ \AA}$, Ge(111) monochromator, Mythen1K detector) in parafocusing Debye–Scherrer geometry. The data were Rietveld refined with the TOPAS Academic V6 package applying the fundamental parameters approach (direct convolution of source emission profiles, axial instrument contributions, crystallite size and microstrain effects).^[49-52] Absorption effects were corrected using the calculated absorption coefficient. Preferred orientation of crystallites was handled with the spherical harmonics model of fourth order. The structure model of $Yb_{6-x}Ca_{1.5x}Si_{11}N_{20}O$ ($x \approx 2.2$), which was obtained from single-crystal X-ray diffraction data, was used as a starting point for all refinements.

2.4.5 Fourier Transform Infrared (FTIR) Spectroscopy

An FTIR spectrum of $Yb_{6-x}Ca_{1.5x}Si_{11}N_{20}O$ ($x \approx 2.2$) was measured with a Jasco FT/IR-4100 spectrometer using the ATR method.

2.4.6 UV/Vis Spectroscopy

For the measurement of diffuse reflectance spectra of $RE_{6-x}Ca_{1.5x}Si_{11}N_{20}O$ ($RE = Yb, Lu; x \approx 2.2$) in the range of 240 to 800 nm with 1 nm step size, a Jasco V-650 UV/vis spectrophotometer equipped with a deuterium and a halogen lamp (Czerny-Turner monochromator with 1200 lines/mm concave grating, photomultiplier tube detector) was used.

2.4.7 Luminescence

Photoluminescence properties of $Lu_{6-x}Ca_{1.5x}Si_{11}N_{20}O:RE$ ($RE = Eu^{2+}, Ce^{3+}; x \approx 2.2$) were measured on microcrystalline powder samples in PTFE sample holders using an in-house built system (5.3 in. integrating sphere, spectrofluorimeter equipped with a 150 W Xe lamp, two 500 mm Czerny-Turner monochromators, 1800 1/mm lattices, 250/500 nm lamps with a spectral range from 230 to 820 nm). Determination of the internal quantum efficiency (IQE) was accomplished by comparing integrated emission intensities and absorption at excitation wavelength with standard materials ($BaSO_4$, Merck p.a.; commercial $(Sr,Ca)AlSiN_3:Eu^{2+}$, Mitsubishi Chemical, and $Y_3Al_5O_{12}:Ce^{3+}$, Philips). For investigations on thermal quenching of the emission an AvaSpec-2048 spectrometer and a stabilized light-emitting-diode (LED) light source was used for sample excitation. Cryospectroscopy between 300 and 6 K was measured on a thick-bed powder layer with a fiber-coupled spectroscopy system containing

a thermally stabilized LED light source and a fiber-optic spectrometer (HR2000+ES spectrometer, Ocean Optics) with the sample placed in an evacuated cooling chamber, equipped with a liquid-He compressor system (ARS4HW, Advance Research System Inc.).

2.5 Acknowledgements

We thank Dr. Peter Mayer (Department of Chemistry at University of Munich (LMU)) for the collection of the single-crystal data and Petra Huppertz, Detlef Wiechert, Dr. Philipp Strobel, and Volker Weiler (all at Lumileds Phosphor Center Aachen) for luminescence measurements. Inspiring discussions with Christian Maak (Department of Chemistry, LMU) are gratefully appreciated.

2.6 References

- [1] *Energy Savings Forecast of Solid-State Lighting in General Illumination Applications*. Building Technologies Office, Energy Efficiency and Renewable Energy, U.S. Department of Energy: Washington, D.C., **2016**.
- [2] J. Heber, Nobel Prize 2014: Akasaki, Amano & Nakamura. *Nat. Phys.* **2014**, *10*, 791.
- [3] P. Pust, P. J. Schmidt, W. Schnick, *Nat. Mater.* **2015**, *14*, 454–458.
- [4] G. Blasse, A. Bril, *Appl. Phys. Lett.* **1967**, *11*, 53–55.
- [5] Z. Xia, A. Meijerink, *Chem. Soc. Rev.* **2017**, *46*, 275–299.
- [6] H. A. Höpfe, *Angew. Chem. Int. Ed.* **2009**, *48*, 3572–3582; *Angew. Chem.* **2009**, *121*, 3626–3636.
- [7] Y. Narukawa, J. Narita, T. Sakamoto, T. Yamada, H. Narimatsu, M. Sano, T. Mukai, *Phys. Status Solidi A* **2007**, *204*, 2087–2093.
- [8] H. Watanabe, N. Kijima, *J. Alloys Compd.* **2009**, *475*, 434–439.
- [9] H. A. Höpfe, H. Lutz, P. Morys, W. Schnick, A. Seilmeier, *J. Phys. Chem. Solids* **2000**, *61*, 2001–2006.
- [10] P. Pust, V. Weiler, C. Hecht, A. Tücks, A. S. Wochnik, A.-K. Henß, D. Wiechert, C. Scheu, P. J. Schmidt, W. Schnick, *Nat. Mater.* **2014**, *13*, 891–896.
- [11] C. Feldmann, *Z. Anorg. Allg. Chem.* **2012**, *638*, 2169–2171.
- [12] S. Schmiechen, P. Pust, P. J. Schmidt, W. Schnick, *Nachr. Chem.* **2014**, *62*, 847–851.
- [13] M. Zeuner, S. Pagano, W. Schnick, *Angew. Chem. Int. Ed.* **2011**, *50*, 7754–7775; *Angew. Chem.* **2011**, *123*, 7898–7920.
- [14] T. Suehiro, N. Hirosaki, R.-J. Xie, *ACS Appl. Mater. Interfaces*, **2011**, *3*, 811–816.
- [15] D. Durach, L. Neudert, P. J. Schmidt, O. Oeckler, W. Schnick, *Chem. Mater.* **2015**, *27*, 4832–4838.
- [16] Y. Q. Li, N. Hirosaki, R.-J. Xie, T. Takeda, M. Mitomo, *Chem. Mater.* **2008**, *20*, 6704–6714.

- [17] J. Ruan, R.-J. Xie, S. Funahashi, Y. Tanaka, T. Takeda, T. Suehiro, N. Hirotsuki, Y.-Q. Li, *J. Solid State Chem.* **2013**, *208*, 50–57.
- [18] J. Bhardwaj, J. Cesaratto, I. Wildeson, H. Choy, A. Tandon, W. Soer, P. Schmidt, B. Spinger, P. Deb, O. Shchekin, W. Götz, *Phys. Status Solidi A* **2017**, *214*, 1600826.
- [19] G. M. Sheldrick, *SADABS, v. 2: Multi-Scan Absorption Correction*; Bruker-AXS: Billerica, MA, **2012**.
- [20] M. Woike, W. Jeitschko, *J. Solid State Chem.* **1997**, *129*, 312–319.
- [21] K. Köllisch, H. Höpfe, H. Huppertz, M. Orth, W. Schnick, *Z. Anorg. Allg. Chem.* **2001**, *627*, 1371–1376.
- [22] H. Huppertz, O. Oeckler, A. Lieb, R. Glaum, D. Johrendt, M. Tegel, R. Kaindl, W. Schnick, *Chem. Eur. J.* **2012**, *18*, 10857–10864.
- [23] H. Huppertz, W. Schnick, *Angew. Chem. Int. Ed. Engl.* **1996**, *35*, 1983–1984; *Angew. Chem.* **1996**, *108*, 2115–2116.
- [24] A. Lieb, J. A. Kechele, R. Kraut, W. Schnick, *Z. Anorg. Allg. Chem.* **2007**, *633*, 166–171.
- [25] A. Lieb, W. Schnick, *Solid State Sci.* **2006**, *8*, 185–191.
- [26] V. Vinograd, E. Juarez-Arellano, A. Lieb, K. Knorr, W. Schnick, J. D. Gale, B. Winkler, *Z. Kristallogr.* **2007**, *222*, 402–415.
- [27] The term *sechser* ring was established by F. Liebau and is derived from the German word “sechser”. A *sechser* ring comprises six tetrahedra centers. F. Liebau, *Structural Chemistry of Silicates*, Springer, Berlin, **1985**.
- [28] R. Lauterbach, E. Irran, P. Henry, M. Weller, W. Schnick, *J. Mater. Chem.* **2000**, *10*, 1357–1364.
- [29] E. Irran, K. Köllisch, S. Leoni, R. Nesper, P. Henry, M. Weller, W. Schnick, *Chem. Eur. J.* **2000**, *6*, 2714–2720.
- [30] S. Krivovichev, S. Filatov, T. Semenova, *Russ. Chem. Rev.* **1998**, *67*, 137–155.
- [31] R. D. Shannon, *Acta Crystallogr., Sect. A: Cryst. Phys., Diffr., Theor. Gen. Crystallogr.* **1976**, *32*, 751–767.
- [32] R. Hübenal, *Maple, Program for the Calculation of MAPLE values, version 4*; University of Gießen: Gießen, Germany, **1993**.
- [33] R. Hoppe, *Angew. Chem. Int. Ed. Engl.* **1966**, *5*, 95–106; *Angew. Chem.* **1966**, *78*, 52–63.
- [34] N. E. Brese, M. O’Keeffe, *Acta Crystallogr., Sect. B* **1991**, *47*, 192–197.
- [35] I. D. Brown, D. Altermatt, *Acta Crystallogr., Sect. B* **1985**, *41*, 244–247.
- [36] P. E. D. Morgan, *J. Mater. Sci.* **1986**, *21*, 4305–4309.
- [37] T. Seto, M. Brik, *RSC Adv.* **2017**, *7*, 40152–40157.
- [38] R. López, R. Gómez, *J. Sol-Gel Sci. Technol.* **2012**, *61*, 1–7.

- [39] J. Tauc, R. Grigorovici, A. Vancu, *Phys. Status Solidi B* **1966**, *15*, 627–637.
- [40] Z. Zhang, O. M. ten Kate, A. C. A. Delsing, Z. Man, R. Xie, Y. Shen, M. J. H. Stevens, P. H. L. Notten, P. Dorenbos, J. Zhao, H. T. Hintzen, *J. Mater. Chem. C* **2013**, *1*, 7856–7865.
- [41] *Optical Testing for SuperFlux, SnapLED and LUXEON®Emitters*, Philips Lumileds: Application Brief AB08, **2006**.
- [42] G. Blasse, B. C. Grabmaier, *Luminescent Materials*, Springer, Berlin, Heidelberg, NY, **1994**.
- [43] M. R. Krames, O. B. Shchekin, R. Mueller-Mach, G. O. Mueller, L. Zhou, G. Harbers, M. G. Craford, *J. Display Technol.* **2007**, *3*, 160–175.
- [44] T. Seto, T. Izawa, *ECS J. Solid State Sci. Technol.* **2015**, *4*, R83–R88.
- [45] P. Dorenbos, *J. Phys.: Condens. Matter* **2005**, *17*, 8103–8111.
- [46] G. M. Sheldrick, *SHELXS-97: A Program for Crystal Structure Solution*; University of Göttingen: Göttingen, Germany, **1997**.
- [47] G. M. Sheldrick, *SHELXL-97: A Program for Crystal Structure Refinement*; University of Göttingen: Göttingen, Germany, **1997**.
- [48] G. M. Sheldrick, *Acta Crystallogr., Sect. A: Found. Crystallogr.* **2008**, *64*, 112–122.
- [49] H. M. Rietveld, *J. Appl. Crystallogr.* **1969**, *2*, 65–71.
- [50] A. A. Coelho, *TOPAS Version 6: A program for Rietveld refinement*, Coelho Software **2016**.
- [51] J. Bergmann, R. Kleeberg, A. Haase, B. Breidenstein, *Mater. Sci. Forum* **2000**, *347–349*, 303–308.
- [52] R. W. Cheary, A. A. Coelho, J. P. Cline, *J. Res. Natl. Inst. Stand. Technol.* **2004**, *109*, 1–25.

3 Missing Member in the $M^{\text{II}}M^{\text{III}}\text{Si}_4\text{N}_7$ Compound Class: Carbothermal Reduction and Nitridation Synthesis Revealing Substitution of N by C and O in $\text{CaLu}[\text{Si}_4\text{N}_{7-2x}\text{C}_x\text{O}_x]:\text{Eu}^{2+}/\text{Ce}^{3+}$ ($x \approx 0.3$)

Published in: *Chem. Eur. J.* **2022**, 28, e202104007– e202104014

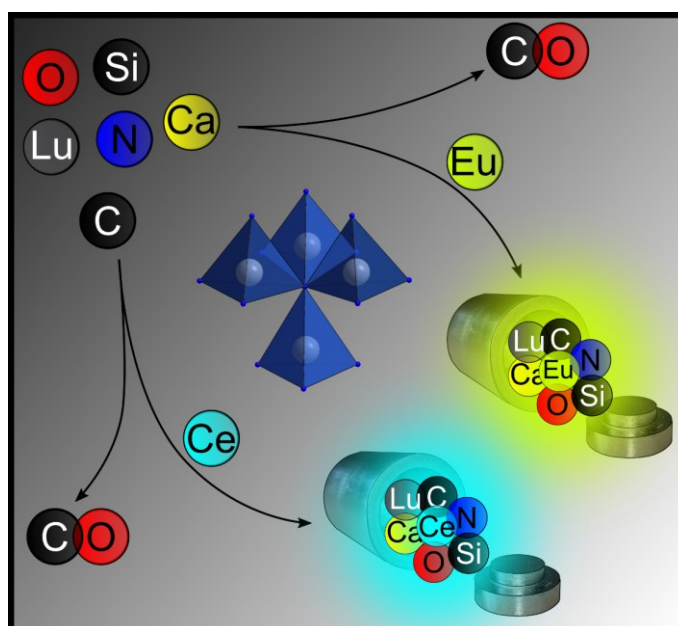
Authors: Lisa Gamperl, Otto E. O. Zeman, Philipp Strobel, Peter J. Schmidt, and Wolfgang Schnick

DOI: 10.1002/chem.202104007

Copyright © 2022 Wiley-VCH Verlag GmbH & Co. KGaA

<https://chemistry->

[europe.onlinelibrary.wiley.com/doi/epdf/10.1002/chem.202104007](https://chemistry-europe.onlinelibrary.wiley.com/doi/epdf/10.1002/chem.202104007)



Abstract. The oxonitridocarbidosilicate $\text{CaLu}[\text{Si}_4\text{N}_{7-2x}\text{C}_x\text{O}_x]$ ($x \approx 0.3$) was synthesized by carbothermal reduction and nitridation starting from CaH_2 , Lu_2O_3 , graphite and amorphous Si_3N_4 at $1550\text{ }^\circ\text{C}$ using a radiofrequency furnace. $\text{CaLu}[\text{Si}_4\text{N}_{7-2x}\text{C}_x\text{O}_x]$ ($x \approx 0.3$) crystallizes isotypic to many previously known $M^{\text{II}}M^{\text{III}}\text{Si}_4\text{N}_7$ compounds in space group $P6_3mc$, which was confirmed by Rietveld refinement based on powder X-ray diffraction data. Incorporation of C into the crystal structure as a result from the carbothermal synthesis route was confirmed via ^{13}C - and ^{29}Si -MAS-NMR spectroscopy. For the first time in the $M^{\text{II}}M^{\text{III}}\text{Si}_4\text{N}_7$ compound class, complementary EDX measurements suggest that simultaneous incorporation of oxygen compensates for the negative charge excess induced by C, resulting in an adjusted sum formula, $\text{CaLu}[\text{Si}_4\text{N}_{7-2x}\text{C}_x\text{O}_x]$ ($x \approx 0.3$). When excited with UV to blue light, $\text{CaLu}[\text{Si}_4\text{N}_{7-2x}\text{C}_x\text{O}_x]$

($x \approx 0.3$) shows an emission maximum in the blue spectral region ($\lambda_{\text{em}} = 484 \text{ nm}$; $fwhm = 4531 \text{ cm}^{-1}$) upon doping with Ce^{3+} , while Eu^{2+} -doped $\text{CaLu}[\text{Si}_4\text{N}_{7-2x}\text{C}_x\text{O}_x]$ ($x \approx 0.3$) exhibits a yellow-green emission ($\lambda_{\text{em}} = 546 \text{ nm}$; $fwhm = 3999 \text{ cm}^{-1}$).

3.1 Introduction

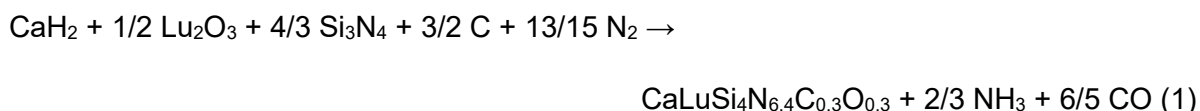
Several compounds with stoichiometric formulae $M^II M^III \text{Si}_4\text{N}_7$ have been investigated in recent years. Most $M^II M^III \text{Si}_4\text{N}_7$ compounds with different sized M^II and M^III cations crystallize in hexagonal space group $P6_3mc$, while lower symmetric orthorhombic space groups are predominantly observed when both M^II and M^III cations are of comparable size.^[1-13] Compounds containing Al^{3+} crystallize in the orthorhombic space group $Pna2_1$ owing to the fact that Al does not act as a counter ion but is incorporated in form of $[\text{AlN}_4]$ tetrahedra into the anionic network, leading to nitridoalumosilicates.^[14-16] Different synthetic strategies have been applied to facilitate the synthesis of the various $M^II M^III \text{Si}_4\text{N}_7$ compounds. Most Sr^{2+} and Ba^{2+} containing compounds have been obtained starting from metals or nitrides.^[1-3, 5-7, 10, 13] However, especially compounds with $M^II = \text{Ca}^{2+}$ were not successfully synthesized applying this approach due to the decreasing cation size going from Ba^{2+} to Ca^{2+} , limiting the access to $\text{Ca}M^III \text{Si}_4\text{N}_7$ compounds.^[7, 8, 11, 13] Therefore, only few examples obtained by other synthetic strategies are known. Successful synthesis of $\text{Ca}M^III \text{Si}_4\text{N}_7$ ($M^III = \text{Y}, \text{Sc}$) was exclusively achieved by carbothermal reduction and nitridation (CRN) using elemental carbon as a reducing agent to facilitate the reaction.^[8, 9, 11, 12] Carbon was either acting as an impurity phase or incorporated into the structures, which can be investigated by ^{13}C -MAS-NMR. In order to compensate the negative charge excess caused by an incorporation of C^{4-} onto the N^{3-} sites, an equimolar substitution of M^II by M^III was assumed.^[4, 8, 9, 11, 12] The $M^II M^III \text{Si}_4\text{N}_7$ compound class does not only offer interesting structural features like star shaped $[\text{N}^{4-}(\text{SiN}_3)_4]$ units containing a fourfold bridging ammonium-type nitrogen, but also provides doping possibilities for both application relevant rare earth activator ions Eu^{2+} and Ce^{3+} due to similar sizes and charges compared to the M^II and M^III cations, respectively. Doping $M^II M^III \text{Si}_4\text{N}_7$ with Eu^{2+} was shown to result in green to yellow emission while Ce^{3+} -doped compounds exhibit emission in the blue spectral region.^[6, 7, 11-16] Doped compounds can exhibit interesting luminescence properties relevant for application in one or two phosphor-converted light emitting diodes (1/2pcLEDs) in the lighting and display industries. The first and so far most widely used phosphor in white 1pcLEDs is $\text{Y}_{3-x}\text{Gd}_x\text{Al}_{5-y}\text{Ga}_y\text{O}_{12}:\text{Ce}^{3+}$ (YAG: Ce^{3+}), whose yellow emission combined with a blue emitting $\text{Ga}_{1-x}\text{In}_x\text{N}$ primary LED, for which the 2014 Nobel Prize in Physics has been awarded to *Isamu Akasaki, Hiroshi Amano* and *Shuji Nakamura*, leads to cold white light.^[17, 18] Blue phosphors with a broad emission band could be used to cover the blue-cyan gap between the spectrum of a narrow emitting nUV primary LED and the emission of the yellow phosphor or green-red phosphor

mixture, leading to high color quality and making the nUV primary LEDs more appealing.^[19, 20] The CRN synthesis method offers the advantage of using commonly available and stable starting materials, which makes it suitable for mass production, and provides access to compounds that are not accessible by other synthetic routes so far. Therefore, this method, besides other synthetic approaches, could enable the synthesis of previously unknown host structures or compounds for rare earth doping to develop novel luminescent materials. In this contribution, we report on the CRN synthesis of $\text{CaLu}[\text{Si}_4\text{N}_{7-2x}\text{C}_x\text{O}_x]$ ($x \approx 0.3$), a previously not observed, missing member of the $M^{\text{II}}M^{\text{III}}\text{Si}_4\text{N}_7$ compound class. $\text{CaLu}[\text{Si}_4\text{N}_{7-2x}\text{C}_x\text{O}_x]$ ($x \approx 0.3$) was investigated by ^{13}C - and ^{29}Si -MAS-NMR spectroscopy to specify the incorporation of carbon. Through the combination of NMR and elemental analysis, the simultaneous incorporation of oxygen rather than the previously assumed substitution of M^{II} by M^{III} was specified. This makes $\text{CaLu}[\text{Si}_4\text{N}_{7-2x}\text{C}_x\text{O}_x]$ the first oxonitridocarbidosilicate in this compound class and just the second oxonitridocarbidosilicate besides $\text{RE}_4\text{Ba}_2[\text{Si}_{12}\text{O}_2\text{N}_{16}\text{C}_3]:\text{Eu}^{2+}$ ($\text{RE} = \text{Lu}, \text{Y}$) known so far.^[21] Additional luminescence investigations reveal emission in the yellow-green and blue spectral regions upon doping with either Eu^{2+} or Ce^{3+} , respectively.

3.2 Results and Discussion

3.2.1 Synthesis and Chemical Analysis

$\text{CaLu}[\text{Si}_4\text{N}_{7-2x}\text{C}_x\text{O}_x]$ ($x \approx 0.3$) was obtained by carbothermal reduction and nitridation according to Equation (1) using carbon as a reducing agent.



Since the reaction yielded a fine powder, the structure and phase purity of the obtained product was confirmed by Rietveld refinement based on powder X-ray diffraction (PXRD) data, for which literature known isotypic $\text{SrYbSi}_4\text{N}_7$ ^[2] served as a starting model. As shown in Figure 3.1, the observed and calculated XRD profiles match well, with reasonable values of the reliability factors.

Crystallographic data from the Rietveld refinement are given in Table 3.1, while Wyckoff positions, atomic coordinates and isotropic displacement parameters are listed in Table B1.

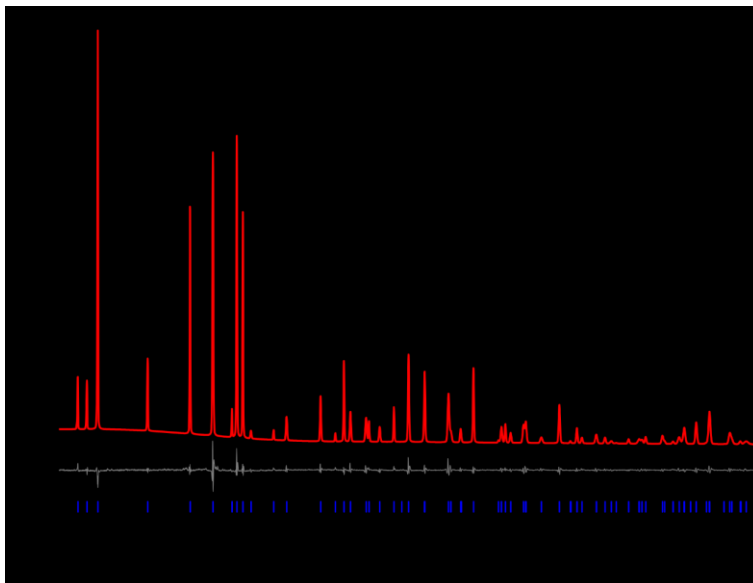


Figure 3.1. Rietveld refinement for $\text{CaLu}[\text{Si}_4\text{N}_{7-2x}\text{C}_x\text{O}_x]$ ($x \approx 0.3$) with observed (black) and calculated (red) powder X-ray diffraction patterns and the corresponding difference profile (gray). Vertical blue bars indicate the position of the Bragg reflections of the title compound.

Despite the use of stoichiometric amounts of carbon and oxygen in the starting materials to avoid impurities as carbon and oxygen are ideally withdrawn from the reaction in form of gaseous CO, the synthesis yielded grayish powders. A yellow-grayish powder with yellow-green luminescence was obtained upon doping with Eu^{2+} while doping with Ce^{3+} led to a white-grayish powder with blue luminescence, respectively. SEM- and TEM-EDX measurements (Table B2, B3; Figure B1a) are in good agreement with each other and with the theoretical values. Both investigations revealed an atomic ratio Ca:Lu of about 1:1 and in each case very similar values for oxygen. Furthermore, TEM investigations have shown values for carbon resulting in an atomic ratio C:O also of about 1:1. However, since the products have a grayish tint, the C content could originate from the sample itself as well as from an amorphous C side phase. To exclude that carbon remained as a side phase, the products obtained by the CRN method were purified through oxidation of remaining carbon by heating the material in a muffle furnace for 24h at 800 °C under air. This resulted in optically more lucid products with brighter luminescence but without a grayish tint. As can be seen in the luminescence spectra by the absence of line emission, Eu^{2+} was not oxidized to Eu^{3+} in this purification process. This can be explained by the fact that Eu^{2+} , which is larger than Eu^{3+} , occupies the large Ca site and is thus stabilized in its oxidation state.

Table 3.1. Details of the Rietveld refinement of $\text{CaLu}[\text{Si}_4\text{N}_{7-2x}\text{C}_x\text{O}_x]$ ($x \approx 0.3$)

Formula		$\text{CaLu}[\text{Si}_4\text{N}_{6.4}\text{C}_{0.3}\text{O}_{0.3}]$
formula weight / $\text{g}\cdot\text{mol}^{-1}$		425.433
crystal system		hexagonal
space group		$P6_3mc$ (no. 186)
lattice parameters / Å	$a =$	5.9616(1)
	$c =$	9.7392(1)
$V / \text{Å}^3$		299.76(1)
formula units per cell		2
density / $\text{g}\cdot\text{cm}^{-3}$		4.7131
diffractometer		STOE Stadi P
detector		Mythen 1K
radiation		$\text{Cu-K}\alpha_1$ ($\lambda = 1.5406 \text{ Å}$)
monochromator		Ge(111)
2θ range / °		$5 \leq 2\theta \leq 95$
data points		6042
total number of reflections		70
refined parameters		49
background function		Chebyshev polynomial (12 terms)
R values	$R_p =$	0.0408
	$R_{wp} =$	0.0564
	$R_{exp} =$	0.0232
	$R_{Bragg} =$	0.0217
$GooF (\chi^2)$		2.4241

In addition, Eu^{2+} is mainly coordinated by N^{3-} , which is known to have a certain degree of reducing potential.^[22] EDX measurements (Figure B1b, Table B4) show increased oxygen content caused by superficially bound oxygen. CHNS analysis (Table B5) was used for quantification of the carbon content. Since a certain C content could still be determined despite purification, it was assumed that C is no longer present as a secondary phase but has also been incorporated into the structure. In order to confirm the carbon incorporation, NMR spectroscopy was performed. In addition, CHNS analysis shows the absence of hydrogen in the sample.

3.2.2 Structure Description

$\text{CaLu}[\text{Si}_4\text{N}_{7-2x}\text{C}_x\text{O}_x]$ ($x \approx 0.3$) crystallizes like many other representatives of the $M^{\text{II}}M^{\text{III}}\text{Si}_4\text{N}_7$ compound class in hexagonal space group $P6_3mc$.^[1-3, 5-7, 9, 11-13] The structure exhibits a three-dimensional network of all-side vertex-sharing $[\text{SiN}_4]$ tetrahedra. Four tetrahedra are linked via one common fourfold bridging $(\text{N,C})^{[4]}$ to form a star shaped unit, which was first reported by Huppertz *et al.* for $\text{BaYbSi}_4\text{N}_7$ (Figure 3.2a).^[1] These $[(\text{N,C})^{[4]}(\text{Si}(\text{N,O})_3^{[2]})_4]$ units are all-

3 Missing Member in the $M^II M^III \text{Si}_4 \text{N}_7$ Compound Class: Carbothermal Reduction and Nitridation Synthesis Revealing Substitution of N by C and O in $\text{CaLu}[\text{Si}_4 \text{N}_{7-2x} \text{C}_x \text{O}_x]:\text{Eu}^{2+}/\text{Ce}^{3+}$ ($x \approx 0.3$)

side vertex sharing and stacked along [001], leading to a ${}^3_{\infty}[(\text{Si}_4^{[4]}(\text{N},\text{O})_6^{[2]}(\text{N},\text{C})^{[4]})_5^-]$ network. Stacking and linking the star shaped units leads to *dreier* and *sechser* ring channels along [010] with Ca^{2+} and Lu^{3+} located in the distorted *sechser* ring channels (Figure 3.2b).^[23]

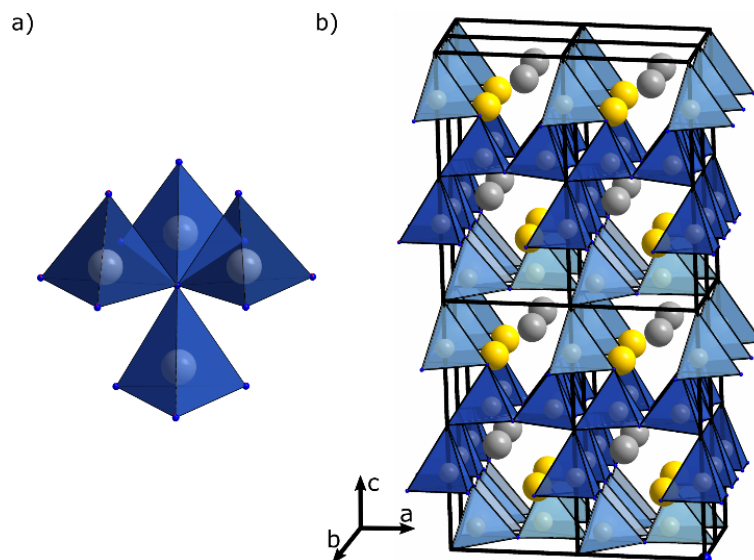


Figure 3.2. (a) Star shaped $[(\text{N},\text{C})^{[4]}(\text{Si}(\text{N},\text{O})_3^{[2]})_4]$ unit and (b) crystal structure of $\text{CaLu}[\text{Si}_4 \text{N}_{7-2x} \text{C}_x \text{O}_x]$ ($x \approx 0.3$). $[\text{Si}(\text{N},\text{C},\text{O})_4]$ tetrahedra in blue, N/C atoms blue/black, N/O atoms blue/red, Si atoms gray, Ca atoms yellow, Lu atoms light gray.

The one crystallographic Lu^{3+} site is thereby octahedrally coordinated by six $(\text{N},\text{O})^{[2]}$, while twelve $(\text{N},\text{O})^{[2]}$ coordinate the only crystallographic Ca^{2+} site in form of an anticuboctahedron (Figure 3.3).

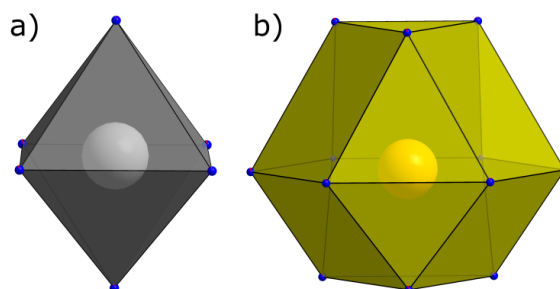


Figure 3.3. Coordination spheres of (a) Lu and (b) Ca. N/O atoms blue/red, Lu light gray, Ca yellow.

The interatomic $\text{Si}-(\text{N},\text{O})^{[2]}$ distances in the anionic network range from 1.676(7) to 1.746(6) Å while the $\text{Si}-(\text{N},\text{C})^{[4]}$ distances are between 1.868(2) and 1.891(6) Å. The slightly elongated bonds result from the repulsion of formally positively charged $\text{N}^{[4]}$ and positively polarized Si. $\text{Lu}-(\text{N},\text{O})$ and $\text{Ca}-(\text{N},\text{O})$ distances vary from 2.296(7) to 2.315(7) Å and 2.819(6) to 2.983(7) Å, respectively. The observed distances are in good agreement with the reported values from other $M^II M^III \text{Si}_4 \text{N}_7$ compounds.^[1-3, 5-7, 9, 11, 12]

3.2.3 NMR Spectroscopy

^{13}C and ^{29}Si magic-angle spinning (MAS) NMR experiments were conducted to determine the incorporation of carbon into the tetrahedral network. The star shaped unit $[\text{N}3^{[4]}(\text{SiN}_3)_4]$ (for detailed atom assignment see Figure B2) consists of one $[\text{Si}1(\text{N}2)_3\text{N}3]$ and three $[\text{Si}2(\text{N}1)_2\text{N}2\text{N}3]$ tetrahedra connected via $\text{N}3^{[4]}$. $\text{N}1^{[2]}$ and $\text{N}2^{[2]}$ are suitable for substitution by O, while C can be incorporated onto the $\text{N}3^{[4]}$ site, which leads to $[\text{Si}1(\text{N}2)_3(\text{N}_{1-x}\text{C}_x)_3]$ and $[\text{Si}2(\text{N}1)_2\text{N}2(\text{N}_{1-x}\text{C}_x)_3]$. The ^{13}C -NMR spectrum (Figure 3.4) shows one narrow peak corresponding to an isotropic chemical shift of about 32 ppm, which is consistent with the expectation of the one possible C site $[\text{C}3^{[4]}(\text{SiN}_3)_4]$ and matches with the value reported in literature.^[8]

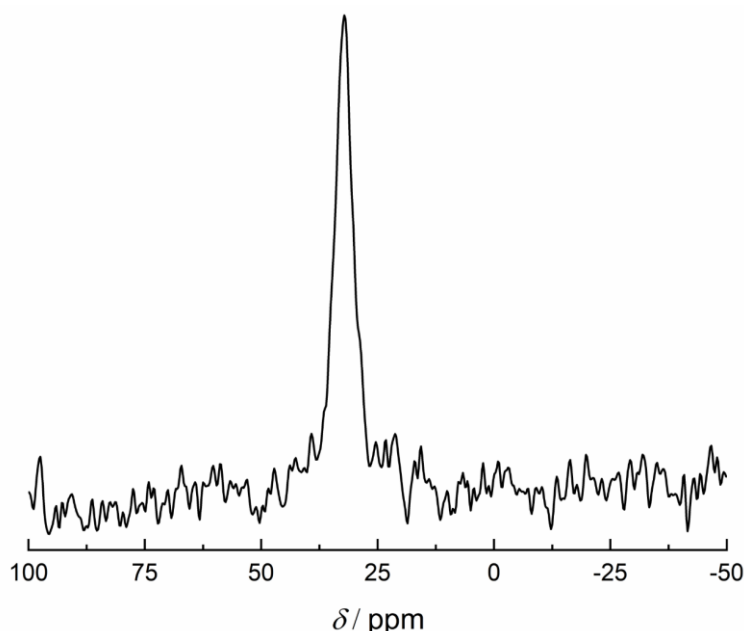


Figure 3.4. ^{13}C -MAS-NMR spectrum of polycrystalline $\text{CaLu}[\text{Si}_4\text{N}_{7-2x}\text{C}_x\text{O}_x]$ ($x \approx 0.3$), acquired at the MAS frequency of 10 kHz.

Two signals with very similar chemical shift and an intensity ratio of 1:3 are expected in the ^{29}Si -NMR spectrum. The slightly different chemical shifts originate from marginally different Si-N3 distances (Si1-N3: 1.868(2) Å, Si2-N3: 1.891(6) Å) but otherwise similar chemical surroundings. Partial substitution of N3 by C would lead to two additional signals shifted towards larger chemical shift values.^[24] Figure 3.5 shows the obtained ^{29}Si -MAS-NMR spectrum with a maximum peak at -36.4 ppm and at least one shoulder observable at larger δ , which is in accordance with the literature as well.^[8]

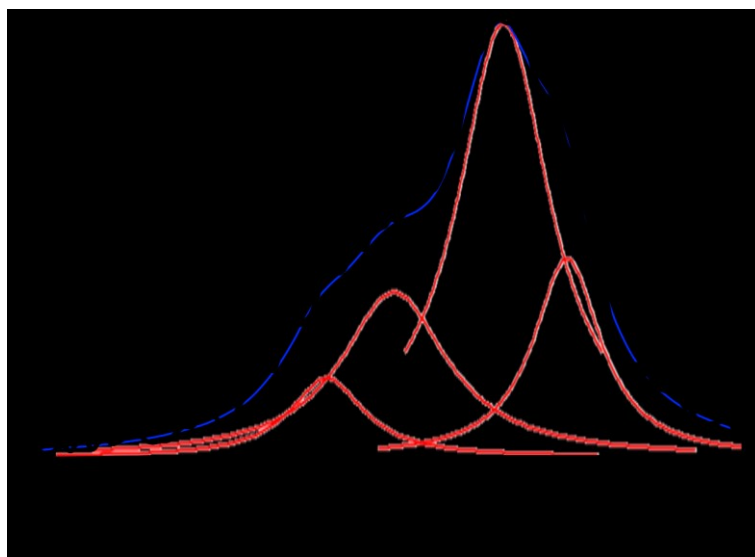


Figure 3.5. Acquired ^{29}Si -MAS-NMR spectrum (black, MAS frequency: 10 kHz) of polycrystalline $CaLu[Si_4 N_{7-2x} C_x O_x]$ ($x \approx 0.3$) along with four deconvoluted Lorentz functions (red) and the corresponding calculated fit (blue).

The measured signal was deconvoluted by four Lorentz functions (Figure 3.6, B3), in accordance with the four expected signals.

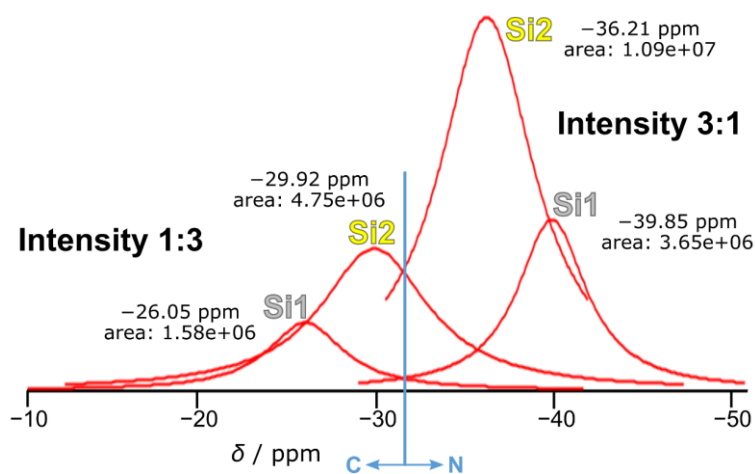


Figure 3.6. Detailed analysis of the deconvoluted ^{29}Si -MAS-NMR spectrum of polycrystalline $CaLu[Si_4 N_{7-2x} C_x O_x]$ ($x \approx 0.3$) by four Lorentz functions.

Two signals at lower δ (-36.2 ppm and -39.9 ppm) with an intensity ratio of 3:1 can be assigned to the isotropic chemical shift of Si2 and Si1, respectively, solely coordinated by N. C incorporation leads to larger δ and therefore the signals at -26.0 ppm and -29.9 ppm with an intensity ratio of 1:3 can be assigned to the ^{29}Si isotropic shifts of $[Si1(N2)_3(N_{1-x}C_x3)]$ and $[Si2(N1)_2N2(N_{1-x}C_x3)]$, respectively. The larger chemical shift value of $[Si1(N2)_3(N_{1-x}C_x3)]$ compared to $[Si1(N2)_3N3]$ is a consequence of a shorter Si1-(N,C)3 distance compared to Si2-(N,C)3. The intensity ratio Si-N:Si-C of 1:2.3 in both cases leads to $N_{0.7}C_{0.3}$. To preserve

valency balance, a simultaneous substitution of 0.3 N by 0.3 O equally distributed on the N1 and N2 sites is necessary, which leads to a composition close to $\text{CaLuSi}_4\text{N}_{6.4}\text{C}_{0.3}\text{O}_{0.3}$. This is in good agreement with the results obtained by EDX and CHNS investigations. Previous works on the substitution of carbon by nitrogen confirmed by ^{13}C -NMR assume charge compensation through substitution of M^{II} by M^{III} shown by EDX measurements of the $M^{\text{II}}:M^{\text{III}}:\text{Si}$ ratios, which revealed an excess of M^{III} . However, no statements were made on the possibility of oxygen incorporation despite using oxides or carbonates as starting materials.^[8, 9, 11] Therefore, $\text{CaLu}[\text{Si}_4\text{N}_{7-2x}\text{C}_x\text{O}_x]$ ($x \approx 0.3$) is the first oxonitridocarbidosilicate described in this compound class and only the second literature known oxonitridocarbidosilicate so far.^[21]

3.2.4 UV/Vis Reflectance Spectroscopy

The optical band gap of nondoped $\text{CaLu}[\text{Si}_4\text{N}_{7-2x}\text{C}_x\text{O}_x]$ ($x \approx 0.3$) was determined using solid-state UV/Vis spectroscopy. The measured diffuse reflectance spectrum was transformed into a pseudo-absorption spectrum using the Kubelka–Munk function $F(R) = (1-R)^2/2R$ with R being the measured reflectance.^[25] The optical band gap was determined from a Tauc plot, where $h\nu$ is plotted against $(F(R) \cdot h\nu)^{1/n}$ with $n = 1/2$ for a direct allowed transition by intersecting the aligned tangent on the linear region with the abscissa.^[26] Thereby, the optical band gap was estimated to be approx. 4.5 eV (Figure 3.7), which makes $\text{CaLu}[\text{Si}_4\text{N}_{7-2x}\text{C}_x\text{O}_x]$ ($x \approx 0.3$) a suitable host material for doping, as wide band gaps ≥ 4 eV are desired for pcLED applications.^[27, 28] This is in good agreement with band gap values obtained for other $M^{\text{II}}M^{\text{III}}\text{Si}_4\text{N}_7$ compounds.^[5-7, 11]

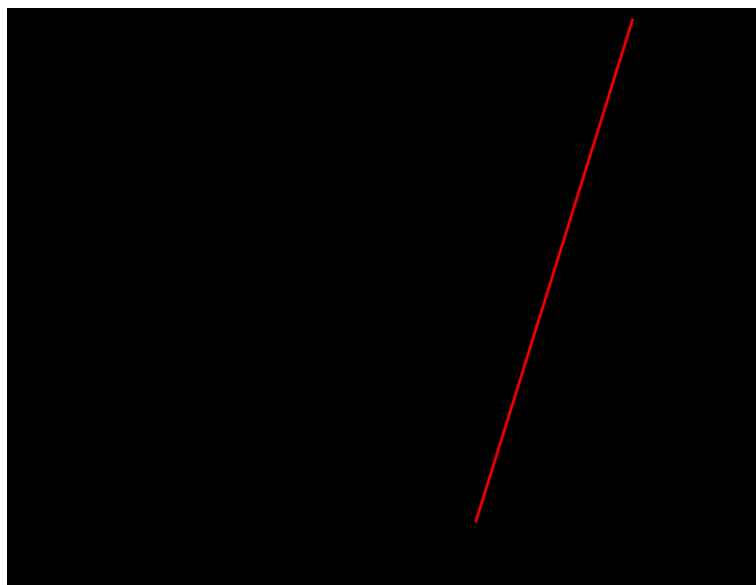


Figure 3.7. Tauc plot ($n = 1/2$) for a nondoped $\text{CaLu}[\text{Si}_4\text{N}_{7-2x}\text{C}_x\text{O}_x]$ ($x \approx 0.3$) powder sample.

3.2.5 Luminescence

Due to similar sizes and charges compared to Ca^{2+} and Lu^{3+} , doping with both rare earth activator ions Eu^{2+} and Ce^{3+} , respectively, is feasible. A comparison of charges and ionic radii indicates that Ce^{3+} ($r(\text{coordination number } CN: 6) = 1.01 \text{ \AA}$) preferably occupies the octahedrally coordinated Lu^{3+} site ($r(CN: 6) = 0.861 \text{ \AA}$) while the larger Eu^{2+} ($r(CN: 10) = 1.35 \text{ \AA}$) prefers the anticuboctahedral Ca^{2+} ($r(CN: 12) = 1.34 \text{ \AA}$) site.^[29] Luminescence properties were measured on single luminescent particles of Eu^{2+} or Ce^{3+} -doped $CaLu[Si_4N_{7-2x}C_xO_x]$ ($x \approx 0.3$). Upon excitation of the samples with UV to blue light, $CaLu[Si_4N_{7-2x}C_xO_x]:Ce^{3+}$ ($x \approx 0.3$; 1 mol%) shows strong blue luminescence and exhibits an emission maximum at $\lambda_{em} \approx 484 \text{ nm}$ and a full width at half-maximum (*fwhm*) of about $109 \text{ nm}/4531 \text{ cm}^{-1}$ (Figure 3.8).

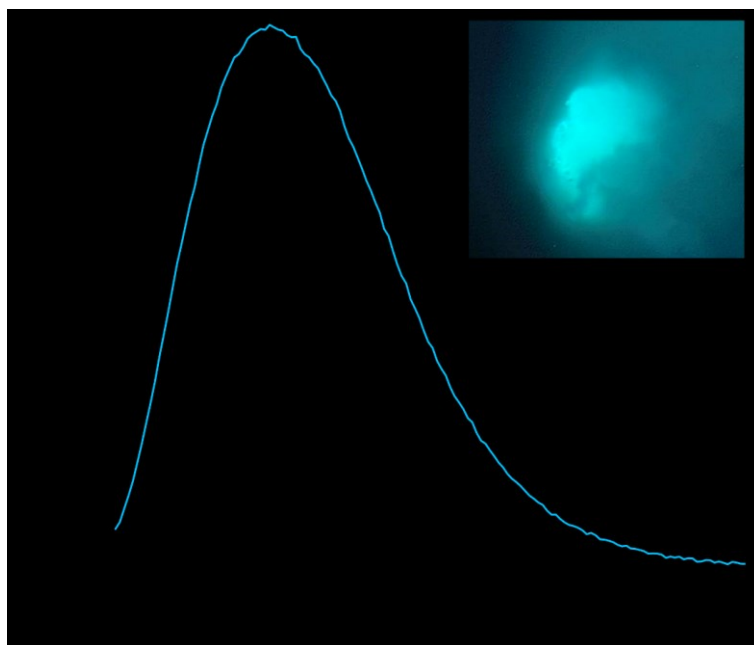


Figure 3.8. Normalized excitation (black, $\lambda_{mon} = 490 \text{ nm}$) and emission spectra (blue, $\lambda_{exc} = 400 \text{ nm}$) of $CaLu[Si_4N_{7-2x}C_xO_x]:Ce^{3+}$ ($x \approx 0.3$; 1 mol%) with a micrograph of the measured particle.

The typical broadband emission observed with Ce^{3+} activated phosphors originates from a spin and parity allowed transition from the lowest excited $5d^1$ level to the $4f^1$ ground state split into the two $^2F_{5/2}$ and $^2F_{7/2}$ levels separated by about 2000 cm^{-1} due to spin-orbit coupling.^[30] The broad emission bandwidth might additionally be increased due to the substitution of N by C and O leading to different environments in the crystal field of the dopant. The luminescence characteristics agree well with the values of other Ce^{3+} -doped $M''M'''Si_4N_7$ compounds and continues the trend of red shift for decreasing cation sizes going from Ba over Sr to Ca due to lattice strain caused by the differently sized alkaline earth ions.^[6, 7, 13] Due to the broadband emission, an application as a blue phosphor in nUV pumped

pcLEDs to fill the blue-cyan gap could be conceivable since an *fwhm* of ≥ 60 nm is necessary for a high color quality.^[19, 20]

An as-synthesized sample of $\text{CaLu}[\text{Si}_4\text{N}_{7-2x}\text{C}_x\text{O}_x]:\text{Eu}^{2+}$ ($x \approx 0.3$; 0.5 mol%) shows yellow-green emission when excited by UV to blue light with an emission maximum at $\lambda_{\text{em}} \approx 548$ nm, *fwhm* of about 128 nm/4026 cm^{-1} and a low internal quantum efficiency (IQE) of 12% (Figure 3.9) for a doping concentration of approx. 0.5 mol% referred to Ca^{2+} .

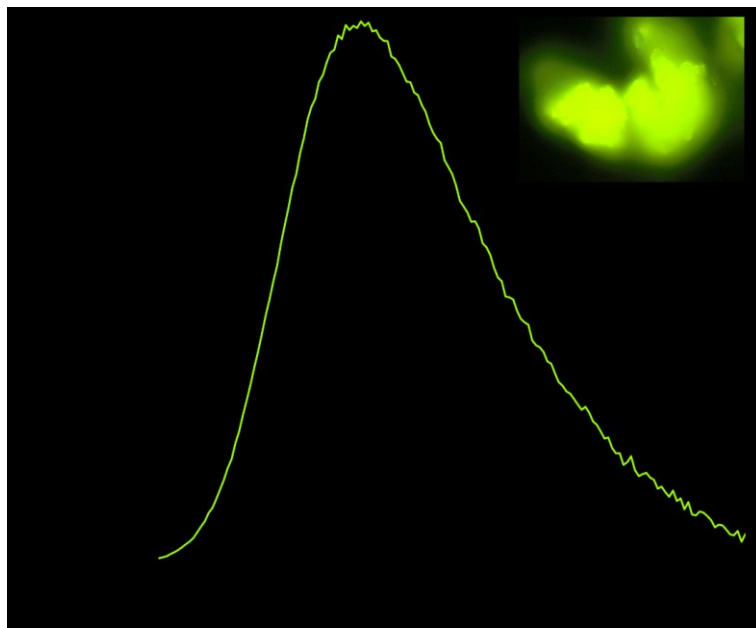


Figure 3.9. Normalized excitation (black, $\lambda_{\text{mon}} = 562$ nm) and emission spectra (green, $\lambda_{\text{exc}} = 400$ nm) of unpurified $\text{CaLu}[\text{Si}_4\text{N}_{7-2x}\text{C}_x\text{O}_x]:\text{Eu}^{2+}$ ($x \approx 0.3$; 0.5 mol%) with a micrograph of the measured particle.

The rather broad emission can be assigned to the $4f^65d^1 \rightarrow 4f^7$ transition of Eu^{2+} , which implies the reduction of Eu^{3+} to Eu^{2+} due to the CRN method and incorporation into the anionic network. Broadband emission may again be enhanced by a range of environments due to anionic substitutions. Luminescence originating from Eu^{3+} would lead to sharp emission lines mostly in the red spectral region due to $4f \rightarrow 4f$ transitions from excited $^5\text{D}_0$ to the $^7\text{F}_J$ ($J = 0-6$) levels of the ground state $4f^6$ configuration.^[30]

After purification of yellow-grayish $\text{CaLu}[\text{Si}_4\text{N}_{7-2x}\text{C}_x\text{O}_x]:\text{Eu}^{2+}$ ($x \approx 0.3$; 0.5 mol%) by heating, luminescence properties of the lighter yellow powder were re-measured. There was practically no change in the emission maximum of $\lambda_{\text{em}} \approx 546$ nm at ~ 0.5 mol%, however, *fwhm* was decreased to about 123 nm/3999 cm^{-1} due to annealing while the internal quantum efficiency increased to 23% (Figure 3.10) by removal of carbon residues.

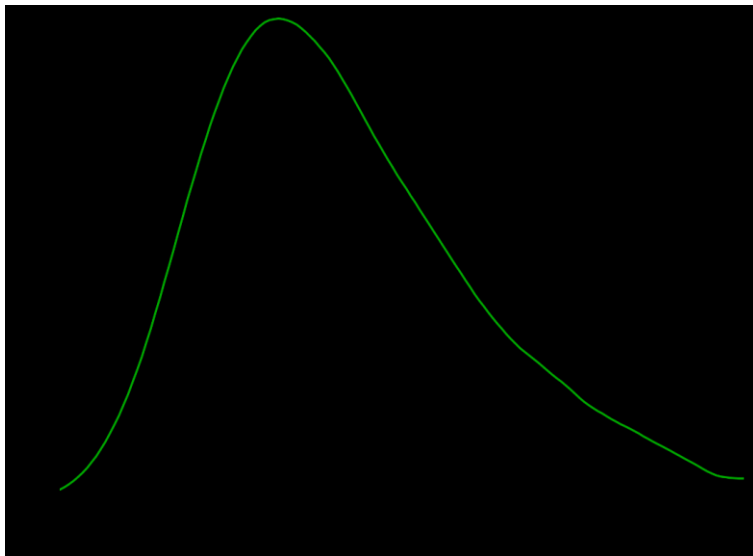


Figure 3.10. Smoothed emission spectra ($\lambda_{\text{exc}} = 400 \text{ nm}$) of as-synthesized (black) and purified (green) $\text{CaLu}[\text{Si}_4\text{N}_{7-2x}\text{C}_x\text{O}_x]:\text{Eu}^{2+}$ ($x \approx 0.3$; 0.5 mol%).

Varying the doping concentration of $\text{CaLu}[\text{Si}_4\text{N}_{7-2x}\text{C}_x\text{O}_x]:\text{Eu}^{2+}$ ($x \approx 0.3$) from 0.5 to 4 mol% leads to a slight red shift of the emission maxima and an increase in *fwhm* (Figure B4, Table B6), which is frequently observed with increasing doping concentrations due to a higher probability of reabsorption.^[31]

Thermal quenching behavior is an important characteristic for phosphors used in LEDs as the operating temperature of LED chips can reach around 200 °C. It is therefore important that the phosphor retains its luminescence properties for any potential application. In order to determine the thermal quenching behavior of $\text{CaLu}[\text{Si}_4\text{N}_{7-2x}\text{C}_x\text{O}_x]:\text{Eu}^{2+}$ ($x \approx 0.3$; 0.5 mol%), cryo-spectroscopy measurements between 300 K and 6 K were carried out on a 0.5 mol% doped sample and combined with measurements with a thermal quenching set-up up to 598 K (Figure B5). As it can be derived from the thermal quenching analysis, the maximum achievable IQE at room temperature is about 40% compared to 6 K. Data of thermal quenching measurements show significant thermal quenching at 150 °C with a relative photoemission intensity of about 27% compared to room temperature. However, heating at elevated temperatures does not lead to noticeable degeneration of the sample during the measurement period. To further discuss the thermal quenching behavior, two dominant mechanisms have been proposed. *Dorenbos* postulates that thermal quenching is caused by thermal excitation of the $5d^1$ electron of the activator ion into the conduction band of the host.^[27, 32] However, this mechanism, also called thermal ionization model, only dominates in structures with low band gaps $E_g < 4 \text{ eV}$.^[27] Since the band gap of nondoped $\text{CaLu}[\text{Si}_4\text{N}_{7-2x}\text{C}_x\text{O}_x]$ ($x \approx 0.3$) was determined to be approx. 4.5 eV, this mechanism only plays a minor role in explaining the thermal quenching behavior. The second theory proposed by

Blasse et al. is called crossover mechanism and results from nonradiative relaxation of the excited $5d^1$ electron of the activator ion to its ground state.^[27, 30, 33] This is the reason for the search for host structures with high rigidity. Typical nitride phosphors such as $(\text{Sr},\text{Ba})_2\text{Si}_5\text{N}_8:\text{Eu}^{2+}$ or $(\text{Sr},\text{Ca})\text{AlSiN}_3:\text{Eu}^{2+}$ maintain higher relative photoemission intensities of more than 80% at 150 °C compared to room temperature due to the high rigidity of their three-dimensional tetrahedron networks, which is among other things determined by a large number of multi-bridging atoms like $\text{N}^{[3]}$ or $\text{N}^{[4]}$ and therefore shorter Si-N bond lengths. $(\text{Sr},\text{Ba})_2\text{Si}_5\text{N}_8:\text{Eu}^{2+}$ and $(\text{Sr},\text{Ca})\text{AlSiN}_3:\text{Eu}^{2+}$ contain a high ratio of $\text{N}^{[3]}$ compared to $\text{N}^{[2]}$ while $\text{CaLuSi}_4\text{N}_7:\text{Eu}^{2+}$ is comprised of only one seventh of highly bridging $\text{N}^{[4]}$ but multiple weaker bridging $\text{N}^{[2]}$. Hence, Si-N bond lengths of about 1.67–1.80 Å can be found in $(\text{Sr},\text{Ba})_2\text{Si}_5\text{N}_8:\text{Eu}^{2+}$ and $(\text{Sr},\text{Ca})\text{AlSiN}_3:\text{Eu}^{2+}$ while Si-N^[4] bond lengths in $\text{CaLu}[\text{Si}_4\text{N}_{7-2x}\text{C}_x\text{O}_x]:\text{Eu}^{2+}$ are significant longer with 1.84 Å on average. This leads to lower structural rigidity and the observed weaker temperature dependent stability.^[12, 34-39] In addition, cation substitution in $(\text{Sr},\text{Ca})\text{AlSiN}_3:\text{Eu}^{2+}$ induced lattice distortions, which also resulted in a more ridged structure and therefore improved the thermal quenching behavior.^[40] However, some phosphors suffer from thermal quenching despite high structural rigidity.^[27] The size of the host lattice cation also plays an important role in thermal quenching behavior since the activator ions occupy their sites.^[41] With decreasing radius of the cation as is the case for Ca, relaxation in the $4f^n5d^1$ excited state of the activator ion becomes less restricted. This leads to an increased Stokes shift and therefore a lower quenching temperature as well a broader emission band, which can be seen in the emission spectra.^[41]

The known Lu containing phosphors $M^{\text{II}}\text{LuSi}_4\text{N}_7:\text{Eu}^{2+}$ ($M^{\text{II}} = \text{Ba}, \text{Sr}$) show an emission maximum peaking at $\lambda_{\text{em}} \approx 525$ nm independent of the incorporation of Sr or Ba, which is contrary to the expected blue shift for heavier alkaline earth metals. However, $M^{\text{II}}\text{LuSi}_4\text{N}_7:\text{Eu}^{2+}$ shows mixed occupation of M^{II} and Lu on the two crystallographic cation sites whereas this was not observed with $\text{CaLu}[\text{Si}_4\text{N}_{7-2x}\text{C}_x\text{O}_x]:\text{Eu}^{2+}$ ($x \approx 0.3$), which could explain this phenomenon.^[13] Comparing the luminescence properties of $\text{CaLu}[\text{Si}_4\text{N}_{7-2x}\text{C}_x\text{O}_x]:\text{Eu}^{2+}$ ($x \approx 0.3$) with already known phosphors shows that $\text{CaLu}[\text{Si}_4\text{N}_{7-2x}\text{C}_x\text{O}_x]:\text{Eu}^{2+}$ ($x \approx 0.3$) has very similar characteristics as broadband green–yellow emitting $\text{Y}_{3-x}\text{Gd}_x\text{Al}_{5-y}\text{Ga}_y\text{O}_{12}:\text{Ce}^{3+}$ (YAG: Ce^{3+} , Lumileds Phosphor Center Aachen) with its emission maximum at $\lambda_{\text{em}} = 552$ nm ($\lambda_{\text{exc}} = 440$ nm) and *fwhm* of 118 nm/3600 cm^{-1} (Figure B6). YAG: Ce^{3+} shows a relative photoemission intensity at 150 °C of about 53% compared to room temperature.^[12, 17, 42, 43] It is most commonly used in state-of-the-art white light single phosphor converted light emitting diodes (1pcLEDs), which could therefore also be a possible application for $\text{CaLuSi}_4\text{N}_7:\text{Eu}^{2+}$. Its narrow excitation band could also be an interesting feature for an application as a color point stabilizer in LEDs.

3.3 Conclusion

In this contribution, we report on the luminescence properties of Eu^{2+} and Ce^{3+} activated $\text{CaLu}[\text{Si}_4\text{N}_{7-2x}\text{C}_x\text{O}_x]$ ($x \approx 0.3$) synthesized by carbothermal reduction and nitridation, which is the only method to facilitate the formation of $\text{Ca}M^{\text{III}}\text{Si}_4\text{N}_7$ so far. $\text{CaLu}[\text{Si}_4\text{N}_{7-2x}\text{C}_x\text{O}_x]$ ($x \approx 0.3$) crystallizes isotypic to many previously known $M^{\text{II}}M^{\text{III}}\text{Si}_4\text{N}_7$ compounds in space group $P6_3mc$. As carbon was used as a starting material, ^{13}C - and ^{29}Si -MAS-NMR spectroscopy were used to determine the incorporation of carbon into the tetrahedron network. Prior to this, the samples were purified by heating under air to remove residual carbon, which leads to optically more lucid powders with brighter luminescence. The analysis shows a partial substitution of N^{3-} by C^{4-} on the fourfold bridging $\text{N}^{[4]}$ site. Combining NMR spectroscopy with elemental analyses like EDX and CHNS leads to the assumption that the negative charge excess caused by the incorporation of C^{4-} is compensated by equimolar incorporation of O^{2-} rather than by substitution of M^{III} onto the M^{II} site as reported for other $M^{\text{II}}M^{\text{III}}\text{Si}_4\text{N}_7$ compounds synthesized by the CRN method. This leads to an actual composition close to $\text{CaLuSi}_4\text{N}_{6.4}\text{C}_{0.3}\text{O}_{0.3}$ and is therefore the only oxonitridocarbidosilicate in this compound class as well as only the second oxonitridocarbidosilicate in general known yet. Since CRN is the only known method for the synthesis of $\text{Ca}M^{\text{III}}\text{Si}_4\text{N}_7$ so far, carbon incorporation and therefore a possible stabilization of the crystal structure due to more covalent Si–C bonds, which leads to a higher rigidity and stability of the network despite the incorporation of a smaller M^{II} cation, may be essential for the formation also of other $\text{Ca}M^{\text{III}}\text{Si}_4\text{N}_7$ compounds. Since the presence of M^{II} and M^{III} sites, doping with Eu^{2+} as well as Ce^{3+} is possible. The latter leads to an emission maximum at $\lambda_{\text{em}} \approx 484$ nm and a *fwhm* of about 109 nm/4531 cm^{-1} upon irradiation with UV to blue light ($\lambda_{\text{exc}} = 400$ nm). Purified $\text{CaLu}[\text{Si}_4\text{N}_{7-2x}\text{C}_x\text{O}_x]:\text{Eu}^{2+}$ ($x \approx 0.3$) exhibits an emission maximum of $\lambda_{\text{em}} \approx 546$ nm and a *fwhm* of about 123 nm/3999 cm^{-1} , which can be compared to commercially used YAG: Ce^{3+} . Both Eu^{2+} - and Ce^{3+} -doped phosphors offer properties which could be relevant for applications. Since the $M^{\text{II}}M^{\text{III}}\text{Si}_4\text{N}_7$ compound class offers a variety of full or partial substitution possibilities even for activator ions, it is a promising host lattice to cover a very broad emission spectrum.

3.4 Experimental Part

3.4.1 Synthesis

Due to the air and moisture sensitivity of CaH_2 , all manipulations were carried out under Ar-atmosphere either in an Ar-filled glovebox (Unilab, MBraun, Garching; $\text{O}_2 < 1$ ppm; $\text{H}_2\text{O} < 1$ ppm) or in Ar-filled glassware applying the Schlenk technique. $\text{CaLu}[\text{Si}_4\text{N}_{7-2x}\text{C}_x\text{O}_x]$ ($x \approx 0.3$) was synthesized starting from 29.7 mg CaH_2 (0.705 mmol, Sigma-Aldrich, 99.99%), 140.3 mg Lu_2O_3 (0.353 mmol, Sigma-Aldrich, 99.9%), 131.9 mg amorphous Si_3N_4 (0.940 mmol, Ube Industries, SNA-00), 12.7 mg graphite (1.058 mmol, Chempur, 99.9%) and either EuF_3 (Sigma-Aldrich, 99.99%) or CeF_3 (Sigma-Aldrich, 99.99%) as dopants. The starting materials were thoroughly ground in an agate mortar and filled into a tungsten crucible, which was then transferred into a water-cooled silica glass reactor of a radiofrequency furnace (TIG 10/100; Hüttinger Elektronik Freiburg, Germany) attached to a Schlenk line. The crucible was heated under N_2 -atmosphere to 1550 °C within one hour, maintained at that temperature for 2 h, cooled down to 500 °C within 2 h, and finally, the product was quenched by switching off the furnace.^[44] Upon doping with Eu^{2+} , the product was obtained as a yellow-grayish powder with yellow-green luminescence when excited with UV to blue light. Ce^{3+} doping led to a white-grayish powder, which shows blue luminescence upon irradiation with UV to blue light. In order to remove residual carbon, which led to the grayish tint of the products, the powders were heated under air in a muffle furnace for one day at 800 °C. This purification led to optically more lucid powders with no grayish tint and brighter luminescence.

3.4.2 Powder X-ray Diffraction

Powder X-ray diffraction (PXRD) data of the ground products sealed into glass capillaries (0.2 mm diameter, wall thickness 0.01 mm; Hilgenberg GmbH, Malsfeld, Germany) were collected on a STOE STADI P diffractometer ($\text{Cu-K}\alpha_1$ radiation, $\lambda = 1.5406$ Å, Stoe & Cie, Darmstadt, Germany) equipped with an Ge(111) monochromator and a Mythen1K detector (Dectris, Baden-Dättwil, Switzerland) in parafocusing Debye–Scherrer geometry. Rietveld refinements were performed using the TOPAS Academic V6 package applying the fundamental parameters approach (direct convolution of source emission profiles, axial instrument contributions, crystallite size and microstrain effects).^[45–47] Absorption effects were corrected using the calculated absorption coefficient. A spherical harmonics model of fourth order was applied to describe preferred orientation, while the background was modeled with a shifted Chebychev function. Deposition number CSD-2116432 contains the supplementary crystallographic data for this paper. The data are provided free of charge by the joint Cambridge Crystallographic Data Centre and Fachinformationszentrum Karlsruhe Access Structures service (<http://www.ccdc.cam.ac.uk/structures>).

3.4.3 CHNS Analysis

Elemental CHNS analysis was performed using a Vario Micro Cube device (Elementar, Langensfeld, Germany).

3.4.4 Scanning Electron Microscopy (SEM) and Energy-dispersive X-ray Spectroscopy (EDX)

Investigations concerning the chemical composition and morphology of the samples, a Dualbeam Helios Nanolab G3 UC (FEI, Hillsboro, Oregon, USA) equipped with an X-Max 80 SDD detector (Oxford Instruments, Abingdon, UK) for energy dispersive X-ray (EDX) measurements was used. To prevent electrostatic charging of the samples, a carbon-coating using a high-vacuum sputter coater (CCU-010, Safematic GmbH, Zizers, Switzerland) was applied.

3.4.5 Transmission Electron Microscopy (TEM)

For TEM-EDX, the sample was ground, suspended in ethanol and drop-cast on a copper grid with holey carbon film (S160NH2C, Plano GmbH, Wezlar, Germany), which was then fixed on a double-tilt low-background holder. The measurements were performed with a Titan 80–300 (FEI, USA) with a field emission gun (FEG) operated at 300 kV and equipped with a TOPS 30 EDX spectrometer (EDAX, Germany).

3.4.6 Solid-state NMR spectroscopy

^{13}C and ^{29}Si MAS solid-state NMR spectra were recorded at ambient temperature on a Bruker Avance III-500 spectrometer in an external magnetic field of 11.74 T, with the samples contained in 4 mm ZrO_2 rotors at spinning frequencies of 10 kHz. The signals were referenced indirectly to 0.1% TMS in $CDCl_3$. All spectra were acquired using direct excitation, at the Larmor frequencies $\nu_0(^{13}C) = 125.78$ MHz and $\nu_0(^{29}Si) = 99.38$ MHz.

3.4.7 UV/Vis Spectroscopy

Diffuse reflectance spectra in the range of 240 to 800 nm with 1 nm step size were measured with a Jasco V-650 UV/Vis spectrophotometer equipped with a deuterium and a halogen lamp (Czerny-Turner monochromator with 1200 lines/mm concave grating, photomultiplier tube detector).

3.4.8 Luminescence

Photoluminescence properties of the Eu^{2+} - and Ce^{3+} -doped samples were measured at room temperature on a HORIBA Fluoromax4 spectrofluorimeter system, which is connected to an Olympus BX51 microscope via optical fibers. Excitation spectra were acquired with the monitoring wavelength λ_{mon} ranging from 425 to 516 nm. Internal quantum efficiencies (IQEs)

were determined by comparing the integrated emission intensities and the absorption at the excitation wavelength with reference materials (BaSO_4 , Merck p.a.; commercial $(\text{Sr,Ca})\text{AlSiN}_3:\text{Eu}^{2+}$, Mitsubishi Chemical; and $\text{Y}_3\text{Al}_5\text{O}_{12}:\text{Ce}^{3+}$, Philips). Thermal quenching behavior was investigated using an AvaSpec-2048 spectrometer and a stabilized light-emitting-diode (LED) light source for sample excitation. A fiber-coupled spectroscopy system containing a thermally stabilized LED light source and a fiber-optic spectrometer (HR2000+ES spectrometer, Ocean Optics) with the sample placed in an evacuated cooling chamber, equipped with a liquid-He compressor system (ARS4HW, Advanced Research System Inc., Macungie, Pennsylvania, USA) was used for cryo-spectroscopy between 300 and 6 K measured on a thick-bed powder layer.

3.5 Acknowledgements

The authors gratefully thank Dr. Thomas Bräuniger and Christian Minke (both Department of Chemistry, University of Munich) for NMR measurements and inspiring discussions. We also thank Volker Weiler (Lumileds Phosphor Center, Aachen, Germany) for luminescence measurements.

3.6 References

- [1] H. Huppertz, W. Schnick, *Angew. Chem. Int. Ed. Engl.* **1996**, *35*, 1983–1984; *Angew. Chem.* **1996**, *108*, 2115–2116.
- [2] H. Huppertz, W. Schnick, *Z. Anorg. Allg. Chem.* **1997**, *623*, 212–217.
- [3] H. Huppertz, W. Schnick, *Acta Crystallogr. Sect. C: Struct. Chem.* **1997**, *53*, 1751–1753.
- [4] H. A. Höpfe, G. Kotzyba, R. Pöttgen, W. Schnick, *J. Mater. Chem. C* **2001**, *11*, 3300–3306.
- [5] C. M. Fang, Y. Q. Li, H. T. Hintzen, G. de With, *J. Mater. Chem. C* **2003**, *13*, 1480–1483.
- [6] Y. Q. Li, G. de With, H. T. Hintzen, *J. Alloys Compd.* **2004**, *385*, 1–11.
- [7] Y. Q. Li, C. M. Fang, G. de With, H. T. Hintzen, *J. Solid State Chem.* **2004**, *177*, 4687–4694.
- [8] K. Liddell, D. P. Thompson, T. Bräuniger, R. K. Harris, *J. Eur. Ceram. Soc.* **2005**, *25*, 37–47.
- [9] K. Liddell, D. P. Thompson, S. J. Teat, *J. Eur. Ceram. Soc.* **2005**, *25*, 49–54.
- [10] A. Lieb, J. Kechele, R. Kraut, W. Schnick, *Z. Anorg. Allg. Chem.* **2007**, *633*, 166–171.
- [11] T. Kurushima, G. Gundiah, Y. Shimomura, M. Mikami, N. Kijima, A. Cheetham, *J. Electrochem. Soc.* **2010**, *157*, J64–J68.

- [12] T. Horikawa, M. Fujitani, H. Hanzawa, K.-i. Machida, *ECS J. Solid State Sci. Technol.* **2012**, *1*, R113–R118.
- [13] W. B. Park, K. H. Son, S. P. Singh, K. S. Sohn, *ACS Comb. Sci.* **2012**, *14*, 537–544.
- [14] C. Hecht, F. Stadler, P. J. Schmidt, J. S. auf der Günne, V. Baumann, W. Schnick, *Chem. Mater.* **2009**, *21*, 1595–1601.
- [15] J. Ruan, R.-J. Xie, N. Hirosaki, T. Takeda, *J. Am. Ceram. Soc.* **2010**, *94*, 536–542.
- [16] Z.-J. Zhang, O. ten Kate, A. C. A. Delsing, Z. Man, R.-J. Xie, Y. Shen, M. Stevens, P. Notten, P. Dorenbos, J. Zhao, H. Hintzen, *J. Mater. Chem. C* **2013**, *1*, 7856–7865.
- [17] Z. Xia, A. Meijerink, *Chem. Soc. Rev.* **2017**, *46*, 275–299.
- [18] J. Heber, *Nat. Phys.* **2014**, *10*, 791.
- [19] J. J. Joos, J. Botterman, P. F. Smet, *J. Solid State Light.* **2014**, *1*, 1–16.
- [20] A. Piquette, W. Bergbauer, B. Galler, K. Mishra, *ECS J. Solid State Sci. Technol.* **2016**, *5*, R3146–R3159.
- [21] C. Maak, L. Eisenburger, J. P. Wright, M. Nentwig, P. J. Schmidt, O. Oeckler, W. Schnick, *Inorg. Chem.* **2018**, *57*, 13840–13846.
- [22] Y. Wang, J. Ding, Y. Wang, *J. Mater. Chem. C* **2017**, *5*, 981–994.
- [23] The term *sechser* (*dreier*, *achter*) ring was established by F. Liebau and is derived from the German word “sechser” (“dreier”, “achter”). A *sechser* (*dreier*, *achter*) ring comprises six (three, eight) tetrahedra centers. F. Liebau, *Structural Chemistry of Silicates*, Springer, Berlin, **1985**.
- [24] K. J. D. MacKenzie, M. E. Smith, *Multinuclear Solid-State NMR of Inorganic Materials*, Pergamon, Amsterdam, **2002**.
- [25] R. López, R. Gómez, *J. Sol-Gel Sci. Technol.* **2012**, *61*, 1–7.
- [26] J. Tauc, R. Grigorovici, A. Vancu, *Phys. Status Solidi B* **1966**, *15*, 627–637.
- [27] M. Amachraa, Z. Wang, C. Chen, S. Hariyani, H. Tang, J. Brgoch, S. P. Ong, *Chem. Mater.* **2020**, *32*, 6256–6265.
- [28] T. M. Tolhurst, P. Strobel, P. J. Schmidt, W. Schnick, A. Moewes, *Chem. Mater.* **2017**, *29*, 7976–7983.
- [29] R. D. Shannon, *Acta Crystallogr., Sect. A* **1976**, *32*, 751–767.
- [30] G. Blasse, B. C. Grabmaier, *Luminescent Materials*, Springer, Berlin, Heidelberg, **1994**.
- [31] K. Sakuma, N. Hirosaki, R.-J. Xie, *J. Lumin.* **2007**, *126*, 843–852.
- [32] P. Dorenbos, *J. Phys.: Condens. Matter* **2005**, *17*, 8103–8111.
- [33] G. Blasse, A. Bril, *Philips Tech. Rev.* **1970**, *31*, 304–332.
- [34] X. Q. Piao, K. Machida, T. Horikawa, H. Hanzawa, *Appl. Phys. Lett.* **2006**, *88*, 161908-161901–161908-161903.

-
- [35] X. Q. Piao, K. Machida, T. Horikawa, H. Hanzawa, *Appl. Phys. Lett.* **2007**, *91*, 041908-041901–041908-041903.
- [36] X. Q. Piao, K. Machida, T. Horikawa, H. Hanzawa, Y. Shimomura, N. Kijima, *Chem. Mater.* **2007**, *19*, 4592–4599.
- [37] K. Uheda, N. Hirosaki, Y. Yamamoto, A. Naito, T. Nakajima, H. Yamamoto, *Electrochem. Solid-State Lett.* **2006**, *9*, H22–H25.
- [38] K. Uheda, N. Hirosaki, H. Yamamoto, *Phys. Status Solidi A* **2006**, *203*, 2712–2717.
- [39] W.-Y. Huang, F. Yoshimura, K. Ueda, W. K. Pang, B.-J. Su, L.-Y. Jang, C.-Y. Chiang, W. Zhou, N. H. Duy, R.-S. Liu, *Inorg. Chem.* **2014**, *53*, 12822–12831.
- [40] Y.-T. Tsai, C.-Y. Chiang, W. Zhou, J.-F. Lee, H.-S. Sheu, R.-S. Liu, *J. Am. Chem. Soc.* **2015**, *137*, 8936–8939.
- [41] A. Meijerink, G. Blasse, *J. Lumin.* **1989**, *43*, 283–289.
- [42] G. Blasse, A. Bril, *Appl. Phys. Lett.* **1967**, *11*, 53–55.
- [43] P. Pust, P. J. Schmidt, W. Schnick, *Nat. Mater.* **2015**, *14*, 454–458.
- [44] W. Schnick, H. Huppertz, R. Lauterbach, *J. Mater. Chem.* **1999**, *9*, 289–296.
- [45] J. Bergmann, R. Kleeberg, A. Haase, B. Breidenstein, *Mater. Sci. Forum* **2000**, *347–349*, 303–308.
- [46] R. W. Cheary, A. A. Coelho, J. P. Cline, *J. Res. Natl. Inst. Stand. Technol.* **2004**, *109*, 1–25.
- [47] A. A. Coelho, *TOPAS Version 6: A program for Rietveld refinement*, Coelho Software, Brisbane, Australia, **2016**.

4 Synthesis and Luminescence Properties of Amber Emitting $\text{La}_7\text{Sr}[\text{Si}_{10}\text{N}_{19}\text{O}_3]:\text{Eu}^{2+}$ and Syntheses of the Substitutional Variants $\text{RE}_{8-x}\text{AE}_x[\text{Si}_{10}\text{N}_{20-x}\text{O}_{2+x}]:\text{Eu}^{2+}$ with $\text{RE} = \text{La}, \text{Ce}$; $\text{AE} = \text{Ca}, \text{Sr}, \text{Ba}$; $0 \leq x \leq 2$

Published in: *Chem. Eur. J.* **2022**, *28*, e202200760–e202200767

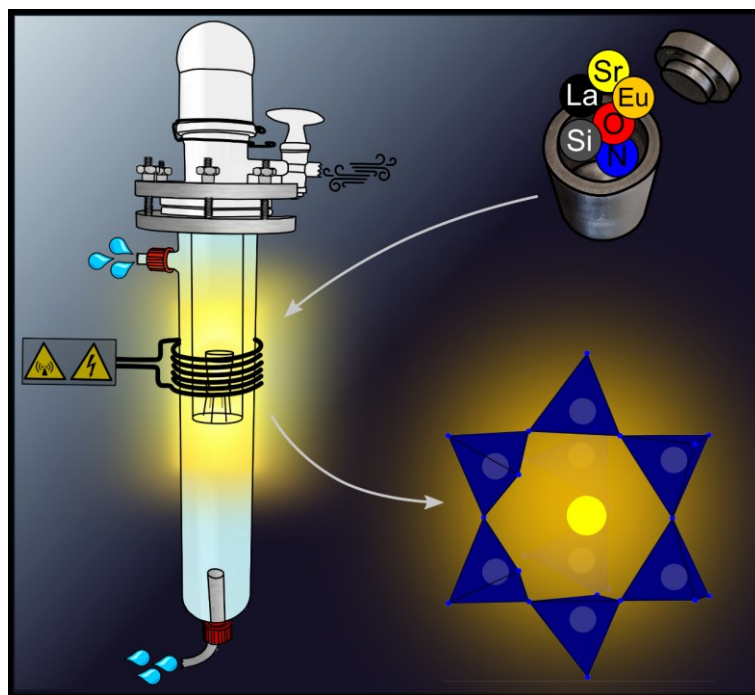
Authors: Lisa Gamperl, Philipp Strobel, Peter J. Schmidt, and Wolfgang Schnick

DOI: 10.1002/chem.202200760

Copyright © 2022 Wiley-VCH Verlag GmbH & Co. KGaA

<https://chemistry->

[europe.onlinelibrary.wiley.com/doi/epdf/10.1002/chem.202200760](https://chemistry-europe.onlinelibrary.wiley.com/doi/epdf/10.1002/chem.202200760)



Abstract. The oxonitridosilicate $\text{La}_7\text{Sr}[\text{Si}_{10}\text{N}_{19}\text{O}_3]:\text{Eu}^{2+}$ and its substitutional variants $\text{RE}_{8-x}\text{AE}_x[\text{Si}_{10}\text{N}_{20-x}\text{O}_{2+x}]:\text{Eu}^{2+}$ with $\text{RE} = \text{La}, \text{Ce}$; $\text{AE} = \text{Ca}, \text{Sr}, \text{Ba}$ and $0 \leq x \leq 2$ were synthesized starting from REN , $\text{SrN}/\text{Ca}_3\text{N}_2/\text{Ba}_2\text{N}$, SiO_2 , amorphous Si_3N_4 and Eu_2O_3 as doping agent at $1600\text{ }^\circ\text{C}$ in a radiofrequency furnace. The crystal structure of $\text{La}_7\text{Sr}[\text{Si}_{10}\text{N}_{19}\text{O}_3]$ was solved and refined based on single-crystal X-ray diffraction data in the orthorhombic space group $Pmn2_1$ (no. 31). The crystal structures of the isotopic compounds $\text{RE}_{8-x}\text{AE}_x[\text{Si}_{10}\text{N}_{20-x}\text{O}_{2+x}]$ were confirmed by Rietveld refinements based on powder X-ray diffraction data using the single-crystal data of $\text{La}_7\text{Sr}[\text{Si}_{10}\text{N}_{19}\text{O}_3]$ as starting point. Crystal structure elucidation reveals a 3D network of vertex sharing $[\text{SiN}_4]$ and $[\text{SiN}_2(\text{N}_{1/2-x/4}\text{O}_{1/2+x/4})_2]$ ($0 \leq x \leq 2$) tetrahedra. When excited with UV to blue light, $\text{La}_7\text{Sr}[\text{Si}_{10}\text{N}_{19}\text{O}_3]:\text{Eu}^{2+}$ shows amber

luminescence with $\lambda_{\text{em}} = 612 \text{ nm}$ and $\text{fwhm} = 84 \text{ nm}/2194 \text{ cm}^{-1}$, which makes it interesting for application in amber phosphor-converted light emitting diodes.

4.1 Introduction

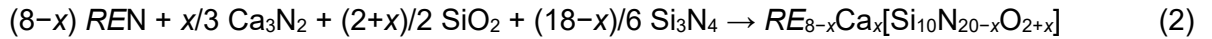
The U.S. Department of Energy, Office of Energy Efficiency and Renewable Energy states in its latest “Energy Savings Forecast of Solid-State Lighting in General Illumination Applications” report that in 2017, 38% of the total energy consumption in the United States (U.S.) was needed for electricity use, of which lighting consumed 6% of total energy and 16% of total electricity used.^[1] Thereby, solid-state lighting based on phosphor converted light emitting diodes (pcLEDs), which had their breakthrough with the invention of efficient blue light-emitting diodes based on $\text{Ga}_{1-x}\text{In}_x\text{N}$ primary LEDs by Akasaki, Amano and Nakamura, lead the revolution of the lighting market.^[1, 2] LEDs exceed traditional lighting technologies like incandescent light bulbs and fluorescent tubes with regard to the combination of energy efficiency, lifetime, versatility, color quality and cost efficiency and can therefore be used in a wide range of lighting applications. Current state-of-the-art white light emitting LEDs are based on a two phosphor approach (2pcLED), for which orange-red and yellow-green emitting phosphors are used to down-convert the blue emission of the primary LED, which then results in warm white light by additive color mixing.^[3, 4] $(\text{Ca},\text{Sr})\text{Si}_2\text{O}_2\text{N}_2:\text{Eu}^{2+}$ can be used as the yellow-green emitting component, while $(\text{Sr},\text{Ba})_2\text{Si}_5\text{N}_8:\text{Eu}^{2+}$ or $(\text{Sr},\text{Ca})\text{AlSiN}_3:\text{Eu}^{2+}$ serve as orange-red emitting phosphors.^[4-9] Despite the favorable properties of $(\text{Sr},\text{Ba})_2\text{Si}_5\text{N}_8:\text{Eu}^{2+}$ or $(\text{Sr},\text{Ca})\text{AlSiN}_3:\text{Eu}^{2+}$, like tunability, good thermal behavior, high efficacy and high color rendition, they suffer from energy loss by emission in the infrared spectral range (IR spillover) due to their rather broad emission bands ($2050\text{--}2600 \text{ cm}^{-1}$).^[3, 10] Therefore, research is focused on exploring new highly efficient narrow-band orange-red phosphors. Promising candidates have been found with $\text{Sr}[\text{LiAl}_3\text{N}_4]:\text{Eu}^{2+}$ (SLA, $\lambda_{\text{em}} = 650 \text{ nm}$, full width at half-maximum (fwhm) = 1180 cm^{-1}), $\text{Sr}[\text{Li}_2\text{Al}_2\text{O}_2\text{N}_2]:\text{Eu}^{2+}$ (SALON, $\lambda_{\text{em}} = 614 \text{ nm}$, 1286 cm^{-1}) and $\text{Sr}[\text{Mg}_3\text{SiN}_4]:\text{Eu}^{2+}$ (SMS) with SMS being the so far most narrow orange-red emitting Eu^{2+} -doped nitride phosphor ($\lambda_{\text{em}} = 615 \text{ nm}$, $\text{fwhm} = 1170 \text{ cm}^{-1}$).^[11-13] (Oxo)nitridosilicates are a promising compound class in the research for novel host lattices used as phosphor materials. They offer a huge structural variability as nitrogen can crosslink up to four tetrahedra centers and $[\text{SiN}_4]$ tetrahedra can be linked by sharing edges or corners. This versatility leads to high potential for applications not only in the lighting sector.^[14, 15] Therefore, scientific research is still focused on discovering new auspicious (oxo)nitridosilicate phosphors to further broaden the application of pcLEDs. To the best of our knowledge, only two phosphors are known so far in the La-Sr-Si-O-N system, namely $\text{La}_{26-x}\text{Sr}_x\text{Si}_{41}\text{O}_{x+1}\text{N}_{80-x}:\text{Eu}^{2+}$ ($x = 12.72\text{--}12.90$), which emits in the red spectral region ($\lambda_{\text{em}} = 643 \text{ nm}$, $\text{fwhm} = 142 \text{ nm}$), and narrow-band red emitting $\text{La}_{4-x}\text{Sr}_{2+x}\text{Si}_5\text{N}_{12-x}\text{O}_x:\text{Pr}^{3+}$

($x \approx 1.69$) with $\lambda_{em} = 625$ nm and $fwhm = 40$ nm.^[16, 17] Thus, the barely investigated La-Sr-Si-N-O system is promising for containing more host compounds that result in red emitting phosphors with potential for usage in lighting applications. In this contribution, we report on the synthesis and characterization of the oxonitridosilicate $La_7Sr[Si_{10}N_{19}O_3]$ and its substitutional variants $RE_{8-x}AE_x[Si_{10}N_{20-x}O_{2+x}]$ with $RE = La, Ce$; $AE = Ca, Sr, Ba$ and $0 \leq x \leq 2$. Amber emitting $La_7Sr[Si_{10}N_{19}O_3]:Eu^{2+}$ exhibits an emission maximum at $\lambda_{em} = 612$ nm with a full width at half-maximum of 84 nm/ 2194 cm^{-1} upon excitation with UV to blue light. The observed luminescence properties will be discussed in detail.

4.2 Results and Discussion

4.2.1 Synthesis and Chemical Analysis

$La_7Sr[Si_{10}N_{19}O_3]:Eu^{2+}$ and the solid solution series of its substitutional variants $RE_{8-x}AE_x[Si_{10}N_{20-x}O_{2+x}]:Eu^{2+}$ with $RE = La, Ce$; $AE = Ca, Sr, Ba$ and $0 \leq x \leq 2$ were obtained as described in the Experimental Section according to the following reaction equations using Eu_2O_3 as a dopant:



However, for the syntheses with $AE = Sr$, a sevenfold excess of SrN, which can be described more precisely as $(Sr^{2+})_4[N^{3-}]_2[N_2^{2-}]$, was necessary due to decomposition of SrN at high temperatures and deposition on the cold reactor wall.^[18] The synthesis of $La_7Sr[Si_{10}N_{19}O_3]:Eu^{2+}$ yielded single crystals (Figure C1) used for X-ray diffraction measurements to obtain the crystal structure. The single-crystal data were used for a Rietveld refinement based on powder X-ray diffraction data for determination of the bulk phase composition, which revealed a phase pure synthesis (Figure 4.1, Table C1).

4 Synthesis and Luminescence Properties of Amber Emitting $\text{La}_7\text{Sr}[\text{Si}_{10}\text{N}_{19}\text{O}_3]:\text{Eu}^{2+}$ and Syntheses of the Substitutional Variants $\text{RE}_{8-x}\text{AE}_x[\text{Si}_{10}\text{N}_{20-x}\text{O}_{2+x}]:\text{Eu}^{2+}$ with $\text{RE} = \text{La}, \text{Ce}$; $\text{AE} = \text{Ca}, \text{Sr}, \text{Ba}$; $0 \leq x \leq 2$

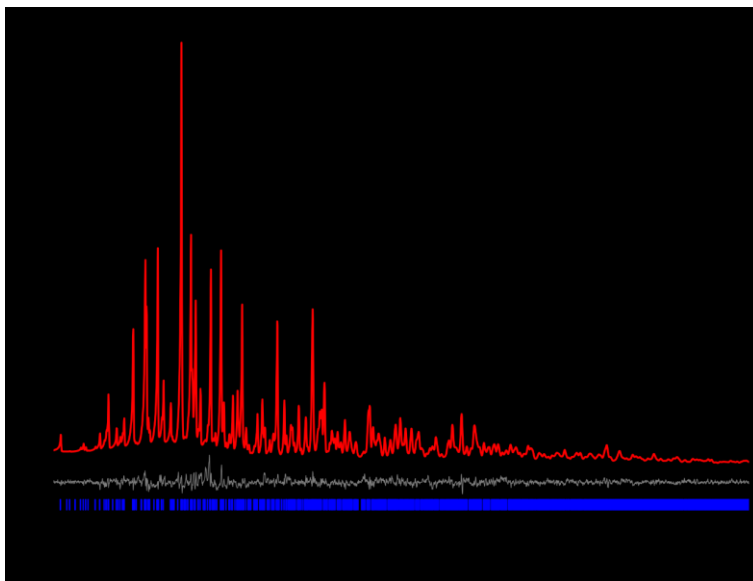


Figure 4.1. Rietveld refinement based on PXRD data collected from a powder sample containing $\text{La}_7\text{Sr}[\text{Si}_{10}\text{N}_{19}\text{O}_3]:\text{Eu}^{2+}$ based on the structure model obtained by SCXRD data with observed (black) and calculated (red) powder X-ray diffraction patterns and the corresponding difference profile (gray). Vertical blue bars indicate the position of the Bragg reflections of the title compound.

The crystal structure of $\text{La}_7\text{Sr}[\text{Si}_{10}\text{N}_{19}\text{O}_3]:\text{Eu}^{2+}$ exhibits mixed occupied heavy cation sites. Therefore, the terminal representatives of the solid solution series $\text{La}_{8-x}\text{Sr}_x[\text{Si}_{10}\text{N}_{20-x}\text{O}_{2+x}]:\text{Eu}^{2+}$ with $x = 0$ and 2 , namely $\text{La}_8[\text{Si}_{10}\text{N}_{20}\text{O}_2]:\text{Eu}^{2+}$ and $\text{La}_6\text{Sr}_2[\text{Si}_{10}\text{N}_{18}\text{O}_4]:\text{Eu}^{2+}$, were synthesized as well and the phase compositions of the obtained powders were determined by Rietveld refinements based on powder X-ray diffraction data using the single-crystal data of $\text{La}_7\text{Sr}[\text{Si}_{10}\text{N}_{19}\text{O}_3]$ as a starting point (Figure C2, Table C2a and C2b). Furthermore, due to similar sizes and charges of both the alkaline earth ions Sr^{2+} ($r(\text{CN}: 9) = 1.31 \text{ \AA}$), Ca^{2+} ($r(\text{CN}: 8/9) = 1.12/1.18 \text{ \AA}$) and Ba^{2+} ($r(\text{CN}: 9) = 1.47 \text{ \AA}$) as well as the rare earth ions La^{3+} ($r(\text{CN}: 8/9) = 1.16/1.22 \text{ \AA}$) and Ce^{3+} ($r(\text{CN}: 8/9) = 1.14/1.20 \text{ \AA}$),^[19] the solid solution series $\text{RE}_{8-x}\text{AE}_x[\text{Si}_{10}\text{N}_{20-x}\text{O}_{2+x}]:\text{Eu}^{2+}$ with $\text{RE} = \text{La}, \text{Ce}$; $\text{AE} = \text{Ca}, \text{Sr}, \text{Ba}$ and $0 \leq x \leq 2$ were also synthesized and Rietveld refined based on the powder X-ray diffraction data using the obtained structure model of $\text{La}_7\text{Sr}[\text{Si}_{10}\text{N}_{19}\text{O}_3]$ as a starting point, whereby only lattice parameters and fractional coordinates of the heavy cation sites were refined. Due to similar ionic radii of Ca^{2+} and La^{3+} , it is possible that Ca occupies those sites, which in the Sr containing compound are solely occupied by La. However, it is not possible to determine which sites exactly are occupied by Ca and to which extent by the Rietveld method. Therefore, the Rietveld refinements of the Ca containing compounds were based on the obtained structure model of $\text{La}_7\text{Sr}[\text{Si}_{10}\text{N}_{19}\text{O}_3]$ without further changes. All Rietveld refinements and corresponding data are shown in Figures C2, C3 and Tables C2–C4, respectively.^[19] For SEM-EDX measurements (Table C5), only the cation

values and the atomic ratios ($RE + AE$)/Si were considered since the anion values were more affected by shadowing caused by unfavorable orientation of the crystals with respect to the EDX detector and by superficially bound oxygen on the samples. Both the measured values for the individual atoms and the calculated atomic ratios agree well within the typical limits of accuracy with the theoretical values. Although Eu could not be detected by EDX because of its small amount, its occurrence is proven by the observed luminescence. Therefore, Eu was subsequently neglected in structure refinements.

4.2.2 Crystal Structure Elucidation

The crystal structure of $\text{La}_7\text{Sr}[\text{Si}_{10}\text{N}_{19}\text{O}_3]$ was solved and refined based on single-crystal X-ray diffraction data in the orthorhombic space group $Pmn2_1$ (no. 31). Crystallographic data is given in Table 4.1, while Wyckoff positions, atomic coordinates, and isotropic displacement parameters as well as anisotropic displacement parameters are listed in Table C6 and C7, respectively.

Table 4.1. Crystallographic data of the single-crystal structure determination of $\text{La}_7\text{Sr}[\text{Si}_{10}\text{N}_{19}\text{O}_3]$

Formula		$\text{La}_7\text{Sr}[\text{Si}_{10}\text{N}_{19}\text{O}_3]$
formula weight / $\text{g}\cdot\text{mol}^{-1}$		1655.08
crystal system		orthorhombic
space group		$Pmn2_1$ (no. 31)
lattice parameters / Å	$a =$	9.5027(11)
	$b =$	19.0471(19)
	$c =$	12.0753(14)
$V / \text{Å}^3$		2185.62(4)
Z		4
X-ray density / $\text{g}\cdot\text{cm}^{-3}$		5.02954
abs. coefficient / $\mu\cdot\text{mm}^{-1}$		16.393
absorption correction		multiscan ^[20]
diffractometer		Bruker D8 Venture
radiation		Mo- $K\alpha_1$ ($\lambda = 0.70930 \text{ Å}$)
$F(000)$		2936
θ range / °		$2.138 \leq \theta \leq 24.996$
independent reflections (all / with $I > 2\sigma(I)$)		4104 / 3910
refined parameters / restraints		220 / 6
R_{int}		0.0481
R_{σ}		0.0529
$R1$ (all data / for $I > 2\sigma(I)$)		0.0318 / 0.0294
$wR2$ (all data / for $I > 2\sigma(I)$)		0.0746 / 0.0735
$\Delta\rho_{\text{max}} / \Delta\rho_{\text{min}} / \text{e Å}^{-3}$		2.44 / -2.39
$\text{GooF} (\chi^2)$		1.115

4 Synthesis and Luminescence Properties of Amber Emitting $\text{La}_7\text{Sr}[\text{Si}_{10}\text{N}_{19}\text{O}_3]:\text{Eu}^{2+}$ and Syntheses of the Substitutional Variants $\text{RE}_{8-x}\text{AE}_x[\text{Si}_{10}\text{N}_{20-x}\text{O}_{2+x}]:\text{Eu}^{2+}$ with $\text{RE} = \text{La}, \text{Ce}; \text{AE} = \text{Ca}, \text{Sr}, \text{Ba}; 0 \leq x \leq 2$

The structure exhibits twelve cation sites, of which eight are fully occupied with La, while four sites show a mixed occupation of La and Sr, resulting in the reported atomic ratio La:Sr of 7:1. Fully occupied sites show similar coordination spheres, distances, and polyhedron volumes among themselves, the same applies to the mixed occupied sites (Table C8). The results were supported by charge distribution (CHARDI) and bond-valence sum (BVS) calculations (Table C9).^[21-25] During the refinement, an elongated anisotropic displacement parameter for Sr/La12 was observed. Therefore, a difference Fourier synthesis ($F_{\text{obs}} - F_{\text{calc}}$) of the electron density located at this site was calculated, however, there was no indication for splitting of the electron density at high isosurface levels (Figure C4). The elongated anisotropic displacement parameter may be explained by mixed occupation and a slightly enlarged Sr/La12–N distance (Table C8). For charge compensation, incorporation of oxygen was assumed. Eight terminal anionic sites with shorter Si–X^[1] (X = N, O) distances are suitable for an occupation with oxygen while all other twofold bridging sites were fully occupied with nitrogen, which is in agreement with Pauling’s second rule.^[26] The differentiation between O and N was not only based on connectivity and distances, but also on the HSAB principle, according to which the harder Lewis acid La^{3+} is expected to be coordinated by the harder Lewis base O^{2-} .^[27-29] To obtain a charge neutral composition, the eight terminal anionic sites were equally mixed occupied and constrained to 0.75 O and 0.25 N on each site, respectively. Chemically identical Si, N and N/O positions, respectively, were refined with constrained anisotropic displacement parameters.

As mixed cation and anion sites are present and LaN vs. SrO can be exchanged for each other without violating charge neutrality, solid solutions $\text{La}_{8-x}\text{Sr}_x[\text{Si}_{10}\text{N}_{20-x}\text{O}_{2+x}]$ with $0 \leq x \leq 2$ resulting in $\text{La}_8[\text{Si}_{10}\text{N}_{20}\text{O}_2]$ with fully La occupied cation sites and each terminal anionic site occupied with 0.5 O and 0.5 N, respectively, and $\text{La}_6\text{Sr}_2[\text{Si}_{10}\text{N}_{18}\text{O}_4]$ with the previously mixed occupied sites now fully occupied by Sr and O, respectively, were obtained. Due to similar ionic radii, solid solution series of the substitutional variants with La exchanged by Ce and Sr exchanged by Ca and Ba were synthesized, resulting in an overall sum formula $\text{RE}_{8-x}\text{AE}_x[\text{Si}_{10}\text{N}_{20-x}\text{O}_{2+x}]$ ($\text{RE} = \text{La}, \text{Ce}; \text{AE} = \text{Ca}, \text{Sr}, \text{Ba}; 0 \leq x \leq 2$).

4.2.3 Structure Description

$\text{La}_7\text{Sr}[\text{Si}_{10}\text{N}_{19}\text{O}_3]$ exhibits a three-dimensional network (Figure 4.2) of vertex sharing Q^4 -type $\text{SiN}^{[2]_4}$ and Q^2 -type $\text{SiN}^{[2]_2}(\text{N}_{0.25}\text{O}_{0.75})^{[1]_2}$ tetrahedra.^[30, 31]

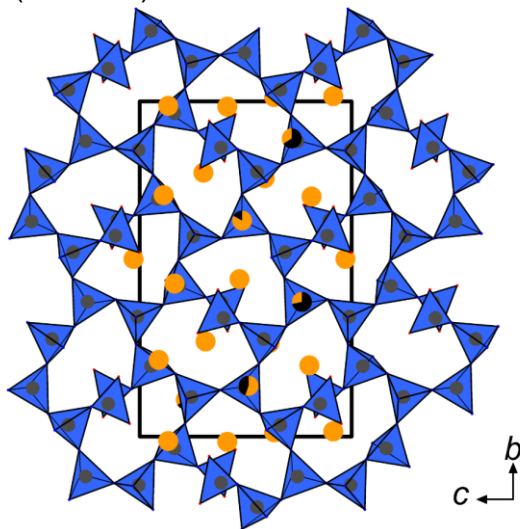


Figure 4.2. Crystal structure of $\text{La}_7\text{Sr}[\text{Si}_{10}\text{N}_{19}\text{O}_3]$. $[\text{Si}(\text{N},\text{O})_4]$ tetrahedra in blue, Si atoms dark gray, La atoms orange, Sr atoms black. Mixed occupied cation sites colored in the respective atom colors with the section size corresponding to the percentage occupancy.

The structure can be divided into two quasi-identical, but slightly tilted ribbons along $[001]$ consisting of $[\text{SiN}_4]$ tetrahedra, one ribbon colored in blue shades, the other one in green shades, respectively (Figure 4.3, C5).

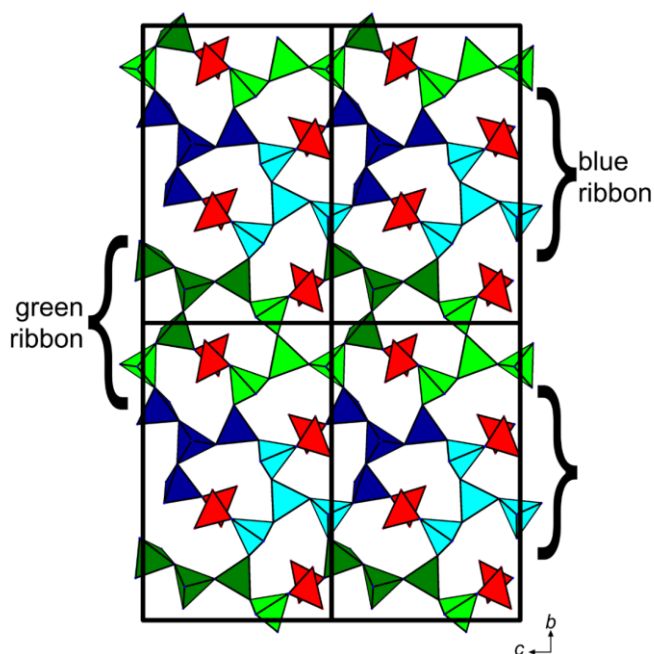


Figure 4.3. $2 \times 2 \times 2$ super cell viewed along $[100]$ of $\text{La}_7\text{Sr}[\text{Si}_{10}\text{N}_{19}\text{O}_3]$ illustrating the substructure consisting of two different ribbons. $[\text{SiN}_4]$ tetrahedra in blue and green shades, $[\text{SiN}_2(\text{N}_{0.25}\text{O}_{0.75})_2]$ in red.

The ribbons can be subdivided into two units depicted in dark and light shades, where both the dark blue and green units and the light blue and green units, respectively, are quasi-identical among each other but slightly tilted (Figure 4.4).

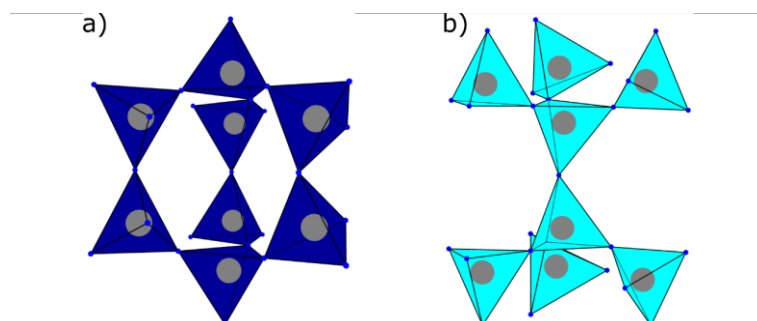


Figure 4.4. Eight $[\text{SiN}_4]$ tetrahedra forming (a) a cage or (b) an inverted structure. Si atoms dark gray, N atoms blue.

The darker units form a cage consisting of three *sechser* rings, while the lighter units can be described as an inverted structure formally formed by a mirror plane at $a/2$ crossing at half of the cage (Figure C5).^[32] The units are interconnected via common vertices, whereby a cage is surrounded by four inverted structures and vice versa leading to additional cages. Q^2 -type $\text{SiN}^{[2]}_2(\text{N}_{0.25}\text{O}_{0.75})^{[1]}_2$ tetrahedra are only interconnected within one unit or equal units along $[100]$ forming *dreier* rings in the (100) plane (Figure C5). Accordingly, the seeming *achter* ring channels as viewed along $[100]$ are not closed *achter* rings but intersecting counterclockwise and clockwise distorted screws along $[100]$ with internal offsets of 5.59(2) and 5.62(2) Å, respectively (Figure C6). La and Sr occupy twelve cation sites, of which eight are solely occupied by La (Figure C7). These sites are coordinated by six N and two N/O in form of partly more or less distorted hexagonal bipyramids, respectively. Four sites are mixed occupied by La and Sr and coordinated solely by nine N in form of distorted triple capped trigonal prisms. These sites are located inside the cavities formed by the cages. Interatomic La–N/O distances are in the range of 2.41(2)–3.30(2) Å, while Sr/La–N distances vary from 2.62(2) to 3.37(2) Å and Si–N/O distances are between 1.65(1) to 1.77(1) Å and Si–N between 1.64(2) to 1.70(2) Å, which are in good agreement with reported values of other RE-AE-Si-N-O compounds.^[33-41] For the substitutional variants $\text{RE}_{8-x}\text{AE}_x[\text{Si}_{10}\text{N}_{20-x}\text{O}_{2+x}]:\text{Eu}^{2+}$ ($\text{RE} = \text{La}, \text{Ce}; \text{AE} = \text{Ca}, \text{Sr}, \text{Ba}; 0 \leq x \leq 2$), the mixed occupied sites La/Sr9–12 can be substituted by Ce and Ca or Ba, respectively, whereas Ca^{2+} could also occupy solely La^{3+} occupied sites due to similar ionic radii. For charge compensation, this requires the simultaneous incorporation of oxygen on the mixed occupied anionic sites, leading to $\text{SiN}_2(\text{N}_{1/2-x/4}\text{O}_{1/2+x/4})_2$ ($0 \leq x \leq 2$) tetrahedra.

4.2.4 UV/Vis Reflectance Spectroscopy

For the determination of the optical band gap of nondoped $\text{La}_7\text{Sr}[\text{Si}_{10}\text{N}_{19}\text{O}_3]$, UV/Vis spectroscopy was used. The measured diffuse reflectance spectrum was transformed into a pseudo-absorption spectrum applying the Kubelka–Munk function $F(R) = (1-R)^2/2R$ (R : measured reflectance).^[42] The optical band gap was determined from a Tauc plot, whereby $h\nu$ is plotted against $(F(R) \cdot h\nu)^{1/n}$ with $n = 1/2$ for a direct allowed transition by intersecting the aligned tangent on the linear region with the abscissa.^[43] Thereby, the optical band gap was estimated to be approx. 3.55 eV (Figure 4.5), although host materials with larger band gaps ≥ 4 eV are desired for pcLED applications.^[13, 17, 44-48]

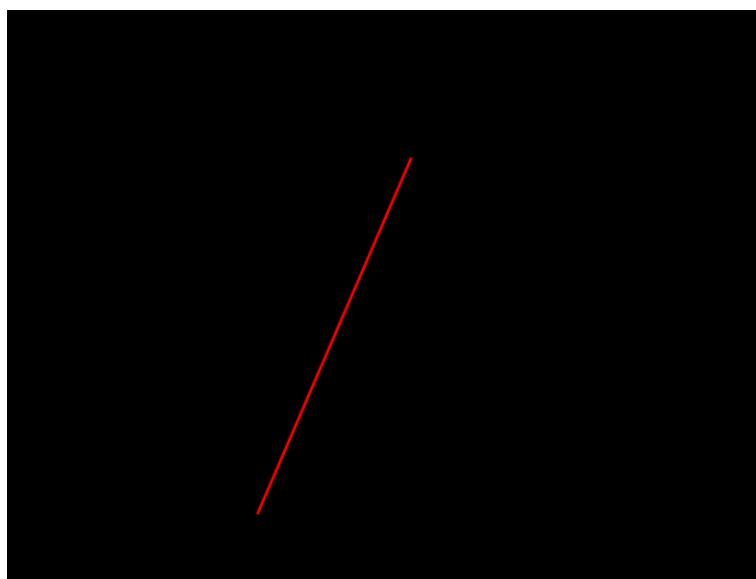


Figure 4.5. Tauc plot ($n = 1/2$) for a nondoped $\text{La}_7\text{Sr}[\text{Si}_{10}\text{N}_{19}\text{O}_3]$ powder sample. The artifact around 3.65 eV (340 nm) corresponds to the lamp switch.

4.2.5 Luminescence

Luminescence properties were measured on single luminescent particles of Eu^{2+} -doped $\text{La}_7\text{Sr}[\text{Si}_{10}\text{N}_{19}\text{O}_3]$. Upon excitation of the samples with UV to blue light, $\text{La}_7\text{Sr}[\text{Si}_{10}\text{N}_{19}\text{O}_3]:\text{Eu}^{2+}$ (0.2 mol%) shows orange luminescence and exhibits an emission maximum at $\lambda_{\text{em}} = 612$ nm with $\text{fwhm} = 84$ nm/ 2194 cm^{-1} (Figure 4.6). Due to the excitation maximum at $\lambda_{\text{exc}} \approx 445$ nm, $\text{La}_7\text{Sr}[\text{Si}_{10}\text{N}_{19}\text{O}_3]:\text{Eu}^{2+}$ (0.2 mol%) can efficiently be excited by an $\text{Ga}_{1-x}\text{In}_x\text{N}$ LED light source.

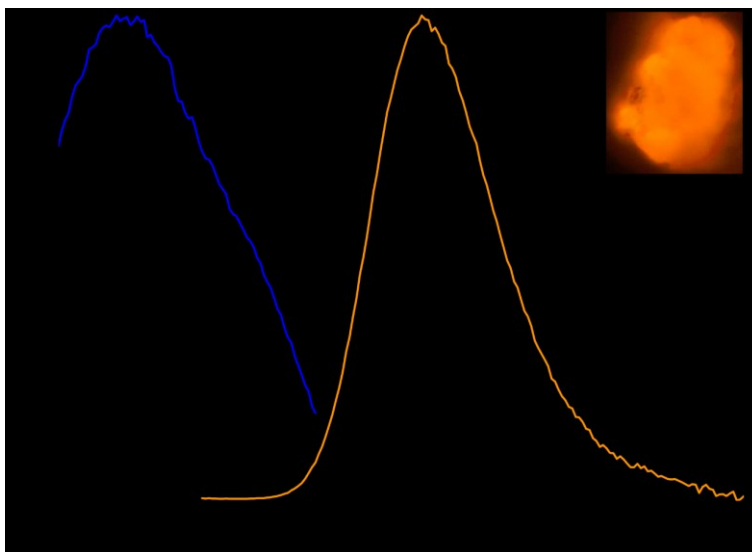


Figure 4.6. Normalized excitation (blue, $\lambda_{\text{mon}} = 608 \text{ nm}$) and emission spectra (orange, $\lambda_{\text{exc}} = 450 \text{ nm}$) of $\text{La}_7\text{Sr}[\text{Si}_{10}\text{N}_{19}\text{O}_3]:\text{Eu}^{2+}$ (0.2 mol%) with a micrograph of the measured particle.

The rather broad emission band can be assigned to the parity-allowed $4f^65d^1 (^7F_0) \rightarrow 4f^7(^8S_{7/2})$ transition of Eu^{2+} .^[49] The emission properties of $\text{La}_7\text{Sr}[\text{Si}_{10}\text{N}_{19}\text{O}_3]:\text{Eu}^{2+}$ (0.2 mol%) can be compared to other amber emitting phosphors that already found applications like $(\text{Ba},\text{Sr})_2\text{Si}_5\text{N}_8:\text{Eu}^{2+}$ ($\lambda_{\text{em}} \approx 590\text{--}625 \text{ nm}$, $\text{fwhm} \approx 2050\text{--}2600 \text{ cm}^{-1}$) and $(\text{Sr},\text{Ca})\text{AlSiN}_3:\text{Eu}^{2+}$ ($\lambda_{\text{em}} \approx 610\text{--}660 \text{ nm}$, $\text{fwhm} \approx 2100\text{--}2500 \text{ cm}^{-1}$) or other oxonitridosilicates like $\text{Y}_4\text{Ba}_2[\text{Si}_9\text{ON}_{16}]\text{O}:\text{Eu}^{2+}$ ($\lambda_{\text{em}} = 622 \text{ nm}$, $\text{fwhm} = 111 \text{ nm}/2875 \text{ cm}^{-1}$).^[4-9, 47] Phosphors of other compound classes like $\text{Sr}[\text{Mg}_3\text{SiN}_4]$ ($\lambda_{\text{em}} = 615 \text{ nm}$, $\text{fwhm} = 43 \text{ nm}/1170 \text{ cm}^{-1}$), $\text{Sr}[\text{Li}_2\text{Al}_2\text{O}_2\text{N}_2]$ ($\lambda_{\text{em}} = 614 \text{ nm}$, $\text{fwhm} = 48 \text{ nm}/1286 \text{ cm}^{-1}$) or $\text{Sr}[\text{Mg}_2\text{Al}_2\text{N}_4]$ ($\lambda_{\text{em}} = 612 \text{ nm}$, $\text{fwhm} = 1823 \text{ cm}^{-1}$) show similar emission maxima but more narrow emission bands due to higher symmetric crystal structures and fewer but higher symmetric activator sites.^[12, 13, 50]

Samples of $\text{La}_7\text{Sr}[\text{Si}_{10}\text{N}_{19}\text{O}_3]:\text{Eu}^{2+}$ exhibit little intense luminescence presumably due to the small band gap that may give rise to thermal de-excitation via the conduction band. Merely, a low doping concentration of 0.2 mol% lead to measurable luminescence making quantum efficiency determinations of doping series unreliable ($\text{IQE} \ll 10\%$), although room temperature luminescence was visible for samples with different doping levels and variation of RE and AE . Solely, a bulk sample of $\text{Ce}_6\text{Ca}_2[\text{Si}_{10}\text{N}_{18}\text{O}_4]:\text{Eu}^{2+}$ was measurable, resulting in $\lambda_{\text{em}} = 627 \text{ nm}$ with $\text{fwhm} = 139 \text{ nm}/3516 \text{ cm}^{-1}$ (Figure C10), whereby the red shift of the luminescence maximum compared to $\text{La}_7\text{Sr}[\text{Si}_{10}\text{N}_{19}\text{O}_3]:\text{Eu}^{2+}$ is in agreement with the decreasing cation sizes causing an increased Stokes shift. Due to the weak luminescence at room temperature, cryo-spectroscopy measurements were recorded to determine whether the luminescence intensity increases at lower temperatures (Figure 4.7).

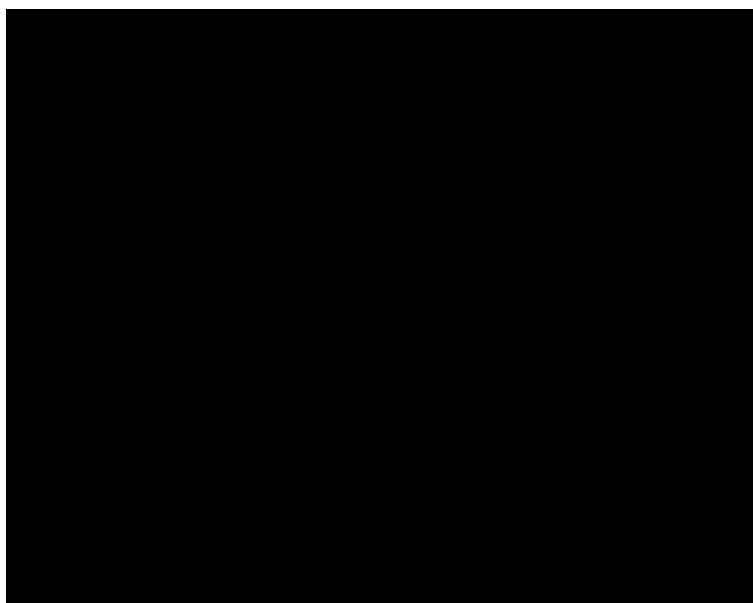


Figure 4.7. Temperature dependent relative integrated emission intensities of $\text{La}_7\text{Sr}[\text{Si}_{10}\text{N}_{19}\text{O}_3]:\text{Eu}^{2+}$ (0.2 mol%).

As it can be derived from Figure 4.7, the luminescence intensity at 6 K was merely higher by a factor of about 2. There are two predominant theories to describe the thermal quenching behavior of activator ions in phosphors: the crossover mechanism according to *Blasse et al.* and the thermal ionization mechanism after *Dorenbos* (Figure C8). The crossover mechanism results from nonradiative relaxation of the excited activator $5d^1$ electron to the ground state when the temperature is sufficiently high to exceed an activation energy. This activation energy is defined as the energy difference between the vibrationally relaxed but electronically excited state and the intersection of the parabola axes of the ground and excited states, which can be illustrated in a configurational coordinate diagram (Figure C8). Therefore, research is focused on structurally rigid host materials because rigid structures allow only few vibrational modes, reducing the probability of nonradiative relaxation. Rigidity can be indicated by the degree of condensation κ , defined as the ratio of tetrahedra centers to its coordinating anions, and the number of multi-bridging atoms like $\text{N}^{[3]}$ or $\text{N}^{[4]}$. However, stability against local shifts within an activator vicinity are more reliable compared to a general descriptor such as structural rigidity.^[44, 49, 51] Thermal quenching induced by the thermal ionization mechanism can be described by thermally overcoming the activation energy for elevation of the excited activator $5d^1$ electron to the conduction band minimum of the host. Resonant inelastic X-ray scattering (RIXS) measurements have been used to determine the influence of the host lattice on the highly sensitive position of the $5d$ levels of the activator ion and therefore, the $5d$ to conduction band separation. The position of the $5d$ levels is influenced by effects caused by the ligand field surrounding the activator ions namely, among

4 Synthesis and Luminescence Properties of Amber Emitting $\text{La}_7\text{Sr}[\text{Si}_{10}\text{N}_{19}\text{O}_3]:\text{Eu}^{2+}$ and Syntheses of the Substitutional Variants $\text{RE}_{8-x}\text{AE}_x[\text{Si}_{10}\text{N}_{20-x}\text{O}_{2+x}]:\text{Eu}^{2+}$ with $\text{RE} = \text{La}, \text{Ce}; \text{AE} = \text{Ca}, \text{Sr}, \text{Ba}; 0 \leq x \leq 2$

other things, by the nephelauxetic effect, centroid shift, and crystal field splitting, which depend on the host material. The valence band maximum is mainly dominated by N and O p -states while the conduction band minimum is formed by network forming elements like Si or by elements filling up the network structures such as RE or AE . Going from Ca to Ba d -states, the band gap decreases due to the lower energy of Ba d -states.^[17, 44, 45, 52, 53] The determination of the $5d$ to conduction band separation by RIXS can be a very useful tool for the distinction whether thermal quenching is an intrinsic material property when the separation is determined to be small or if thermal quenching is extrinsically influenced and can be reduced by optimizing the synthesis.^[44, 45, 52] The influence of thermal ionization and crossover mechanisms compete and depend on the size of the band gap of the host material, whereas the influence of the crossover mechanism increases for larger band gaps ($E_g > 4$ eV). With smaller band gaps, it is possible that both mechanisms occur simultaneously.^[44]

An important factor to consider in this context is the Stokes shift, which correlates with the energetic position of the excitation and emission bands as well as with the width of those bands and negatively influences thermal quenching behavior and thus the luminescence efficiency. According to Equation (4),^[51]

$$E_{\text{Stokes}} = 2S \times \hbar\omega \quad (4)$$

the Stokes shift depends on the phonon frequencies ω of local lattice vibrations and is related to the atomic weight of the host material atoms, with smaller ω for larger molar masses. The Huang-Rhys parameter S is a scale for the magnitude of the electron-phonon coupling and therefore depends on the rigidity of the host lattice, with low rigidity corresponding to large values of S .^[51, 54-57] In the case of $\text{La}_7\text{Sr}[\text{Si}_{10}\text{N}_{19}\text{O}_3]$, the degree of condensation equals $\kappa = n(\text{Si})/n(\text{N},\text{O}) = 10/22 \approx 0.45$ and consists besides terminal mixed occupied (N,O)^[1] sites solely of twofold bridging N^[2] sites. Therefore, $\text{La}_7\text{Sr}[\text{Si}_{10}\text{N}_{19}\text{O}_3]$ cannot be denominated as a highly condensed network and may suffer from reduced structural rigidity. This leads to larger values for both S and E_{Stokes} , so the parabola offset (Figure C9) increases and the crossover of the two parabola axes occur at lower E . Consequently, the activation energy for the crossover mechanism decreases, leading to a higher probability for thermal quenching. Since cryo-spectroscopy measurements did not result in stronger luminescence, thermal ionization may not be the determining factor for the observed thermal quenching despite the comparably small band gap. The rather large Stokes shift due to low structural rigidity leads to an increased probability for thermal quenching according to the crossover mechanism as the determining factor in $\text{La}_7\text{Sr}[\text{Si}_{10}\text{N}_{19}\text{O}_3]$.

4.3 Conclusion

In this contribution, we report on the syntheses of $\text{La}_7\text{Sr}[\text{Si}_{10}\text{N}_{19}\text{O}_3]:\text{Eu}^{2+}$ and the solid-solution series of its substitutional variants $\text{RE}_{8-x}\text{AE}_x[\text{Si}_{10}\text{N}_{20-x}\text{O}_{2+x}]$ with $\text{RE} = \text{La}, \text{Ce}$; $\text{AE} = \text{Ca}, \text{Sr}, \text{Ba}$ and $0 \leq x \leq 2$. $\text{La}_7\text{Sr}[\text{Si}_{10}\text{N}_{19}\text{O}_3]:\text{Eu}^{2+}$ is only the second known Eu^{2+} -doped phosphor in the La-Sr-Si-O-N system so far. The crystal structure of $\text{La}_7\text{Sr}[\text{Si}_{10}\text{N}_{19}\text{O}_3]$ was solved and refined in the orthorhombic space group $Pmn2_1$ (no. 31) based on single-crystal X-ray diffraction data. It exhibits a new three-dimensional network of vertex sharing $\text{SiN}^{[2]_4}$ and $\text{SiN}^{[2]_2}(\text{N}_{0.25}\text{O}_{0.75})^{[1]_2}$ tetrahedra leading to a cage like structure filled by sites occupied solely by lanthanum or mixed occupied by lanthanum and strontium. Due to the mixed cation and anion sites and the charge neutral exchangeability of LaN vs. SrO , the solid solution series $\text{La}_{8-x}\text{Sr}_x[\text{Si}_{10}\text{N}_{20-x}\text{O}_{2+x}]$ with $0 \leq x \leq 2$ was synthesized. In addition to that, similar ionic radii of La and Ce as well as Sr, Ca and Ba led to the syntheses of the solid solution series of the substitutional variants $\text{RE}_{8-x}\text{AE}_x[\text{Si}_{10}\text{N}_{20-x}\text{O}_{2+x}]$ ($\text{RE} = \text{La}, \text{Ce}$; $\text{AE} = \text{Ca}, \text{Sr}, \text{Ba}$; $0 \leq x \leq 2$). This was confirmed by Rietveld refinements based on powder X-ray diffraction data using the obtained structure model of $\text{La}_7\text{Sr}[\text{Si}_{10}\text{N}_{19}\text{O}_3]$ as a starting point and by EDX measurements. The compound class $\text{RE}_{8-x}\text{AE}_x[\text{Si}_{10}\text{N}_{20-x}\text{O}_{2+x}]$ offers a broad variety of full or partial substitution possibilities and therefore, could be an interesting host material class for tunability upon Eu^{2+} doping. Solid-state UV/Vis spectroscopy was used to determine the optical band gap of nondoped $\text{La}_7\text{Sr}[\text{Si}_{10}\text{N}_{19}\text{O}_3]$ and resulted in a comparable small band gap of $E_g \approx 3.55$ eV. Luminescence measurements on single particles of 0.2 mol% doped $\text{La}_7\text{Sr}[\text{Si}_{10}\text{N}_{19}\text{O}_3]:\text{Eu}^{2+}$ led to amber emission upon excitation with UV to blue light with an emission maximum at $\lambda_{\text{em}} \approx 612$ nm and $\text{fwhm} \approx 84$ nm/2194 cm^{-1} . The emission characteristics are comparable to commercially utilized amber emitting $(\text{Ba},\text{Sr})_2\text{Si}_5\text{N}_8:\text{Eu}^{2+}$ and $(\text{Sr},\text{Ca})\text{AlSiN}_3:\text{Eu}^{2+}$. Since the luminescence at room temperature was weak, cryo-spectroscopy was used to investigate whether the luminescence intensity can be raised at lower temperatures which resulted in a factor of 2 higher intensity. The two predominant theories for explaining the thermal quenching behavior of activator ions in phosphors, namely the crossover mechanism according to Blasse *et al.* and the thermal ionization mechanisms after Dorenbos, were discussed. Due to the comparable small band gap, both quenching mechanisms probably occur simultaneously. Thermal ionization may not be the determining factor because cryo-spectroscopy measurements did not result in significantly higher luminescence. The crystal structure of $\text{La}_7\text{Sr}[\text{Si}_{10}\text{N}_{19}\text{O}_3]$ appears to offer less structural rigidity, which leads to a larger Stokes shift and therefore increases the probability for thermal quenching as described by the crossover mechanism. Further syntheses of $\text{RE}_{8-x}\text{AE}_x[\text{Si}_{10}\text{N}_{20-x}\text{O}_{2+x}]:\text{Eu}^{2+}$ and extensive investigations regarding luminescence properties, band structures and RIXS measurements are necessary to further understand

4 Synthesis and Luminescence Properties of Amber Emitting $\text{La}_7\text{Sr}[\text{Si}_{10}\text{N}_{19}\text{O}_3]:\text{Eu}^{2+}$ and Syntheses of the Substitutional Variants $\text{RE}_{8-x}\text{AE}_x[\text{Si}_{10}\text{N}_{20-x}\text{O}_{2+x}]:\text{Eu}^{2+}$ with $\text{RE} = \text{La}, \text{Ce}$; $\text{AE} = \text{Ca}, \text{Sr}, \text{Ba}$; $0 \leq x \leq 2$

the influences of different RE and AE on band structures, band gap sizes and position of Eu^{2+} 5d levels. With this knowledge, potential host materials and their luminescent properties can be improved and possibly be tunable to develop the highly desired narrow-band and super-efficient red phosphors.

4.4 Experimental Part

4.4.1 Synthesis

Due to some air and moisture sensitive starting materials, all manipulations were carried out under Ar-atmosphere either in an Ar-filled glovebox (Unilab, MBraun, Garching; $\text{O}_2 < 1$ ppm; $\text{H}_2\text{O} < 1$ ppm) or in Ar-filled glassware applying the Schlenk technique. For the synthesis of the starting materials SrN and CeN used as for the main syntheses, the respective metals were first placed in a tungsten crucible and then positioned into a corundum crucible. This assembly was transferred into the pressure chamber of a hot isostatic press (HIP, AIP6-30H, American Isostatic Presses, Inc., Columbus, Ohio, USA) equipped with a carbon fiber reinforced carbon furnace ($T_{\text{max}} = 2000$ °C, $\varnothing = 70$ mm, $h = 125$ mm). The atmosphere in the pressure vessel ($p_{\text{max}} = 207$ MPa) was first flushed with N_2 for 10 times and then, a pressure booster (Maximator, DLE-5-30-2, $p_{\text{max}} = 60$ MPa) to build up the necessary pressure to operate the main compressor was used. When the pressure was subsequently increased and reached 70 MPa, the samples were heated to 1000 °C within 3.5 h while ending up with a pressure of 150 MPa. After heating for 10 h, the setup was cooled down to 20 °C and the pressure was released. SrN and CeN were obtained as black and dark brown powders, respectively (see Figure C11 and Table C10). The chemicals required for the phase-pure syntheses of $\text{RE}_{8-x}\text{AE}_x[\text{Si}_{10}\text{N}_{20-x}\text{O}_{2+x}]$ ($\text{RE} = \text{La}, \text{Ce}$; $\text{AE} = \text{Ca}, \text{Sr}, \text{Ba}$; $0 \leq x \leq 2$), as well as their respective amounts are listed in Table C11 and C12. The thoroughly ground starting materials were filled into a tungsten crucible and transferred into a water-cooled silica glass reactor of a radiofrequency furnace (TIG 10/100; Hüttinger Elektronik Freiburg, Germany) attached to a Schlenk line.^[58] The crucible was heated within 5 min to 1600 °C under N_2 -atmosphere, maintained at that temperature for 5 h, cooled down to 1200 °C within 15 h, and finally quenched by switching off the furnace. All body colors and luminescence impressions are listed in Table C13.

4.4.2 Single-Crystal X-ray Diffraction

A single crystal of $\text{La}_7\text{Sr}[\text{Si}_{10}\text{N}_{19}\text{O}_3]$ was isolated and fixed on a MicroMount (50 μm , MiTeGen, Ithaca, New York, USA). X-ray diffraction data were collected with a Bruker D8 Venture diffractometer with rotating anode (Mo- $\text{K}\alpha$ radiation). For indexing, integration, semi-empirical absorption correction and determination of the space group, the software package APEX3 was used, while WinGX with the implemented tools SHELXT and SHELXL was used

for structure solution and refinement by full-matrix least-squares method.^[20, 59-65] Deposition Number(s) 2104245 (for $\text{La}_7\text{Sr}[\text{Si}_{10}\text{N}_{19}\text{O}_3]$), 2141282 (for $\text{La}_8[\text{Si}_{10}\text{N}_{20}\text{O}_2]$), 2141280 (for $\text{La}_6\text{Sr}_2[\text{Si}_{10}\text{N}_{18}\text{O}_4]$), 2141281 (for $\text{La}_7\text{Ca}[\text{Si}_{10}\text{N}_{19}\text{O}_3]$), 2141318 (for $\text{La}_6\text{Ca}_2[\text{Si}_{10}\text{N}_{18}\text{O}_4]$), 2141284 (for $\text{La}_7\text{Ba}[\text{Si}_{10}\text{N}_{19}\text{O}_3]$), 2141283 (for $\text{La}_6\text{Ba}_2[\text{Si}_{10}\text{N}_{18}\text{O}_4]$), 2141285 (for $\text{Ce}_7\text{Sr}[\text{Si}_{10}\text{N}_{19}\text{O}_3]$), 2141287 (for $\text{Ce}_8[\text{Si}_{10}\text{N}_{20}\text{O}_2]$), 2141319 (for $\text{Ce}_6\text{Sr}_2[\text{Si}_{10}\text{N}_{18}\text{O}_4]$), 2141288 (for $\text{Ce}_7\text{Ca}[\text{Si}_{10}\text{N}_{19}\text{O}_3]$), 2141289 (for $\text{Ce}_6\text{Ca}_2[\text{Si}_{10}\text{N}_{18}\text{O}_4]$), 2141290 (for $\text{Ce}_7\text{Ba}[\text{Si}_{10}\text{N}_{19}\text{O}_3]$), 2141320 (for $\text{Ce}_6\text{Ba}_2[\text{Si}_{10}\text{N}_{18}\text{O}_4]$) contain(s) the supplementary crystallographic data for this paper (Table C14). These data are provided free of charge by the joint Cambridge Crystallographic Data Centre and Fachinformationszentrum Karlsruhe (<http://www.ccdc.cam.ac.uk/structures>).

4.4.3 Powder X-ray Diffraction

For the collection of powder X-ray diffraction (PXRD) data of the ground products sealed into glass capillaries (0.2 mm diameter, wall thickness 0.01 mm; Hilgenberg GmbH, Malsfeld, Germany), a STOE STADI P diffractometer (Mo- $K\alpha_1$ radiation, $\lambda = 0.70930 \text{ \AA}$, Stoe & Cie, Darmstadt, Germany) equipped with an Ge(111) monochromator and a Mythen1K detector (Dectris, Baden-Dättwil, Switzerland) in parafocusing Debye–Scherrer geometry was used. The TOPAS Academic V6 package applying the fundamental parameters approach (direct convolution of source emission profiles, axial instrument contributions, crystallite size and microstrain effects) was used to perform Rietveld refinements.^[66, 67] Absorption effects were corrected using the calculated absorption coefficient. A spherical harmonics model of fourth order was applied to describe preferred orientation, while the background was modeled with a shifted Chebychev function.^[68-70]

4.4.4 Scanning Electron Microscopy (SEM) and Energy-dispersive X-ray Spectroscopy (EDX)

Energy dispersive X-ray (EDX) measurements were used to investigate the chemical composition and morphology of the samples, for which a Dualbeam Helios Nanolab G3 UC (FEI, Hillsboro, Oregon, USA) equipped with an X-Max 80 SDD detector (Oxford Instruments, Abingdon, UK) was used. The samples were carbon-coated to prevent electrostatic charging of the samples using a high-vacuum sputter coater (CCU-010, Safematic GmbH, Zizers, Switzerland).

4.4.5 UV/Vis Spectroscopy

A Jasco V-650 UV/Vis spectrophotometer equipped with a deuterium and a halogen lamp (Czerny-Turner monochromator with 1200 lines/mm concave grating, photomultiplier tube detector) was used to measure diffuse reflectance spectra in the range of 240 to 800 nm with 1 nm step size.

4.4.6 Luminescence

Photoluminescence properties of Eu^{2+} -doped samples were measured at room temperature on a HORIBA Fluoromax4 spectrofluorimeter system connected to an Olympus BX51 microscope via optical fibers. Excitation spectra were acquired with the monitoring wavelength λ_{mon} ranging from 425 to 516 nm. For cryo-spectroscopy between 300 and 6 K measured on a thick-bed powder layer, a fiber-coupled spectroscopy system containing a thermally stabilized LED light source and a fiber-optic spectrometer (HR2000+ES spectrometer, Ocean Optics) was used. During the measurement, the sample was placed in an evacuated cooling chamber, equipped with a liquid-He compressor system (ARS4HW, Advanced Research System Inc., Macungie, Pennsylvania, USA).

4.5 Acknowledgements

We thank Dr. Peter Mayer (Department of Chemistry at University of Munich (LMU)) for the collection of the single-crystal data. Inspiring discussions with Reinhard Pritzl and Tobias Giffthaler (both Department of Chemistry, LMU) are gratefully appreciated.

4.6 References

- [1] C. Elliott, M. Yamada, J. Penning, S. Schober, K. Lee, *Energy Savings Forecast of Solid-State Lighting in General Illumination Applications*, U.S. Department of Energy, Office of Energy Efficiency and Renewable Energy, Building Technologies Office, Washington, D.C., **2019**.
- [2] J. Heber, *Nat. Phys.* **2014**, *10*, 791.
- [3] J. L. Leañó Jr., M.-H. Fang, R.-S. Liu, *ECS J. Solid State Sci. Technol.* **2018**, *7*, R3111–R3133.
- [4] R. Mueller-Mach, G. Mueller, M. R. Krames, H. A. Höpfe, F. Stadler, W. Schnick, T. Juestel, P. Schmidt, *Phys. Status Solidi A* **2005**, *202*, 1727–1732.
- [5] M. Krames, G. O. Mueller, R. Mueller-Mach, H. Bechtel, P. J. Schmidt, *PCT Int. Appl.* **2010**, WO2010131133A1.
- [6] H. A. Höpfe, H. Lutz, P. Morys, W. Schnick, A. Seilmeier, *J. Phys. Chem. Solids* **2000**, *61*, 2001–2006.
- [7] H. Watanabe, N. Kijima, *J. Alloys Compd.* **2009**, *475*, 434–439.
- [8] K. Uheda, N. Hirosaki, Y. Yamamoto, A. Naito, T. Nakajima, H. Yamamoto, *Electrochem. Solid-State Lett.* **2006**, *9*, H22–H25.
- [9] K. Uheda, N. Hirosaki, H. Yamamoto, *Phys. Status Solidi A* **2006**, *203*, 2712–2717.
- [10] P. Pust, P. J. Schmidt, W. Schnick, *Nat. Mater.* **2015**, *14*, 454–458.
- [11] P. Pust, V. Weiler, C. Hecht, A. Tücks, A. S. Wochnik, A.-K. Henß, D. Wiechert, C. Scheu, P. J. Schmidt, W. Schnick, *Nat. Mater.* **2014**, *13*, 891–896.

- [12] G. J. Hoerder, M. Seibald, D. Baumann, T. Schröder, S. Peschke, P. C. Schmid, T. Tyborski, P. Pust, I. Stoll, M. Bergler, C. Patzig, S. Reißaus, M. Krause, L. Berthold, T. Höche, D. Johrendt, H. Huppertz, *Nat. Commun.* **2019**, *10*, 1824–1832.
- [13] S. Schmiechen, H. Schneider, P. Wagatha, C. Hecht, P. J. Schmidt, W. Schnick, *Chem. Mater.* **2014**, *26*, 2712–2719.
- [14] W. Schnick, H. Huppertz, *Chem. - Eur. J.* **1997**, *3*, 679–683.
- [15] M. Zeuner, S. Pagano, W. Schnick, *Angew. Chem. Int. Ed.* **2011**, *50*, 7754–7775; *Angew. Chem.* **2011**, *123*, 7898–7920.
- [16] Y. Zhang, S. Li, T. Takeda, S. Funahashi, N. Hirotsuki, R.-J. Xie, *J. Mater. Chem. C* **2020**, *8*, 13458–13466.
- [17] H.-W. Zheng, X.-M. Wang, H.-W. Wei, Y. Zheng, C.-L. Yin, Z.-P. Yang, H. Jiao, *Chem. Commun.* **2021**, *57*, 3761–3764.
- [18] G. Auffermann, Y. Prots, R. Kniep, *Angew. Chem. Int. Ed.* **2001**, *40*, 547–549; *Angew. Chem.* **2001**, *113*, 565–567.
- [19] R. D. Shannon, *Acta Crystallogr., Sect. A* **1976**, *32*, 751–767.
- [20] G. M. Sheldrick, *SADABS Version 2: Multi-Scan Absorption Correction*, Bruker AXS Inc., Madison, Wisconsin, **2012**.
- [21] K. Momma, F. Izumi, *J. Appl. Crystallogr.* **2011**, *44*, 1272–1276.
- [22] R. Hoppe, S. Voigt, H. Glaum, J. Kissel, H. P. Müller, K. Bernet, *J. Less-Common Met.* **1989**, *156*, 105–122.
- [23] A. S. Wills, *VaList*, v. 4.0.7, University College London, **2010**.
- [24] I. D. Brown, D. Altermatt, *Acta Crystallogr., Sect. B* **1985**, *41*, 244–247.
- [25] N. E. Brese, M. O’Keeffe, *Acta Crystallogr., Sect. B* **1991**, *47*, 192–197.
- [26] P. E. D. Morgan, *J. Mater. Sci.* **1986**, *21*, 4305–4309.
- [27] R. G. Pearson, *J. Chem. Educ.* **1968**, *45*, 581–587.
- [28] R. G. Pearson, *J. Chem. Educ.* **1968**, *45*, 643–648.
- [29] R. G. Pearson, *Inorg. Chim. Acta* **1995**, *240*, 93–98.
- [30] Superscript numbers in square brackets within a sum formula indicate the coordination number according to the Niggli notation. U. Müller, *Anorganische Strukturchemie*, Vol. 6, Vieweg+Teubner, Wiesbaden, **2009**.
- [31] J. Lima-de-Faria, E. Hellner, F. Liebau, E. Makovicky, E. Parthé, *Acta Crystallogr. Sect. A* **1990**, *46*, 1–11.
- [32] The term *sechser* (*dreier*, *achter*) ring was established by F. Liebau and is derived from the German word “sechser” (“dreier”, “achter”). A *sechser* (*dreier*, *achter*) ring comprises six (three, eight) tetrahedra centers. F. Liebau, *Structural Chemistry of Silicates*, Springer, Berlin, **1985**.

4 Synthesis and Luminescence Properties of Amber Emitting $\text{La}_7\text{Sr}[\text{Si}_{10}\text{N}_{19}\text{O}_3]:\text{Eu}^{2+}$ and Syntheses of the Substitutional Variants $\text{RE}_{8-x}\text{AE}_x[\text{Si}_{10}\text{N}_{20-x}\text{O}_{2+x}]:\text{Eu}^{2+}$ with $\text{RE} = \text{La}, \text{Ce}; \text{AE} = \text{Ca}, \text{Sr}, \text{Ba}; 0 \leq x \leq 2$

- [33] D. Durach, P. Schultz, O. Oeckler, W. Schnick, *Inorg. Chem.* **2016**, *55*, 3624–3629.
- [34] Z. A. Gál, P. M. Mallinson, H. J. Orchard, S. J. Clarke, *Inorg. Chem.* **2004**, *43*, 3998–4006.
- [35] H. Ma, X. Li, R. Ye, Y. Hua, *J. Alloys Compd.* **2017**, *703*, 486–499.
- [36] O. Oeckler, F. Stadler, T. Rosenthal, W. Schnick, *Solid State Sci.* **2007**, *9*, 205–212.
- [37] T. Schlieper, W. Milius, W. Schnick, *Z. Anorg. Allg. Chem.* **1995**, *621*, 1380–1384.
- [38] C. Schmolke, S. Lupart, W. Schnick, *Solid State Sci.* **2009**, *11*, 305–309.
- [39] J. Takahashi, H. Yamane, N. Hirosaki, Y. Yamamoto, T. Suehiro, T. Kamiyama, M. Shimada, *Chem. Mater.* **2003**, *15*, 1099–1104.
- [40] Z. Xia, M. S. Molokeev, W. B. Im, S. Unithrattil, Q. Liu, *J. Phys. Chem. C* **2015**, *119*, 9488–9495.
- [41] H. Yamane, T. Nagura, T. Miyazaki, *Acta Crystallogr., Sect. E: Struct. Rep. Online* **2014**, *E70*, i23–i24.
- [42] R. López, R. Gómez, *J. Sol-Gel Sci. Technol.* **2012**, *61*, 1–7.
- [43] J. Tauc, R. Grigorovici, A. Vancu, *Phys. Status Solidi B* **1966**, *15*, 627–637.
- [44] M. Amachraa, Z. Wang, C. Chen, S. Hariyani, H. Tang, J. Brgoch, S. P. Ong, *Chem. Mater.* **2020**, *32*, 6256–6265.
- [45] T. M. Tolhurst, P. Strobel, P. J. Schmidt, W. Schnick, A. Moewes, *Chem. Mater.* **2017**, *29*, 7976–7983.
- [46] T. M. Tolhurst, S. Schmiechen, P. Pust, P. J. Schmidt, W. Schnick, A. Moewes, *Adv. Opt. Mater.* **2016**, *4*, 584–591.
- [47] C. Maak, R. Niklaus, F. Friedrich, A. Mähringer, P. J. Schmidt, W. Schnick, *Chem. Mater.* **2017**, *29*, 8377–8384.
- [48] C. Maak, D. Durach, C. Martiny, P. J. Schmidt, W. Schnick, *Chem. Mater.* **2018**, *30*, 3552–3558.
- [49] G. Blasse, B. C. Grabmaier, *Luminescent Materials*, Springer, Berlin, Heidelberg, **1994**,
- [50] P. Pust, F. Hintze, C. Hecht, V. Weiler, A. Locher, D. Zitnanska, S. Harm, D. Wiechert, P. J. Schmidt, W. Schnick, *Chem. Mater.* **2014**, *26*, 6113–6119.
- [51] G. Blasse, A. Bril, *Philips Tech. Rev.* **1970**, *31*, 304–332.
- [52] P. Dorenbos, *J. Phys.: Condens. Matter* **2005**, *17*, 8103–8111.
- [53] T. M. Tolhurst, C. Braun, W. Schnick, A. Moewes, *J. Phys. Chem. C* **2021**, *125*, 25799–25806.
- [54] G. G. Stokes, *Phil. Trans. R. Soc. Lond.* **1852**, *142*, 463–562.
- [55] G. Blasse, *Prog. Solid State Chem.* **1988**, *18*, 79–171.
- [56] S. Shionoya, W. M. Yen, *Phosphor Handbook*, CRC Press, New York, **1998**,

-
- [57] M. de Jong, L. Seijo, A. Meijerink, F. T. Rabouw, *Phys. Chem. Chem. Phys.* **2015**, *17*, 16959–16969.
- [58] W. Schnick, H. Huppertz, R. Lauterbach, *J. Mater. Chem.* **1999**, *9*, 289–296.
- [59] *Data Integration Software*, SAINT, Madison, Wisconsin, **1997**.
- [60] Bruker AXS Inc., *APEX3*, Karlsruhe, Germany, **2016**.
- [61] Bruker AXS Inc., *XPREP Reciprocal Space Exploration*, Karlsruhe, Germany, **2001**.
- [62] L. J. Farrugia, *J. Appl. Cryst.* **2012**, *45*, 849–854.
- [63] G. M. Sheldrick, *Acta Crystallogr., Sect. A* **2008**, *64*, 112–122.
- [64] G. M. Sheldrick, *Acta Crystallogr., Sect. A* **2015**, *71*, 3–8.
- [65] G. M. Sheldrick, *Acta Crystallogr., Sect. C* **2015**, *71*, 3–8.
- [66] A. A. Coelho, *TOPAS Version 6: A program for Rietveld refinement*, Coelho Software, Brisbane, Australia, **2016**,
- [67] H. Rietveld, *J. Appl. Crystallogr.* **1969**, *2*, 65–71.
- [68] J. Bergmann, R. Kleeberg, A. Haase, B. Breidenstein, *Mater. Sci. Forum* **2000**, *347–349*, 303–308.
- [69] R. W. Cheary, A. A. Coelho, J. P. Cline, *J. Res. Natl. Inst. Stand. Technol.* **2004**, *109*, 1–25.
- [70] R. W. Cheary, A. Coelho, *J. Appl. Crystallogr.* **1992**, *25*, 109–121.

5 State-of-the-Art Complex Structure Elucidation and Luminescence Properties of Barium and Strontium Lanthanum Oxonitridosilicate Oxides

5.1 Structure Elucidation of Complex Endotaxially Intergrown Barium Lanthanum Oxonitridosilicate Oxides by Combination of Microfocused Synchrotron Radiation and Transmission Electron Microscopy

Published in: *Chem. Eur. J.* **2021**, 27, 12835–12844

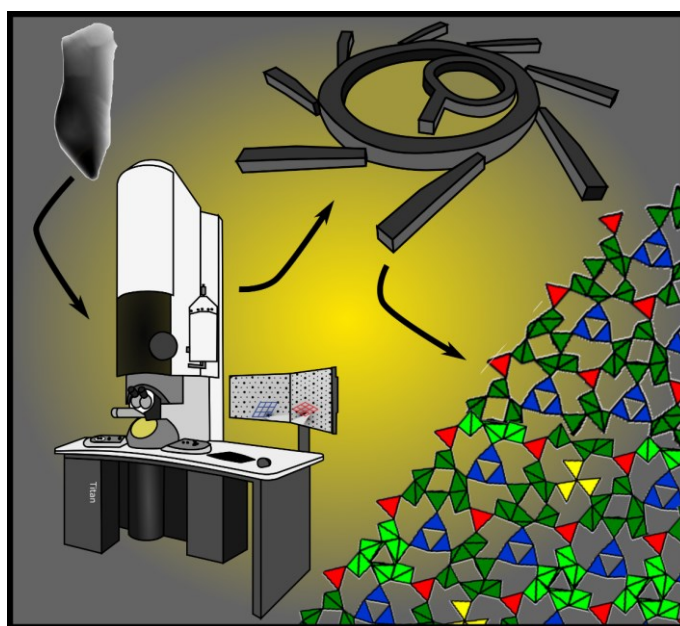
Authors: Lisa Gamperl, Lukas Neudert, Peter Schultz, Dajana Durach, Wolfgang Schnick, and Oliver Oeckler

DOI: 10.1002/chem.202200760

Copyright © 2022 Wiley-VCH Verlag GmbH & Co. KGaA

<https://chemistry->

[europe.onlinelibrary.wiley.com/doi/10.1002/chem.202101665](https://chemistry-europe.onlinelibrary.wiley.com/doi/10.1002/chem.202101665)



Abstract. Single crystalline domains in intergrown microcrystalline material of the new compounds $\text{Ba}_{22.5+x}\text{La}_{55-x}[\text{Si}_{129}\text{N}_{240-x}\text{O}_x]\text{O}_3:\text{Ce}^{3+}$ and $\text{Ba}_{25.5+x}\text{La}_{77-x}[\text{Si}_{170}\text{N}_{312-x}\text{O}_{9+x}]\text{O}_4:\text{Ce}^{3+}$ were identified by transmission electron microscopy (TEM). Precise diffraction data from these domains were collected with microfocused synchrotron radiation so that crystal structure elucidation of the complex disordered networks became possible. They are composed of two different interconnected slabs of which one is similar in both compounds, which explains their notorious intergrowth. The distribution of Ba and La is indicated by the analysis of bond-valence sums and by comparison with isostructural

5.1 Structure Elucidation of Complex Endotaxially Intergrown Barium Lanthanum Oxonitridosilicate Oxides by Combination of Microfocused Synchrotron Radiation and Transmission Electron Microscopy

$\text{Sr}_{28.5+x}\text{La}_{75-x}[\text{Si}_{170}\text{N}_{312-x}\text{O}_{9+x}]\text{O}_4$. Ce^{3+} doping leads to yellow luminescence. This showcase highlights the discovery and accurate characterization of new compounds relevant for luminescence applications from heterogeneous microcrystalline samples by exploiting the capability of the combination of TEM and diffraction using the latest focusing techniques for synchrotron radiation.

5.1.1 Introduction

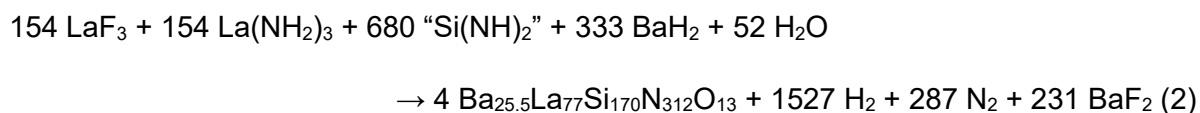
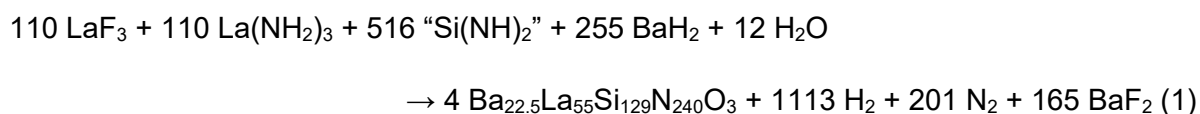
(Oxo-)nitridosilicates are an important class of compounds since they offer intriguing material properties. The compounds $M_2\text{Si}_5\text{N}_8:\text{Eu}^{2+}$ ($M = \text{Ca}, \text{Sr}, \text{Ba}$), for instance, constitute a prominent example as they made it into everyday use. These compounds are used in common amber-emitting phosphor-converted light emitting diodes (pcLEDs) adapted to specific requirements in the automotive field or general lighting.^[1] Potential applications of (oxo-)nitridosilicates are diverse and cover a wide range from pcLEDs, for which Eu^{2+} - or Ce^{3+} -doped luminescent materials such as above mentioned $M_2\text{Si}_5\text{N}_8:\text{Eu}^{2+}$ ($M = \text{Ca}, \text{Sr}, \text{Ba}$) and $M\text{Si}_2\text{O}_2\text{N}_2:\text{Eu}^{2+}$ ($M = \text{Ca}, \text{Sr}, \text{Ba}$) are used, to lithium ion batteries, e.g. with ionic conductors like $\text{Li}_{14}\text{Ln}_5[\text{Si}_{11}\text{N}_{19}\text{O}_5]\text{O}_2\text{F}_2$ ($\text{Ln} = \text{Ce}, \text{Nd}$).^[2–9] Even when new (oxo-)nitridosilicates exhibit no remarkable properties, there is still great interest in elucidation of their crystal structures as the systematic crystal chemistry of (oxo-)nitridosilicates is still fragmentary. However, it is sometimes impossible to obtain sufficiently sized single crystals or phase pure powder samples from various syntheses, which often require extreme conditions, to elucidate the structure of new compounds with conventional single-crystal or powder X-ray diffraction.^[10] Challenges concerning the structure determination of microcrystalline and often inhomogeneous samples have recently been approached by the combination of transmission electron microscopy (TEM) – especially selected area electron diffraction (SAED), scanning transmission electron microscopy (STEM) and energy dispersive X-ray spectroscopy (EDX) – with synchrotron methods that exploit the brilliance of microfocused X-ray beams.^[11,12] Since the advent of compound refractive lenses,^[13–16] synchrotron beams can be focused down to less than 1 μm , which enables the collection of single-crystal X-ray data from crystallites with the same size that have been pre-characterized by TEM. This methodical combination enables the precise structural characterization of unique phases accessible only in form of crystallites with an interaction volume less than 1 μm^3 . So far, this approach has not been applied to get access to single-crystal data from samples that feature oriented intergrowth of different phases with overlapping diffraction patterns, which often impedes accurate crystal structure determination. Even if structure solution and refinement may be possible, the partial overlap of the individual reciprocal lattices is difficult to deal with; it reduces accuracy and may be ambiguous. Furthermore, synchrotron measurements provide high-resolution data, which are essential for an accurate structure solution and the

combination of high-energy radiation and tiny crystals minimize absorption effects and associated artifacts. Exact knowledge of crystals structures is the essential feature of the single-particle-diagnosis approach^[17, 18] as the basis for the derivation of structure-property relations and the overall understanding of (oxo-)nitridosilicates. This aims at tuning properties so that they optimally suit the required applications of e.g., luminescent materials. The influence of the structure on luminescence properties has exemplarily been shown by investigations on the $\text{Sr}_{1-x}\text{Ba}_x\text{Si}_2\text{O}_2\text{N}_2:\text{Eu}^{2+}$ phases.^[19] The combination of synchrotron and TEM is certainly expected to become more and more important in order to make accurate predictions and thus to control application-relevant properties. In this contribution, we report on the structure elucidation of two luminescent oxonitridosilicate oxides, namely $\text{Ba}_{22.5+x}\text{La}_{55-x}[\text{Si}_{129}\text{N}_{240-x}\text{O}_x]\text{O}_3:\text{Ce}^{3+}$ and $\text{Ba}_{25.5+x}\text{La}_{77-x}[\text{Si}_{170}\text{N}_{312-x}\text{O}_{9+x}]\text{O}_4:\text{Ce}^{3+}$ with intergrown complex structures. Single-crystalline domains were selected by TEM so that synchrotron diffraction data could be collected from the individual phases. The structure elucidation is supported by crystal-chemical considerations and comparison with $\text{Sr}_{28.5+x}\text{La}_{75-x}[\text{Si}_{170}\text{N}_{312-x}\text{O}_{9+x}]\text{O}_4$ for the assignment of the cation distribution in isostructural $\text{Ba}_{25.5+x}\text{La}_{77-x}[\text{Si}_{170}\text{N}_{312-x}\text{O}_{9+x}]\text{O}_4$.

5.1.2 Results and Discussion

5.1.2.1 Synthesis and Chemical Analysis

The synthesis described in the Experimental Section led to $\text{Ba}_{22.5+x}\text{La}_{55-x}[\text{Si}_{129}\text{N}_{240-x}\text{O}_x]\text{O}_3:\text{Ce}^{3+}$ ($x \approx 0.24$) and $\text{Ba}_{25.5+x}\text{La}_{77-x}[\text{Si}_{170}\text{N}_{312-x}\text{O}_{9+x}]\text{O}_4:\text{Ce}^{3+}$ ($x \approx 0.24$) as luminescent crystallites, both present in the pale orange powder sample. Their formation may be explained according to the following idealized reaction equations (all samples contain 2 mol% of Ce^{3+} , which is not always mentioned for the sake of conciseness):



TEM-EDX measurements (Tables D1, D2, Figure D1) of the crystals used for SCXRD led to an average atomic ratio Ba:La of about 1:2.1 for $\text{Ba}_{22.5+x}\text{La}_{55-x}[\text{Si}_{129}\text{N}_{240-x}\text{O}_x]\text{O}_3$ and of about 1:2.6 for $\text{Ba}_{25.5+x}\text{La}_{77-x}[\text{Si}_{170}\text{N}_{312-x}\text{O}_{9+x}]\text{O}_4$. Within the typical limits of accuracy, this agrees with the values corresponding to the sum formulas derived from SCXRD data (Ba:La \approx 1:2.4 and 1:3.3, respectively). The absolute values, however, somehow deviate from the expected ones. This can be explained by shadowing owing to the unfavorable orientation of the crystal with respect to the EDX detector. The values for Si, N and O are more strongly affected and

5.1 Structure Elucidation of Complex Endotaxially Intergrown Barium Lanthanum Oxonitridosilicate Oxides by Combination of Microfocused Synchrotron Radiation and Transmission Electron Microscopy

thus determined too low compared to the values for the heavier atoms Ba and La. Even though Ce as a dopant could not be detected by EDX, its occurrence is proven by the luminescence observed. Due to the small amount of Ce and the lack of scattering contrast between La and Ce, the latter was subsequently neglected in structure refinements. An IR spectrum of the sample shows no O-H or N-H vibrations and thus corroborates the absence of hydrogen in the reaction products (Figure D2a) as assumed due to the reaction conditions. Since both mixed and underoccupied cation sites are present and since LaN vs. BaO can formally be exchanged for each other without violating charge neutrality, one may assume solid solutions $\text{Ba}_{22.5+x}\text{La}_{55-x}[\text{Si}_{129}\text{N}_{240-x}\text{O}_x]\text{O}_3$ ($x \approx 0.24$) and $\text{Ba}_{25.5+x}\text{La}_{77-x}[\text{Si}_{170}\text{N}_{312-x}\text{O}_{9+x}]\text{O}_4$ ($x \approx 0.24$). A Rietveld refinement based on the powder X-ray diffraction data using non refined atom parameters from single crystal data (see below) was performed for the determination of the bulk phase composition. The sample contains approx. 32 wt% $\text{Ba}_{22.5+x}\text{La}_{55-x}[\text{Si}_{129}\text{N}_{240-x}\text{O}_x]\text{O}_3$ and approx. 68 wt% $\text{Ba}_{25.5+x}\text{La}_{77-x}[\text{Si}_{170}\text{N}_{312-x}\text{O}_{9+x}]\text{O}_4$ (Figure 51, Table D3). The refinement therefore confirms the presence of the crystal structures elucidated by single-crystal analysis. Although according to the idealized reaction equations, a large amount of BaF_2 should be formed, this was not found in the PXRD pattern. As described in literature,^[20] it is possible that binary halides formed during the reaction deposit on the inside wall of the water-cooled silica glass reactor through transport reactions at high reaction temperatures.

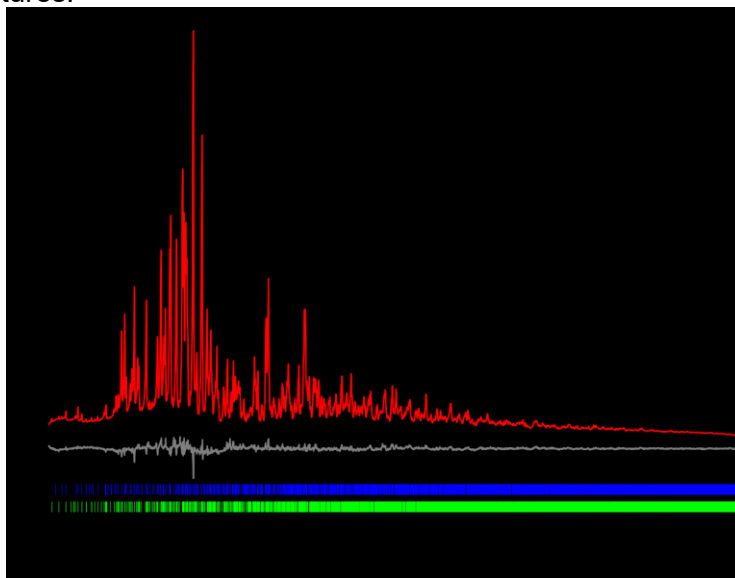
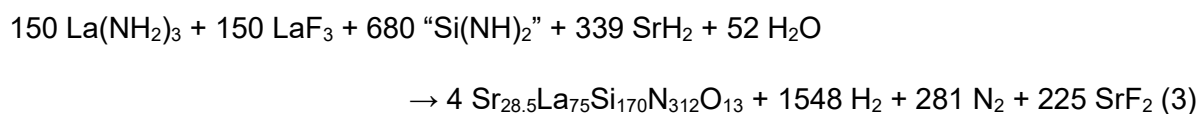


Figure 5.1. Rietveld refinement based on PXRD data (Mo- $K\alpha_1$ radiation, $\lambda = 0.70930 \text{ \AA}$) collected from a sample containing $\text{Ba}_{22.5+x}\text{La}_{55-x}[\text{Si}_{129}\text{N}_{240-x}\text{O}_x]\text{O}_3$ with $x \approx 0.24$ (32 wt%, vertical blue bars for indication of the position of its Bragg reflections) and $\text{Ba}_{25.5+x}\text{La}_{77-x}[\text{Si}_{170}\text{N}_{312-x}\text{O}_{9+x}]\text{O}_4$ with $x \approx 0.24$ (68 wt%, vertical green bars for indication of the position of its Bragg reflections) based on the structure models obtained by SCXRD data. Observed (black) and calculated (red) powder X-ray diffraction patterns with corresponding difference profile (gray).

$\text{Sr}_{28.5+x}\text{La}_{75-x}[\text{Si}_{170}\text{N}_{312-x}\text{O}_{9+x}]\text{O}_4:\text{Ce}^{3+}$ ($x \approx -3.71$) was synthesized analogous to the Ba compound according to the following idealized reaction equation:



TEM-EDX measurements (Table D4) of the single crystal used for synchrotron SCXRD resulted in a Sr:La ratio of about 1:1 compared to the theoretical value from the single crystal X-ray data of Sr:La \approx 1:3.3. This deviation is again due to pronounced shadowing, which reduces the amount of emitted Sr X-rays reaching the detector. For other crystals less suitable for synchrotron data collection due to their too small volume, inferior crystal quality or unfavorable positions on the TEM grid, higher Sr contents were detected. IR spectroscopy again confirms the absence of hydrogen in the reaction products (Figure D2b). Rietveld refinement using powder X-ray diffraction data (Figure D3, Table D5) shows that $\text{Sr}_{28.5+x}\text{La}_{75-x}[\text{Si}_{170}\text{N}_{312-x}\text{O}_{9+x}]\text{O}_4$ was obtained as a side phase (approx. 28 wt%) alongside $\text{La}_{13.68}\text{Sr}_{12.32}[\text{Si}_{60}\text{N}_{96}]\text{F}_{6.32}\text{O}_{5.68}^{[21]}$ (approx. 72 wt%) and a small amount of an additional unknown phase. Although the latter's reflections could neither be assigned to an already known phase nor indexed, R_{Bragg} values of 0.0425 for $\text{Sr}_{28.5+x}\text{La}_{75-x}[\text{Si}_{170}\text{N}_{312-x}\text{O}_{9+x}]\text{O}_4$ and 0.0244 for $\text{La}_{13.68}\text{Sr}_{12.32}[\text{Si}_{60}\text{N}_{96}]\text{F}_{6.32}\text{O}_{5.68}$ confirm the presence of these compounds.

5.1.2.2 Diffraction Patterns

Since only crystals with maximum sizes up to 10 μm (Figure 5.2a–c) along with low scattering volumes were obtained for the three compounds and structure solution based on the PXRD data was impeded by samples that were not phase pure, a microfocused synchrotron beam was used for collecting single crystal X-ray diffraction data.

5.1 Structure Elucidation of Complex Endotaxially Intergrown Barium Lanthanum Oxonitridosilicate Oxides by Combination of Microfocused Synchrotron Radiation and Transmission Electron Microscopy

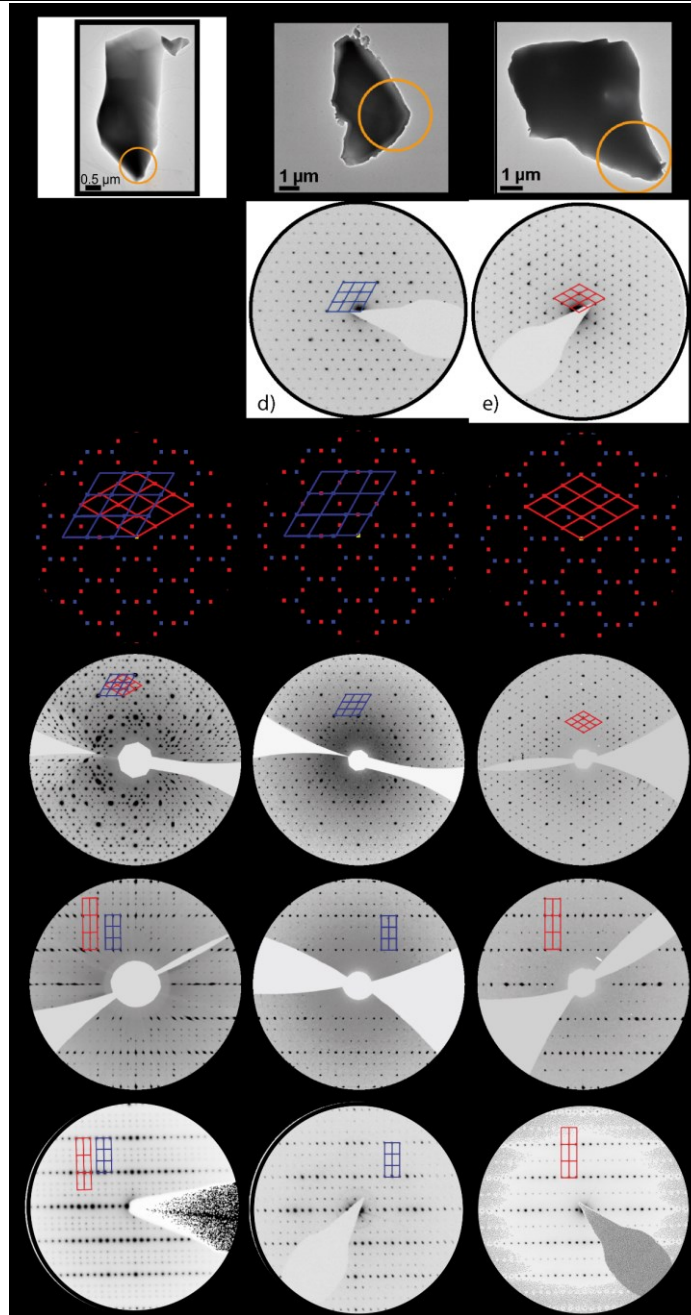


Figure 5.2: TEM bright-field images of (a) an intergrown crystal as well as (b) $\text{Ba}_{22.5+x}\text{La}_{55-x}[\text{Si}_{129}\text{N}_{240-x}\text{O}_x]\text{O}_3$ ($a \approx 17.5 \text{ \AA}$) and (c) $\text{Ba}_{25.5+x}\text{La}_{77-x}[\text{Si}_{170}\text{N}_{312-x}\text{O}_{9+x}]\text{O}_4$ ($a \approx 22.7 \text{ \AA}$) single crystals. All sections corresponding to the crystallites shown in (a–c) are depicted in the same column. (d) and (e) SAED patterns along [001] for both crystallites. (f–h) Sketched reciprocal lattices with lattice nodes of $\text{Ba}_{22.5+x}\text{La}_{55-x}[\text{Si}_{129}\text{N}_{240-x}\text{O}_x]\text{O}_3$ in blue and $\text{Ba}_{25.5+x}\text{La}_{77-x}[\text{Si}_{170}\text{N}_{312-x}\text{O}_{9+x}]\text{O}_4$ in red along [001]. (i–k) Reciprocal lattice sections $hk0$. (m–o) Reciprocal lattice sections $Ok\bar{l}$ for $\text{Ba}_{22.5+x}\text{La}_{55-x}[\text{Si}_{129}\text{N}_{240-x}\text{O}_x]\text{O}_3$, $h\bar{2}hl$ for $\text{Ba}_{25.5+x}\text{La}_{77-x}[\text{Si}_{170}\text{N}_{312-x}\text{O}_{9+x}]\text{O}_4$ and their overlapping pattern. (p–r) SAED patterns along [100] for all variants. Note that reciprocal lattice sections of the $\text{Ba}_{22.5+x}\text{La}_{55-x}[\text{Si}_{129}\text{N}_{240-x}\text{O}_x]\text{O}_3$ crystal exhibit very weak reflections of the second variant (Figure 2j, honeycomb-like patterns near the beam stop).

The combined analysis of reciprocal lattice sections reconstructed from synchrotron X-ray data of several crystallites and SAED patterns as part of preceding TEM characterization (Figures 5.2, D4) showed systematically absent classes of reflections that were incompatible with systematic absences of any space group (Figure 5.2i and 5.2m). The observed diffraction patterns could also not be explained assuming non-merohedral twinning. However, further electron diffraction experiments revealed a superposition of SAED patterns of two different types. Patterns along different viewing directions with respect to the two different unit cells can be completely interpreted assuming oriented intergrowth with a 30° tilt (Figure 5.2f) of two compounds with hexagonal metrics: type 1 with $a \approx 17.5 \text{ \AA}$ and $c \approx 22.7 \text{ \AA}$ (blue lattice in Figure 5.2, D4) and type 2 with $a \approx 20.2 \text{ \AA}$ and $c \approx 22.7 \text{ \AA}$ (red lattice in Figures 5.2, D4). The c lattice parameters are similar and with respect to a , the following relations are valid: $a_2 = \sqrt{3}a_1/2$, $3V_2 = 4V_1$ and $a_1 = \cos(30^\circ) \cdot a_2 = \cos(30^\circ) \cdot 20.2 \text{ \AA} \approx 17.5 \text{ \AA}$. The $2mm$ and 6 symmetries of the SAED patterns along zone axis $\langle 100 \rangle$ and $[001]$, respectively, correspond to hexagonal P lattices and suggest Laue class $6/m$. The observed reflection positions match those of simulated ones assuming this intergrowth. TEM-EDX measurements revealed the two intergrown phases as barium lanthanum oxonitridosilicates with different Ba:La ratios (type 1 $\approx 1:2$ and type 2 $\approx 1:3$, Figure D4b). This insight forced the search for non-intergrown crystallites of each compound by SAED and EDX. In extensive TEM investigations, separate single crystallites of both variants were identified. The structure models of the two related oxonitridosilicate frameworks were determined from microfocused synchrotron X-ray diffraction data of the sub-micron-sized crystallites characterized by TEM, which were re-located at the beamline using X-ray fluorescence scans. For $\text{Sr}_{28.5+x}\text{La}_{75-x}[\text{Si}_{170}\text{N}_{312-x}\text{O}_{9+x}]\text{O}_4$, suitable crystallites were identified by TEM in a similar fashion and diffraction data were also collected with microfocused synchrotron radiation. The data revealed a new phase with hexagonal metrics similar to that of type 2 but Sr instead of Ba leading to shorter lattice parameters ($a \approx 19.6$, $c \approx 21.9 \text{ \AA}$, Figure D4d).

5.1.2.3 Crystal Structure Determination

In all structure analyses, the distribution of elements with low scattering contrast such as the combinations N/O and Ba/La was analyzed using bond-valence sum (BVS) calculations.^[22-24] The structure solution of $\text{Ba}_{22.5+x}\text{La}_{55-x}[\text{Si}_{129}\text{N}_{240-x}\text{O}_x]\text{O}_3$ in space group $P\bar{6}$ with direct methods yielded mainly heavy atom (La, Ba) and Si atom positions, light atoms were localized in subsequent difference Fourier syntheses. An only moderately higher $R_{\text{sym}} = 0.122$ for the higher Laue symmetry $6/mmm$ compared to $R_{\text{sym}} = 0.072$ for $6/m$ indicated merohedral twinning (twin law $010|100|00\bar{1}$). Taking this into account decreased $R1$ from 0.219 to 0.047 with a resulting twin ratio of 64.4(1):35.6. The refinement was further checked for additional inversion twinning. However, volume fractions for the domains with inverted structure were

5.1 Structure Elucidation of Complex Endotaxially Intergrown Barium Lanthanum Oxonitridosilicate Oxides by Combination of Microfocused Synchrotron Radiation and Transmission Electron Microscopy

not significant (less than one standard deviation). Therefore, inversion twinning was not taken into account. A three-dimensional tetrahedra network was obtained. However, some hypothetical Si atom positions located unrealistically close to each other turned out to be split heavy-atom positions as the coordinating light atoms are located at typical interatomic distances in La/Ba–N/O bonds. The total occupancy of split-atom pairs was set to 100%, which was consistent with the scattering density observed. The occupancy of the non-split La/Ba17 position refined to a value of 0.55(3), which agreed with that of the nearby split position La/Ba5B while being too close to the alternative site La/Ba5A. The positional shift of La/Ba5A relative to La/Ba5B can easily be explained as a cation vacancy on the La/Ba17 position is balanced by rearrangement of nearby cations (Figure D5). The occupancy factors of La/Ba17 and La/Ba5B were thus constrained to be equal without a significant increase in R values. In order to validate the presence of split positions in space group $P\bar{6}$, twin refinements in lower symmetries were performed, always taking merohedral twinning into account as suggested by group-subgroup relations. Direct subgroups $P3$ (additional mirror twinning) and Pm (additional threefold rotation twinning) yielded rather unstable refinements unless displacement parameters of atoms, which are equivalent in $P\bar{6}$, were constrained to the same values. Space group $P1$ was also tentatively tested. These calculations did not yield ordered models as they still show the same split positions in difference Fourier syntheses as the model in $P\bar{6}$. One example for Pm , which theoretically enables ordering, is shown in the difference Fourier maps of Figure D6. The simultaneous presence of Ba/La and O/N impedes the determination of the atom distribution with X-ray methods due to lacking scattering contrast. Furthermore, the charge-neutral exchange BaO vs. LaN renders the use of charge neutrality constraints impractical. Bond-valence sum (BVS) calculations require some presumptions as derived Ba:La ratios depend on the O/N distribution and vice versa. According to various examples in literature and very low O contents suggested by EDX, initially a model with only $[\text{SiN}_4]$ tetrahedra was considered.^[10, 25, 26] Discrete non-tetrahedral anions were assigned as O in both cases according to Pauling's rule and as their distances of 2.26(2) Å to the nearest cations are in the range of La–O bonds but too short for La–N bonds.^[27–29] Ba:La ratios for each position were then derived by BVS (Table D6) and transferred with minor corrections to achieve charge neutrality to the single-crystal structure refinements as fixed values. During the refinements, the obtained model was repeatedly checked for plausibility based on EDX data, R -values, residual electron density as well as cation-anion distances and adjusted if necessary. Some cation positions turned out not to be fully occupied. Charge neutrality was achieved by adapting the values from BVS calculations with minor corrections.

For the structure determination of $\text{Ba}_{25.5+x}\text{La}_{77-x}[\text{Si}_{170}\text{N}_{312-x}\text{O}_{9+x}]\text{O}_4$, a similar approach was applied. In this case, the simultaneous presence of the analogous Sr compound was a great advantage because, in contrast to Ba and La, Sr and La have different scattering factors and can thus be distinguished by X-ray diffraction. Due to the notorious intergrowth of crystals of the two Ba compounds, it is likely that their structures are closely related, at least with respect to their lattices, but possibly also concerning their symmetry and atom arrangement. It turned out that they exhibit the same space group $P\bar{6}$. The structures of $\text{Ba}_{25.5+x}\text{La}_{77-x}[\text{Si}_{170}\text{N}_{312-x}\text{O}_{9+x}]\text{O}_4$ and $\text{Sr}_{28.5+x}\text{La}_{75-x}[\text{Si}_{170}\text{N}_{312-x}\text{O}_{9+x}]\text{O}_4$ were solved by direct methods and as they turned out to be similar, they were refined simultaneously. The SCXRD data of the Sr compound were used to identify all sites that are completely occupied by La atoms, which in addition was supported by BVS calculations (Tables D7, D8). These sites were then identified in the Ba containing compound and also assumed to be completely occupied by La atoms. Sites not fully occupied by La atoms were assumed to be mixed occupied with Sr and La. To determine whether these sites completely occupied by a mixture of both atoms, it was checked whether the corresponding sites in the Ba containing compound are fully occupied when refined as La atoms, since La and Ba exhibit almost the same scattering factor. This information, including possible vacancies, was again transferred to the Sr compound, for which then the mixed occupation was refined, and the obtained occupation was applied to the Ba compound and not further refined. Discrete non-tetrahedral anions were assigned as O in both compounds, while threefold bridging anions were set as N according to Pauling's rule.^[40] Terminal anions were assumed with a mixed O/N occupancy restoring charge neutrality, whereas twofold bridging anions were solely defined as N. During the refinement process, the results were continuously checked for plausibility based on BVS calculations, EDX data, *R*-values, residual electron density as well as cation-anion distances and adjusted if necessary to achieve charge neutrality. The structure refinement of type 2 is also supported by STEM-HAADF at atomic resolution viewed along special directions (Figure D7a–c). Z-contrast images along zone axis [100] showed similar heavy atom positions of the type 2 La/Ba and La/Sr oxonitridosilicates and suggest isotypic crystal structures (Figure D7c, d).

Important crystallographic data is given in Table 5.1. Atomic coordinates, isotropic displacement parameters, site occupancy factors (Table D9, D11, D13) as well as anisotropic displacement parameters (Table D10, D12, D14) for all three compounds are summarized in the Appendix.

5.1 Structure Elucidation of Complex Endotaxially Intergrown Barium Lanthanum Oxonitridosilicate Oxides by Combination of Microfocused Synchrotron Radiation and Transmission Electron Microscopy

Table 5.1. Crystallographic data of the single-crystal structure determinations of $\text{Ba}_{22.5+x}\text{La}_{55-x}[\text{Si}_{129}\text{N}_{240-x}\text{O}_x]\text{O}_3$ ($x \approx 0.24$), $\text{Ba}_{25.5+x}\text{La}_{77-x}[\text{Si}_{170}\text{N}_{312-x}\text{O}_{9+x}]\text{O}_4$ ($x \approx 0.24$) and $\text{Sr}_{28.5+x}\text{La}_{75-x}[\text{Si}_{170}\text{N}_{312-x}\text{O}_{9+x}]\text{O}_4$ ($x \approx -3.71$)

Formula	$\text{Ba}_{22.74}\text{La}_{54.84}[\text{Si}_{129}\text{N}_{240}]\text{O}_3$	$\text{Ba}_{25.79}\text{La}_{76.74}[\text{Si}_{170}\text{N}_{311.76}\text{O}_{9.24}]\text{O}_4$	$\text{Sr}_{24.79}\text{La}_{78.75}[\text{Si}_{170}\text{N}_{315.71}\text{O}_{5.24}]\text{O}_4$
formula mass / $\text{g}\cdot\text{mol}^{-1}$	17774.9	23556.8	22458.3
crystal system		hexagonal	
space group		$P\bar{6}$ (no. 174)	
lattice parameters	$a =$	17.480(1)	20.137(1)
	$c =$	22.687(2)	22.644(2)
$V / \text{\AA}^3$		6003.3(9)	7951.9(1)
Z		1	1
X-ray density / $\text{g}\cdot\text{cm}^{-3}$	4.916	4.919	4.758
abs. coefficient / $\mu\cdot\text{mm}^{-1}$	7.334	3.199	5.715
absorption correction		semiempirical	
temperature / K		294(2)	
radiation		synchrotron ($\lambda = 0.41325 \text{ \AA}$)	synchrotron ($\lambda = 0.2947 \text{ \AA}$)
$F(000)$	7909	10486.7	10095.1
θ range / $^\circ$	$1.56 \leq \theta \leq 16.44$	$2.08 \leq \theta \leq 17.17$	$1.49 \leq \theta \leq 12.15$
independent reflections	10726	16414	14855
refined parameters / restraints	520 / 0	677 / 299	461 / 299
$GooF (\chi^2)$	1.199	1.181	1.517
R_{int}	0.0823	0.0604	0.0866
R_σ	0.0700	0.0553	0.0678
$R1$ (all data / for $I > 2\sigma(I)$)	0.0469 / 0.0449	0.0415 / 0.0397	0.0860 / 0.0775
$wR2$ (all data / for $I > 2\sigma(I)$)	0.1102 / 0.1083	0.0956 / 0.0947	0.1785 / 0.1737

5.1.2.4 Structure Description

Both $\text{Ba}_{22.5+x}\text{La}_{55-x}[\text{Si}_{129}\text{N}_{240-x}\text{O}_x]\text{O}_3$, $\text{Ba}_{25.5+x}\text{La}_{77-x}[\text{Si}_{170}\text{N}_{312-x}\text{O}_{9+x}]\text{O}_4$ and $\text{Sr}_{28.5+x}\text{La}_{75-x}[\text{Si}_{170}\text{N}_{312-x}\text{O}_{9+x}]\text{O}_4$ crystallize in space group $P\bar{6}$ and show very similar crystal structures built up from vertex- and edge-sharing $[\text{Si}(\text{N},\text{O})_4]$ tetrahedra. The three-dimensional networks can formally be divided into two interconnected layers (Figure 5.3). The layer depicted in blue and red color in Figure 3 is present in all three compounds and consists of triple tetrahedral sharing one vertex (orange in Figure 5.4), which are aligned in one plane but tilted with respect to each other (Figure 5.4b) and interconnected according to the scheme shown in Figure 5.4a. Two adjacent triple tetrahedra units are connected *via* three vertices of single tetrahedra with inverted orientation in the same plane as well as by

tetrahedra (blue) connecting two tetrahedron vertices. Three of those tetrahedra are linked by another tetrahedron above the “missing” triple tetrahedra unit. This arrangement is mirrored (Figure 5.4b), and therefore forms *achter* ring cages.^[30] The cavity of those cages is filled by an unbound oxygen atom, which is coordinated by five La/Ba/Sr atoms in a distorted trigonal bipyramid (Figure 5.4c, red). This similar layer might be the reason for the intergrowth of $\text{Ba}_{22.5+x}\text{La}_{55-x}[\text{Si}_{129}\text{N}_{240-x}\text{O}_x]\text{O}_3$ and $\text{Ba}_{25.5+x}\text{La}_{77-x}[\text{Si}_{170}\text{N}_{312-x}\text{O}_{9+x}]\text{O}_4$ single crystallites.

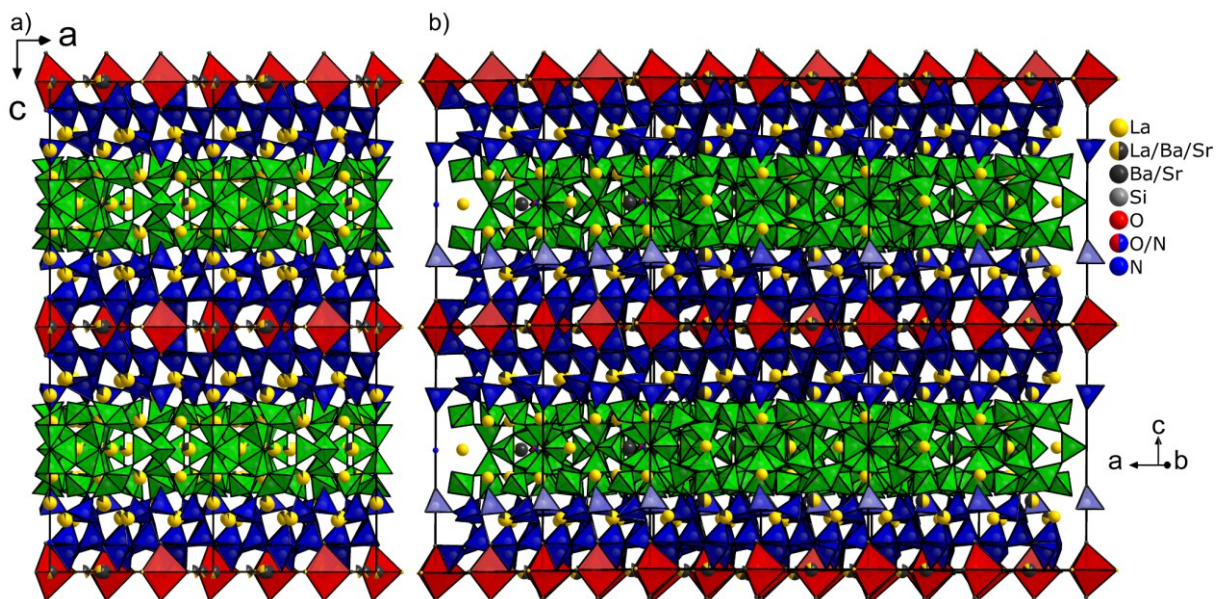


Figure 5.3. Crystal structures of (a) $\text{Ba}_{22.5+x}\text{La}_{55-x}[\text{Si}_{129}\text{N}_{240-x}\text{O}_x]\text{O}_3$ and (b) $\text{Ba}_{25.5+x}\text{La}_{77-x}[\text{Si}_{170}\text{N}_{312-x}\text{O}_{9+x}]\text{O}_4$ viewed along [010]. The structure of $\text{Ba}_{25.5+x}\text{La}_{77-x}[\text{Si}_{170}\text{N}_{312-x}\text{O}_{9+x}]\text{O}_4$ is homeotypic to $\text{Sr}_{28.5+x}\text{La}_{75-x}[\text{Si}_{170}\text{N}_{312-x}\text{O}_{9+x}]\text{O}_4$. $[\text{Si}(\text{N},\text{O})_4]$ tetrahedra in blue and green, $[\text{O}(\text{La},\text{Ba})_5]$ polyhedra in red; unit cell outlined in black.

5.1 Structure Elucidation of Complex Endotaxially Intergrown Barium Lanthanum Oxonitridosilicate Oxides by Combination of Microfocused Synchrotron Radiation and Transmission Electron Microscopy

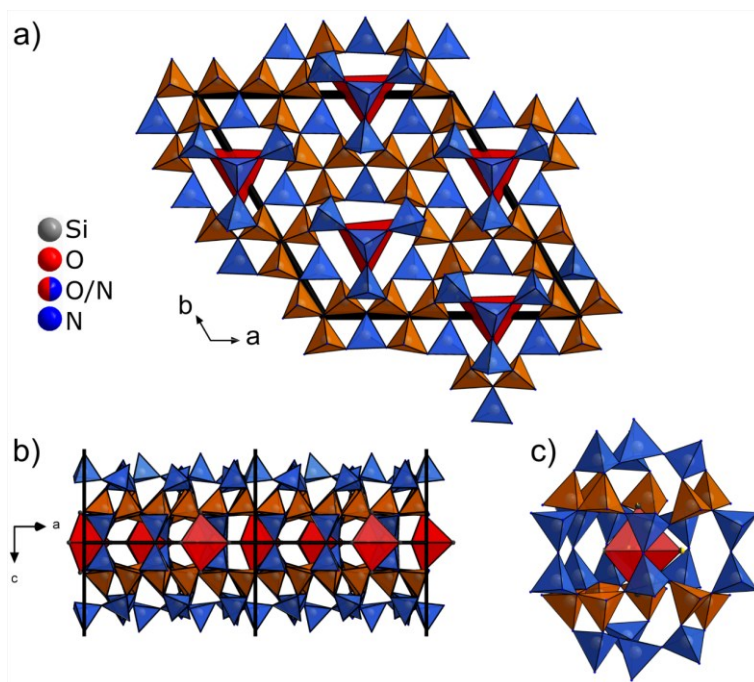


Figure 5.4. (a) Structure of the layer that occurs both in $\text{Ba}_{22.5+x}\text{La}_{55-x}[\text{Si}_{129}\text{N}_{240-x}\text{O}_x]\text{O}_3$ and $\text{Ba}_{25.5+x}\text{La}_{77-x}[\text{Si}_{170}\text{N}_{312-x}\text{O}_{9+x}]\text{O}_4$ (similar to $\text{Sr}_{28.5+x}\text{La}_{75-x}[\text{Si}_{170}\text{N}_{312-x}\text{O}_{9+x}]\text{O}_4$) viewed along [001]. (b) Same layer viewed along [010]. (c) cage of $[\text{Si}(\text{N},\text{O})_4]$ tetrahedra around an $[\text{O}(\text{La},\text{Ba})_5]$ trigonal bipyramid (red); $[\text{Si}(\text{N},\text{O})_4]$ tetrahedra in blue and orange; unit cell outlined in black.

The compounds differ with respect to the structure of the second layer (green layers in Figure 5.3), which is the same for $\text{Ba}_{25.5+x}\text{La}_{77-x}[\text{Si}_{170}\text{N}_{312-x}\text{O}_{9+x}]\text{O}_4$ and $\text{Sr}_{28.5+x}\text{La}_{75-x}[\text{Si}_{170}\text{N}_{312-x}\text{O}_{9+x}]\text{O}_4$ with the exception of the cation occupancies. In $\text{Ba}_{22.5+x}\text{La}_{55-x}[\text{Si}_{129}\text{N}_{240-x}\text{O}_x]\text{O}_3$, this layer consists of three different units (Figure 5.5).

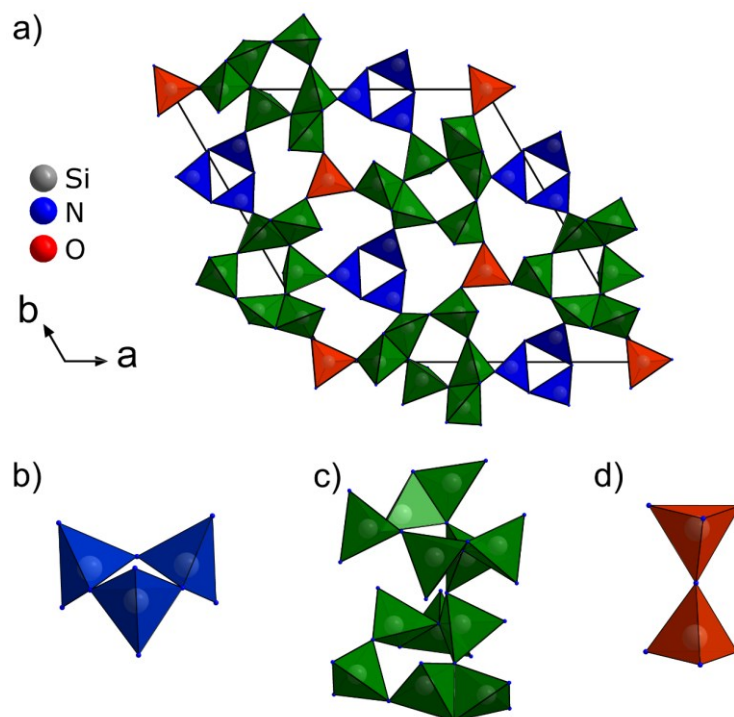


Figure 5.5. (a) Structure of the layer occurring in $\text{Ba}_{22.5+x}\text{La}_{55-x}[\text{Si}_{129}\text{N}_{240-x}\text{O}_x]\text{O}_3$ viewed along [001]. (b) *Dreier* ring unit. (c) Pair of *vierer* rings. (d) Pair of tetrahedra. $[\text{Si}(\text{N},\text{O})_4]$ tetrahedra in blue, green and red; unit cell outlined in black.

Three tetrahedra form a *dreier* ring (blue, Figure 5.5b), which interconnects three units built up from six tetrahedra each (darker green, Figure 5.5c) *via* shared corners. In this entity, two pairs of tetrahedra share a common edge and are interconnected by the remaining two tetrahedra *via* shared vertices, forming a branched *vierer* ring. Two of these units are linked *via* one shared vertex and mapped onto one another by a mirror plane. These units are again interconnected by pairs of tetrahedra (red, Figure 5.5d) around the mirror plane. A closely related, but different layer can be found in $\text{Ba}_{25.5+x}\text{La}_{77-x}[\text{Si}_{170}\text{N}_{312-x}\text{O}_{9+x}]\text{O}_4$ (Figure 5.6).

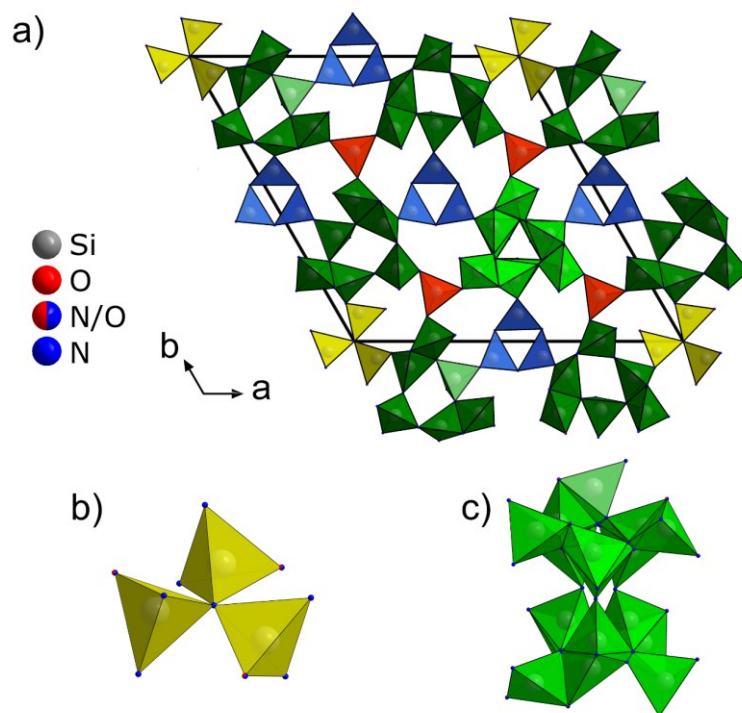


Figure 5.6. (a) Structure of the layer occurring in $\text{Ba}_{25.5+x}\text{La}_{77-x}[\text{Si}_{170}\text{N}_{312-x}\text{O}_{9+x}]\text{O}_4$ and $\text{Sr}_{28.5+x}\text{La}_{75-x}[\text{Si}_{170}\text{N}_{312-x}\text{O}_{9+x}]\text{O}_4$ viewed along [001]. (b) Triple tetrahedron unit. (c) Disordered unit. $[\text{Si}(\text{N},\text{O})_4]$ tetrahedra in blue, green and red; unit cell outlined in black.

One third of the blue *dreier* rings with only twofold bridging N is replaced by a triple tetrahedra unit (yellow, Figure 5.6b) with one threefold bridging, three terminal N/O and six twofold bridging N atoms in the same plane. Furthermore, one third of the branched *vierer* ring units (darker green), which are oriented differently, is replaced by a disordered unit (lighter green, Figure 5.6c) that is formed by superposition of three units, each of which is only occupied by one third, respectively. These units emerge from each other by a 120° rotation of one of the units along [001] (Figure 5.7).

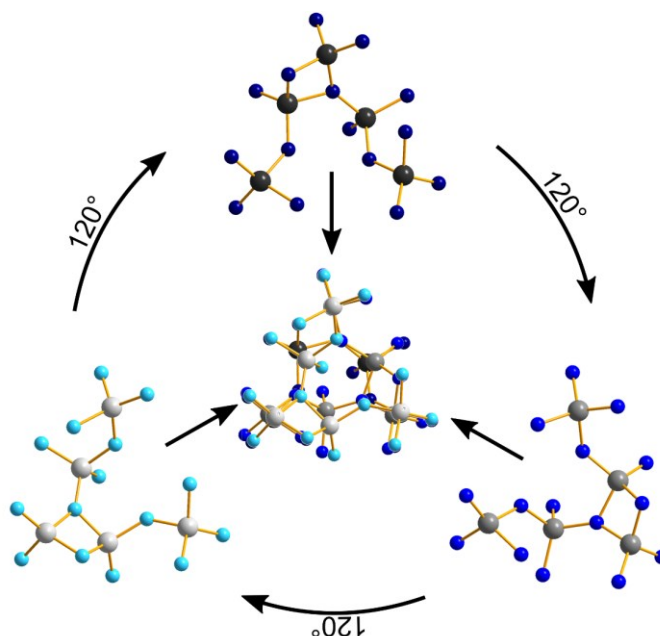


Figure 5.7. Schematic interpretation of the disordered unit resulting from the superposition of three entities linked by the threefold axis along [001]. Si atoms in shades of gray, N atoms in shades of blue. As a simplification, the sites with mixed O/N occupations were solely occupied by N.

The basic unit is built from five tetrahedra, of which two share an edge whereas the remaining ones share vertices. These units were identified by difference Fourier syntheses taking into account the underlying symmetry operations, respective. The superposition is due to the fact that the size of possibly ordered, lower symmetry domains is smaller than the X-ray's length of coherence. For all three compounds discussed, interatomic distances within the Si–N/O tetrahedra, O–La/Ba and O–La/Sr distances as well as the cation coordination polyhedra with the corresponding distances are listed in Tables D15–18 and agree well with those reported for other (oxo-)nitridosilicates.^[31–44]

5.1.2.5 Luminescence

Photoluminescence properties were measured on a Ce³⁺-doped (2 mol%) thick-bed powder sample containing both Ba_{22.5+x}La_{55-x}[Si₁₂₉N_{240-x}O_x]₃ and Ba_{25.5+x}La_{77-x}[Si₁₇₀N_{312-x}O_{9+x}]₄. The sample shows yellow luminescence upon irradiation with UV to blue light ($\lambda_{\text{exc}} = 440 \text{ nm}$) with an emission maximum at $\lambda_{\text{em}} \approx 588 \text{ nm}$ and a full width at half-maximum (*fwhm*) of about 166 nm/4541 cm⁻¹ (Figure 5.8).

5.1 Structure Elucidation of Complex Endotaxially Intergrown Barium Lanthanum Oxonitridosilicate Oxides by Combination of Microfocused Synchrotron Radiation and Transmission Electron Microscopy

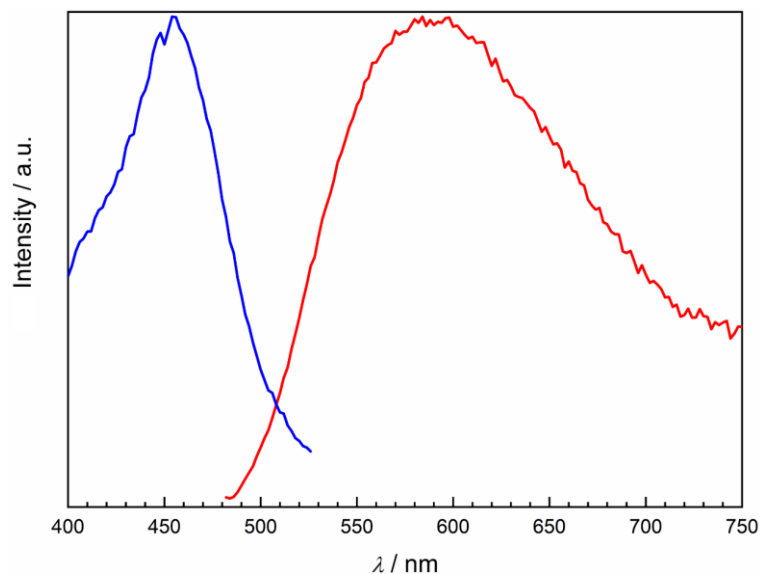


Figure 5.8. Normalized excitation (blue) and emission spectra (red, $\lambda_{\text{exc}} = 440 \text{ nm}$) of a sample containing $\text{Ba}_{22.5+x}\text{La}_{55-x}[\text{Si}_{129}\text{N}_{240-x}\text{O}_x]\text{O}_3:\text{Ce}^{3+}$ and $\text{Ba}_{25.5+x}\text{La}_{77-x}[\text{Si}_{170}\text{N}_{312-x}\text{O}_{9+x}]\text{O}_4:\text{Ce}^{3+}$.

The maximum intensity of the excitation spectrum is located approx. at 455 nm, so the material can be excited very well by blue light as emitted by a (Ga,In)N-LED. The luminescence probably originates from both compounds present in the sample. Comparison of the charges and ionic radii indicates that Ce^{3+} ($\text{CN} = 6-9$: 1.01–1.20 Å) preferably replaces La^{3+} ($\text{CN} = 6-9$: 1.03–1.22 Å) rather than the larger Ba^{2+} .^[45] The broadband emission of the $5d-4f$ transition of Ce^{3+} corresponds to a superposition of light emitted from various low-symmetrical and chemically different cation sites with surroundings of mixed N/O occupancy present in both compounds.^[46, 47] Comparison of the emission characteristics with other LED phosphor materials such as $\text{La}_3\text{BaSi}_5\text{N}_9\text{O}_2:\text{Ce}^{3+}$ ($\lambda_{\text{em}} \approx 578 \text{ nm}$, $\text{fwhm} \approx 167 \text{ nm}/4700 \text{ cm}^{-1}$, 12 cation sites),^[48] $\text{CaAlSi}_3\text{N}_3:\text{Ce}^{3+}$ ($\lambda_{\text{em}} \approx 570-603 \text{ nm}$, $\text{fwhm} \approx 150 \text{ nm}/3900 \text{ cm}^{-1}$, 1 cation site),^[49] $(\text{La,Ca})_3\text{Si}_6\text{N}_{11}:\text{Ce}^{3+}$ ($\lambda_{\text{em}} \approx 577-581 \text{ nm}$, $\text{fwhm} \approx 130-143 \text{ nm}/3760-3960 \text{ cm}^{-1}$, 2 cation sites)^[50] and $\text{Y}_3\text{Al}_5\text{O}_{12}:\text{Ce}^{3+}$ ($\lambda_{\text{em}} \approx 550-570 \text{ nm}$, $\text{fwhm} \approx 3700 \text{ cm}^{-1}$, 1 cation site)^[51] all with fewer cation sites than $\text{Ba}_{22.5+x}\text{La}_{55-x}[\text{Si}_{129}\text{N}_{240-x}\text{O}_x]\text{O}_3$ (21 cation sites) and $\text{Ba}_{25.5+x}\text{La}_{77-x}[\text{Si}_{170}\text{N}_{312-x}\text{O}_{9+x}]\text{O}_4$ (27 cation sites) shows that the observed emission of the latter compounds is not particularly broader despite the larger number of cation sites. Further investigations of the luminescence properties of single-phase materials would be required to clarify the influence of their slightly different structures on the individual luminescence properties.

5.1.3 Conclusion

$\text{Ba}_{22.5+x}\text{La}_{55-x}[\text{Si}_{129}\text{N}_{240-x}\text{O}_x]\text{O}_3$, $\text{Ba}_{25.5+x}\text{La}_{77-x}[\text{Si}_{170}\text{N}_{312-x}\text{O}_{9+x}]\text{O}_4$ and $\text{Sr}_{28.5+x}\text{La}_{75-x}[\text{Si}_{170}\text{N}_{312-x}\text{O}_{9+x}]\text{O}_4$ were obtained as microcrystallites through high-temperature solid-state reactions. Extensive TEM investigations enabled the discovery of endotaxially intergrown $\text{Ba}_{22.5+x}\text{La}_{55-x}[\text{Si}_{129}\text{N}_{240-x}\text{O}_x]\text{O}_3$ and $\text{Ba}_{25.5+x}\text{La}_{77-x}[\text{Si}_{170}\text{N}_{312-x}\text{O}_{9+x}]\text{O}_4$ domains. Single-crystalline fragments of each phase were identified by electron diffraction. Due to the small crystallite size, microfocused synchrotron radiation was essential for the collection of single-crystal data and thus the elucidation of the crystal structures, which was supported by BVS calculations and STEM imaging. As Sr and La can be distinguished by X-ray methods, the determination of the cation distribution in $\text{Ba}_{25.5+x}\text{La}_{77-x}[\text{Si}_{170}\text{N}_{312-x}\text{O}_{9+x}]\text{O}_4$ was substantially supported by the discovery of the analogous compound $\text{Sr}_{28.5+x}\text{La}_{75-x}[\text{Si}_{170}\text{N}_{312-x}\text{O}_{9+x}]\text{O}_4$. The two new structure types feature complex, rather similar silicate networks. The presence of similar layers explains the notorious intergrowth of $\text{Ba}_{22.5+x}\text{La}_{55-x}[\text{Si}_{129}\text{N}_{240-x}\text{O}_x]\text{O}_3$ and $\text{Ba}_{25.5+x}\text{La}_{77-x}[\text{Si}_{170}\text{N}_{312-x}\text{O}_{9+x}]\text{O}_4$. The difference between these is due to a second type of layer that is characteristic for each phase. A sample containing both compounds shows broad yellow luminescence upon doping with Ce^{3+} . Compared to phosphors with similar emission characteristics but fewer cation sites, the reported compounds do not show significantly broader emission. These compounds represent yet another example for a complex structure with interesting luminescence properties. Disorder does not have a negative effect on these properties, quite similar to the situation in $\text{Sr}_{1-x}\text{Ba}_x\text{Si}_2\text{O}_2\text{N}_2:\text{Eu}^{2+}$ phases.^[6,17,52–54] The elucidation of such complex crystal structures in microcrystalline samples with intergrown domains would not have been possible a few years ago because they rely on advances both concerning the development of TEM methods and focusing of the synchrotron beam. The search for new compounds will probably lead to more and more complex structures and therefore, in future research, microfocused synchrotron radiation assisted by TEM studies are expected to become an established tool that can provide high resolution data for accurate structure information even with smallest crystallites. Such data enable more precise statements about structure-property relations and may indicate how to optimally tune materials for required applications.

5.1 Structure Elucidation of Complex Endotaxially Intergrown Barium Lanthanum Oxonitridosilicate Oxides by Combination of Microfocused Synchrotron Radiation and Transmission Electron Microscopy

5.1.4 Experimental Part

5.1.4.1 Synthesis

Due to air and moisture sensitivity of some starting materials, all preparation steps were carried out under Ar-atmosphere either in an argon-filled glovebox (Unilab, MBraun, Garching; $O_2 < 1$ ppm; $H_2O < 1$ ppm) or in argon-filled glassware (Schlenk technique). For the synthesis of $Ba_{22.5+x}La_{55-x}[Si_{129}N_{240-x}O_x]O_3$ and $Ba_{25.5+x}La_{77-x}[Si_{170}N_{312-x}O_{9+x}]O_4$, a thoroughly ground mixture of 20.1 mg $La(NH_2)_3$ (0.108 mmol),^[55] 20.3 mg LaF_3 (0.104 mmol, Sigma-Aldrich, 99.99%), 66.3 mg BaH_2 (0.476 mmol, Chemco, 99.7%), 35.6 mg silicon diimide (0.613 mmol),^[56] and 0.8 mg CeF_3 as dopant (0.004 mmol, 2 mol%, Sigma-Aldrich, 99.99%) was filled into a tungsten crucible, which was then transferred into the water-cooled silica glass reactor of a radiofrequency furnace (AXIO 10/450, max. output 10 kW, Hüttinger Elektronik, Freiburg) attached to a Schlenk line. H_2O may be present due to partial hydrolysis of the starting materials, especially amides and imides. The crucible was heated under N_2 -atmosphere to 1600 °C within one hour.^[57] After maintaining the temperature for 10 h, the crucible was slowly cooled to 900 °C within 44 h. The product was finally quenched by switching off the furnace. The orange Ce-doped microcrystalline powder shows yellow luminescence under irradiation with UV to blue light. $Sr_{28.5+x}La_{75-x}[Si_{170}N_{312-x}O_{9+x}]O_4$ was synthesized starting from 20.1 mg $La(NH_2)_3$ (0.108 mmol),^[55] 20.3 mg LaF_3 (0.104 mmol, Sigma-Aldrich, 99.99%), 42.7 mg SrH_2 (0.476 mmol), 35.6 mg silicon diimide (0.613 mmol),^[56] H_2O due to partial hydrolysis and 0.8 mg CeF_3 (0.004 mmol, 2 mol%, Sigma-Aldrich, 99.99%) applying the same temperature program. This also led to an orange microcrystalline powder. All products are insensitive against oxygen and H_2O .

5.1.4.2 Transmission Electron Microscopy

For investigations using transmission electron microscopy, the polycrystalline samples were crushed, dispersed in absolute ethanol and drop-cast on carbon-film-coated copper grids, which were then fixed on double-tilt low-background holders. For STEM, SAED and EDX measurements, a Titan 80–300 (FEI, USA) with a field emission gun (FEG) operated at 300 kV and equipped with a TOPS 30 EDX spectrometer (EDAX, Germany), an UltraScan 1000 camera (Gatan, USA, resolution: 2k×2k) as well as a Titan Themis 60-300 (FEI, USA) with a cold FEG operated at 300 kV acceleration voltage equipped with a X-FEG emitter, monochromator, C_s corrector and windowless four-quadrant Super-X EDX detector were used. In the latter setup, images were acquired using a Ceta CMOS camera (FEI, USA) with a resolution of 4k×4k. High resolution transmission electron microscopy (HRTEM) and SAED data were evaluated using the programs Digital Micrograph (e.g. for Fourier filtering of the HRTEM images) and JEMS for SAED simulations.^[58, 59] EDX data were processed with ES Vision.^[60]

5.1.4.3 Single-Crystal X-ray Diffraction

Single-crystal X-ray diffraction (SCXRD) data of $\text{Ba}_{22.5+x}\text{La}_{55-x}[\text{Si}_{129}\text{N}_{240-x}\text{O}_x]\text{O}_3$, $\text{Ba}_{25.5+x}\text{La}_{77-x}[\text{Si}_{170}\text{N}_{312-x}\text{O}_{9+x}]\text{O}_4$ and $\text{Sr}_{28.5+x}\text{La}_{75-x}[\text{Si}_{170}\text{N}_{312-x}\text{O}_{9+x}]\text{O}_4$ were collected at beamline ID11 of the ESRF in Grenoble, France (Ge(111) double-crystal monochromator, Frelon4K CCD detector).^[61] Suitable single crystallites had previously been identified by SAED and TEM-EDX. The crystallites on TEM grids were centered in the synchrotron beam by a large-magnification telescope and using X-ray fluorescence linescans for La as described in literature.^[11] The beam was microfocused with a Be/Al refractive lens system.^[13–16] Diffraction data were evaluated with the CrysAlis program suite.^[62] Scaling and semi-empirical absorption correction were performed with SADABS and structure solution and refinement with SHELX-2014.^[63, 64] In order to account for the systematic error owing to the diffraction-angle dependence of the beam path through the CCD phosphor, a beam-incidence correction was applied.^[65] Deposition numbers CSD-1958352 (for $\text{Ba}_{22.5+x}\text{La}_{55-x}[\text{Si}_{129}\text{N}_{240-x}\text{O}_x]\text{O}_3$, $x \approx 0.24$), CSD-1958355 (for $\text{Ba}_{25.5+x}\text{La}_{77-x}[\text{Si}_{170}\text{N}_{312-x}\text{O}_{9+x}]\text{O}_4$, $x \approx 0.24$) and CSD-1864686 (for $\text{Sr}_{28.5+x}\text{La}_{75-x}[\text{Si}_{170}\text{N}_{312-x}\text{O}_{9+x}]\text{O}_4$, $x \approx -3.71$) contain the supplementary crystallographic data for this paper. These data are provided free of charge by the joint Cambridge Crystallographic Data Centre and Fachinformationszentrum Karlsruhe Access Structures service (<http://www.ccdc.cam.ac.uk/structures>).

5.1.4.4 Powder X-ray Diffraction

Powder X-ray diffraction (PXRD) data were obtained from finely ground samples sealed into glass capillaries (0.2 mm diameter, wall thickness 0.01 mm; Hilgenberg GmbH, Malsfeld, Germany) using a Stoe StadiP diffractometer (Mo- $K\alpha_1$ radiation, $\lambda = 0.70930 \text{ \AA}$, Stoe & Cie, Darmstadt, Germany) equipped with an Ge(111) monochromator and a Mythen1K detector (Dectris, Baden-Dättwil, Switzerland) in parafocusing modified Debye-Scherrer geometry. Rietveld refinements based on the collected data were performed using the TOPAS Academic V6 package applying the fundamental parameters approach (direct convolution of source emission profiles, axial instrument contributions, crystallite size and microstrain effects).^[66–68] Corrections of the absorption effects were performed using the calculated absorption coefficient. Preferred orientation was modelled using spherical harmonics of fourth order. The structure models obtained from single-crystal synchrotron X-ray diffraction data were used as a starting point for all refinements, in which only lattice parameters were refined, while atomic coordinates, site occupations and isotropic displacement parameters were kept fixed.

5.1 Structure Elucidation of Complex Endotaxially Intergrown Barium Lanthanum Oxonitridosilicate Oxides by Combination of Microfocused Synchrotron Radiation and Transmission Electron Microscopy

5.1.4.5 IR Spectroscopy

Fourier transform infrared (FTIR) spectra were recorded with a BXII spectrometer (PerkinElmer, Rodgau, Germany) mounting ATR (attenuated total reflection) technology.

5.1.4.6 Luminescence

Photoluminescence properties of microcrystalline $\text{Ba}_{22.5+x}\text{La}_{55-x}[\text{Si}_{129}\text{N}_{240-x}\text{O}_x]\text{O}_3$ and $\text{Ba}_{25.5+x}\text{La}_{77-x}[\text{Si}_{170}\text{N}_{312-x}\text{O}_{9+x}]\text{O}_4$ powder samples were measured in PTFE sample holders using an in-house built system based on a 5.3" integrating sphere and a spectrofluorimeter equipped with a 150 W Xe lamp, two 500 mm Czerny-Turner monochromators, 1800 1/mm lattices and 250/500 nm lamps with a spectral range from 230 to 820 nm.

5.1.5 Acknowledgements

The European Synchrotron Radiation Facility (ESRF, Grenoble, France) is acknowledged for granting beamtime (projects CH-4318 and CH-4612) and travel support. The authors thank Petra Huppertz, Detlef Wiechert, and Volker Weiler (all at Lumileds Phosphor Center, Aachen, Germany) for luminescence measurements. Dr. Vadim Dyadkin (ESRF, Grenoble, France), Dr. Felix Fahrnbauer, Dr. Stefan Schwarzmüller, Dr. Markus Nentwig and Dr. Frank Heinke (all at Leipzig University) are acknowledged for help with the synchrotron measurements. Inspiring discussions with Dr. Christian Maak (Department of Chemistry, LMU) are gratefully appreciated.

5.1.6 References

- [1] a) R. Mueller-Mach, G. O. Mueller, M. R. Krames, O. B. Shchekin, P. J. Schmidt, H. Bechtel, C.-H. Chen, O. Steigelmann, *Phys. Status Solidi RRL* **2009**, 3, 215–217; b) PB62 LUXEON Rebel Phosphor-Converted Amber Product Brief. Lumileds Holding B.V. **2009**; c) PB109 LUXEON F PC Amber Product Brief. Lumileds Holding B.V. **2018**.
- [2] M. Zeuner, S. Pagano, W. Schnick, *Angew. Chem. Int. Ed.* **2011**, 50, 7754–7775; *Angew. Chem.* **2011**, 123, 7898–7920.
- [3] H. A. Höpfe, H. Lutz, P. Morys, W. Schnick, A. Seilmeier, *J. Phys. Chem. Solids* **2000**, 61, 2001–2006.
- [4] H. A. Höpfe, F. Stadler, O. Oeckler, W. Schnick, *Angew. Chem. Int. Ed.* **2004**, 43, 5540–5542; *Angew. Chem.* **2004**, 116, 5656–5658.
- [5] J. A. Kechele, O. Oeckler, F. Stadler, W. Schnick, *Solid State Sci.* **2009**, 11, 537–543.
- [6] R. Müller-Mach, G. Müller, M. R. Krames, H. A. Höpfe, F. Stadler, W. Schnick, T. Jüstel, P. Schmidt, *Phys. Status Solidi A* **2005**, 202, 1727–1732.
- [7] H. Höpfe, *Angew. Chem. Int. Ed.* **2009**, 48, 3572–3582; *Angew. Chem.* **2009**, 121, 3626–3636.
- [8] P. Pust, P. J. Schmidt, W. Schnick, *Nat. Mater.* **2015**, 14, 454–458.

- [9] S. Lupart, G. Gregori, J. Maier, W. Schnick, *J. Am. Chem. Soc.* **2012**, *134*, 10132–10137.
- [10] D. Durach, P. Schultz, O. Oeckler, W. Schnick, *Inorg. Chem.* **2016**, *55*, 3624–3629.
- [11] F. Fahrnbauer, T. Rosenthal, T. Schmutzler, G. Wagner, G. B. M. Vaughan, J. P. Wright, O. Oeckler, *Angew. Chem. Int. Ed.* **2015**, *54*, 10020–10023; *Angew. Chem.* **2015**, *127*, 10158–10161.
- [12] S. D. Kloß, L. Neudert, M. Döblinger, M. Nentwig, O. Oeckler, W. Schnick, *J. Am. Chem. Soc.* **2017**, *139*, 12724–12735.
- [13] G. B. M. Vaughan, J. P. Wright, A. Bytchkov, C. Curfs, C. Grundlach, M. Orlova, L. Erra, H. Gleyzolle, T. Buslaps, A. Götz, G. Suchet, S. Petitdemange, M. Rossat, L. Margulies, W. Ludwig, A. Snigirey, I. Snigireva, H. O. Sorensen, E. M. Lauridsen, U. L. Olsen, J. Oddershede, H. F. Poulsen, *Challenges in Materials Science Possibilities in 3D and 4D Characterization Techniques: Proceedings of the 31st Risø International Symposium on Materials Science*; Technical University of Denmark, Lyngby, Denmark, **2010**, 457–476.
- [14] G. B. M. Vaughan, J. P. Wright, A. Bytchkov, M. Rossat, H. Gleyzolle, I. Snigireva, A. Snigirev, *J. Synchrotron Radiat.* **2011**, *18*, 125–133.
- [15] B. Lengeler, C. Schroer, J. Tümmeler, B. Benner, M. Richwin, A. Snigirev, I. Snigireva, M. Drakopoulos, *J. Synchrotron Radiat.* **1999**, *6*, 1153–1167.
- [16] B. Lengeler, C. G. Schroer, B. Benner, A. Gerhardus, T. F. Günzler, M. Kuhlmann, J. Meyer, C. Zimprich, *J. Synchrotron Radiat.* **2002**, *9*, 119–124.
- [17] X.-J. Wang, L. Wang, T. Takeda, S. Funahashi, T. Suehiro, N. Hirosaki, R.-J. Xie, *Chem. Mater.* **2015**, *27*, 7689–7697.
- [18] N. Hirosaki, T. Takeda, S. Funahashi, R.-J. Xie, *Chem. Mater.* **2014**, *26*, 4280–4288.
- [19] M. Seibald, T. Rosenthal, O. Oeckler, W. Schnick, *Crit. Rev. Solid State Mater. Sci.* **2014**, *39*, 215–229.
- [20] C. Maak, D. Durach, C. Martiny, P. J. Schmidt, W. Schnick, *Chem. Mater.* **2018**, *30*, 3552–3558.
- [21] D. Durach, W. Schnick, *Z. Anorg. Allg. Chem.* **2016**, *642*, 101–106.
- [22] A. S. Wills, *VaList*, v. 4.0.7, University College London, UK, **2010**.
- [23] N. E. Brese, M. O’Keeffe, *Acta Crystallogr. Sect. B* **1991**, *47*, 192–197.
- [24] I. D. Brown, D. Altermatt, *Acta Crystallogr. Sect. B* **1985**, *41*, 244–247.
- [25] D. Durach, W. Schnick, *Eur. J. Inorg. Chem.* **2015**, *24*, 4095–4100.
- [26] L. Neudert, D. Durach, F. Fahrnbauer, G. B. M. Vaughan, W. Schnick, O. Oeckler, *Inorg. Chem.* **2017**, *56*, 13070–13077.
- [27] P. E. D. Morgan, *J. Mater. Sci.* **1986**, *21*, 4305–4309.

5.1 Structure Elucidation of Complex Endotaxially Intergrown Barium Lanthanum Oxonitridosilicate Oxides by Combination of Microfocused Synchrotron Radiation and Transmission Electron Microscopy

- [28] N. Garg, K. K. Pandey, C. Murli, K. V. Shanavas, B. P. Mandal, A. K. Tyagi, S. M. Sharma, *Phys. Rev. B* **2008**, *77*, 214105, 1–8.
- [29] S. B. Schneider, D. Baumann, A. Salamat, W. Schnick, *J. Appl. Phys.* **2012**, *111*, 093503, 1–6.
- [30] The term *dreier* (*vierer*, *achter*) ring was established by F. Liebau and is derived from the German word “dreier” (“vierer”, “achter”). A *dreier* (*vierer*, *achter*) ring comprises three (four, eight) tetrahedra centers. F. Liebau, *Structural Chemistry of Silicates*, Springer, Berlin, **1985**.
- [31] H. Yamane, F. J. DiSalvo, *J. Alloys Compd.* **1996**, *240*, 33–36.
- [32] Z. A. Gal, P. R. Mallinson, H. J. Orchard, S. J. Clarke, *Inorg. Chem.* **2004**, *43*, 3998–4006.
- [33] D. Wilhelm, M. Seibald, D. Baumann, K. Wurst, H. Huppertz, *Eur. J. Inorg. Chem.* **2018**, *2018*, 731–738.
- [34] C. Maak, L. Eisenburger, J. P. Wright, M. Nentwig, P. J. Schmidt, O. Oeckler, W. Schnick, *Inorg. Chem.* **2018**, *57*, 13840–13846.
- [35] Z. Inoue, T. Sawada, K. Ohsumi, M. Mitomo, R. Sadanaga, *Acta Crystallogr. Sect. A* **1981**, *37*, C154.
- [36] M. Woike, W. Jeitschko, *Inorg. Chem.* **1995**, *34*, 5105–5108.
- [37] K. Liddell, D. P. Thompson, *J. Mater. Chem.* **2001**, *11*, 507–512.
- [38] H. Müller-Bunz, T. Schleid, *Z. Anorg. Allg. Chem.* **2000**, *626*, 2549–2556.
- [39] M. Abed, H. K. Müller-Buschbaum, *J. Alloys Compd.* **1992**, *190*, 61–64.
- [40] K.-I. Machida, G.-Y. Adachi, J. Shiokawa, M. Shimada, M. Koizumi, *Acta Crystallogr. Sect. B* **1982**, *38*, 386–389.
- [41] C. Schmolke, D. Bichler, D. Johrendt, W. Schnick, *Solid State Sci.* **2009**, *11*, 389–394.
- [42] C. Schmolke, S. Lupart, W. Schnick, *Solid State Sci.* **2009**, *11*, 305–309.
- [43] T. Schlieper, W. Milius, W. Schnick, *Z. Anorg. Allg. Chem.* **1995**, *621*, 1380–1384.
- [44] H. Huppertz, W. Schnick, *Z. Anorg. Allg. Chem.* **1997**, *623*, 212–217.
- [45] R. D. Shannon, *Acta Crystallogr. Sect. A* **1976**, *32*, 751–767.
- [46] A. Meijerink, G. Blasse, *J. Lumin.* **1989**, *43*, 283–289.
- [47] G. Blasse, B. C. Grabmaier, *Luminescent Materials*, Springer, Berlin, Heidelberg, NY, **1994**.
- [48] D. Durach, L. Neudert, P. J. Schmidt, O. Oeckler, W. Schnick, *Chem. Mater.* **2015**, *27*, 4832–4838.
- [49] Y. Q. Li, N. Hirosaki, R.-J. Xie, T. Takeda, M. Mitomo, *Chem. Mater.* **2008**, *20*, 6704–6714.
- [50] T. Suehiro, N. Hirosaki, R.-J. Xie, *ACS Appl. Mater. Interfaces* **2011**, *3*, 811–816.

- [51] T. Moriguchi, Y. Noguchi, K. Sakanao, Y. Shimizu, US 5998925 A, **1997**.
- [52] M. Seibald, T. Rosenthal, O. Oeckler, F. Fahrnbauer, A. Tücks, P. J. Schmidt, W. Schnick, *Chem. Eur. J.* **2012**, *18*, 13446–13452.
- [53] M. Seibald, O. Oeckler, V. R. Celinski, P. J. Schmidt, A. Tücks, W. Schnick, *Solid State Sci.* **2011**, *13*, 1769–1778.
- [54] M. Seibald, T. Rosenthal, O. Oeckler, C. Maak, A. Tücks, P. J. Schmidt, D. Wiechert, W. Schnick, *Chem. Mater.* **2013**, *25*, 1852–1857.
- [55] C. Hadenfeldt, B. Gieger, H. Jacobs, *Z. Anorg. Allg. Chem.* **1974**, *410*, 104–112.
- [56] H. Lange, G. Wötting, G. Winter, *Angew. Chem. Int. Ed.* **1991**, *30*, 1579–1597; *Angew. Chem.* **1991**, *103*, 1606–1625.
- [57] W. Schnick, H. Huppertz, R. Lauterbach, *J. Mater. Chem.* **1999**, *9*, 289–296.
- [58] *Digital Micrograph v3.6.1*, Gatan Software Team, Pleasanton, USA, **1999**.
- [59] a) P. A. Stadelmann, *Ultramicroscopy* **1987**, *21*, 131–145; b) P. A. Stadelmann, *JEMS v3.3425U2008*, CIME-EPFL, Switzerland, **1999–2008**.
- [60] *ES Vision v4.0.164*, Emispec Systems Inc., Tempe, USA, **1994–2002**.
- [61] J. C. Labiche, O. Mathon, S. Pascarelli, M. A. Newton, G. G. Ferre, C. Curfs, G. Vaughan, A. Homs, D. F. Carreiras, *Rev. Sci. Instrum.* **2007**, *78*, 091301, 1–11.
- [62] *CrysAlisPro 1.171.38.41*, Rigaku Oxford Diffraction, **2015**.
- [63] G. M. Sheldrick, *SADABS, v. 2: Multi-Scan Absorption Correction*; Bruker-AXS, Billerica, MA, **2012**.
- [64] G. M. Sheldrick, *Acta Crystallogr. Sect. C.* **2015**, *71*, 3–8.
- [65] G. Wu, B. L. Rodrigues, P. Coppens, *J. Appl. Crystallogr.* **2002**, *35*, 356–359.
- [66] A. A. Coelho, *TOPAS Version 6: A program for Rietveld refinement*, Coelho Software **2016**.
- [67] J. Bergmann, R. Kleeberg, A. Haase, B. Breidenstein, *Mater. Sci. Forum* **2000**, 347–349, 303–308.
- [68] R. W. Cheary, A. A. Coelho, J. P. Cline, *J. Res. Natl. Inst. Stand. Technol.* **2004**, *109*, 1–25.

5.2 Unpublished Results

5.2.1 Introduction

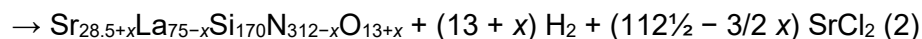
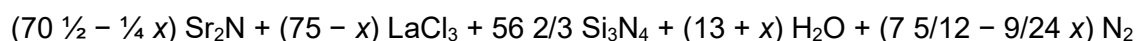
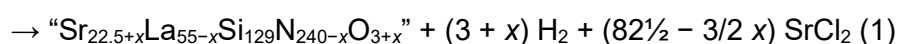
Based on the results presented in the aforementioned chapter, additional experiments were conducted to synthesize the missing Sr analogue to $\text{Ba}_{22.5+x}\text{La}_{55-x}[\text{Si}_{129}\text{N}_{240-x}\text{O}_x]\text{O}_3$ ($x \approx 0.24$) and to perform luminescence measurements of Eu^{2+} doped samples. Upon irradiation with UV to blue light ($\lambda_{\text{exc}} = 440 \text{ nm}$), Ce^{3+} doped $\text{Ba}_{22.5+x}\text{La}_{55-x}[\text{Si}_{129}\text{N}_{240-x}\text{O}_x]\text{O}_3$ ($x \approx 0.24$) and $\text{Ba}_{25.5+x}\text{La}_{77-x}[\text{Si}_{170}\text{N}_{312-x}\text{O}_{9+x}]\text{O}_4$ ($x \approx 0.24$) exhibit broad yellow luminescence with $\lambda_{\text{em}} = 588 \text{ nm}$ and $\text{fwhm} = 166 \text{ nm}/4541 \text{ cm}^{-1}$. It is assumed that luminescence originates from both given compounds. Since emission properties are influenced by the host surrounding the activator site, it could not be stated whether the broadband emission solely originates from the intrinsic broadened Ce^{3+} luminescence due to the split $4f^1$ ground state into the two ${}^2F_{5/2}$ and ${}^2F_{7/2}$ levels separated by approx. 2000 cm^{-1} or is additionally broadened by the highly complex structural environment of the activator ion.^[1] Current LED research on narrow-band red emitting phosphors is focused on host lattices offering highly condensed anionic networks with cation ordering and few, ideally only one, highly symmetric crystallographic activator sites with roughly identical activator-ligand distances.^[2] Eu^{2+} is frequently used in narrow-band emitting phosphors since its emission band is commonly narrower than of Ce^{3+} . These prerequisites are not fulfilled by $\text{Ba}_{22.5+x}\text{La}_{55-x}[\text{Si}_{129}\text{N}_{240-x}\text{O}_x]\text{O}_3$ ($x \approx 0.24$) or $\text{Ba}_{25.5+x}\text{La}_{77-x}[\text{Si}_{170}\text{N}_{312-x}\text{O}_{9+x}]\text{O}_4$ ($x \approx 0.24$). However, comparison with other Ce^{3+} -doped phosphors show that the emission band is not significantly broader although $\text{Ba}_{22.5+x}\text{La}_{55-x}[\text{Si}_{129}\text{N}_{240-x}\text{O}_x]\text{O}_3$ ($x \approx 0.24$) and $\text{Ba}_{25.5+x}\text{La}_{77-x}[\text{Si}_{170}\text{N}_{312-x}\text{O}_{9+x}]\text{O}_4$ ($x \approx 0.24$) consist of highly complex structures. Therefore, luminescence of Eu^{2+} doped samples are interesting for studying the influence of the host lattice on the emission properties. Herein, it was shown that narrow-band luminescence does not necessarily require few highly symmetric crystallographic activator sites or cation ordering, but other factors like e.g., a highly condensed network, can also have a major influence on luminescence properties and lead to narrow-band emission.

5.2.2 Results and Discussion

5.2.2.1 Synthesis and Chemical Analysis

A mixture of $\text{Sr}_{28.5+x}\text{La}_{75-x}[\text{Si}_{170}\text{N}_{312-x}\text{O}_{9+x}]\text{O}_4$ ($x \approx -3.71$) presented in the previous chapter and the Sr analogue to $\text{Ba}_{22.5+x}\text{La}_{55-x}[\text{Si}_{129}\text{N}_{240-x}\text{O}_x]\text{O}_3$ ($x \approx 0.24$, denoted as “ $\text{Sr}_{22.5+x}\text{La}_{55-x}[\text{Si}_{129}\text{N}_{240-x}\text{O}_x]\text{O}_3$ ”) was synthesized according to the following idealized reaction equations resulting in an orange powder with orange-red luminescence upon irradiation with UV to blue light.

5.2 Unpublished Results



Sr_2N was synthesized according to the Experimental Section resulting in a black powder (Figure D8, Table D19). A Sr_2N excess was required owing to the decomposition of Sr_2N at higher temperatures and reposition on the cold reactor wall. The phase composition of the orange powder was determined by Rietveld refinement based on powder X-ray diffraction (PXRD) data using the aforementioned structure models of $\text{Ba}_{22.5+x}\text{La}_{55-x}[\text{Si}_{129}\text{N}_{240-x}\text{O}_x]\text{O}_3$ ($x \approx 0.24$), for which Ba was substituted by Sr, and $\text{Sr}_{28.5+x}\text{La}_{75-x}[\text{Si}_{170}\text{N}_{312-x}\text{O}_{9+x}]\text{O}_4$ ($x \approx -3.71$) as starting points, wherein only lattice parameters and the fractional coordinates of the respective heavy cation sites were refined (Figure 5.9, Table D20).

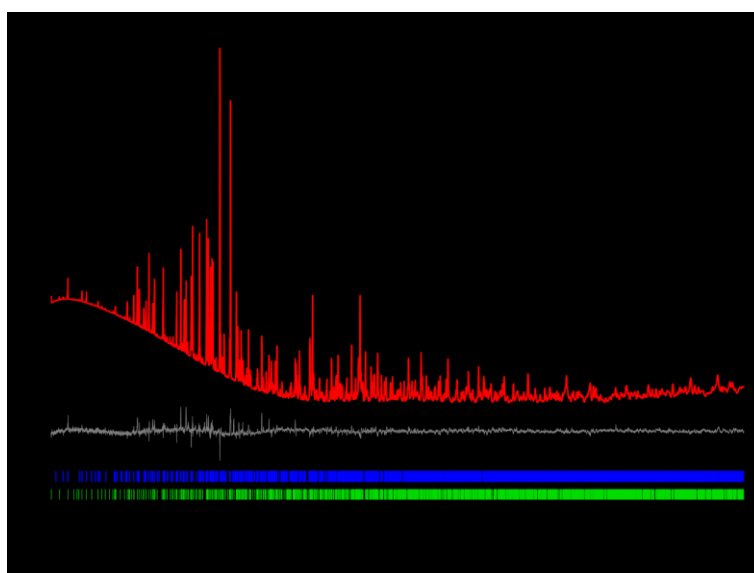


Figure 5.9. Rietveld refinement based on PXRD data collected from a sample containing “ $\text{Sr}_{22.5+x}\text{La}_{55-x}[\text{Si}_{129}\text{N}_{240-x}\text{O}_x]\text{O}_3$ ” ($x \approx 0.24$, corresponding to $\text{Ba}_{22.5+x}\text{La}_{55-x}[\text{Si}_{129}\text{N}_{240-x}\text{O}_x]\text{O}_3$, in which Ba was substituted by Sr, approx. 24 wt%) and $\text{Sr}_{28.5+x}\text{La}_{75-x}[\text{Si}_{170}\text{N}_{312-x}\text{O}_{9+x}]\text{O}_4$ ($x \approx -3.71$, approx. 76 wt%) based on the reported structure models. Observed (black) and calculated (red) powder X-ray diffraction patterns with corresponding difference profile (gray). Vertical blue or green bars indicate the position of the Bragg reflections of “ $\text{Sr}_{22.5+x}\text{La}_{55-x}[\text{Si}_{129}\text{N}_{240-x}\text{O}_x]\text{O}_3$ ” ($x \approx 0.24$) and $\text{Sr}_{28.5+x}\text{La}_{75-x}[\text{Si}_{170}\text{N}_{312-x}\text{O}_{9+x}]\text{O}_4$ ($x \approx -3.71$), respectively.

An extract ($2\theta = 20\text{--}40^\circ$) from the Rietveld refinement shows, that except two unidentified reflections and fitting difficulties, which cause the difference profile, all reflections can be described by the two phases (Figure D9). Since both crystal structures and therefore, the reflection profiles, are very similar, the exact phase fractions cannot be determined reliably.

Rietveld refinements based on only one of the two phases at a time reveal that each single calculation fit well with the measurements, proving that both phases are present (Figure D10, Table D21 and D22). Despite suggested by idealized reaction equations, no SrCl₂ was found in the PXRD during Rietveld refinement. Reactions at high temperatures can lead to transport reactions, in which binary halides can deposit on the inside wall of the water-cooled silica glass reactor of the radiofrequency furnace.^[3] The averaged atomic ratio of the powder sample containing both phases was determined using SEM-EDX (Figure D11) measurements and resulted in a Sr:La:Si:N:O ratio of approx. 5(1):11(1):27(2):52(2):5(1), which is in good agreement with the theoretical values (Table D23). The slightly higher values for O result from superficially bound oxygen on the crystals. Though Eu could not be identified by EDX due to the small amounts, its presence is demonstrated by the observed luminescence. Hence, Eu was subsequently neglected in the structure refinements.

5.2.2.2 Crystal Structure Elucidation and Description

As depicted in the previous chapter, despite variation of starting materials and synthesis conditions, no phase-pure bulk synthesis of the individual compounds was possible due to very similar crystal structures and thus resulting in intergrowth. It was possible to prepare a single crystal of “Sr_{22.5+x}La_{55-x}[Si₁₂₉N_{240-x}O_x]O₃” ($x \approx 0.24$), which had previously not been synthesized, for collecting single-crystal X-ray diffraction data. Initial elucidation results in space group $P\bar{6}$ (no. 174) with $a = 17.4055(5)$, $c = 22.4642(7)$ Å and $Z = 1$ showing the similarity to Ba_{22.5+x}La_{55-x}[Si₁₂₉N_{240-x}O_x]O₃ ($x \approx 0.24$), which also crystallizes in space group $P\bar{6}$ (no. 174) with $a = 17.480(1)$, $c = 22.687(2)$ Å and $Z = 1$, but exhibits minor differences in structural motifs. However, crystal structure determination could not be finalized yet due to the crystallographic challenges known from the analogous Ba_{22.5+x}La_{55-x}[Si₁₂₉N_{240-x}O_x]O₃ ($x \approx 0.24$) compound like mixed and under-occupied heavy cation sites and notorious intergrowth with other domains (Chapters 5.1.2.2 and 5.1.2.3), of which the latter can be seen by comparing the corresponding reciprocal lattice sections (Figure D12). Since the Rietveld refinement based on PXRD data resulted in a stable refinement with reasonable R values, it can be assumed that “Sr_{22.5+x}La_{55-x}[Si₁₂₉N_{240-x}O_x]O₃” ($x \approx 0.24$) crystallizes in similar manner or at least very closely related to the crystal structure described in Chapter 5.1.2.4.

5.2.2.3 UV/Vis reflectance spectroscopy

UV/Vis spectroscopy was used to determine the optical band gap of nondoped “Sr_{22.5+x}La_{55-x}[Si₁₂₉N_{240-x}O_x]O₃” ($x \approx 0.24$) and Sr_{28.5+x}La_{75-x}[Si₁₇₀N_{312-x}O_{9+x}]O₄ ($x \approx -3.71$), for which the Kubelka–Munk function $F(R) = (1-R)^2/2R$ ($R =$ measured reflectance) was applied to transform the measured diffuse reflectance spectrum into a pseudo-absorption spectrum.^[4] A Tauc plot was used to determine the optical band gap by plotting $h\nu$ against

5.2 Unpublished Results

$(F(R) \cdot h\nu)^{1/n}$ with $n = 1/2$ for a direct allowed transition and intersecting the aligned tangent on the linear region with the abscissa.^[5] Applying this procedure, the optical band gap was estimated to be approx. 3.5 eV (Figure 5.10).

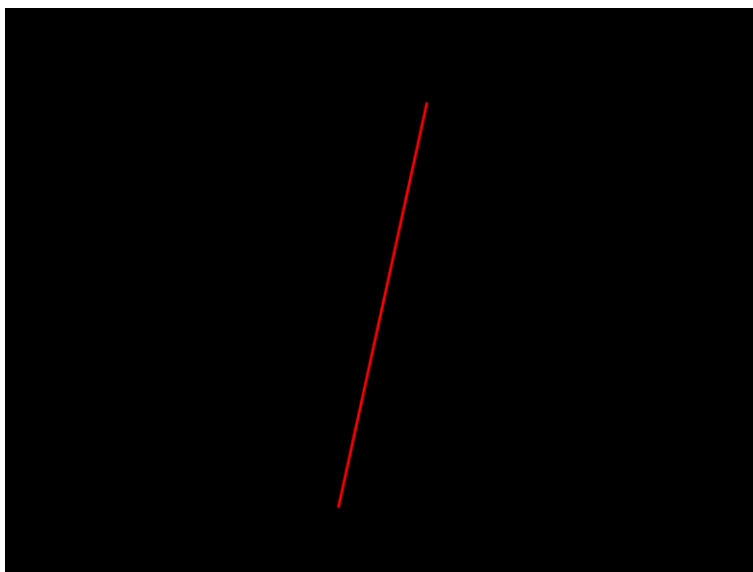


Figure 5.10. Tauc plot ($n = 1/2$) for a nondoped powder sample containing “ $\text{Sr}_{22.5+x}\text{La}_{55-x}[\text{Si}_{129}\text{N}_{240-x}\text{O}_x]\text{O}_3$ ” ($x \approx 0.24$) and $\text{Sr}_{28.5+x}\text{La}_{75-x}[\text{Si}_{170}\text{N}_{312-x}\text{O}_{9+x}]\text{O}_4$ ($x \approx -3.71$). The artifact around 3.65 eV (340 nm) corresponds to the analyzer lamp switch.

5.2.2.4 Luminescence

Luminescence properties of Eu^{2+} -doped “ $\text{Sr}_{22.5+x}\text{La}_{55-x}[\text{Si}_{129}\text{N}_{240-x}\text{O}_x]\text{O}_3$ ” ($x \approx 0.24$) and $\text{Sr}_{28.5+x}\text{La}_{75-x}[\text{Si}_{170}\text{N}_{312-x}\text{O}_{9+x}]\text{O}_4$ ($x \approx -3.71$) were measured on potentially intergrown single luminescent particles. Upon excitation with UV to blue light, the samples show amber luminescence and exhibit emission maxima at $\lambda_{\text{em}} = 600$ nm with $\text{fwhm} = 73$ nm/ 1991 cm^{-1} upon 0.2 mol% doping and $\lambda_{\text{em}} = 606$ nm with $\text{fwhm} = 78$ nm/ 2095 cm^{-1} at a doping concentration of 1.5 mol% (Figure 5.11). The emission bands can be assigned to the parity-allowed $4f^65d^1$ (7F_0) \rightarrow $4f^7$ (${}^8S_{7/2}$) transition of Eu^{2+} .^[1] Due to the excitation maxima around $\lambda_{\text{exc}} \approx 450$ nm, “ $\text{Sr}_{22.5+x}\text{La}_{55-x}[\text{Si}_{129}\text{N}_{240-x}\text{O}_x]\text{O}_3:\text{Eu}^{2+}$ ” ($x \approx 0.24$) and $\text{Sr}_{28.5+x}\text{La}_{75-x}[\text{Si}_{170}\text{N}_{312-x}\text{O}_{9+x}]\text{O}_4:\text{Eu}^{2+}$ ($x \approx -3.71$) can efficiently be excited by an $\text{Ga}_{1-x}\text{In}_x\text{N}$ LED light source.

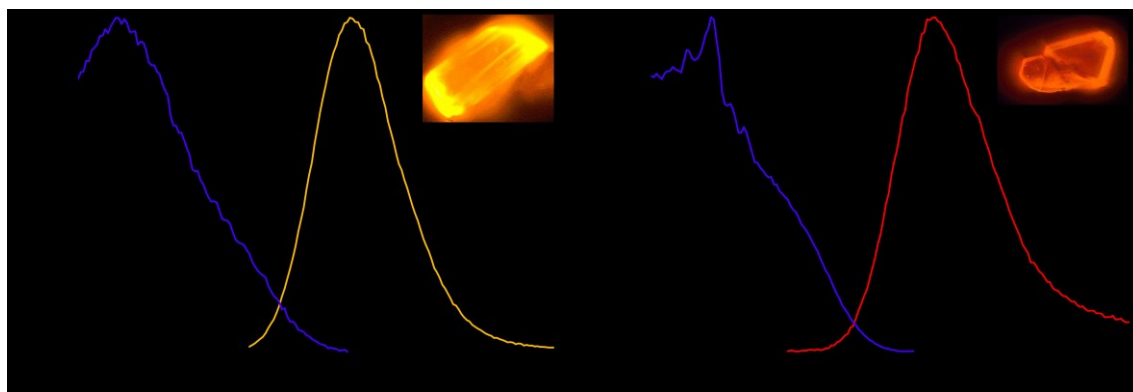


Figure 5.11. Normalized excitation (blue, $\lambda_{\text{mon}} = 630 \text{ nm}$) and emission spectra (orange/red, $\lambda_{\text{exc}} = 420 \text{ nm}$) of a (a) 0.2 mol% and (b) 1.5 mol% doped mixture of “ $\text{Sr}_{22.5+x}\text{La}_{55-x}[\text{Si}_{129}\text{N}_{240-x}\text{O}_x]\text{O}_3:\text{Eu}^{2+}$ ” ($x \approx 0.24$) and $\text{Sr}_{28.5+x}\text{La}_{75-x}[\text{Si}_{170}\text{N}_{312-x}\text{O}_{9+x}]\text{O}_4:\text{Eu}^{2+}$ ($x \approx -3.71$) with micrographs of the respective measured particles.

The emission properties of samples containing both phases, “ $\text{Sr}_{22.5+x}\text{La}_{55-x}[\text{Si}_{129}\text{N}_{240-x}\text{O}_x]\text{O}_3:\text{Eu}^{2+}$ ” ($x \approx 0.24$) and $\text{Sr}_{28.5+x}\text{La}_{75-x}[\text{Si}_{170}\text{N}_{312-x}\text{O}_{9+x}]\text{O}_4:\text{Eu}^{2+}$ ($x \approx -3.71$), can be compared to other amber emitting and application relevant phosphors like $(\text{Ba},\text{Sr})_2\text{Si}_5\text{N}_8:\text{Eu}^{2+}$ ($\lambda_{\text{em}} \approx 590\text{--}625 \text{ nm}$, $fwhm \approx 2050\text{--}2600 \text{ cm}^{-1}$) or $(\text{Sr},\text{Ca})\text{AlSiN}_3:\text{Eu}^{2+}$ ($\lambda_{\text{em}} \approx 610\text{--}660 \text{ nm}$, $fwhm \approx 2100\text{--}2500 \text{ cm}^{-1}$) and show some similarities with narrow red-emitting $\text{Sr}[\text{LiAl}_3\text{N}_4]:\text{Eu}^{2+}$ ($\lambda_{\text{em}} = 650 \text{ nm}$, $fwhm = 50 \text{ nm}/1180 \text{ cm}^{-1}$), $\text{Sr}[\text{Li}_2\text{Al}_2\text{O}_2\text{N}_2]:\text{Eu}^{2+}$ ($\lambda_{\text{em}} = 614 \text{ nm}$, $fwhm = 48 \text{ nm}/1286 \text{ cm}^{-1}$) and $\text{Sr}[\text{Mg}_3\text{SiN}_4]:\text{Eu}^{2+}$ ($\lambda_{\text{em}} = 615 \text{ nm}$, $fwhm = 43 \text{ nm}/1170 \text{ cm}^{-1}$). Compared to “ $\text{Sr}_{22.5+x}\text{La}_{55-x}[\text{Si}_{129}\text{N}_{240-x}\text{O}_x]\text{O}_3:\text{Eu}^{2+}$ ” ($x \approx 0.24$) and $\text{Sr}_{28.5+x}\text{La}_{75-x}[\text{Si}_{170}\text{N}_{312-x}\text{O}_{9+x}]\text{O}_4:\text{Eu}^{2+}$ ($x \approx -3.71$), they crystallize in highly symmetric UCr_4C_4 or therefrom derived structure types with one single activator site, which is cuboid-like coordinated in a highly symmetric manner. The emission band of $(\text{Ba},\text{Sr})_2\text{Si}_5\text{N}_8:\text{Eu}^{2+}$ is broadened due to two less symmetrically coordinated activator sites and $(\text{Sr},\text{Ca})\text{AlSiN}_3:\text{Eu}^{2+}$ exhibits a broad emission band due to only one but less symmetrically coordinated activator site with mixed occupation of Si/Al and N/O with O being introduced as a contaminant.^[2, 6-12] In contrast, “ $\text{Sr}_{22.5+x}\text{La}_{55-x}[\text{Si}_{129}\text{N}_{240-x}\text{O}_x]\text{O}_3:\text{Eu}^{2+}$ ” ($x \approx 0.24$) and $\text{Sr}_{28.5+x}\text{La}_{75-x}[\text{Si}_{170}\text{N}_{312-x}\text{O}_{9+x}]\text{O}_4:\text{Eu}^{2+}$ ($x \approx -3.71$) exhibit similar or slightly broadened emission bands. However, despite conduction of single particle measurements, it cannot be excluded that emission of both components was measured simultaneously due to the prominent intergrowth. Furthermore, “ $\text{Sr}_{22.5+x}\text{La}_{55-x}[\text{Si}_{129}\text{N}_{240-x}\text{O}_x]\text{O}_3:\text{Eu}^{2+}$ ” ($x \approx 0.24$) has 21 and $\text{Sr}_{28.5+x}\text{La}_{75-x}[\text{Si}_{170}\text{N}_{312-x}\text{O}_{9+x}]\text{O}_4:\text{Eu}^{2+}$ ($x \approx -3.71$) 28 cation sites with mixed occupancy and split positions coordinated by both N and O in irregular polyhedra with coordination numbers ranging from 5 to 10 and Sr/La-N/O distances varying from approx. 1.92(1) to 3.56(3) Å. This example shows that narrower band emission is not always necessarily caused by one highly symmetrically coordinated activator environment. All compounds share a highly condensed and rigid network that allows only a few lattice vibrations, minimizing the Stokes shift and

5.2 Unpublished Results

eventually leading to narrow-band emission (Chapter 1.3). However, many different factors play a role in the luminescence process. “ $\text{Sr}_{22.5+x}\text{La}_{55-x}[\text{Si}_{129}\text{N}_{240-x}\text{O}_x]\text{O}_3$ ” ($x \approx 0.24$) and $\text{Sr}_{28.5+x}\text{La}_{75-x}[\text{Si}_{170}\text{N}_{312-x}\text{O}_{9+x}]\text{O}_4$ ($x \approx -3.71$) contain many chemically different cation sites dopable with Eu^{2+} . The emission energy from higher energetic sites can be transferred to lower energetic sites by reabsorption without resulting in visible emission itself. Thus, only the emission from the lowest energetic site(s) is visible. In addition, sites whose $5d$ levels are energetically located too close to the conduction band of the host material do also not result in visible emission because the optically excited electrons can easily be excited into the conduction band by thermal activation and are thus removed from the luminescence process. This results in a lower quantum efficiency, which can be shown by thermal quenching measurements.

The thermal quenching behavior of “ $\text{Sr}_{22.5+x}\text{La}_{55-x}[\text{Si}_{129}\text{N}_{240-x}\text{O}_x]\text{O}_3:\text{Eu}^{2+}$ ” ($x \approx 0.24$, 0.5 mol%) and $\text{Sr}_{28.5+x}\text{La}_{75-x}[\text{Si}_{170}\text{N}_{312-x}\text{O}_{9+x}]\text{O}_4:\text{Eu}^{2+}$ ($x \approx -3.71$, 0.5 mol%) was investigated based on cryo-spectroscopy measurements between 6 K and 300 K combined with measurements with a thermal quenching set-up up to 598 K. As it can be derived from Figure D13, the maximum achievable internal quantum efficiency (IQE) at room temperature is approx. 43% compared to 6 K. Thermal quenching measurements reveal significant thermal quenching at 150 °C with a relative photoemission intensity of approx. 27% compared to room temperature. This can be explained by the above-mentioned close location of the different energetic positions of the $5d$ levels of the various activator sites relative to the conduction band of the host material.

Increasing the doping concentration of “ $\text{Sr}_{22.5+x}\text{La}_{55-x}[\text{Si}_{129}\text{N}_{240-x}\text{O}_x]\text{O}_3:\text{Eu}^{2+}$ ” ($x \approx 0.24$) exhibits 21 and $\text{Sr}_{28.5+x}\text{La}_{75-x}[\text{Si}_{170}\text{N}_{312-x}\text{O}_{9+x}]\text{O}_4:\text{Eu}^{2+}$ ($x \approx -3.71$) from 0.2 mol% to 4 mol% results in red shifted and slightly broadened emission bands (Figure D14, Table D24).

5.2.3 Conclusion

In this contribution, we report on the high-temperature solid-state synthesis of samples containing both “ $\text{Sr}_{22.5+x}\text{La}_{55-x}[\text{Si}_{129}\text{N}_{240-x}\text{O}_x]\text{O}_3$ ” ($x \approx 0.24$) and $\text{Sr}_{28.5+x}\text{La}_{75-x}[\text{Si}_{170}\text{N}_{312-x}\text{O}_{9+x}]\text{O}_4$ ($x \approx -3.71$) as intergrown micro-crystallites. $\text{Sr}_{28.5+x}\text{La}_{75-x}[\text{Si}_{170}\text{N}_{312-x}\text{O}_{9+x}]\text{O}_4$ ($x \approx -3.71$) was already presented in Chapter 5.1. “ $\text{Sr}_{22.5+x}\text{La}_{55-x}[\text{Si}_{129}\text{N}_{240-x}\text{O}_x]\text{O}_3$ ” ($x \approx 0.24$) however has not been reported before. Hitherto existing structure elucidation based on single-crystal X-ray diffraction data of “ $\text{Sr}_{22.5+x}\text{La}_{55-x}[\text{Si}_{129}\text{N}_{240-x}\text{O}_x]\text{O}_3$ ” ($x \approx 0.24$) results in space group $P\bar{6}$ (no. 174) with $a = 17.4055(5)$, $c = 22.4642(7)$ Å and $Z = 1$. This and the preliminary structural motifs indicate that the crystal structure of “ $\text{Sr}_{22.5+x}\text{La}_{55-x}[\text{Si}_{129}\text{N}_{240-x}\text{O}_x]\text{O}_3$ ” ($x \approx 0.24$) is analogue or at least very similar to $\text{Ba}_{22.5+x}\text{La}_{55-x}[\text{Si}_{129}\text{N}_{240-x}\text{O}_x]\text{O}_3$ ($x \approx 0.24$), which is additionally supported by EDX measurements and Rietveld refinements based on the structure model of $\text{Ba}_{22.5+x}\text{La}_{55-x}[\text{Si}_{129}\text{N}_{240-x}\text{O}_x]\text{O}_3$ ($x \approx 0.24$), in which Ba was substituted by

Sr. Structure elucidation could not be completed up to this point due to the crystallographic challenges known from the analogous $\text{Ba}_{22.5+x}\text{La}_{55-x}[\text{Si}_{129}\text{N}_{240-x}\text{O}_x]\text{O}_3$ ($x \approx 0.24$) compound like mixed and under-occupied heavy cation sites and notorious intergrowth with other domains, which are discussed in Chapters 5.1.2.2 and 5.1.2.3. This was shown by comparing the corresponding reciprocal lattice sections of “ $\text{Sr}_{22.5+x}\text{La}_{55-x}[\text{Si}_{129}\text{N}_{240-x}\text{O}_x]\text{O}_3$ ” ($x \approx 0.24$) and $\text{Ba}_{22.5+x}\text{La}_{55-x}[\text{Si}_{129}\text{N}_{240-x}\text{O}_x]\text{O}_3$ ($x \approx 0.24$). The crystal structure description can be found in Chapters 5.1.2.4. Luminescence measurements on Eu^{2+} -doped samples containing intergrown $\text{Sr}_{22.5+x}\text{La}_{55-x}[\text{Si}_{129}\text{N}_{240-x}\text{O}_x]\text{O}_3$ ” ($x \approx 0.24$) and $\text{Sr}_{28.5+x}\text{La}_{75-x}[\text{Si}_{170}\text{N}_{312-x}\text{O}_{9+x}]\text{O}_4$ ($x \approx -3.71$) results in amber emission with the maximum located at $\lambda_{\text{em}} = 600$ nm with $\text{fwhm} = 73$ nm/1991 cm^{-1} upon 0.2 mol% doping. Comparisons with other application relevant amber or narrow-red emitting phosphors like $(\text{Ba},\text{Sr})_2\text{Si}_5\text{N}_8:\text{Eu}^{2+}$ or $\text{Sr}[\text{LiAl}_3\text{N}_4]:\text{Eu}^{2+}$ show, that although the emission band of “ $\text{Sr}_{22.5+x}\text{La}_{55-x}[\text{Si}_{129}\text{N}_{240-x}\text{O}_x]\text{O}_3$ ” ($x \approx 0.24$) and $\text{Sr}_{28.5+x}\text{La}_{75-x}[\text{Si}_{170}\text{N}_{312-x}\text{O}_{9+x}]\text{O}_4$ ($x \approx -3.71$) is broader, it is thus comparably narrow in the context of structural prerequisites. It was shown that narrow-band emission is not necessary a result from few highly symmetrically coordinated activator sites but rather from highly condensed and rigid host networks. Other processes leading to a decreased number of emission bands resulting from different activator sites have been discussed. However, further measurements and calculations on band structures and the energetic position of the different $5d$ levels of the various activator sites like e.g., X-ray spectroscopy, are necessary to fully understand the underlying luminescence mechanisms and give further insight into narrow-band emission. It should further be investigated which additional doping concentrations are possible due to the high number of potential doping sites and therefore, how far λ_{em} and fwhm can be influenced and adapted to required properties. Supplementary quantum efficiency measurements at different doping levels are necessary to identify the ideal doping concentration and may enable statements on the energetic sequence of occupying the different sites by Eu^{2+} .

5.2.4 Experimental Part

5.2.4.1 Synthesis

All preparation steps were carried out under argon atmosphere either in an Ar filled glovebox (Unilab, MBraun, Garching; $\text{O}_2 < 1$ ppm; $\text{H}_2\text{O} < 1$ ppm) or in Ar-filled glassware applying the Schlenk technique. The starting material Sr_2N used for the main synthesis was synthesized using Sr metal. For Sr_2N , 92.6 mg Sr (1.057 mmol, Sigma-Aldrich, 99.99 %) placed in a tungsten crucible were transferred into a water-cooled silica glass reactor of a radiofrequency furnace (IG 10/600; Hüttinger Elektronik Freiburg, Germany), which is attached to a Schlenk line.^[13] The crucible was heated under N_2 -atmosphere to 1000 °C within 1 h, maintained at that temperature for 20 h and cooled down to room temperature within 1 h. The synthesis

5.2 Unpublished Results

resulted in Sr₂N as a black powder (see Figure D8 and Table D19). For the synthesis of a mixture of “Sr_{22.5+x}La_{55-x}[Si₁₂₉N_{240-x}O_x]O₃:Eu²⁺” ($x \approx 0.24$) and Sr_{28.5+x}La_{75-x}[Si₁₇₀N_{312-x}O_{9+x}]O₄:Eu²⁺ ($x \approx -3.71$), 32.3 mg Sr₂N (0.171 mmol), 31.4 mg LaCl₃ (0.128 mmol, abcr, 99.9 %), 18.0 mg amorphous Si₃N₄ (0.128 mmol, Ube Industries, SNA-00) and EuCl₃ (Sigma-Aldrich, 99.99 %) as a dopant were used. The starting materials were thoroughly ground, filled into tungsten crucibles and transferred into a radiofrequency furnace (TIG 10/100; Hüttinger Elektronik Freiburg, Germany) attached to a Schlenk line. The crucibles were one after another first heated under forming gas atmosphere (N₂:H₂ = 95:5) to 1600 °C within 5 min, maintained at that temperature for 2 h, then cooled down to 500 °C within 10 h, and finally quenched by switching off the furnace. “Sr_{22.5+x}La_{55-x}[Si₁₂₉N_{240-x}O_x]O₃:Eu²⁺” ($x \approx 0.24$) and Sr_{28.5+x}La_{75-x}[Si₁₇₀N_{312-x}O_{9+x}]O₄:Eu²⁺ ($x \approx -3.71$) were obtained as an air and moisture stable orange powder with orange-red luminescence upon excitation with UV to blue light.

5.2.4.2 Powder X-ray Diffraction

To collect powder X-ray diffraction (PXRD) data, a STOE STADI P diffractometer (Mo-K α_1 radiation, $\lambda = 0.70930$ Å, Stoe & Cie, Darmstadt, Germany) with a Ge(111) monochromator and a Mythen1K detector (Dectris, Baden-Dättwil, Switzerland) in parafocusing Debye-Scherrer geometry was used with the ground products sealed into glass capillaries (0.2 mm diameter, wall thickness 0.01 mm; Hilgenberg GmbH, Malsfeld, Germany). Rietveld refinements were performed with the TOPAS Academic V6 package applying the fundamental parameters approach (direct convolution of source emission profiles, axial instrument contributions, crystallite size and microstrain effects).^[14, 15] The calculated absorption coefficients were used to correct absorption effects. The background was modeled using a shifted Chebychev function and preferred orientation was described by applying a spherical harmonics model of fourth order.^[16-18]

5.2.4.3 Scanning Electron Microscopy (SEM) and Energy-Dispersive X-ray Spectroscopy (EDX)

The chemical composition and morphology of the samples were investigated performing energy dispersive X-ray (EDX) measurements with a Dualbeam Helios Nanolab G3 UC (FEI, Hillsboro, Oregon, USA) equipped with an X-Max 80 SDD detector (Oxford Instruments, Abingdon, UK). A high-vacuum sputter coater (CCU-010, Safematic GmbH, Zizers, Switzerland) was used for carbon-coating the samples to prevent electrostatic charging of the samples.

5.2.4.4 UV/Vis Spectroscopy

For the measurement of diffuse reflectance spectra in the range of 240 to 800 nm with 1 nm step size, a Jasco V-650 UV/Vis spectrophotometer containing a deuterium and a halogen lamp (Czerny-Turner monochromator with 1200 lines/mm concave grating, photomultiplier tube detector) was used.

5.2.4.5 Luminescence

Room temperature photoluminescence properties of a “ $\text{Sr}_{22.5+x}\text{La}_{55-x}[\text{Si}_{129}\text{N}_{240-x}\text{O}_x]\text{O}_3:\text{Eu}^{2+}$ ” ($x \approx 0.24$) and $\text{Sr}_{28.5+x}\text{La}_{75-x}[\text{Si}_{170}\text{N}_{312-x}\text{O}_{9+x}]\text{O}_4:\text{Eu}^{2+}$ ($x \approx -3.71$) sample was measured using a HORIBA Fluoromax4 spectrofluorimeter system connected to an Olympus BX51 microscope via optical fibers. For the acquisition of excitation spectra, the monitoring wavelength λ_{mon} ranged from 425 to 516 nm. Cryo-spectroscopy measurements of thick-bed powder samples were performed between 300 and 6 K using a fiber-coupled spectroscopy system equipped with a thermally stabilized LED light source and a fiber-optic spectrometer (HR2000+ES spectrometer, Ocean Optics). While measuring, the sample was placed in an evacuated cooling chamber connected to a liquid-He compressor system (ARS4HW, Advanced Research System Inc., Macungie, Pennsylvania, USA).

5.2.5 Acknowledgements

The authors thank Dr. Peter Mayer (Department of Chemistry at University of Munich (LMU)) for the collection of the single-crystal data.

5.2.6 References

- [1] G. Blasse, B. C. Grabmaier, *Luminescent Materials*, Springer, Berlin, Heidelberg, **1994**.
- [2] P. Pust, V. Weiler, C. Hecht, A. Tücks, A. S. Wochnik, A.-K. Henß, D. Wiechert, C. Scheu, P. J. Schmidt, W. Schnick, *Nat. Mater.* **2014**, *13*, 891–896.
- [3] C. Maak, D. Durach, C. Martiny, P. J. Schmidt, W. Schnick, *Chem. Mater.* **2018**, *30*, 3552–3558.
- [4] R. López, R. Gómez, *J. Sol-Gel Sci. Technol.* **2012**, *61*, 1–7.
- [5] J. Tauc, R. Grigorovici, A. Vancu, *Phys. Status Solidi B* **1966**, *15*, 627–637.
- [6] R. Mueller-Mach, G. Mueller, M. R. Krames, H. A. Höpfe, F. Stadler, W. Schnick, T. Juestel, P. Schmidt, *Phys. Status Solidi A* **2005**, *202*, 1727–1732.
- [7] M. Krames, G. O. Mueller, R. Mueller-Mach, H. Bechtel, P. J. Schmidt, *PCT Int. Appl.* **2010**, WO2010131133A1.
- [8] K. Uheda, N. Hirosaki, Y. Yamamoto, A. Naito, T. Nakajima, H. Yamamoto, *Electrochem. Solid-State Lett.* **2006**, *9*, H22–H25.
- [9] K. Uheda, N. Hirosaki, H. Yamamoto, *Phys. Status Solidi A* **2006**, *203*, 2712–2717.
- [10] H. A. Höpfe, H. Lutz, P. Morys, W. Schnick, A. Seilmeier, *J. Phys. Chem. Solids* **2000**, *61*, 2001–2006.

- [11] G. J. Hoerder, M. Seibald, D. Baumann, T. Schröder, S. Peschke, P. C. Schmid, T. Tyborski, P. Pust, I. Stoll, M. Bergler, C. Patzig, S. Reißaus, M. Krause, L. Berthold, T. Höche, D. Johrendt, H. Huppertz, *Nat. Commun.* **2019**, *10*, 1824–1832.
- [12] S. Schmiechen, H. Schneider, P. Wagatha, C. Hecht, P. J. Schmidt, W. Schnick, *Chem. Mater.* **2014**, *26*, 2712–2719.
- [13] W. Schnick, H. Huppertz, R. Lauterbach, *J. Mater. Chem.* **1999**, *9*, 289–296.
- [14] A. A. Coelho, *TOPAS Version 6: A program for Rietveld refinement*, Coelho Software, Brisbane, **2016**.
- [15] H. Rietveld, *J. Appl. Crystallogr.* **1969**, *2*, 65–71.
- [16] J. Bergmann, R. Kleeberg, A. Haase, B. Breidenstein, *Mater. Sci. Forum* **2000**, *347–349*, 303–308.
- [17] R. W. Cheary, A. Coelho, *J. Appl. Crystallogr.* **1992**, *25*, 109–121.
- [18] R. W. Cheary, A. A. Coelho, J. P. Cline, *J. Res. Natl. Inst. Stand. Technol.* **2004**, *109*, 1–25.

6 Conclusion and Outlook

Climate change is currently the single greatest threat to our entire planet, which is strongly amplified by man-made emissions of greenhouse gases such as CO₂.^[1, 2] To mitigate the devastating effects of climate change, both the reliance on renewable energies must be increased as well as current energy consumption must be reduced. The lighting sector offers great potential for energy savings, for which new lighting technologies such as phosphor-converted light-emitting diodes (pcLEDs) paved the way.^[3] However, innovative phosphors are required to further improve pcLEDs and to open up more application areas. Research is therefore focused on modifying known phosphors and exploring new luminescent materials with enhanced luminescent properties specified for applications. Most Ce³⁺-doped phosphors are limited in possible application fields due to emission ranging from blue to only orange-red, resulting in cold-white light. However, to make Ce³⁺-doped phosphors more appealing for applications, broadband emission extending into the red spectral region is desired.^[4] Research on Eu²⁺ as activator ion aims for narrow-band emitting phosphors to enhance efficiency, color point stability and color rendering. Therefore, structure-property relations are important to understand luminescence properties and optimally adapt them to the respective applications.^[5] *RE*- and *AE*-oxonitridosilicates have already proven themselves as promising host materials since they offer among other beneficial properties a high structural and chemical variability, which makes them suitable for adaption to specific requirements.

This thesis focuses on the high-temperature synthesis and characterization of Eu²⁺- and Ce³⁺-doped *RE*- and *AE*-oxonitrido(carbido)silicate-based phosphor materials to possibly fulfill the requirements of the technology development e.g., in the lighting industry. Implementation of multiple cations and anions with dissimilar chemical properties lead to various different crystal structures with a huge variety of structural motifs. The chemical and structural features were utilized to provide tunability through the charge neutral exchange of *REN* by *AEO* and vice versa. Structural characteristics were elucidated based on state-of-the-art techniques like powder and single-crystal diffraction using X-ray or microfocused synchrotron radiation and transmission or scanning electron microscopy (TEM and SEM) supported by elemental analyses (EDX, CHNS, NMR) and bond valence sum, lattice energy, and charge distribution calculations. Additionally, optical properties were investigated using UV/Vis and luminescence measurements. Implementation of the latest techniques for structure elucidation combined with investigations of optical properties are supposed to provide the foundation for further research to make more precise statements about structure-property relations and may indicate how to optimally tune materials for required applications.^[6-9]

Already known structure types are worth to be further explored in terms of structural modification upon cationic or anionic substitution. Although the $\text{Er}_6\text{Si}_{11}\text{N}_{20}\text{O}$ structure type is long known, it was previously not considered as a host material in phosphors.^[10, 11] However, we showed that therefrom derived compounds like $\text{Yb}_6\text{Si}_{11}\text{N}_{20}\text{O}$ or $\text{Lu}_6\text{Si}_{11}\text{N}_{20}\text{O}$ are capable of solely cationic substitution of trivalent RE^{3+} by divalent Ca^{2+} , leading to the filled variant $RE_{6-x}\text{Ca}_{1.5x}\text{Si}_{11}\text{N}_{20}\text{O}$ ($RE = \text{Yb, Lu}; x \approx 2.2$), in which the charge difference caused by the cation substitution is balanced by occupation of an additional third cation site, which is not occupied in the $\text{Er}_6\text{Si}_{11}\text{N}_{20}\text{O}$ structure type and has not been reported for the $\text{Er}_6\text{Si}_{11}\text{N}_{20}\text{O}$ structure type before. $\text{Lu}_{6-x}\text{Ca}_{1.5x}\text{Si}_{11}\text{N}_{20}\text{O}:\text{Ce}^{3+}$ exhibits a broadband yellow emission with a maximum at $\lambda_{\text{em}} \approx 565 \text{ nm}$ and $\text{fwhm} \approx 168 \text{ nm}/5100 \text{ cm}^{-1}$. The emission properties can be compared to $\text{YAG}:\text{Ce}^{3+}$, which is relevant for application in single phosphor converted light emitting diodes (1pcLED) but its application areas are limited due to emission of only cold-white light. Since the emission of $\text{Lu}_{6-x}\text{Ca}_{1.5x}\text{Si}_{11}\text{N}_{20}\text{O}:\text{Ce}^{3+}$ extends more into the red spectral region, it is an interesting phosphor for warm-white 1pcLEDs with an improved color rendering index and higher efficiency.^[6] Thereupon, other researchers have applied this approach also to the $\text{Er}_6\text{Si}_{11}\text{N}_{20}\text{O}$ structure type, leading to $\text{Y}_{6-x}\text{Ca}_{1.5x}\text{Si}_{11}\text{N}_{20}\text{O}:\text{Ce}^{3+}$ ($x = 0-2.5$) with similar emission characteristics compared to $\text{Lu}_{6-x}\text{Ca}_{1.5x}\text{Si}_{11}\text{N}_{20}\text{O}:\text{Ce}^{3+}$.^[12] However, the incorporation of cations with higher molar masses like Lu^{3+} compared to similar sized and charged Y^{3+} has previously shown to reduce phonon frequencies of local lattice vibrations, which leads to a smaller Stokes shift and is therefore beneficial for higher emission efficiencies.^[13]

The aforementioned approach can be extended to solely anionic substitution applied to the $M^{\text{II}}M^{\text{III}}\text{Si}_4\text{N}_7$ compound class with interesting structural features since $\text{BaYbSi}_4\text{N}_7$ is the first compound containing a star shaped $[\text{N}^{4-}(\text{SiN}_3)_4]$ unit containing a fourfold bridging ammonium-type nitrogen.^[14] It is therefore possible to substitute nitrogen not only by oxygen onto N^{2-} sites but also by carbon onto the N^{4-} site, leading to the rarely investigated class of oxonitridocarbidosilicates. Additionally, doping with both Eu^{2+} and Ce^{3+} is possible due to similar sizes and charges compared to the M^{II} and M^{III} cations, respectively, which makes $M^{\text{II}}M^{\text{III}}\text{Si}_4\text{N}_7$ highly variable and thus, interesting for application. This considerations led to the synthesis of $\text{CaLu}[\text{Si}_4\text{N}_{7-2x}\text{C}_x\text{O}_x]$ ($x \approx 0.3$) as the first oxonitridocarbidosilicate in this compound class and just the second oxonitridocarbidosilicate known so far.^[7, 15] $\text{CaLu}[\text{Si}_4\text{N}_{7-2x}\text{C}_x\text{O}_x]$ ($x \approx 0.3$) adds a previously not known member to the $M^{\text{II}}M^{\text{III}}\text{Si}_4\text{N}_7$ compound class. ^{13}C - and ^{29}Si -MAS-NMR spectroscopy were used to specify the amount of carbon incorporation. Additionally, the combination of NMR and elemental analysis revealed the simultaneous incorporation of oxygen rather than the previously assumed substitution of M^{II} by M^{III} for charge compensation. $M^{\text{II}}M^{\text{III}}\text{Si}_4\text{N}_7$ compounds with small cations may not be accessible without the CRN method since carbon incorporation and therefore more covalent

Si–C bonds lead to a higher rigidity and stability of the network.^[7] $\text{CaLu}[\text{Si}_4\text{N}_{7-2x}\text{C}_x\text{O}_x]:\text{Ce}^{3+}$ ($x \approx 0.3$) exhibits blue luminescence with $\lambda_{\text{em}} \approx 484$ nm and $\text{fwhm} \approx 109$ nm/ 4531 cm^{-1} , which makes it interesting for application in near-UV pumped pcLEDs to fill the blue-cyan gap since an fwhm of ≥ 60 nm is necessary for a high color quality.^[7, 16, 17] $\text{CaLu}[\text{Si}_4\text{N}_{7-2x}\text{C}_x\text{O}_x]:\text{Eu}^{2+}$ ($x \approx 0.3$) shows broadband yellow-green emission with $\lambda_{\text{em}} \approx 546$ nm and $\text{fwhm} \approx 123$ nm/ 3999 cm^{-1} when excited by UV to blue light, which can be compared to commercially used $\text{YAG}:\text{Ce}^{3+}$. $\text{CaLu}[\text{Si}_4\text{N}_{7-2x}\text{C}_x\text{O}_x]:\text{Eu}^{2+}$ can not only be used as a phosphor in 1pcLEDs but also as a color point stabilizer. Since the $M^I M^{III} \text{Si}_4\text{N}_7$ compound class offers a variety of full or partial substitution possibilities even for activator ions, it is a promising host lattice to cover a very broad emission spectrum.^[7]

Another important approach towards new application relevant phosphor materials besides the modification of known structure types is the examination of formerly unexplored compound classes. The barely investigated La-Sr-Si-N-O system contains only two known red emitting phosphors, of which only one was doped with industrially relevant Eu^{2+} . It is therefore promising for containing more host compounds resulting in red emitting phosphors with potential for usage in lighting applications, since red emitting phosphors have an immense impact on the overall efficiency and color rendering of pcLEDs.^[18, 19] This resulted in the synthesis of $\text{La}_7\text{Sr}[\text{Si}_{10}\text{N}_{19}\text{O}_3]$, which exhibits a new three-dimensional network and offers unprecedented chemical variability of full or partial substitution possibilities and thus could be an interesting host material class for tunability upon Eu^{2+} doping. Not only a singular or simultaneous exchange of cations (Ca/Sr/Ba and respectively or La/Ce) is possible but also the charge neutral substitution of chemical units like AEO by REN and vice versa, leading to the solid solution series of the substitutional variants $\text{RE}_{8-x}\text{AE}_x[\text{Si}_{10}\text{N}_{20-x}\text{O}_{2+x}]:\text{Eu}^{2+}$ with $\text{RE} = \text{La}, \text{Ce}$; $\text{AE} = \text{Ca}, \text{Sr}, \text{Ba}$ and $0 \leq x \leq 2$. In this work, a total of 14 representatives were synthesized and characterized. Thereof, $\text{La}_7\text{Sr}[\text{Si}_{10}\text{N}_{19}\text{O}_3]:\text{Eu}^{2+}$ is just the second known Eu^{2+} -doped phosphor in the La-Sr-Si-O-N system so far and exhibits amber emission upon excitation with UV to blue light with an emission maximum at $\lambda_{\text{em}} \approx 612$ nm and $\text{fwhm} \approx 84$ nm/ 2194 cm^{-1} , which is comparable to commercially utilized amber emitting $(\text{Ba},\text{Sr})_2\text{Si}_5\text{N}_8:\text{Eu}^{2+}$ and $(\text{Sr},\text{Ca})\text{AlSiN}_3:\text{Eu}^{2+}$. UV/Vis spectroscopy was used to determine the optical bandgap followed by extensive discussions on thermal quenching behavior. This work shows that it is worthwhile to investigate hitherto little or unnoticed compound classes, whereby research should not only concentrate on individual representatives, but rather systematically explore the compound classes. Chemical variability is an important feature of host materials since different cations or anions can impact luminescence properties and therefore, make them adaptable to the desired applications.^[8]

In the search for narrow-band red-emitting phosphors, which have a significant impact on the efficiency and CRI of pcLEDs, researchers are primarily focused on compounds that crystallize in the UCr_4C_4 or thereof derived structure types. Characteristics, which favor narrow-band red emission, of these structure types are few, symmetrically coordinated activator (Eu^{2+}) sites in a preferentially cuboid-shaped environment with nearly identical activator-ligand distances coordinated by preferably only one type of ligand. Examples are $\text{Sr}[\text{LiAl}_3\text{N}_4]:\text{Eu}^{2+}$, $\text{Sr}[\text{Li}_2\text{Al}_2\text{O}_2\text{N}_2]:\text{Eu}^{2+}$ and $\text{Sr}[\text{Mg}_3\text{SiN}_4]:\text{Eu}^{2+}$.^[20-22] Contrary to them, a mixture of “ $\text{Sr}_{22.5+x}\text{La}_{55-x}[\text{Si}_{129}\text{N}_{240-x}\text{O}_x]\text{O}_3$ ” ($x \approx 0.24$) and $\text{Sr}_{28.5+x}\text{La}_{75-x}[\text{Si}_{170}\text{N}_{312-x}\text{O}_{9+x}]\text{O}_4$ ($x \approx -3.71$) exhibits comparatively narrow emission in the red spectral region ($\lambda_{\text{em}} = 606 \text{ nm}$, $\text{fwhm} = 78 \text{ nm}/2083 \text{ cm}^{-1}$) despite complex and fairly low symmetric crystal structures, which crystallize isotypic to $\text{Ba}_{22.5+x}\text{La}_{55-x}[\text{Si}_{129}\text{N}_{240-x}\text{O}_x]\text{O}_3$ ($x \approx 0.24$) and $\text{Ba}_{25.5+x}\text{La}_{77-x}[\text{Si}_{170}\text{N}_{312-x}\text{O}_{9+x}]\text{O}_4$ ($x \approx 0.24$). The crystal structure elucidations of $\text{Ba}_{22.5+x}\text{La}_{55-x}[\text{Si}_{129}\text{N}_{240-x}\text{O}_x]\text{O}_3$ ($x \approx 0.24$) and $\text{Ba}_{25.5+x}\text{La}_{77-x}[\text{Si}_{170}\text{N}_{312-x}\text{O}_{9+x}]\text{O}_4$ ($x \approx 0.24$) were highly sophisticated due to microcrystalline samples of notoriously endotaxially intergrown domains. Extensive TEM investigations with electron diffraction (SAED, STEM-HAADF) were necessary to identify isolated single crystallites of both variants. Due to these sub-micron-sized crystallites, X-ray diffraction with microfocused synchrotron radiation was necessary. Crystal structure elucidations were assisted by EDX measurements and BVS calculations as well as the simultaneous presence of the $\text{Ba}_{25.5+x}\text{La}_{77-x}[\text{Si}_{170}\text{N}_{312-x}\text{O}_{9+x}]\text{O}_4$ analogous Sr compound, namely $\text{Sr}_{28.5+x}\text{La}_{75-x}[\text{Si}_{170}\text{N}_{312-x}\text{O}_{9+x}]\text{O}_4$ ($x \approx -3.71$), which offered a great advantage due to distinguishability of Sr and La based on their different scattering factors contrary to Ba and La. $\text{Ba}_{22.5+x}\text{La}_{55-x}[\text{Si}_{129}\text{N}_{240-x}\text{O}_x]\text{O}_3$ ($x \approx 0.24$) and $\text{Ba}_{25.5+x}\text{La}_{77-x}[\text{Si}_{170}\text{N}_{312-x}\text{O}_{9+x}]\text{O}_4$ ($x \approx 0.24$) show complex but very similar crystal structures. The three-dimensional networks can formally be divided into two interconnected layers, of which one layer is present in both compounds and explains the notorious intergrowth. “ $\text{Sr}_{22.5+x}\text{La}_{55-x}[\text{Si}_{129}\text{N}_{240-x}\text{O}_x]\text{O}_3$ ” ($x \approx 0.24$) and $\text{Sr}_{28.5+x}\text{La}_{75-x}[\text{Si}_{170}\text{N}_{312-x}\text{O}_{9+x}]\text{O}_4$ ($x \approx -3.71$) crystallize isotypic to the Ba analogue compounds. Additionally to the unfavorable intergrowth, their crystal structures exhibit 21 or 28 mixed occupied and/or split cation sites, respectively, coordinated by both N and O in irregular polyhedra with coordination numbers ranging from 5 to 10. From experience, all these mentioned properties do normally not contribute to narrow band emission. Despite these prerequisites, “ $\text{Sr}_{22.5+x}\text{La}_{55-x}[\text{Si}_{129}\text{N}_{240-x}\text{O}_x]\text{O}_3:\text{Eu}^{2+}$ ” ($x \approx 0.24$) and $\text{Sr}_{28.5+x}\text{La}_{75-x}[\text{Si}_{170}\text{N}_{312-x}\text{O}_{9+x}]\text{O}_4$ ($x \approx -3.71$) exhibit unexpected but comparably relative narrow emission with $\lambda_{\text{em}} = 606 \text{ nm}$ and $\text{fwhm} = 78 \text{ nm}/2083 \text{ cm}^{-1}$. This leads to the assumption that narrow-band emission can best be attributed to rigid (highly condensed) host lattices with few lattice vibrations. High rigidity corresponds to small values of the Huang-Rhys parameter S resulting in a small Stokes-Shift (Chapter 1.3), which is favorable for narrow excitation and emission bands. The elucidation

of complex crystal structures in microcrystalline samples with intergrown domains would not have been feasible a few years ago due to the advances concerning both the development of TEM methods and microfocused synchrotron beams. The search for new host compounds will eventually lead to even more complex structures and therefore, the presented procedure of combining diffraction based state-of-the-art techniques like microfocused synchrotron radiation with TEM investigations assisted by charge distribution, lattice energy, and bond valence sum calculations is expected to become an established tool in future research that can provide high resolution data for accurate structure information even with smallest crystallites. This is highly important for more precise statements on structure-property relations and may indicate how to optimally tune materials for their respective applications.^[9] Stable and efficient materials nevertheless have potential, even if the emission is not narrow band as long as the wavelength fits an application area.

The results described in this thesis show that investigations on known compounds upon cationic and respectively or anionic substitution with access through previously less exploited synthesis routes and explorative synthesis of representatives of new or less studied compound classes lead to new phosphor materials for possible applications in various areas and prove the importance of future research. Further examination on $\text{Lu}_{6-x}\text{Ca}_{1.5x}\text{Si}_{11}\text{N}_{20}\text{O}:\text{Ce}^{3+}$ ($x \approx 2.2$), $\text{CaLu}[\text{Si}_4\text{N}_{7-2x}\text{C}_x\text{O}_x]:\text{Ce}^{3+}$ ($x \approx 0.3$) and $\text{CaLu}[\text{Si}_4\text{N}_{7-2x}\text{C}_x\text{O}_x]:\text{Eu}^{2+}$ ($x \approx 0.3$) are necessary to optimize quantum efficiency leading to even more interesting phosphors for modern 1pcLED illumination-grade warm-white lighting applications with increased color rendering index or to fill the blue-cyan gap in RGB-pcLEDs, which are of greater interest today since they target color points more accurately, offer higher efficiencies, and achieve higher CRIs. Further syntheses of $\text{RE}_{8-x}\text{AE}_x[\text{Si}_{10}\text{N}_{20-x}\text{O}_{2+x}]:\text{Eu}^{2+}$ and extensive investigations regarding luminescence properties with band structures and X-ray spectroscopy measurements are necessary to further understand the influences of different RE and AE on band structures, band gap sizes and position of Eu^{2+} 5d levels. With this knowledge, potential host materials and their luminescent properties can be improved and possibly be tunable to develop the highly desired narrow-band, super-efficient and chemically stable red phosphors.

The search for new compounds will eventually lead to more complex structures and therefore, in future research, the combination and advancement of different latest state-of-the-art measurement techniques assisted by various calculation methods is expected to become an established tool providing high resolution data for accurate structure elucidation even with smallest crystallites. Such data enable in combination with investigations on electronic and optical properties using X-ray spectroscopy more precise statements about structure-property relations and may indicate how to optimally tune

materials for their respective applications. “ $\text{Sr}_{22.5+x}\text{La}_{55-x}[\text{Si}_{129}\text{N}_{240-x}\text{O}_x]\text{O}_3:\text{Eu}^{2+}$ ” ($x \approx 0.24$) and $\text{Sr}_{28.5+x}\text{La}_{75-x}[\text{Si}_{170}\text{N}_{312-x}\text{O}_{9+x}]\text{O}_4$ ($x \approx -3.71$) are intended to serve as an example of the fact that it is worthwhile to investigate the possible properties of compounds or compound classes that are actually not very promising at first glance due to structural prerequisites. Even if this does not immediately lead to application-relevant compounds, general research can be expanded by the knowledge of structurally influenced properties in order to eventually directly design compounds with specific structural motifs that are optimally adapted to the desired properties.

References

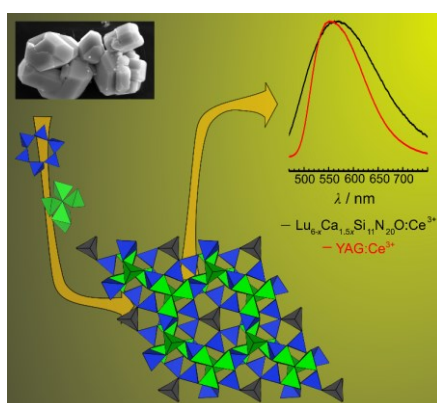
- [1] Deutsche Akademie der Naturforscher Leopoldina e. V., *Klimawandel: Ursachen, Folgen und Handlungsmöglichkeiten*, **2021**.
- [2] Deutsche Meteorologische Gesellschaft Deutsches Klima-Konsortium, Deutscher Wetterdienst, Extremwetterkongress Hamburg, Helmholtz-Klima-Initiative, klimafakten.de, *Was wir heute übers Klima wissen - Basisfakten zum Klimawandel, die in der Wissenschaft unumstritten sind*, **2021**.
- [3] C. Elliott, M. Yamada, J. Penning, S. Schober, K. Lee, *Energy Savings Forecast of Solid-State Lighting in General Illumination Applications*, U.S. Department of Energy, Office of Energy Efficiency and Renewable Energy, Building Technologies Office, Washington, D.C., **2019**.
- [4] Z. Xia, A. Meijerink, *Chem. Soc. Rev.* **2017**, *46*, 275–299.
- [5] J. L. Leaño Jr., M.-H. Fang, R.-S. Liu, *ECS J. Solid State Sci. Technol.* **2018**, *7*, R3111–R3133.
- [6] L. Gamperl, G. Krach, P. J. Schmidt, W. Schnick, *Eur. J. Inorg. Chem.* **2019**, *47*, 4985–4993.
- [7] L. Gamperl, O. E. O. Zeman, P. Strobel, P. J. Schmidt, W. Schnick, *Chem. Eur. J.* **2022**, *28*, e202104007–e202104014.
- [8] L. Gamperl, P. Strobel, P. J. Schmidt, W. Schnick, *Chem. Eur. J.* **2022**, e202200760–e202200767.
- [9] L. Gamperl, L. Neudert, P. Schultz, D. Durach, W. Schnick, O. Oeckler, *Chem. Eur. J.* **2021**, *27*, 12835–12844.
- [10] M. Woike, W. Jeitschko, *J. Solid State Chem.* **1997**, *129*, 312–319.
- [11] K. Köllisch, H. Höpfe, H. Huppertz, M. Orth, W. Schnick, *Z. Anorg. Allg. Chem.* **2001**, *627*, 1371–1376.
- [12] J. Park, J. W. Lee, *Korean J. Mater. Res.* **2021**, *31*, 188–194.
- [13] G. Blasse, *Prog. Solid State Chem.* **1988**, *18*, 79–171.

- [14] H. Huppertz, W. Schnick, *Angew. Chem. Int. Ed.* **1996**, *35*, 1983–1984; *Angew. Chem.* **1996**, *108*, 2115–2116.
- [15] C. Maak, L. Eisenburger, J. P. Wright, M. Nentwig, P. J. Schmidt, O. Oeckler, W. Schnick, *Inorg. Chem.* **2018**, *57*, 13840–13846.
- [16] J. J. Joos, J. Botterman, P. F. Smet, *J. Solid State Light.* **2014**, *1*, 1–16.
- [17] A. Piquette, W. Bergbauer, B. Galler, K. Mishra, *ECS J. Solid State Sci. Technol.* **2016**, *5*, R3146–R3159.
- [18] Y. Zhang, S. Li, T. Takeda, S. Funahashi, N. Hirotsuki, R.-J. Xie, *J. Mater. Chem. C* **2020**, *8*, 13458–13466.
- [19] H.-W. Zheng, X.-M. Wang, H.-W. Wei, Y. Zheng, C.-L. Yin, Z.-P. Yang, H. Jiao, *Chem. Commun.* **2021**, *57*, 3761–3764.
- [20] P. Pust, V. Weiler, C. Hecht, A. Tücks, A. S. Wochnik, A.-K. Henß, D. Wiechert, C. Scheu, P. J. Schmidt, W. Schnick, *Nat. Mater.* **2014**, *13*, 891–896.
- [21] G. J. Hoerder, M. Seibald, D. Baumann, T. Schröder, S. Peschke, P. C. Schmid, T. Tyborski, P. Pust, I. Stoll, M. Bergler, C. Patzig, S. Reißaus, M. Krause, L. Berthold, T. Höche, D. Johrendt, H. Huppertz, *Nat. Commun.* **2019**, *10*, 1824–1832.
- [22] S. Schmiechen, H. Schneider, P. Wagatha, C. Hecht, P. J. Schmidt, W. Schnick, *Chem. Mater.* **2014**, *26*, 2712–2719.

7 Summary

7.1 Synthesis of $RE_{6-x}Ca_{1.5x}Si_{11}N_{20}O$ ($RE = Yb, Lu; x \approx 2.2$) with $Lu_{6-x}Ca_{1.5x}Si_{11}N_{20}O:Ce^{3+}$ Offering Interesting Spectral Properties for Yellow-Emitting Phosphors in 1pcLEDs

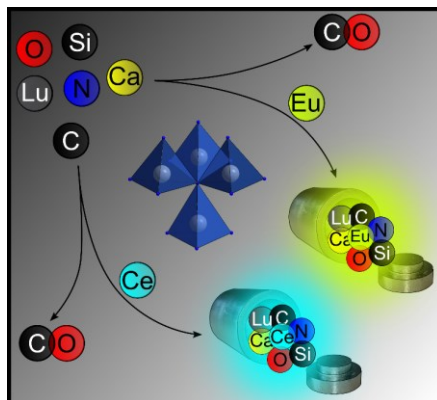
Lisa Gamperl, Georg Krach, Peter J. Schmidt, Wolfgang Schnick, *Eur. J. Inorg. Chem.* **2019**, 47, 4985–4993.



YAG:Ce³⁺ is a very commonly used phosphor in 1pcLED but its application is limited due to emission of cold-white light. In this chapter, the oxonitridosilicates $RE_{6-x}Ca_{1.5x}Si_{11}N_{20}O$ ($RE = Yb, Lu; x \approx 2.2$) are presented, of which $Lu_{6-x}Ca_{1.5x}Si_{11}N_{20}O:Ce^{3+}$ ($x \approx 2.2$) exhibits an interesting broadband yellow luminescence upon irradiation with UV to blue light. With $\lambda_{em} = 565$ nm and $fwhm$ of 168 nm/5100 cm⁻¹, the phosphor emits further in the red spectral region leading to warmer color temperatures and a higher color rendering index compared to YAG:Ce³⁺, thus being more suitable for warm-white illumination-grade 1pcLEDs. The crystal structure of dark red $Yb_{6-x}Ca_{1.5x}Si_{11}N_{20}O$ was solved and refined based on single-crystal X-ray diffraction data in the trigonal space group $P31c$ (no. 159) with $a = 9.8281(10)$, $c = 10.5968(13)$ Å and $Z = 2$. The structure represents a filled variant of the $Er_6Si_{11}N_{20}O$ structure type, in which the charge difference caused by substitution of trivalent RE^{3+} with bivalent Ca^{2+} is balanced by occupation of an additional third cation site. The replacement of RE by Ca leads to new structural features and could lead to the incorporation of oxygen in the anionic framework, which could have an influence on the luminescence properties. The results are confirmed by EDX measurements, Rietveld refinements based on powder X-ray diffraction data using the crystal data obtained from $Yb_{6-x}Ca_{1.5x}Si_{11}N_{20}O$ and both MAPLE and BVS calculations. Rietveld refinement of $Lu_{6-x}Ca_{1.5x}Si_{11}N_{20}O$ ($x \approx 2.2$) based on the refined single-crystal X-ray diffraction data of $Yb_{6-x}Ca_{1.5x}Si_{11}N_{20}O$ ($x \approx 2.2$) indicates that both compounds crystallize in the same structure type. Further research is necessary to optimize the quantum efficiency and therefore make $Lu_{6-x}Ca_{1.5x}Si_{11}N_{20}O:Ce^{3+}$ ($x \approx 2.2$) an even more interesting phosphor for modern illumination-grade warm-white lighting applications with increased color rendering index.

7.2 Missing Member in the $M^I M^{III} \text{Si}_4 \text{N}_7$ Compound Class: Carbothermal Reduction and Nitridation Synthesis Revealing Substitution of N by C and O in $\text{CaLu}[\text{Si}_4 \text{N}_{7-2x} \text{C}_x \text{O}_x]:\text{Eu}^{2+}/\text{Ce}^{3+}$ ($x \approx 0.3$)

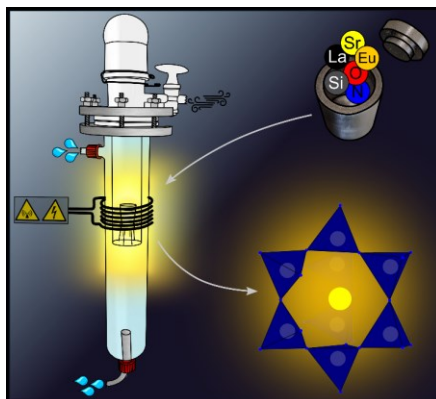
Lisa Gamperl, Otto E. O. Zeman, Philipp Strobel, Peter J. Schmidt, Wolfgang Schnick, *Chem. Eur. J.* **2022**, *28*, e202104007– e202104014.



The $M^I M^{III} \text{Si}_4 \text{N}_7$ compound class does not only offer interesting structural features like star shaped $[\text{N}^{4-}(\text{SiN}_3)_4]$ units with rare fourfold bridging ammonium-type N, but also provides doping possibilities for both application relevant activator ions Eu^{2+} and Ce^{3+} . However, especially the access to compounds with $M^I = \text{Ca}^{2+}$ is limited due to the small cation size. Therefore, other synthetic strategies like carbothermal reduction and nitridation (CRN) using elemental carbon as a reducing agent to facilitate the reaction are necessary. CRN could enable the synthesis of previously unknown host structures for rare earth doping to develop novel luminescent materials. $\text{CaLu}[\text{Si}_4 \text{N}_{7-2x} \text{C}_x \text{O}_x]$ ($x \approx 0.3$) was synthesized via the CRN method and crystallizes in space group $P6_3mc$ (no. 186). Carbon incorporation was confirmed via ^{13}C - and ^{29}Si -MAS-NMR spectroscopy. For the first time in the $M^I M^{III} \text{Si}_4 \text{N}_7$ compound class, complementary EDX measurements suggest that simultaneous incorporation of oxygen compensates for the negative charge excess induced by C. When excited with UV to blue light, $\text{CaLu}[\text{Si}_4 \text{N}_{7-2x} \text{C}_x \text{O}_x]$ ($x \approx 0.3$) shows an emission maximum in the blue spectral region ($\lambda_{\text{em}} = 484 \text{ nm}$; $\text{fwhm} = 4531 \text{ cm}^{-1}$) upon doping with Ce^{3+} , while Eu^{2+} -doped $\text{CaLu}[\text{Si}_4 \text{N}_{7-2x} \text{C}_x \text{O}_x]$ ($x \approx 0.3$) exhibits a yellow-green emission ($\lambda_{\text{em}} = 546 \text{ nm}$; $\text{fwhm} = 3999 \text{ cm}^{-1}$). Broadband emitting yellow emitting phosphors with proportions in the red spectral range could be used to replace YAG: Ce^{3+} in 1pcLEDs leading to warm-white light emission. Blue broadband emitting phosphors can cover the blue-cyan gap between the spectrum of a narrow emitting nUV primary LED and the emission of the yellow-green phosphor in RGB-pcLED, leading to high color quality and making the nUV primary LEDs more appealing. As known so far, $\text{CaLu}[\text{Si}_4 \text{N}_{7-2x} \text{C}_x \text{O}_x]$ is the first oxonitridocarbidosilicate in this compound class and just the second oxonitridocarbidosilicate in general.

7.3 Synthesis and Luminescence Properties of Amber Emitting $\text{La}_7\text{Sr}[\text{Si}_{10}\text{N}_{19}\text{O}_3]:\text{Eu}^{2+}$ and Syntheses of the Substitutional Variants $\text{RE}_{8-x}\text{AE}_x[\text{Si}_{10}\text{N}_{20-x}\text{O}_{2+x}]:\text{Eu}^{2+}$ with $\text{RE} = \text{La}, \text{Ce}; \text{AE} = \text{Ca}, \text{Sr}, \text{Ba}; 0 \leq x \leq 2$

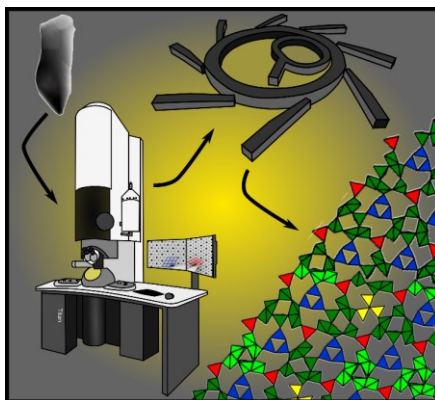
Lisa Gamperl, Philipp Strobel, Peter J. Schmidt, Wolfgang Schnick, *Chem. Eur. J.* **2022**, *28*, e202200760–e202200767.



Current state-of-the-art white light emitting LEDs are based on 2pcLEDs, which suffer from broad red emission bands leading to energy loss in the IR range. Therefore, research is focused on exploring new highly efficient narrow-band orange-red phosphors for usage in lighting applications, for which the barely investigated La-Sr-Si-N-O system is promising. In this chapter, we present the oxonitridosilicate $\text{La}_7\text{Sr}[\text{Si}_{10}\text{N}_{19}\text{O}_3]$ crystallizing in the orthorhombic space group $Pmn2_1$ (no. 31), which was solved and refined based on single-crystal X-ray diffraction data. Due to the mixed cation and anion sites and the charge neutral exchangeability of LaN vs. SrO, the solid solution series $\text{La}_{8-x}\text{Sr}_x[\text{Si}_{10}\text{N}_{20-x}\text{O}_{2+x}]$ ($0 \leq x \leq 2$) was synthesized. Additionally, similar ionic radii of La and Ce as well as Sr, Ca and Ba led to the syntheses of the solid solution series of the substitutional variants $\text{RE}_{8-x}\text{AE}_x[\text{Si}_{10}\text{N}_{20-x}\text{O}_{2+x}]$ ($\text{RE} = \text{La}, \text{Ce}; \text{AE} = \text{Ca}, \text{Sr}, \text{Ba}; 0 \leq x \leq 2$). The compound class $\text{RE}_{8-x}\text{AE}_x[\text{Si}_{10}\text{N}_{20-x}\text{O}_{2+x}]$ offers a broad variety of full or partial substitution possibilities and therefore, could be an interesting host material class for tunability upon Eu^{2+} doping. Upon excitation with UV to blue light, $\text{La}_7\text{Sr}[\text{Si}_{10}\text{N}_{19}\text{O}_3]:\text{Eu}^{2+}$ is only the second known Eu^{2+} -doped phosphor in the La-Sr-Si-O-N system so far and shows amber luminescence with $\lambda_{\text{em}} = 612 \text{ nm}$ and $fwhm = 84 \text{ nm}/2194 \text{ cm}^{-1}$, which makes it interesting for application in amber pcLEDs. Furthermore, the two predominant theories for explaining thermal quenching behavior of activator ions in phosphors were thoroughly discussed with respect to the offered structural characteristics. Further syntheses of $\text{RE}_{8-x}\text{AE}_x[\text{Si}_{10}\text{N}_{20-x}\text{O}_{2+x}]:\text{Eu}^{2+}$ and extensive investigations regarding luminescence properties, band structures and RIXS measurements are necessary to further understand the influences of different RE and AE on band structures, band gap sizes and position of Eu^{2+} 5d levels. With this knowledge, potential host materials and their luminescent properties can be improved and possibly be tunable to develop the highly desired narrow-band and super-efficient red phosphors.

7.4 Structure Elucidation of Complex Endotaxially Intergrown Lanthanum Barium Oxonitridosilicate Oxides by Combination of Microfocused Synchrotron Radiation and Transmission Electron Microscopy

Lisa Gamperl, Lukas Neudert, Peter Schultz, Dajana Durach, Wolfgang Schnick, Oliver Oeckler, *Chem. Eur. J.* **2021**, 27, 12835–12844.



It is sometimes impossible to obtain sufficiently sized single crystals or phase pure powder samples to elucidate the structure of new compounds with conventional X-ray diffraction. The combination of TEM with synchrotron methods enables the precise structural characterization of unique microcrystalline phases. So far, this approach has not been applied to get access to single-crystal data from samples with oriented intergrowth and overlapping diffraction patterns, impeding accurate crystal structure determination. Single crystalline domains of intergrown microcrystalline $\text{Ba}_{22.5+x}\text{La}_{55-x}[\text{Si}_{129}\text{N}_{240-x}\text{O}_x]\text{O}_3$ and $\text{Ba}_{25.5+x}\text{La}_{77-x}[\text{Si}_{170}\text{N}_{312-x}\text{O}_{9+x}]\text{O}_4$ were identified by TEM. Precise diffraction data from these domains were collected with microfocused synchrotron radiation enabling crystal structure elucidation of the complex disordered networks. They are composed of two different interconnected slabs of which one is similar in both compounds explaining their notorious intergrowth. The distribution of Ba and La is indicated by BVS analysis and comparison with isostructural $\text{Sr}_{28.5+x}\text{La}_{75-x}[\text{Si}_{170}\text{N}_{312-x}\text{O}_{9+x}]\text{O}_4$. Ce^{3+} doping leads to yellow luminescence. Compared to phosphors with similar emission characteristics but fewer cation sites, the reported complex and disordered compounds do not show significantly broader emission. This showcase highlights the discovery and accurate characterization of new compounds relevant for luminescence applications from heterogeneous microcrystalline samples by exploiting the capability of the combination of TEM and diffraction using the latest focusing techniques for synchrotron radiation. In future research, microfocused synchrotron radiation assisted by TEM studies are expected to become an established tool providing high resolution data for accurate structure information even with smallest crystallites. Such data enable more precise statements about structure-property relations and may indicate how to optimally tune materials for required applications.

8 Appendix

A. Supporting Information for Chapter 2

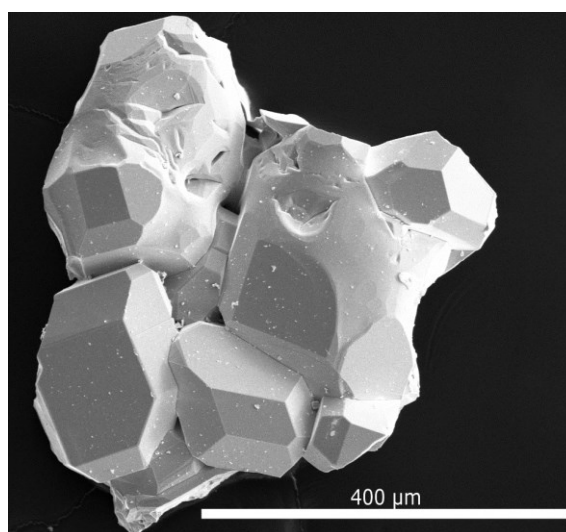


Figure A1. SEM image of $\text{Yb}_{6-x}\text{Ca}_{1.5x}\text{Si}_{11}\text{N}_{20}\text{O}$ ($x \approx 2.2$) crystals.

Table A1. Results in atom% for 12 EDX point-measurements of 12 different $\text{Yb}_{6-x}\text{Ca}_{1.5x}\text{Si}_{11}\text{N}_{20}\text{O}$ ($x \approx 2.2$) crystals

Measurement	Yb	Ca	Si	N	O
1	8.6	5.8	25.2	56.9	3.5
2	8.7	6.0	25.6	53.8	5.9
3	14.1	9.2	31.2	42.3	3.1
4	12.1	7.7	29.9	47.6	2.8
5	8.6	5.9	25.8	53.9	5.8
6	8.9	5.9	26.3	53.4	5.6
7	9.0	6.0	26.8	51.2	7.1
8	13.0	7.6	30.5	46.2	2.7
9	8.8	4.3	24.4	56.2	6.3
10	12.0	7.8	29.5	47.5	2.8
11	12.0	7.4	29.5	48.9	2.2
12	9.6	6.3	27.5	53.5	3.1
Average	10.5	6.7	27.7	50.9	4.2
Deviation	2.1	1.4	2.3	4.4	1.3
Theoretical value $\text{Yb}_{3.79}\text{Ca}_{3.22}\text{Si}_{11}\text{N}_{20}\text{O}$	9.7	8.3	28.2	51.3	2.6

Table A2. Data for the Rietveld refinement of an $\text{Yb}_{6-x}\text{Ca}_{1.5x}\text{Si}_{11}\text{N}_{20}\text{O}$ ($x \approx 2.2$) sample based on the $\text{Yb}_{3.79}\text{Ca}_{3.22}\text{Si}_{11}\text{N}_{20}\text{O}$ single-crystal data (standard deviations in parentheses). Only lattice parameters and the constrained atomic coordinates of Yb/Ca1, Yb/Ca2 and Yb/Ca3 were refined. The site occupancy factors as well as the isotropic displacement parameters for all sites were taken from the single-crystal data of $\text{Yb}_{3.79}\text{Ca}_{3.22}\text{Si}_{11}\text{N}_{20}\text{O}$, in which the single-crystal U_{eq} values were converted into B_{iso} values by $B_{\text{iso}} = U_{\text{eq}} \times 8\pi^2$

Formula	$\text{Yb}_{3.79}\text{Ca}_{3.22}\text{Si}_{11}\text{N}_{20}\text{O}$	
formula mass / $\text{g}\cdot\text{mol}^{-1}$	1416.945	
crystal system	trigonal	
space group	$P31c$ (no. 159)	
lattice parameters / \AA	$a =$	9.85869(9)
	$c =$	10.65021(12)
$V / \text{\AA}^3$	896.452(19)	
Z	2	
X-ray density / $\text{g}\cdot\text{cm}^{-3}$	5.2494(1)	
diffractometer	Stoe StadiP	
radiation	$\text{Cu-K}\alpha_1$ ($\lambda = 1.54056 \text{ \AA}$)	
monochromator	$\text{Ge}(111)$	
detector	MYTHEN 1K	
$F(000)$	1292	
2θ range / $^\circ$	$9 \leq 2\theta \leq 121$	
data points	7488	
number of observed reflections	468	
refined parameters	32	
constraints	7	
structure refinement	Rietveld-Method	
background function	Shifted Chebyshev, 12 polynomials	
R values	$R_p =$	5.435
	$R_{\text{wp}} =$	7.567
	$R_{\text{exp}} =$	1.203
	$R_{\text{Bragg}} =$	3.201
$\text{Goof} (\chi^2)$	6.292	

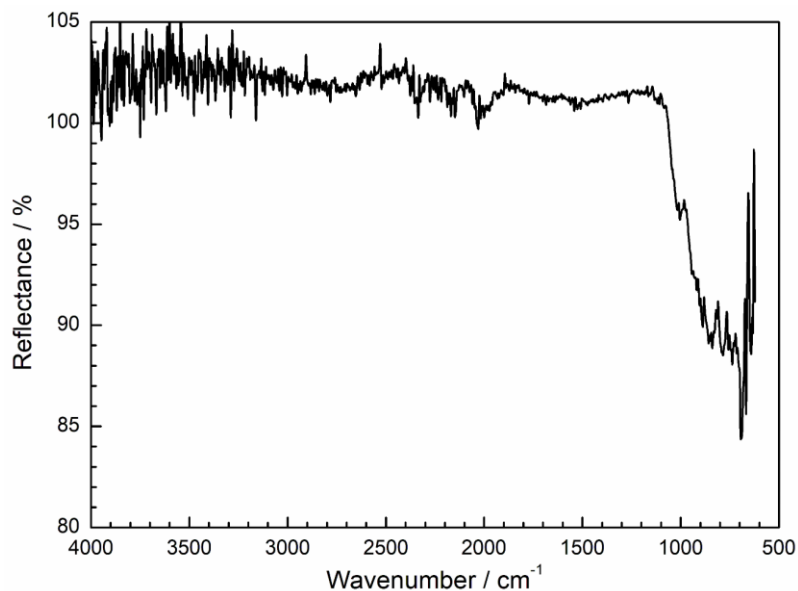


Figure A2. ATR-FTIR spectrum of an $\text{Yb}_{6-x}\text{Ca}_{1.5x}\text{Si}_{11}\text{N}_{20}\text{O}$ ($x \approx 2.2$) powder sample. There are no clearly recognizable signals in the range of $3500\text{--}3000\text{ cm}^{-1}$, the typical region where N-H vibrations would occur.

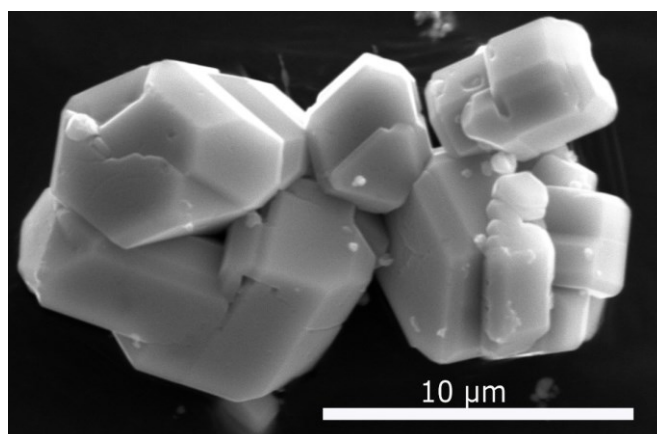


Figure A3. SEM image of $\text{Lu}_{6-x}\text{Ca}_{1.5x}\text{Si}_{11}\text{N}_{20}\text{O}$ ($x \approx 2.2$) crystals.

Table A3. Results in atom% for 21 EDX point-measurements of 21 different $\text{Lu}_{6-x}\text{Ca}_{1.5x}\text{Si}_{11}\text{N}_{20}\text{O}$ ($x \approx 2.2$) crystallites

Measurement	Lu	Ca	Si	N	O	F
1	9.7	9.9	27.7	44.6	9.6	1.2
2	6.0	6.1	22.8	50.0	13.5	1.7
3	9.0	9.5	30.5	45.3	4.7	1.0
4	6.7	7.4	25.9	52.3	6.2	1.5
5	8.6	9.4	28.4	44.9	7.7	1.2
6	5.6	6.6	23.3	56.6	6.5	1.5
7	5.6	6.6	23.5	55.1	7.9	1.2
8	6.6	11.6	29.0	46.5	5.2	1.1
9	7.5	5.8	25.7	53.5	6.4	1.1
10	6.3	5.2	23.0	55.8	8.2	1.4
11	6.1	5.0	21.7	56.2	9.6	1.4
12	7.4	6.1	25.0	51.3	9.1	1.1
13	6.3	5.0	22.6	56.4	8.2	1.5
14	8.5	10.1	30.6	44.5	5.2	1.2
15	6.6	5.5	23.8	56.0	6.8	1.4
16	8.0	6.4	26.0	53.2	5.5	1.0
17	6.9	8.4	27.8	50.4	5.3	1.2
18	7.1	6.4	25.7	53.2	6.4	1.3
19	10.4	9.2	30.8	44.0	4.5	1.1
20	9.8	4.4	26.5	52.5	6.1	0.7
21	10.0	4.2	26.4	52.4	6.0	1.0
Average	7.5	7.1	26.0	51.2	6.9	1.2
Deviation	1.5	2.1	2.8	4.5	2.0	0.2
Theoretical value $\text{Lu}_{3.79}\text{Ca}_{3.22}\text{Si}_{11}\text{N}_{20}\text{O}$	9.7	8.3	28.2	51.3	2.6	--

Table A4. Data for the Rietveld refinement of a $\text{Lu}_{6-x}\text{Ca}_{1.5x}\text{Si}_{11}\text{N}_{20}\text{O}$ ($x \approx 2.2$) sample based on the $\text{Yb}_{3.79}\text{Ca}_{3.22}\text{Si}_{11}\text{N}_{20}\text{O}$ single-crystal data (standard deviations in parentheses). Only lattice parameters and the constrained atomic coordinates of Lu/Ca1, Lu/Ca2 and Lu/Ca3 were refined. The site occupancy factors as well as the isotropic displacement parameters for all sites were taken from the single-crystal data of $\text{Yb}_{3.79}\text{Ca}_{3.22}\text{Si}_{11}\text{N}_{20}\text{O}$, in which the single-crystal U_{eq} values were converted into B_{iso} values by $B_{\text{iso}} = U_{\text{eq}} \times 8\pi^2$

Formula	$\text{Lu}_{3.79}\text{Ca}_{3.22}\text{Si}_{11}\text{N}_{20}\text{O}$
formula mass / $\text{g}\cdot\text{mol}^{-1}$	1424.24
crystal system	trigonal
space group	$P31c$ (no. 159)
lattice parameters / \AA	$a =$
	$c =$
$V / \text{\AA}^3$	887.45(7)
Z	2
X-ray density / $\text{g}\cdot\text{cm}^{-3}$	5.32955
diffractometer	Stoe StadiP
radiation	$\text{Cu-K}\alpha_1$ ($\lambda = 1.54056 \text{ \AA}$)
monochromator	Ge(111)
detector	MYTHEN 1K
$F(000)$	1300
2θ range / $^\circ$	$9 \leq 2\theta \leq 122$
data points	7560
number of observed reflections	468
number of parameters	32
constraints	7
structure refinement	Rietveld-Method
background function	Shifted Chebyshev, 12 polynomials
R values	$R_p =$
	$R_{wp} =$
	$R_{\text{exp}} =$
	$R_{\text{Bragg}} =$
$\text{GooF} (\chi^2)$	2.989

Table A5. Wyckoff positions, atomic coordinates, isotropic displacement parameters (\AA^2) and site occupancy factors of $\text{Yb}_{3.79}\text{Ca}_{3.22}\text{Si}_{11}\text{N}_{20}\text{O}$. Standard deviations in parentheses. Si4/Si5 split position. Yb/Ca1, Yb/Ca2 and Yb/Ca3 occupy the same site, respectively

Atom	Wyckoff Positions	x	y	z	U_{eq}	s.o.f.
Yb1	6c	-0.26225(6)	-0.13314(7)	-0.41327(4)	0.0099(2)	0.760(11)
Ca1	6c	-0.26225(6)	-0.13314(7)	-0.41327(4)	0.0099(2)	0.241(18)
Yb2	6c	-0.39893(10)	-0.20032(10)	-0.09095(9)	0.0134(4)	0.474(10)
Ca2	6c	-0.39893(10)	-0.20032(10)	-0.09095(9)	0.0134(4)	0.526(16)
Yb3	2b	-1/3	-2/3	-0.3618(3)	0.0126(11)	0.083(11)
Ca3	2b	-1/3	-2/3	-0.3618(3)	0.0126(11)	0.916(17)
Si1	6c	-0.1286(3)	-0.5729(4)	-0.0779(3)	0.0070(6)	1
Si2	6c	-0.1593(4)	-0.3402(4)	-0.2290(3)	0.0069(6)	1
Si3	6c	-0.5297(4)	-0.0002(3)	-0.3380(3)	0.0075(6)	1
Si4	2b	-1/3	-2/3	-0.8453(10)	0.0070(13)	0.514(13)
Si5	2b	-1/3	-2/3	-0.7577(12)	0.0070(13)	0.485(13)
Si6	2a	0	0	-0.1612(6)	0.0066(9)	1
N1	6c	-0.4912(11)	-0.3144(11)	-0.2970(9)	0.0094(17)	1
N2	6c	-0.4309(11)	-0.0132(12)	-0.4693(9)	0.0104(18)	1
N3	6c	-0.1696(13)	-0.0071(13)	-0.2174(10)	0.0119(18)	1
N4	6c	-0.2674(11)	-0.3810(12)	-0.3671(9)	0.0102(18)	1
N5	6c	-0.2775(12)	-0.3682(11)	-0.0986(8)	0.0082(16)	1
N6	2b	-1/3	-2/3	-0.040(2)	0.017(4)	1
N7	2a	0	0	0.0000(17)	0.017(4)	1
N8	6c	-0.0982(12)	-0.4814(11)	-0.2242(9)	0.0100(17)	1
O1	2b	-1/3	-2/3	-0.576(2)	0.025(4)	1

Table A6. Anisotropic displacement parameters (U_{ij} in \AA^2) of $\text{Yb}_{3.79}\text{Ca}_{3.22}\text{Si}_{11}\text{N}_{20}\text{O}$. Standard deviations in parentheses. Yb/Ca1, Yb/Ca2, Yb/Ca3 and Si4/Si5 were refined with equal atomic displacement parameters, respectively

Atom	U_{11}	U_{22}	U_{33}	U_{23}	U_{13}	U_{12}
Yb1	0.0117(3)	0.0098(3)	0.0072(3)	0.0045(2)	-0.0007(2)	-0.00097(18)
Ca1	0.0117(3)	0.0098(3)	0.0072(3)	0.0045(2)	-0.0007(2)	-0.00097(18)
Yb2	0.0174(5)	0.0133(5)	0.0106(5)	0.0086(4)	0.0016(3)	-0.0007(3)
Ca2	0.0174(5)	0.0133(5)	0.0106(5)	0.0086(4)	0.0016(3)	-0.0007(3)
Yb3	0.0092(12)	U_{11}	0.0195(17)	0.0046(6)	0	0
Ca3	0.0092(12)	U_{11}	0.0195(17)	0.0046(6)	0	0
Si1	0.0088(13)	0.0079(13)	0.0041(12)	0.0040(11)	0.0004(10)	0.0008(10)
Si2	0.0074(12)	0.0090(14)	0.0042(11)	0.0041(11)	0.0009(10)	-0.0004(10)
Si3	0.0080(13)	0.0101(14)	0.0047(11)	0.0048(12)	-0.001(1)	-0.0013(10)
Si4	0.0073(18)	U_{11}	0.006(2)	0.0037(9)	0	0
Si5	0.0073(18)	U_{11}	0.006(2)	0.0037(9)	0	0
Si6	0.0073(13)	U_{11}	0.0052(18)	0.0037(6)	0	0
N1	0.006(4)	0.008(4)	0.012(4)	0.003(3)	0.002(3)	0.001(3)
N2	0.008(4)	0.014(4)	0.012(4)	0.007(4)	0.000(3)	-0.004(4)
N3	0.013(4)	0.009(4)	0.018(4)	0.009(3)	-0.002(4)	-0.002(4)
N4	0.008(4)	0.013(4)	0.010(4)	0.006(3)	-0.001(3)	0.000(3)
N5	0.008(4)	U_{11}	0.006(4)	0.002(3)	-0.001(3)	-0.002(3)
N6	0.004(4)	U_{11}	0.043(13)	0.002(2)	0	0
N7	0.022(6)	U_{11}	0.008(7)	0.011(3)	0	0
N8	0.012(4)	0.011(4)	0.010(4)	0.008(4)	-0.001(3)	0.000(3)
O1	0.012(5)	U_{11}	0.052(13)	0.006(2)	0	0

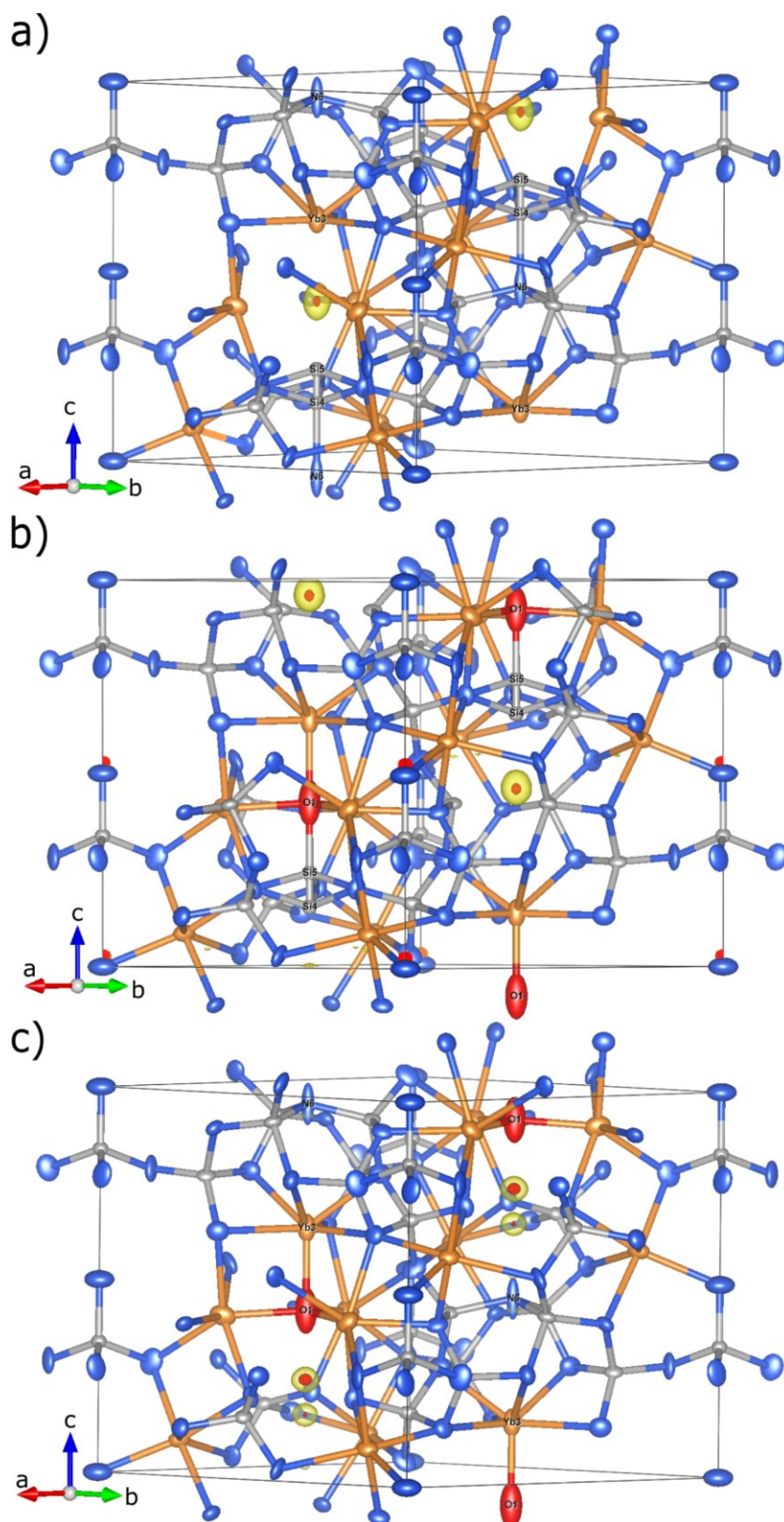


Figure A4. Isosurface levels of the difference Fourier synthesis ($F_{\text{obs}} - F_{\text{calc}}$) of the electron density of $\text{Yb}_{6-x}\text{Ca}_{1.5x}\text{Si}_{11}\text{N}_{20}\text{O}$ ($x \approx 2.2$) located at (a) $\text{O1}^{[1]}$ (isosurface levels: yellow: 3, red: 8), (b) $\text{N6}^{[4]}$ (yellow: 2, red: 7) and (c) Si4/Si5 (yellow: 5, red: 13) of $\text{Yb}_{6-x}\text{Ca}_{1.5x}\text{Si}_{11}\text{N}_{20}\text{O}$. Displacement ellipsoids show 95% probability. N: blue, O: red, Si: gray, Yb/Ca: orange. Visualized by VESTA.^[1]

Table A7. Partial and total MAPLE^[2] values in $\text{kJ}\cdot\text{mol}^{-1}$ calculated for $\text{Yb}_{3.79}\text{Ca}_{3.22}\text{Si}_{11}\text{N}_{20}\text{O}$ (1.) with variations (“O7”, 4. and “N11”, 5.) and “ $\text{Yb}_6\text{Si}_{11}\text{N}_{20}\text{O}$ ” (Si and N sites renamed according to $\text{Yb}_{3.79}\text{Ca}_{3.22}\text{Si}_{11}\text{N}_{20}\text{O}$ for better comparison, 3.), sum of total MAPLE values of ionic compounds, which form $\text{Yb}_{3.79}\text{Ca}_{3.22}\text{Si}_{11}\text{N}_{20}\text{O}$ in a theoretical reaction (2.) and deviations of the calculated MAPLE value sums. Approximations made for an accurate representation of the actual structure: for mixed occupancy, the ionic radii and the charges were weighted by the site occupancy factors of Yb and Ca for the respective sites. Under-occupation was taken into account by multiplying the site occupancy factors with the charge of the respective ions. For the split position, the z values of Si4 and Si5 were averaged (better representation of the actual structural situation in the crystal than two very close Si atoms ($d = 0.929(17)$ Å) with charges of about +2 each according to their site occupancy factors). The difference of the total MAPLE values for the title compound and “ $\text{Yb}_6\text{Si}_{11}\text{N}_{20}\text{O}$ ” could be owed to the cation mixed. Comparison of the total MAPLE sum of the hypothetical reactions of binary and ternary starting materials leads to a higher deviation probably due to the adjustments made

1.

Yb/Ca1 (76%/24%)	Yb/Ca2 (47%/53%)	Yb/Ca3 (9%/91%)	Si1	Si2	Si3	Si45	Si6		
4076	3274	2011	9514	9961	9713	9734	10670		
N1 ^[3]	N2 ^[2]	N3 ^[2]	N4 ^[2]	N5 ^[2]	N6 ^[4]	N7 ^[1]	N8 ^[3]	O1 ^[1]	
5724	5346	5165	5332	5540	6122	4357	6085	2012	

Total MAPLE value: **244215**

2.

$(9.37 \text{ YbN}^{[3]} + \text{Yb}_2\text{O}_3^{[4]} + 2 \text{ Si}_3\text{N}_4^{[5]} + 5.4 \text{ Ca}_2\text{Si}_5\text{N}_8^{[6]} - 0.57 \text{ Ca}_2\text{N}^{[7]})/3$
 $(9.37 \times 9125 + 15523 + 2 \times 52964 + 5.4 \times 98596 - 0.57 \times 5846)/3$

Total MAPLE value: **240498**

$\Delta = 1.5\%$

3. “ $\text{Yb}_6\text{Si}_{11}\text{N}_{20}\text{O}$ ”^[8]

Yb1 (99.1%)	Yb2 (99.1%)	Yb3 (5%)	Si1	Si2	Si3	Si45	Si6		
4569	4402	34	9496	9733	9678	9899	10186		
N1 ^[3]	N2 ^[2]	N3 ^[2]	N4 ^[2]	N5 ^[2]	N6 ^[4]	N7 ^[1]	N8 ^[3]	O1 ^[1]	
5711	5283	5302	5282	5635	5872	4566	6308	2235	

Total MAPLE value: **246990**

$\Delta = 1.18\%$

4. “O7”

Yb/Ca1 (76%/24%)	Yb/Ca2 (47%/53%)	Yb/Ca3 (9%/91%)	Si1	Si2	Si3	Si45	Si6		
3512	2985	1861	9188	9441	9376	9447	9256		
N1	N2	N3	N4	N5	N6	“O7”	N8	O1	
5981	5626	5789	5682	5909	6342	2727	6341	2158	

Total MAPLE value: **241397**

$\Delta = 1.15\%$

5. “O7”, “N11”

Yb/Ca1 (76%/24%)	Yb/Ca2 (47%/53%)	Yb/Ca3 (9%/91%)	Si1	Si2	Si3	Si45	Si6		
3760	3484	2298	9638	9834	9905	10235	9548		
N1	N2	N3	N4	N5	N6	“O7”	N8	“N11”	
5509	5217	5532	5301	5594	6041	2580	5983	3582	

Total MAPLE value: **243671**

$\Delta = 0.22\%$

Typical partial MAPLE values in nitridosilicates ($\text{kJ}\cdot\text{mol}^{-1}$):^[9]

RE^{3+}	3500–5100	$N^{[1]3-}$	4300–5000	$O^{[1]2-}$	2000–2800
Ca^{2+}	1700–2200	$N^{[2]3-}$	4600–6000	$O^{[2]2-}$	2400–2800
Si^{4+}	9000–10200	$N^{[3]3-}$	5000–6200		

Table A8. Values of bond valence sum (BVS) calculations for $\text{Yb}_{3.79}\text{Ca}_{3.22}\text{Si}_{11}\text{N}_{20}\text{O}$ using VaList^[10]

Atom	$\text{Yb}_{3.79}\text{Ca}_{3.22}\text{Si}_{11}\text{N}_{20}\text{O}$	“O7”	“O7”, “N11”
Yb/Ca1	2.58	2.47	2.47
Yb/Ca2	2.36	2.36	2.55
Yb/Ca3	2.57	2.57	2.82
Si1	3.95	3.95	3.95
Si2	3.98	3.98	3.98
Si3	3.95	3.95	3.95
Si4/Si5	3.67	3.67	3.74
Si6	3.98	3.74	3.74
N1	-3.05	-3.05	-3.05
N2	-2.68	-2.68	-2.68
N3	-2.94	-2.94	-2.94
N4	-2.98	-2.98	-2.98
N5	-3.00	-3.00	-3.00
N6	-2.85	-2.85	-2.85
N7	-2.35	-1.75 “O7”	-1.75 “O7”
N8	-3.20	-3.20	-3.20
O1	-1.97	-1.97	-2.88 “N11”

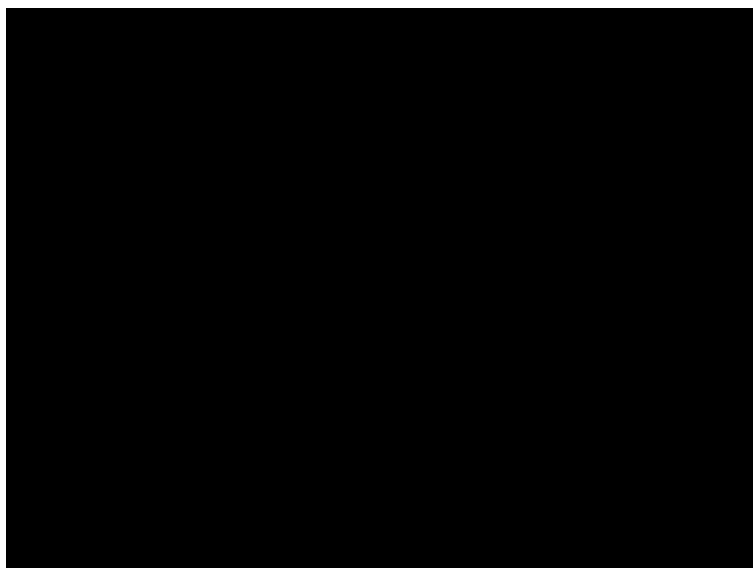


Figure A5. Normalized emission spectrum of $\text{Lu}_{6-x}\text{Ca}_{1.5x}\text{Si}_{11}\text{N}_{20}\text{O}:\text{Eu}^{2+}$ ($x \approx 2.2$, $\lambda_{\text{exc}} = 440$ nm).

Table A9. Comparison of $\text{Lu}_{6-x}\text{Ca}_{1.5x}\text{Si}_{11}\text{N}_{20}\text{O}:\text{Ce}^{3+}$ samples with different nominal doping contents ($x \approx 2.2$, $\lambda_{\text{exc}} = 440$ nm)

mol%	$\lambda_{\text{em}} / \text{nm}$	<i>fwhm</i> / nm / cm^{-1}	QE / %	Color Coordinates (CIE 1931)	
				x	y
0.5	546	175 / 5428	14	0.417	0.502
1	584	179 / 5164	17	0.460	0.494
2	598	187 / 5243	12	0.470	0.484
4	603	173 / 4643	14	0.502	0.473

References

- [1] K. Momma, F. Izumi, *J. Appl. Crystallogr.* **2011**, *44*, 1272–1276.
- [2] R. Hübenthal, *Maple, Program for the Calculation of MAPLE values*, version 4; University of Gießen: Gießen, Germany, **1993**.
- [3] W. Klemm, G. Winkelmann, *Z. Anorg. Allg. Chem.* **1956**, *228*, 87–90.
- [4] T. Schleid, G. Meyer, *J. Less-Common Met.* **1989**, *149*, 73–80.
- [5] P. Yang, H.-K. Fun, I. A. Rahman, M. I. Saleh, *Ceram. Int.* **1995**, *21*, 137–142.
- [6] T. Schlieper, W. Schnick, *Z. Anorg. Allg. Chem.* **1995**, *621*, 1037–1041.
- [7] O. Reckeweg, F. J. DiSalvo, *Z. Anorg. Allg. Chem.* **2001**, *627*, 371–377.
- [8] K. Köllisch, H. Höpfe, H. Huppertz, M. Orth, W. Schnick, *Z. Anorg. Allg. Chem.* **2001**, *627*, 1371–1376.
- [9] M. Zeuner, S. Pagano, W. Schnick, *Angew. Chem. Int. Ed.* **2011**, *50*, 7754–7775; *Angew. Chem.* **2011**, *123*, 7898–7920.
- [10] A. S. Wills, *Valist*, Program available from www.ccp14.ac.uk, **2010**.

B. Supporting Information for Chapter 3

Table B1. Wyckoff positions, atomic coordinates, and isotropic displacement parameters (\AA^2) of $\text{CaLuSi}_4\text{N}_{6.4}\text{C}_{0.3}\text{O}_{0.3}$. Estimated standard deviations are given in in parentheses

Atom	Wyckoff Position	s.o.f.	x	y	z	U_{iso}
Lu1	2b	1	1/3	2/3	0.07984(12)	0.0105(3)
Ca1	2b	1	1/3	2/3	0.4386(3)	0.0123(9)
Si1	2a	1	0	0	0.0057(8)	0.014(2)
Si2	6c	1	0.8299(4)	0.1701(4)	0.2664(4)	0.0103(6)
N1		0.95				
O1	6c	0.05	0.5155(10)	0.4845(10)	0.2200(7)	0.010(2)
N2		0.95				
O2	6c	0.05	0.8406(12)	0.1594(12)	0.4352(8)	0.034(3)
N3		0.7				
C3	2a	0.3	0	0	0.1959(15)	0.050(5)

Table B2. Results (in atom%) of SEM-EDX point measurements of $\text{CaLuSi}_4\text{N}_{6.4}\text{C}_{0.3}\text{O}_{0.3}$ before heating for purification (estimated standard deviations in parentheses)

Measurement	Ca	Lu	Si	N	O	C
1	7	8	31	45	8	-
2	7	7	30	47	10	-
3	6	7	29	50	8	-
4	8	10	34	41	7	-
average and standard deviation	7(1)	8(2)	31(2)	46(4)	8(1)	-
calculated for $\text{CaLuSi}_4\text{N}_{6.4}\text{C}_{0.3}\text{O}_{0.3}$	8	8	31	49	2	2

Table B3. Results (in atom%) of TEM-EDX point measurements of $\text{CaLuSi}_4\text{N}_{6.4}\text{C}_{0.3}\text{O}_{0.3}$ before heating for purification (estimated standard deviations in parentheses)

Measurement	Ca	Lu	Si ^[a]	N ^[a]	O	C
1	10	8	40	23	9	10
2	11	10	45	21	8	6
3	11	9	44	22	6	8
4	11	9	44	22	6	8
average and standard deviation	10(1)	9(1)	43(2)	22(1)	7(1)	8(2)
calculated for $\text{CaLuSi}_4\text{N}_{6.4}\text{C}_{0.3}\text{O}_{0.3}$	8	8	31	49	2	2

[a] The measured values of Si (N) are higher (lower) than the calculated values. However, this circumstance in TEM-EDX measurements has been previously reported.^[1]

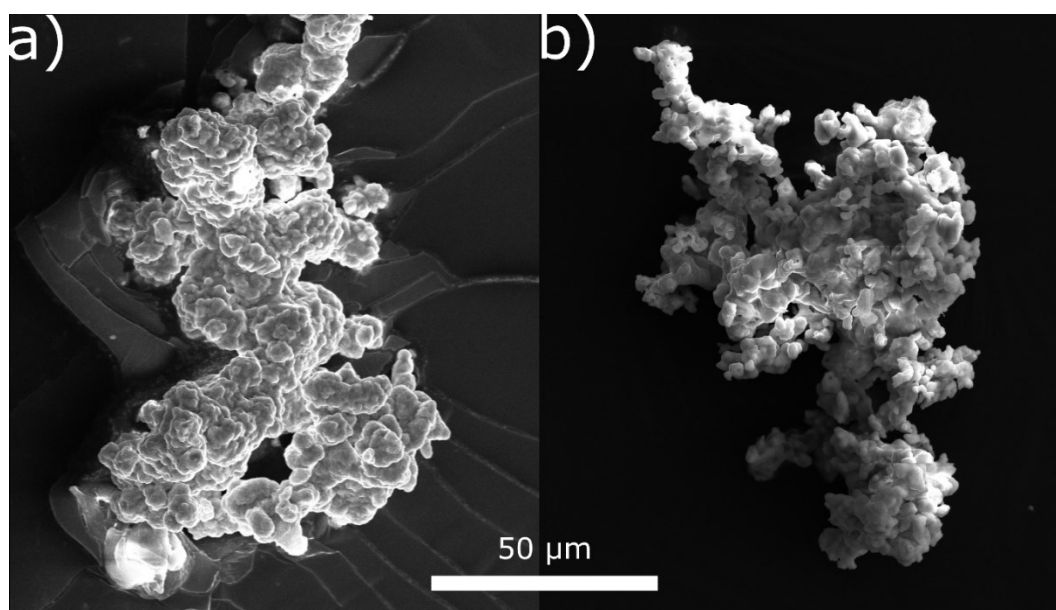


Figure B1. SEM images of $\text{CaLu}[\text{Si}_4\text{N}_{7-2x}\text{C}_x\text{O}_x]$ ($x \approx 0.3$) (a) before and (b) after heating for purification.

Table B4. Results (in atom%) of SEM-EDX point measurements of $\text{CaLuSi}_4\text{N}_{6.4}\text{C}_{0.3}\text{O}_{0.3}$ after heating for purification (estimated standard deviations in parentheses)

Measurement	Ca	Lu	Si	N	O	C
1	7	7	32	38	16	-
2	7	7	30	40	16	-
3	7	7	32	38	16	-
4	7	7	31	39	16	-
average and standard deviation	7(1)	7(1)	31(1)	39(1)	16(1)	-
calculated for $\text{CaLuSi}_4\text{N}_{6.4}\text{C}_{0.3}\text{O}_{0.3}$	8	8	31	49	2	2

Table B5. CHNS analysis (in weight%) of $\text{CaLuSi}_4\text{N}_{6.4}\text{C}_{0.3}\text{O}_{0.3}$ after heating for purification

	C	H	N	S
measured	1.63	-	16.03	-
calculated for $\text{CaLuSi}_4\text{N}_{6.4}\text{C}_{0.3}\text{O}_{0.3}$	0.8	-	21.1	-

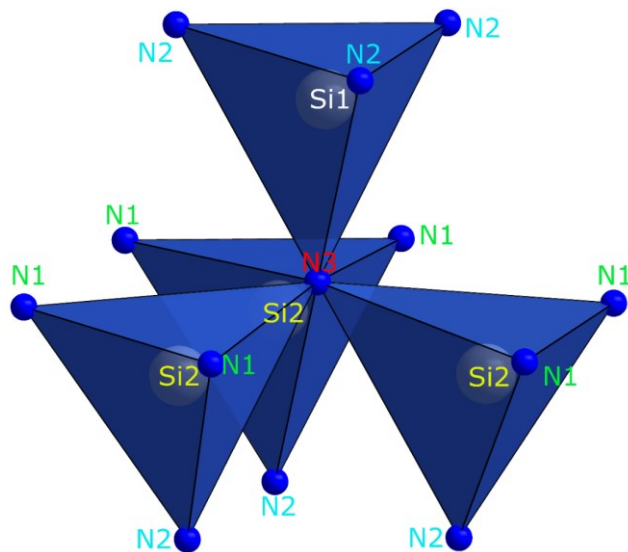


Figure B2. Atom assignment in the star shaped unit.

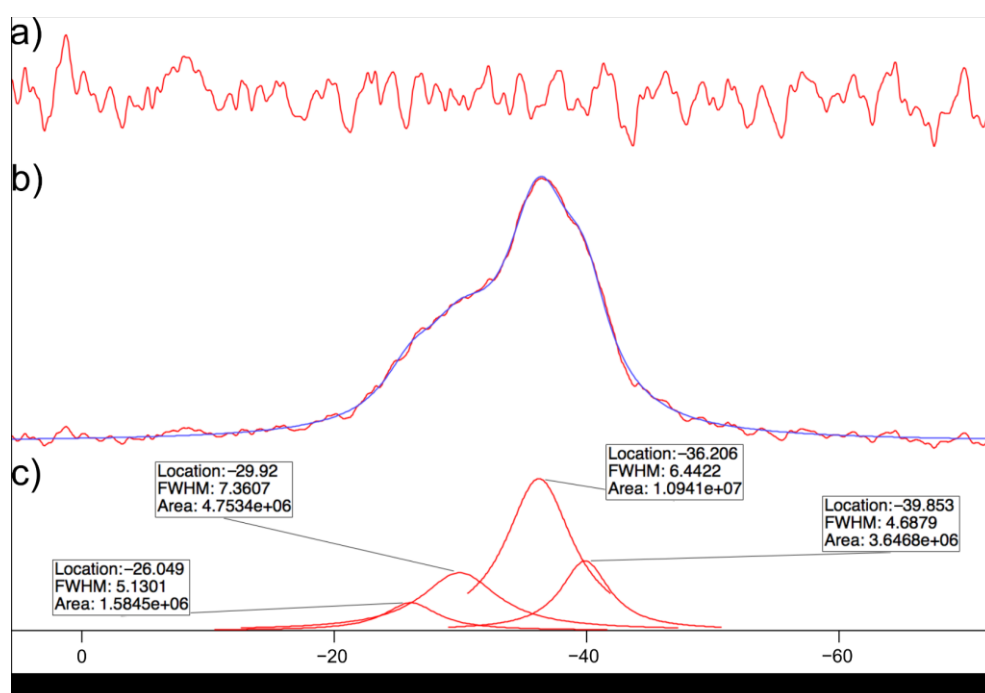


Figure B3. Deconvolution of the ^{29}Si -NMR spectrum by four Lorentz functions. (a) Difference profile between measured signal and fit function. (b) Measured signal (red) and calculated fit consisting of Lorentz functions (blue). (c) Four deconvoluted Lorentz functions with their maximum chemical shifts and integrals, respectively.

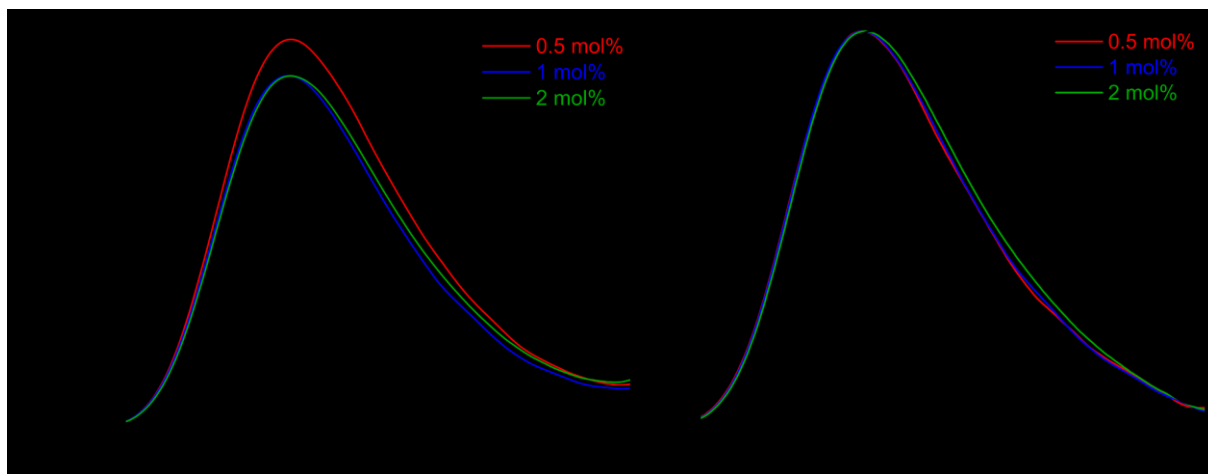


Figure B4. Smoothed (a) relative and (b) normalized emission spectra ($\lambda_{\text{exc}} = 400 \text{ nm}$) of $\text{CaLu}[\text{Si}_4\text{N}_{7-2x}\text{C}_x\text{O}_x]:\text{Eu}^{2+}$ ($x \approx 0.3$) with varying doping concentrations.

Table B6. Comparison of emission maxima and full width at half-maximum for varying doping concentrations of $\text{CaLu}[\text{Si}_4\text{N}_{7-2x}\text{C}_x\text{O}_x]:\text{Eu}^{2+}$ ($x \approx 0.3$) after purification

		0.5 mol%	1 mol%	2 mol%	3 mol%
λ_{em}	nm	546	546	548	552
$fwhm$	nm	123	124	127	128
	cm^{-1}	3999	4000	4051	4058

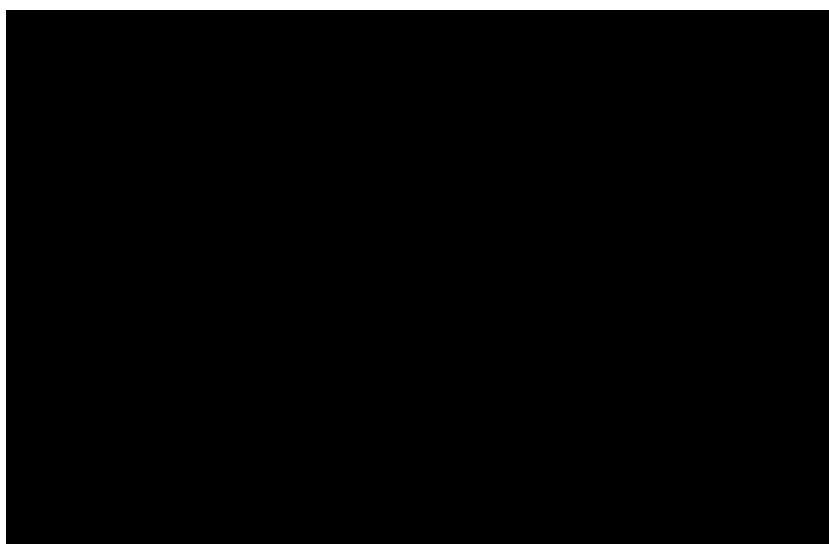


Figure B5. Temperature dependent relative integrated emission intensities of $\text{CaLu}[\text{Si}_4\text{N}_{7-2x}\text{C}_x\text{O}_x]:\text{Eu}^{2+}$ ($x \approx 0.3$; 0.5 mol%).

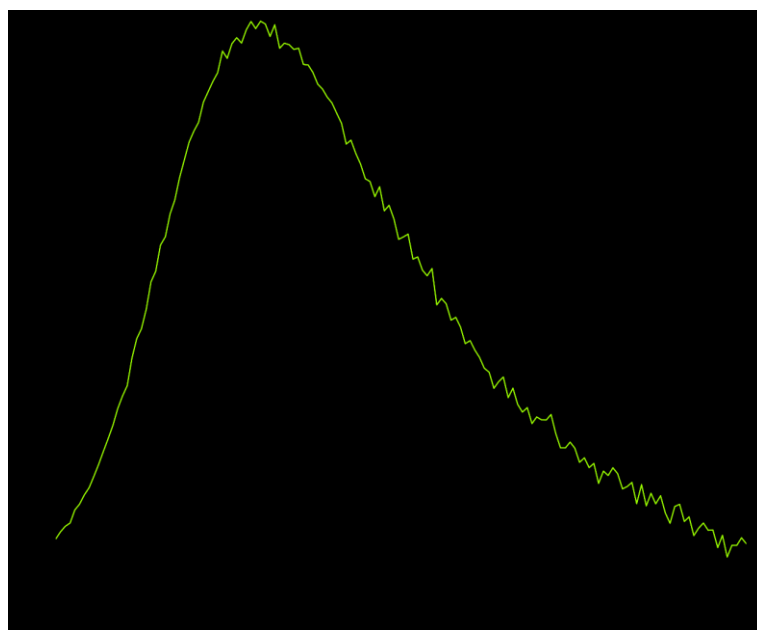


Figure B6. Comparison of the emission spectra ($\lambda_{\text{exc}} = 400 \text{ nm}$) of purified $\text{CaLu}[\text{Si}_4\text{N}_{7-2x}\text{C}_x\text{O}_x]:\text{Eu}^{2+}$ (green; $x \approx 0.3$; 0.5 mol%) and $\text{YAG}:\text{Ce}^{3+}$ (black).

Reference

- [1] C. Maak, L. Eisenburger, J. P. Wright, M. Nentwig, P. J. Schmidt, O. Oeckler, W. Schnick, *Inorg. Chem.* **2018**, *57*, 13840–13846.

C. Supporting Information for Chapter 4

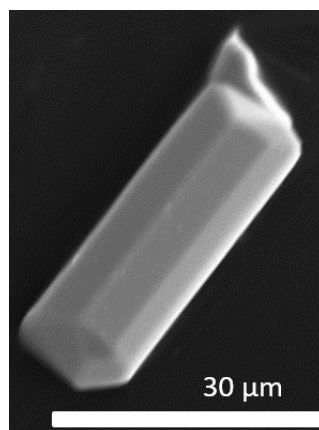


Figure C1. SEM image of the La₇Sr[Si₁₀N₁₉O₃] single-crystal used for single-crystal X-ray diffraction.

Table C1. Data for the Rietveld refinement of a $\text{La}_7\text{Sr}[\text{Si}_{10}\text{N}_{19}\text{O}_3]$ sample based on its structure model obtained by single-crystal X-ray diffraction (standard deviations in parentheses). Only lattice parameters and fractional coordinates of the heavy cation sites were refined

Formula	$\text{La}_7\text{Sr}[\text{Si}_{10}\text{N}_{19}\text{O}_3]$	
formula weight / $\text{g}\cdot\text{mol}^{-1}$	1654.94	
crystal system	orthorhombic	
space group	$Pmn2_1$ (no. 31)	
lattice parameters / Å	$a =$	9.4994(3)
	$b =$	19.0854(7)
	$c =$	12.0598(5)
$V / \text{Å}^3$	2186.44(15)	
Z	4	
X-ray density / $\text{g}\cdot\text{cm}^{-3}$	5.02722	
diffractometer	STOE Stadi P	
radiation	Mo- $K\alpha_1$ ($\lambda = 0.70930 \text{ Å}$)	
monochromator	Ge(111)	
detector	Mythen 1K	
2θ range / °	$5 \leq 2\theta \leq 60$	
data points	3672	
number of reflections	3616	
refined parameters	65	
background function	shifted Chebyshev, 12 polynomials	
R values	$R_p =$	0.0240
	$R_{wp} =$	0.0327
	$R_{exp} =$	0.0179
	$R_{Bragg} =$	0.0145
$Goof (\chi^2)$	1.8334	

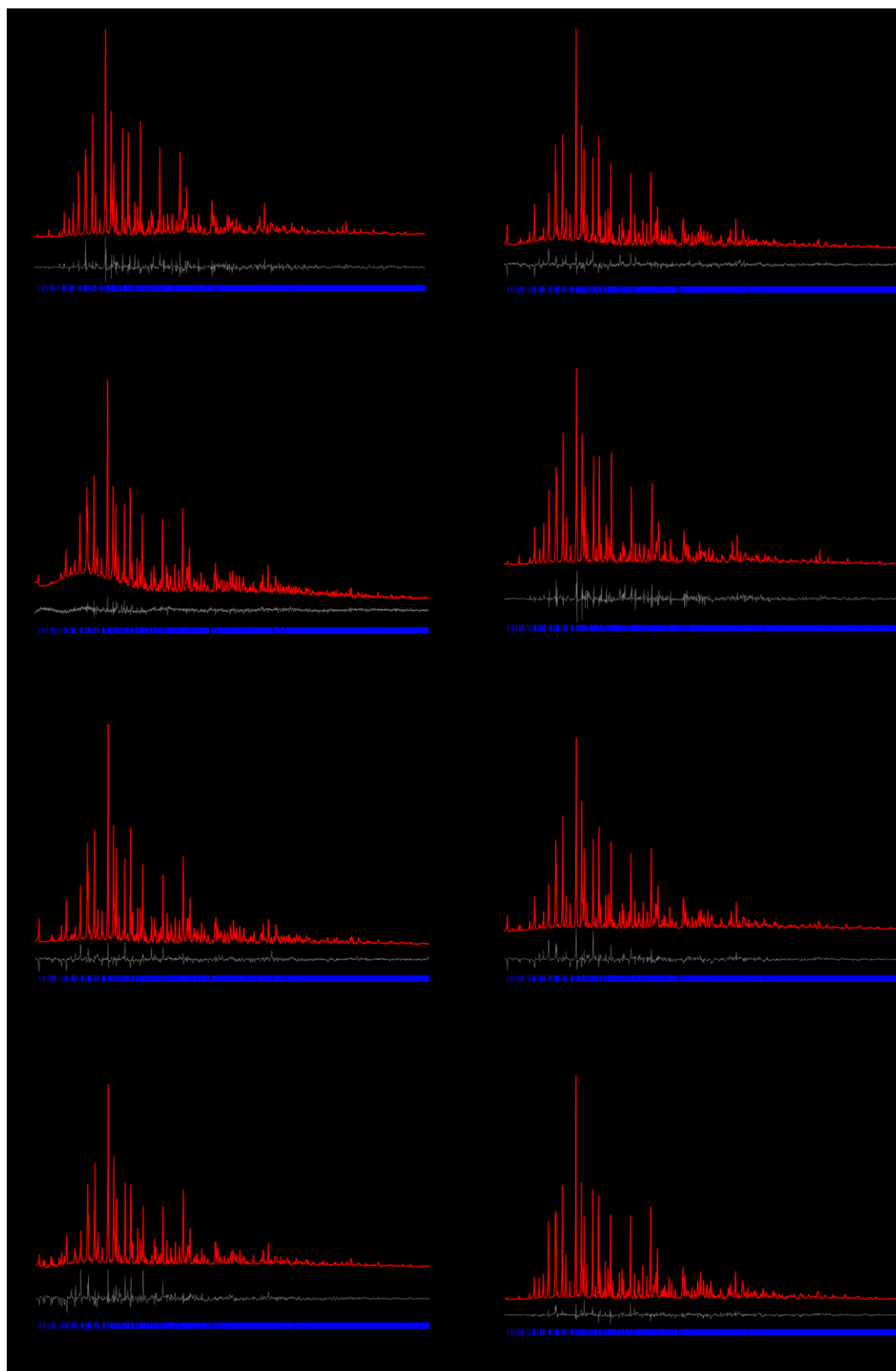


Figure C2. Rietveld refinements based on PXRD data collected from powder samples based on the structure model of $\text{La}_7\text{Sr}[\text{Si}_{10}\text{N}_{19}\text{O}_3]$ obtained by SCXRD data with observed (black) and calculated (red) powder X-ray diffraction patterns and the corresponding difference profiles (gray). Vertical blue bars indicate the position of the Bragg reflections of the respective compounds.

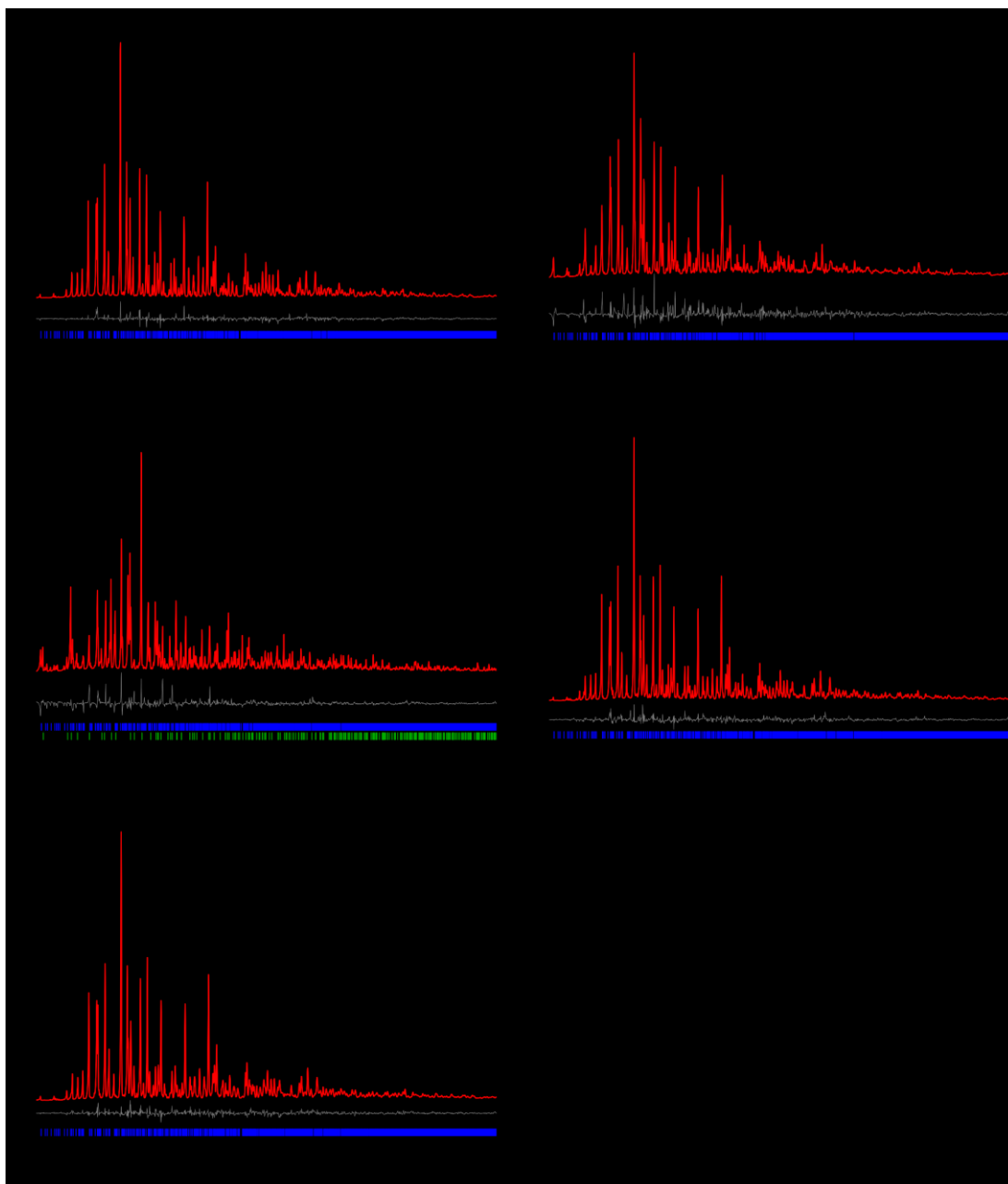


Figure C3. Rietveld refinements based on PXRD data collected from powder samples based on the structure model of $\text{La}_7\text{Sr}[\text{Si}_{10}\text{N}_{19}\text{O}_3]$ obtained by SCXRD data with observed (black) and calculated (red) powder X-ray diffraction patterns and the corresponding difference profiles (gray). Vertical blue bars indicate the position of the Bragg reflections of the respective compounds. $\text{Ce}_6\text{Ca}_2[\text{Si}_{10}\text{N}_{18}\text{O}_4]$ was obtained with $\text{Ce}_3\text{Si}_6\text{N}_{11}$ (28%) as a side phase indicated by green bars.^[1]

Table C2a. Data for the Rietveld refinement of $RE_{8-x}AE_x[Si_{10}N_{20-x}O_{2+x}]$ ($RE = La, Ce$; $AE = Ca, Sr, Ba$; $0 \leq x \leq 2$) samples based on the $La_7Sr[Si_{10}N_{19}O_3]$ structure model obtained by single-crystal X-ray diffraction (standard deviations in parentheses). Only lattice parameters and fractional coordinates of the heavy cation sites were refined

Formula	$La_8[Si_{10}N_{20}O_2]$	$La_6Sr_2[Si_{10}N_{18}O_4]$	
formula weight / $g \cdot mol^{-1}$	1704.38	1605.65	
crystal system	orthorhombic		
space group	$Pmn2_1$ (no. 31)		
lattice parameters / Å	$a =$	9.4305(3)	9.4451(3)
	$b =$	19.0227(8)	18.9740(6)
	$c =$	11.9968(7)	12.0130(5)
$V / \text{Å}^3$	2152.15(17)	2152.87(13)	
Z	4		
X-ray density / $g \cdot cm^{-3}$	5.25944	4.95354	
diffractometer	STOE Stadi P		
radiation	Mo- $K\alpha_1$ ($\lambda = 0.7093 \text{ Å}$)		
monochromator	Ge(111)		
detector	Mythen 1K		
2θ range / °	$5 \leq 2\theta \leq 59$	$5 \leq 2\theta \leq 59$	
data points	3572	3588	
number of reflections	3335	3371	
refined parameters	54	53	
background function	shifted Chebyshev, 12 polynomials		
R values	$R_p =$	0.1119	0.0396
	$R_{wp} =$	0.1454	0.0560
	$R_{exp} =$	0.0263	0.0229
	$R_{Bragg} =$	0.0623	0.0377
Goof (χ^2)	5.5355	2.4459	

Table C2b. Data for the Rietveld refinement of $RE_{8-x}AE_x[Si_{10}N_{20-x}O_{2+x}]$ ($RE = La, Ce$; $AE = Ca, Sr, Ba$; $0 \leq x \leq 2$) samples based on the $La_7Sr[Si_{10}N_{19}O_3]$ structure model obtained by single-crystal X-ray diffraction (standard deviations in parentheses). Only lattice parameters and fractional coordinates of the heavy cation sites were refined

Formula	$Ce_7Sr[Si_{10}N_{19}O_3]$	$Ce_8[Si_{10}N_{20}O_2]$	$Ce_6Sr_2[Si_{10}N_{18}O_4]$	
formula weight / $g \cdot mol^{-1}$	1663.55	1714.06	1613.04	
crystal system		orthorhombic		
space group		$Pmn2_1$ (no. 31)		
lattice parameters / Å	$a =$	9.4084(2)	9.3895(3)	9.4085(2)
	$b =$	18.8861(4)	18.9305(9)	18.8823(5)
	$c =$	11.9353(3)	11.9144(7)	11.9317(3)
$V / \text{Å}^3$	2120.76(8)	2117.76(17)	2119.72(9)	
Z		4		
X-ray density / $g \cdot cm^{-3}$	5.20942	5.37519	5.05375	
diffractometer		STOE Stadi P		
radiation		Mo- $K\alpha_1$ ($\lambda = 0.7093 \text{ Å}$)		
monochromator		Ge(111)		
detector		Mythen 1K		
2θ range / °	$5 \leq 2\theta \leq 60$	$5 \leq 2\theta \leq 60$	$5 \leq 2\theta \leq 59$	
data points	3698	3655	3645	
number of reflections	3578	3475	3451	
refined parameters	53	64	54	
background function		shifted Chebyshev, 12 polynomials		
R values	$R_p =$	0.0292	0.0965	0.0429
	$R_{wp} =$	0.0373	0.1297	0.0599
	$R_{exp} =$	0.0249	0.0293	0.0243
	$R_{Bragg} =$	0.0183	0.0428	0.0419
$Goof (\chi^2)$	1.4976	4.4316	2.4584	

Table C3a. Data for the Rietveld refinement $RE_{8-x}AE_x[\text{Si}_{10}\text{N}_{20-x}\text{O}_{2+x}]$ ($RE = \text{La, Ce}$; $AE = \text{Ca, Sr, Ba}$; $0 \leq x \leq 2$) samples based on the $\text{La}_7\text{Sr}[\text{Si}_{10}\text{N}_{19}\text{O}_3]$ structure model obtained by single-crystal X-ray diffraction (standard deviations in parentheses). Only lattice parameters and fractional coordinates of the heavy cation sites were refined

Formula	$\text{La}_7\text{Ca}[\text{Si}_{10}\text{N}_{19}\text{O}_3]$	$\text{La}_6\text{Ca}_2[\text{Si}_{10}\text{N}_{18}\text{O}_4]$	
formula weight / $\text{g}\cdot\text{mol}^{-1}$	1607.54	1510.56	
crystal system	orthorhombic		
space group	$Pmn2_1$ (no. 31)		
lattice parameters / Å	$a =$	9.4224(3)	9.4228(4)
	$b =$	18.9720(8)	18.9727(10)
	$c =$	11.9747(7)	11.9730(8)
$V / \text{Å}^3$	2140.62(17)	2140.48(20)	
Z	4		
density / $\text{g}\cdot\text{m}^{-3}$	4.98776		
diffractometer	STOE Stadi P		
radiation	Mo- $K\alpha_1$ ($\lambda = 0.7093 \text{ Å}$)		
monochromator	Ge(111)		
detector	Mythen 1K		
2θ range / °	$5 \leq 2\theta \leq 59$	$5 \leq 2\theta \leq 60$	
data points	3572	3698	
number of reflections	3324	3606	
refined parameters	65	66	
background function	shifted Chebyshev, 12 polynomials		
R values	$R_p =$	0.1003	0.1075
	$R_{wp} =$	0.1345	0.1492
	$R_{exp} =$	0.0253	0.0291
	$R_{Bragg} =$	0.0783	0.0817
Goof (χ^2)	5.3242	5.1239	

Table C3b. Data for the Rietveld refinement $RE_{8-x}AE_x[Si_{10}N_{20-x}O_{2+x}]$ ($RE = La, Ce$; $AE = Ca, Sr, Ba$; $0 \leq x \leq 2$) samples based on the $La_7Sr[Si_{10}N_{19}O_3]$ structure model obtained by single-crystal X-ray diffraction (standard deviations in parentheses). Only lattice parameters and fractional coordinates of the heavy cation sites were refined

Formula	$La_7Ba[Si_{10}N_{19}O_3]$	$La_6Ba_2[Si_{10}N_{18}O_4]$	
formula weight / $g \cdot mol^{-1}$	1704.79	1705.20	
crystal system	orthorhombic		
space group	$Pmn2_1$ (no. 31)		
lattice parameters / Å	$a =$	9.4567(2)	9.4829(2)
	$b =$	19.0125(4)	19.0235(4)
	$c =$	12.0089(3)	11.9979(1)
$V / \text{Å}^3$	2159.15(8)	2164.39(6)	
Z	4		
density / $g \cdot m^{-3}$	5.24367	5.23223	
diffractometer	STOE Stadi P		
radiation	Mo- $K\alpha_1$ ($\lambda = 0.7093 \text{ Å}$)		
monochromator	Ge(111)		
detector	Mythen 1K		
2θ range / °	$5 \leq 2\theta \leq 59$	$5 \leq 2\theta \leq 60$	
data points	3612	3663	
number of reflections	3441	3563	
refined parameters	55	65	
background function	shifted Chebyshev, 12 polynomials		
R values	$R_p =$	0.0671	0.0597
	$R_{wp} =$	0.0872	0.0784
	$R_{exp} =$	0.0249	0.0231
	$R_{Bragg} =$	0.0468	0.0395
$Goof$ (χ^2)	3.4981	3.3965	

Table C4a. Data for the Rietveld refinement of $RE_{8-x}AE_x[\text{Si}_{10}\text{N}_{20-x}\text{O}_{2+x}]$ ($RE = \text{La}, \text{Ce}; AE = \text{Ca}, \text{Sr}, \text{Ba}; 0 \leq x \leq 0$) samples based on the $\text{La}_7\text{Sr}[\text{Si}_{10}\text{N}_{19}\text{O}_3]$ structure model obtained by single-crystal X-ray diffraction (standard deviations in parentheses. Only lattice parameters and fractional coordinates of the heavy cation sites were refined

Formula	$\text{Ce}_7\text{Ca}[\text{Si}_{10}\text{N}_{19}\text{O}_3]$	$\text{Ce}_6\text{Ca}_2[\text{Si}_{10}\text{N}_{18}\text{O}_4]$	
formula weight / $\text{g}\cdot\text{mol}^{-1}$	1616.01	1517.96	
crystal system	orthorhombic		
space group	$Pmn2_1$ (no. 31)		
lattice parameters / Å	$a =$	9.3828(4)	9.3650(3)
	$b =$	18.9048(10)	18.8694(8)
	$c =$	11.9111(8)	11.9313(6)
$V / \text{Å}^3$	2112.79(20)	2108.40(15)	
Z	4		
density / $\text{g}\cdot\text{cm}^{-3}$	5.08008	4.78178	
diffractometer	STOE Stadi P		
radiation	Mo- $K\alpha_1$ ($\lambda = 0.7093 \text{ Å}$)		
monochromator	Ge(111)		
detector	Mythen 1K		
2θ range / °	$5 \leq 2\theta \leq 60$	$5 \leq 2\theta \leq 60$	
data points	3698	3698	
number of reflections	3564	3557	
refined parameters	65	76	
background function	shifted Chebyshev, 12 polynomials		
R values	$R_p =$	0.1080	0.0895
	$R_{wp} =$	0.1497	0.1582
	$R_{exp} =$	0.0290	0.0288
	$R_{Bragg} =$	0.0627	0.0871
$Goof$ (χ^2)	5.1542	4.5171	

Table C4b. Data for the Rietveld refinement of $RE_{8-x}AE_x[Si_{10}N_{20-x}O_{2+x}]$ ($RE = La, Ce$; $AE = Ca, Sr, Ba$; $0 \leq x \leq 2$) samples based on the $La_7Sr[Si_{10}N_{19}O_3]$ structure model obtained by single-crystal X-ray diffraction (standard deviations in parentheses. Only lattice parameters and fractional coordinates of the heavy cation sites were refined

Formula	$Ce_7Ba[Si_{10}N_{19}O_3]$	$Ce_6Ba_2[Si_{10}N_{18}O_4]$	
formula weight / $g \cdot mol^{-1}$	1713.26	1712.46	
crystal system	orthorhombic		
space group	$Pmn2_1$ (no. 31)		
lattice parameters / \AA	$a =$	9.4473(3)	9.4441(2)
	$b =$	18.9015(6)	18.9011(6)
	$c =$	11.9317(4)	11.9340(4)
$V / \text{\AA}^3$	2130.62(12)	2130.27(11)	
Z	4		
density / $g \cdot cm^{-3}$	5.34072	5.33912	
diffractometer	STOE Stadi P		
radiation	Mo- $K\alpha_1$ ($\lambda = 0.7093 \text{ \AA}$)		
monochromator	Ge(111)		
detector	Mythen 1K		
2θ range / $^\circ$	$5 \leq 2\theta \leq 60$	$5 \leq 2\theta \leq 60$	
data points	3698	3655	
number of reflections	3592	3492	
refined parameters	65	66	
background function	shifted Chebyshev, 12 polynomials		
R values	$R_p =$	0.0715	0.0630
	$R_{wp} =$	0.1002	0.0841
	$R_{exp} =$	0.0265	0.0287
	$R_{Bragg} =$	0.0445	0.0336
$Goof (\chi^2)$	3.7841	2.9274	

Table C5. Results (in atom%) of SEM-EDX point measurements of $RE_{8-x}AE_x[Si_{10}N_{20-x}O_{2+x}]$ ($RE = La, Ce$; $AE = Ca, Sr, Ba$; $0 \leq x \leq 2$). Top row: calculated theoretical values, bottom row: average of several measurements with standard deviation in parentheses

		<i>RE</i>	<i>AE</i>	Si	$(RE + AE)/Si$
La ₇ Sr[Si ₁₀ N ₁₉ O ₃]	calc.	17.5	2.5	25	0.8
	avg.	14(1)	3(1)	22(1)	0.77
La ₈ [Si ₁₀ N ₂₀ O ₂]	calc.	20	-	25	0.8
	avg.	18(2)	-	24(1)	0.75
La ₆ Sr ₂ [Si ₁₀ N ₁₈ O ₄]	calc.	15	5	25	0.8
	avg.	16(1)	5(4)	26(2)	0.81
Ce ₇ Sr[Si ₁₀ N ₁₉ O ₃]	calc.	17.5	2.5	25	0.8
	avg.	16(4)	4(1)	23(3)	0.87
Ce ₈ [Si ₁₀ N ₂₀ O ₂]	calc.	20	-	25	0.8
	avg.	18(2)	-	24(1)	0.75
Ce ₆ Sr ₂ [Si ₁₀ N ₁₈ O ₄]	calc.	15	5	25	0.8
	avg.	14(2)	4(1)	25(2)	0.72
La ₇ Ca[Si ₁₀ N ₁₉ O ₃]	calc.	17.5	2.5	25	0.8
	avg.	18(3)	2(1)	24(3)	0.83
La ₆ Ca ₂ [Si ₁₀ N ₁₈ O ₄]	calc.	15	5	25	0.8
	avg.	16(2)	4(2)	23(3)	0.87
La ₇ Ba[Si ₁₀ N ₁₉ O ₃]	calc.	17.5	2.5	25	0.8
	avg.	17(2)	1(1)	24(1)	0.75
La ₆ Ba ₂ [Si ₁₀ N ₁₈ O ₄]	calc.	15	5	25	0.8
	avg.	16(4)	2(1)	24(2)	0.75
Ce ₇ Ca[Si ₁₀ N ₁₉ O ₃]	calc.	17.5	2.5	25	0.8
	avg.	18(4)	2(1)	24(2)	0.83
Ce ₆ Ca ₂ [Si ₁₀ N ₁₈ O ₄]	calc.	15	5	25	0.8
	avg.	16(2)	3(1)	23(2)	0.83
Ce ₇ Ba[Si ₁₀ N ₁₉ O ₃]	calc.	17.5	2.5	25	0.8
	avg.	17(3)	2(1)	25(2)	0.76
Ce ₆ Ba ₂ [Si ₁₀ N ₁₈ O ₄]	calc.	15	5	25	0.8
	avg.	17(1)	2(1)	25(2)	0.76

8 Appendix

Table C6. Wyckoff positions, atomic coordinates and isotropic displacement parameters (\AA^2) of $\text{La}_7\text{Sr}[\text{Si}_{10}\text{N}_9\text{O}_3]$. Estimated standard deviations are given in parentheses

Atom	Wyckoff Position	x	y	z	U_{iso}	s.o.f
La1	2a	0	0.98695(7)	0.86558(11)	0.0075(3)	1
La2	4b	0.2257(1)	0.21265(5)	0.19957(8)	0.0084(2)	1
La3	4b	0.27750(11)	0.01557(5)	0.08684(8)	0.0096(2)	1
La4	4b	0.27705(11)	0.53023(5)	0.02946(8)	0.0112(2)	1
La5	2a	0	0.22893(7)	0.91047(11)	0.0106(3)	1
La6	2a	0	0.72045(7)	0.88712(11)	0.0121(3)	1
La7	2a	0	0.45662(8)	0.83553(11)	0.0171(3)	1
La8	4b	0.22469(13)	0.71614(7)	0.18924(13)	0.0338(3)	1
Sr9					0.0095(3)	0.171(6)
La9	2a	0	0.64439(7)	0.51683(12)	0.0095(3)	0.829(6)
Sr10					0.0162(4)	0.446(6)
La10	2a	0	0.15153(9)	0.48636(16)	0.0162(4)	0.554(6)
Sr11					0.0162(5)	0.718(7)
La11	2a	0	0.40196(11)	0.23458(17)	0.0162(5)	0.282(6)
Sr12					0.0633(12)	0.665(7)
La12	2a	0	0.88964(13)	0.2827(4)	0.0633(12)	0.335(6)
Si1	4b	0.1626(5)	0.2912(2)	0.4143(3)	0.0058(3)	1
Si2	4b	0.3241(4)	0.1445(2)	0.5051(4)	0.0058(3)	1
Si3	2a	0	0.3540(3)	0.6051(5)	0.0069(6)	1
Si4	4b	0.1628(4)	0.5504(2)	0.3143(3)	0.0058(3)	1
Si5	4b	0.1806(4)	0.3581(2)	0.0108(4)	0.0058(3)	1
Si6	4b	0.3213(4)	0.4023(2)	0.2466(4)	0.0058(3)	1
Si7	4b	0.1767(5)	0.1187(2)	0.7559(3)	0.0058(3)	1
Si8	2a	0	0.5995(3)	0.1152(5)	0.0069(6)	1
Si9	2a	0	0.0976(3)	0.1490(5)	0.0069(6)	1
Si10	2a	0	0.8623(3)	0.6163(5)	0.0069(6)	1
Si11	4b	0.1641(5)	0.7897(2)	0.4469(3)	0.0058(3)	1
Si12	4b	0.1639(5)	0.0350(2)	0.3365(3)	0.0058(3)	1
O1					0.0143(12)	0.75
N1	2a	0	0.8003(9)	0.7158(14)	0.0143(12)	0.25
O2					0.0143(12)	0.75
N2	2a	0	0.4386(9)	0.6311(14)	0.0143(12)	0.25
O3					0.0143(12)	0.75
N3	2a	0	0.6859(9)	0.0855(15)	0.0143(12)	0.25
O4	2a	0	0.3088(9)	0.7265(13)	0.0143(12)	0.75

B. Supporting Information for Chapter 3

N4					0.0143(12)	0.25
O5	2a	0	0.9419(9)	0.6728(14)	0.0143(12)	0.75
N5					0.0143(12)	0.25
O6	2a	0	0.0386(9)	0.0478(14)	0.0143(12)	0.75
N6					0.0143(12)	0.25
O7	2a	0	0.1788(9)	0.0997(14)	0.0143(12)	0.75
N7					0.0143(12)	0.25
O8	2a	0	0.5494(9)	0.0020(14)	0.0143(12)	0.75
N8					0.0143(12)	0.25
N9	4b	0.2579(15)	0.3288(7)	0.3087(11)	0.0126(7)	1
N10	2a	0	0.6039(10)	0.7408(17)	0.0126(7)	1
N11	2a	0	0.2659(10)	0.3605(17)	0.0126(7)	1
N12	4b	0.1490(14)	0.0897(7)	0.2278(11)	0.0126(7)	1
N13	2a	0	0.0195(10)	0.4014(17)	0.0126(7)	1
N14	4b	0.2546(15)	0.4089(7)	0.1129(12)	0.0126(7)	1
N15	4b	0.2383(15)	0.1881(7)	0.8323(12)	0.0126(7)	1
N16	4b	0.2582(15)	0.0394(7)	0.7863(12)	0.0126(7)	1
N17	2a	0	0.356(1)	0.0192(18)	0.0126(7)	1
N18	2a	0	0.761(1)	0.4016(16)	0.0126(7)	1
N19	4b	0.2481(15)	0.2759(7)	0.0178(12)	0.0126(7)	1
N20	4b	0.2770(15)	0.0685(7)	0.4317(12)	0.0126(7)	1
N21	4b	0.2614(16)	0.2172(7)	0.4376(12)	0.0126(7)	1
N22	4b	0.3525(15)	0.1420(7)	0.0390(11)	0.0126(7)	1
N23	4b	0.2176(14)	0.1390(7)	0.6202(12)	0.0126(7)	1
N24	4b	0.1486(14)	0.5846(7)	0.1866(12)	0.0126(7)	1
N25	4b	0.1491(15)	0.3407(7)	0.5301(12)	0.0126(7)	1
N26	2a	0	0.5341(10)	0.3774(17)	0.0126(7)	1
N27	2a	0	0.8527(10)	0.0309(17)	0.0126(7)	1
N28	4b	0.2629(15)	0.4740(7)	0.3180(12)	0.0126(7)	1
N29	2a	0	0.1124(10)	0.7799(16)	0.0126(7)	1
N30	4b	0.2588(15)	0.6059(7)	0.3875(12)	0.0126(7)	1

8 Appendix

Table C7. Anisotropic displacement parameters (\AA^2) of $\text{La}_7\text{Sr}[\text{Si}_{10}\text{N}_{19}\text{O}_3]$. Standard deviations in parentheses. Mixed occupied sites as well as chemically identical Si and N sites, respectively, were refined with equal atomic displacement parameters

Atom	U_{11}	U_{22}	U_{33}	U_{12}	U_{13}	U_{23}
La1	0.0049(7)	0.0088(6)	0.0089(6)	0	0	-0.0039(5)
La2	0.0095(5)	0.0073(4)	0.0084(4)	-0.0015(3)	0.0019(4)	-0.0018(3)
La3	0.0104(5)	0.0098(5)	0.0085(5)	-0.0001(4)	-0.0009(4)	-0.0032(4)
La4	0.0094(5)	0.0105(4)	0.0136(5)	-0.0004(4)	-0.0007(4)	0.0005(4)
La5	0.0073(7)	0.0125(7)	0.0120(7)	0	0	-0.0049(5)
La6	0.0067(7)	0.0184(7)	0.0111(7)	0	0	-0.0002(5)
La7	0.0036(7)	0.0358(9)	0.0120(7)	0	0	0.0080(6)
La8	0.0137(6)	0.0351(7)	0.0526(8)	-0.0041(5)	0.0043(6)	-0.0326(6)
Sr9						
La9	0.0074(7)	0.0088(7)	0.0124(7)	0	0	0.0032(5)
Sr10						
La10	0.0081(9)	0.0110(8)	0.0294(10)	0	0	0.0055(7)
Sr11						
La11	0.0098(10)	0.0219(11)	0.017(1)	0	0	-0.0096(8)
Sr12						
La12	0.0092(12)	0.0136(11)	0.167(4)	0	0	0.0243(17)
Si1	0.0051(6)	0.0050(7)	0.0072(7)	0.0000(5)	-0.0007(6)	-0.0005(6)
Si2	0.0051(6)	0.0050(7)	0.0072(7)	0.0000(5)	-0.0007(6)	-0.0005(6)
Si3	0.0048(12)	0.0081(14)	0.0078(14)	0	0	0.0021(13)
Si4	0.0051(6)	0.0050(7)	0.0072(7)	0.0000(5)	-0.0007(6)	-0.0005(6)
Si5	0.0051(6)	0.0050(7)	0.0072(7)	0.0000(5)	-0.0007(6)	-0.0005(6)
Si6	0.0051(6)	0.0050(7)	0.0072(7)	0.0000(5)	-0.0007(6)	-0.0005(6)
Si7	0.0051(6)	0.0050(7)	0.0072(7)	0.0000(5)	-0.0007(6)	-0.0005(6)
Si8	0.0048(12)	0.0081(14)	0.0078(14)	0	0	0.0021(13)
Si9	0.0048(12)	0.0081(14)	0.0078(14)	0	0	0.0021(13)
Si10	0.0048(12)	0.0081(14)	0.0078(14)	0	0	0.0021(13)
Si11	0.0051(6)	0.0050(7)	0.0072(7)	0.0000(5)	-0.0007(6)	-0.0005(6)
Si12	0.0051(6)	0.0050(7)	0.0072(7)	0.0000(5)	-0.0007(6)	-0.0005(6)
O1						
N1	0.012(3)	0.019(3)	0.012(3)	0	0	0.000(3)
O2						
N2	0.012(3)	0.019(3)	0.012(3)	0	0	0.000(3)
O3						
N3	0.012(3)	0.019(3)	0.012(3)	0	0	0.000(3)

B. Supporting Information for Chapter 3

O4	0.012(3)	0.019(3)	0.012(3)	0	0	0.000(3)
N4						
O5	0.012(3)	0.019(3)	0.012(3)	0	0	0.000(3)
N5						
O6	0.012(3)	0.019(3)	0.012(3)	0	0	0.000(3)
N6						
O7	0.012(3)	0.019(3)	0.012(3)	0	0	0.000(3)
N7						
O8	0.012(3)	0.019(3)	0.012(3)	0	0	0.000(3)
N8						
N9	0.0121(14)	0.0132(16)	0.0124(16)	0.0001(15)	0.0014(16)	0.0001(14)
N10	0.0121(14)	0.0132(16)	0.0124(16)	0.0001(15)	0.0014(16)	0.0001(14)
N11	0.0121(14)	0.0132(16)	0.0124(16)	0.0001(15)	0.0014(16)	0.0001(14)
N12	0.0121(14)	0.0132(16)	0.0124(16)	0.0001(15)	0.0014(16)	0.0001(14)
N13	0.0121(14)	0.0132(16)	0.0124(16)	0.0001(15)	0.0014(16)	0.0001(14)
N14	0.0121(14)	0.0132(16)	0.0124(16)	0.0001(15)	0.0014(16)	0.0001(14)
N15	0.0121(14)	0.0132(16)	0.0124(16)	0.0001(15)	0.0014(16)	0.0001(14)
N16	0.0121(14)	0.0132(16)	0.0124(16)	0.0001(15)	0.0014(16)	0.0001(14)
N17	0.0121(14)	0.0132(16)	0.0124(16)	0.0001(15)	0.0014(16)	0.0001(14)
N18	0.0121(14)	0.0132(16)	0.0124(16)	0.0001(15)	0.0014(16)	0.0001(14)
N19	0.0121(14)	0.0132(16)	0.0124(16)	0.0001(15)	0.0014(16)	0.0001(14)
N20	0.0121(14)	0.0132(16)	0.0124(16)	0.0001(15)	0.0014(16)	0.0001(14)
N21	0.0121(14)	0.0132(16)	0.0124(16)	0.0001(15)	0.0014(16)	0.0001(14)
N22	0.0121(14)	0.0132(16)	0.0124(16)	0.0001(15)	0.0014(16)	0.0001(14)
N23	0.0121(14)	0.0132(16)	0.0124(16)	0.0001(15)	0.0014(16)	0.0001(14)
N24	0.0121(14)	0.0132(16)	0.0124(16)	0.0001(15)	0.0014(16)	0.0001(14)
N25	0.0121(14)	0.0132(16)	0.0124(16)	0.0001(15)	0.0014(16)	0.0001(14)
N26	0.0121(14)	0.0132(16)	0.0124(16)	0.0001(15)	0.0014(16)	0.0001(14)
N27	0.0121(14)	0.0132(16)	0.0124(16)	0.0001(15)	0.0014(16)	0.0001(14)
N28	0.0121(14)	0.0132(16)	0.0124(16)	0.0001(15)	0.0014(16)	0.0001(14)
N29	0.0121(14)	0.0132(16)	0.0124(16)	0.0001(15)	0.0014(16)	0.0001(14)
N30	0.0121(14)	0.0132(16)	0.0124(16)	0.0001(15)	0.0014(16)	0.0001(14)

Table C8. List of cation sites of $\text{La}_7\text{Sr}[\text{Si}_{10}\text{N}_{19}\text{O}_3]$ with their respective site occupancy factors, coordination numbers, coordinating anions, distances and polyhedral volumes according to VESTA^[2]

Site	s.o.f	CN	X	$d_{\text{Sr/La-N/O}} / \text{\AA}$	$V / \text{\AA}^3$
La1	1	8	6× N, 2× (N,O)	2.41(2)–3.24(2)	30.71
La2	1	8	6× N, 2× (N,O)	2.48(1)–3.07(2)	31.58
La3	1	8	6× N, 2× (N,O)	2.49(1)–3.15(2)	31.73
La4	1	8	6× N, 2× (N,O)	2.48(2)–3.13(1)	32.13
La5	1	8	6× N, 2× (N,O)	2.48(2)–2.84(2)	31.68
La6	1	8	6× N, 2× (N,O)	2.48(2)–3.06(2)	31.71
La7	1	8	6× N, 2× (N,O)	2.49(2)–3.03(2)	31.24
La8	1	8	6× N, 2× (N,O)	2.51(2)–3.30(2)	30.62
Sr/La9	0.171 / 0.829	9	9× N	2.62(2)–3.00(2)	36.11
Sr/La10	0.446 / 0.554	8 + 1	9× N	2.64(1)–3.14(2) [N29: 3.62(2)]	35.08
Sr/La11	0.718 / 0.282	9	9× N	2.74(3)–3.05(2)	35.43
Sr/La12	0.665 / 0.335	9	9× N	2.67(2)–3.37(2)	36.03

Table C9. Charge distribution (CHARDI) calculated with VESTA^[2] and bond valence sums (BVS) calculated with Valist^[3] of $\text{La}_7\text{Sr}[\text{Si}_{10}\text{N}_{19}\text{O}_3]$ compared to the theoretical values

Site	Theoretical	CHARDI	BVS	Site	Theoretical	CHARDI	BVS
La1	3	2.86	3.54	Si1	4	4.07	4.63
La2	3	2.90	3.41	Si2	4	4.34	4.56
La3	3	2.89	3.26	Si3	4	3.74	4.42
La4	3	2.88	3.04	Si4	4	4.22	4.81
La5	3	2.85	3.09	Si5	4	4.06	4.63
La6	3	2.93	3.10	Si6	4	4.05	4.70
La7	3	2.99	3.04	Si7	4	4.02	4.56
La8	3	2.81	2.85	Si8	4	3.78	4.53
Sr/La9	2.83	3.00	3.51	Si9	4	3.72	4.41
Sr/La10	2.55	2.79	2.26	Si10	4	3.88	4.51
Sr/La11	2.28	2.35	1.56	Si11	4	4.00	4.53
Sr/La12	2.34	2.43	1.71	Si12	4	4.12	4.69

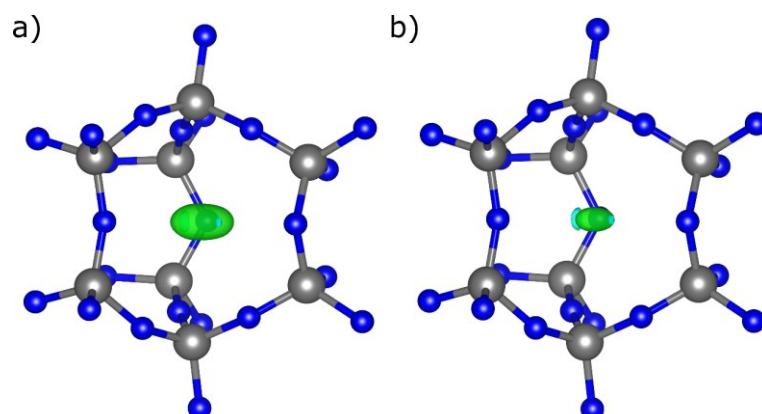


Figure C4. Isosurface levels of the difference Fourier synthesis ($F_{\text{obs}} - F_{\text{calc}}$) of the electron density located at Sr/La12 in $\text{La}_7\text{Sr}[\text{Si}_{10}\text{N}_{19}\text{O}_3]$ in e^-/a_0^3 (a_0 : Bohr radius). (a) Green = +7, blue = -4. (b) Green = +21, blue = -4. N atoms blue, Si atoms gray. Visualized by VESTA.^[2]

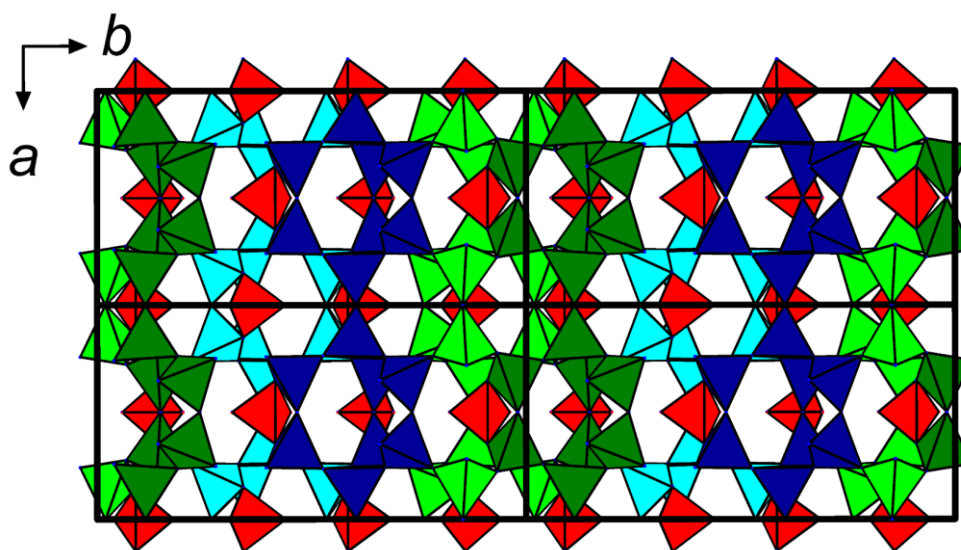


Figure C5. $2 \times 1 \times 1$ super cell viewed along [001] of $\text{La}_7\text{Sr}[\text{Si}_{10}\text{N}_{19}\text{O}_3]$ illustrating the connection between the unit cells. $[\text{SiN}_4]$ tetrahedra in blue and green shades, $[\text{SiN}_2(\text{N}_{0.25}\text{O}_{0.75})_2]$ in red.

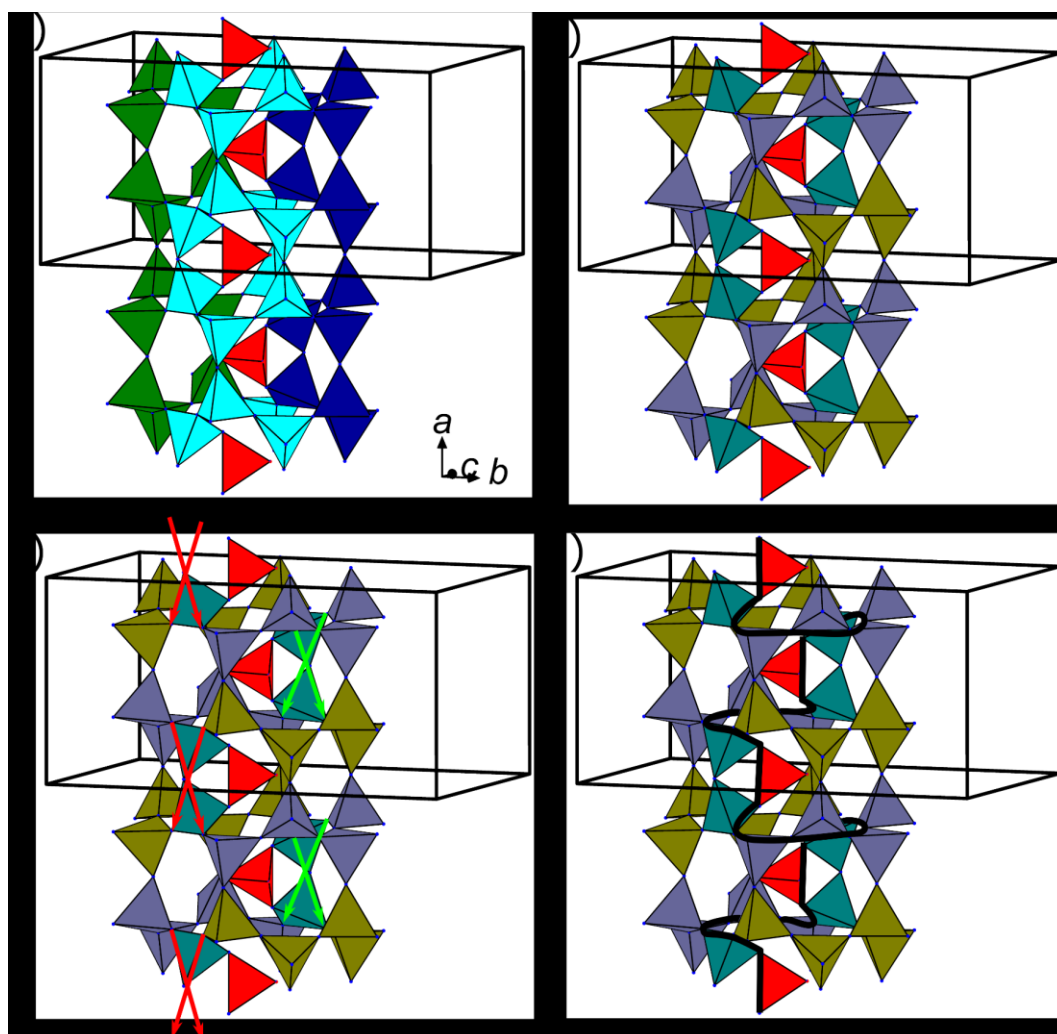


Figure C6. Cages and inverted structures stacked along [100]. (a) Cages in dark blue and green and inverted structure in light blue. (b) Intersecting counterclockwise and clockwise distorted screws with internal offsets in blue gray and dark yellow, respectively, with shared tetrahedra in teal. (c) Red (5.59(2) Å) and green (5.62(2) Å) arrows indicating the respective offsets. (d) Counterclockwise screw with offsets highlighted by a black line. $[\text{SiN}_2(\text{N}_{0.25}\text{O}_{0.75})_2]$ tetrahedra red.

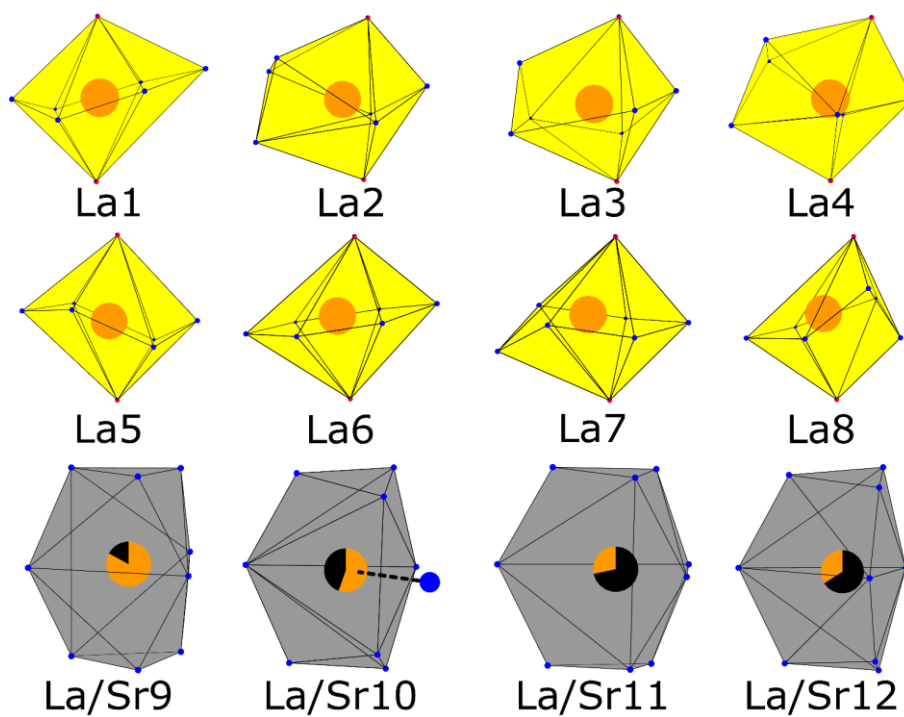


Figure C7. Coordination spheres of La and La/Sr mixed occupied sites in $\text{La}_7\text{Sr}[\text{Si}_{10}\text{N}_{19}\text{O}_3]$. La atoms orange, Sr atoms black, N blue, O red. Mixed occupied cation sites colored in the respective atom colors with the section size corresponding to the percentage occupancy.

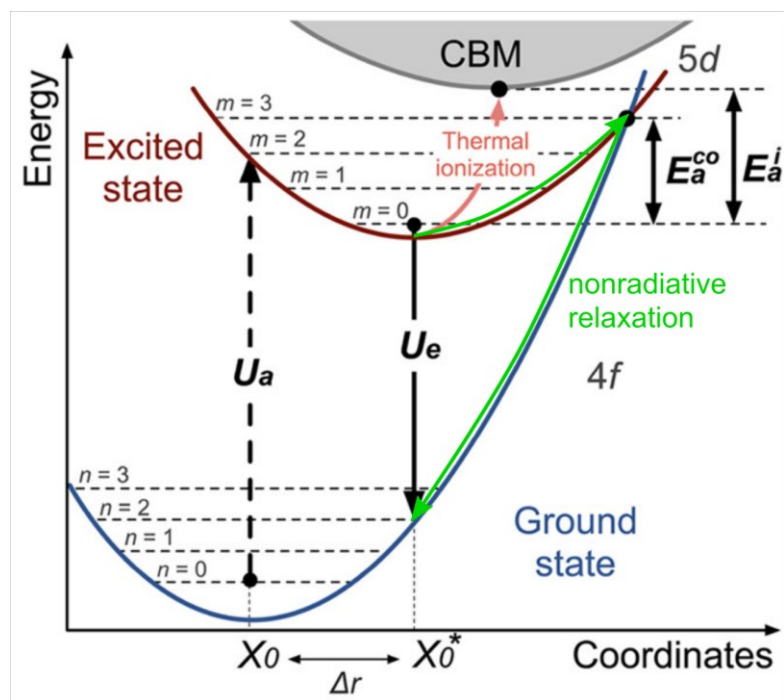


Figure C8. Configurational coordinate diagram for an activator like Eu^{2+} in a host material. Blue: $4f$ ground state, dark red: $5d$ excited state. U_a , U_e : absorption and emission energy, respectively. n , m : vibrational levels. CBM: conduction band minimum. $\Delta r = X_0^* - X_0$: displacement of the activation ion between excited and ground state. E_a^{co} , E_a^i : activation energy for crossover and thermal ionization mechanisms, respectively. Green: Thermal quenching in the crossover model results from thermally exceeding the activation energy for the $5d$ electron from the excited state to the intersection with the parabola of the ground state resulting in a nonradiative relaxation. Light red: Thermal excitation of the electronically excited $5d$ electron to the conduction band minimum is described in the thermal ionization mechanism.^[4]

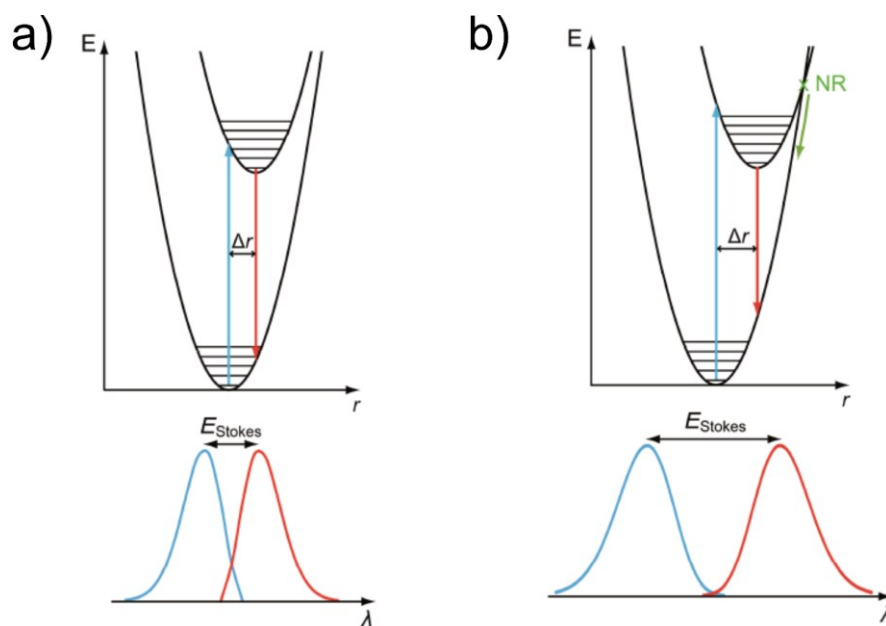


Figure C9. Top row: configurational coordinate diagrams, bottom row: corresponding excitation (blue) and emission (red) spectra. Δr : parabola offset between excited and ground state. (a) Smaller S and (b) larger S value with identical ω for both cases. With increasing S , the Stokes shift E_{Stokes} , the excitation and emission band widths and Δr increase, leading to a crossover of the parabolas at lower E and therefore, a higher probability for a nonradiative relaxation from the excited to the ground state.^[5-8]

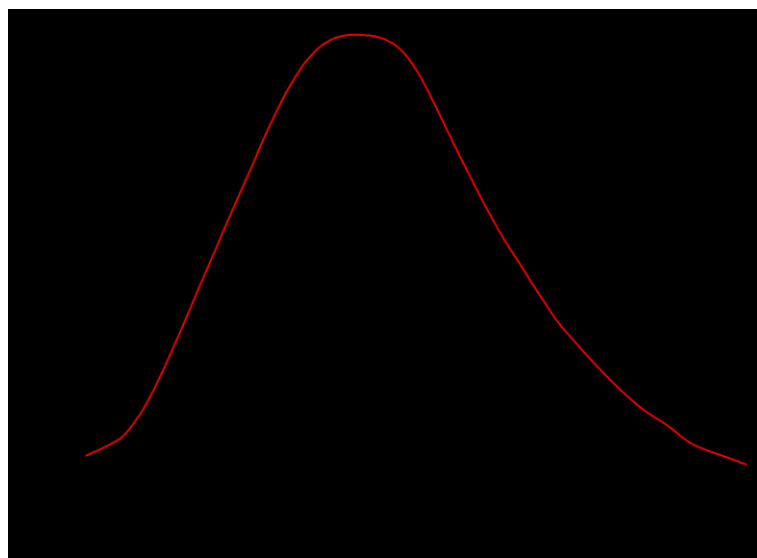


Figure C10. Normalized (black) and Lowess smoothed (red) emission spectra ($\lambda_{\text{exc}} = 450 \text{ nm}$) of $\text{Ce}_6\text{Ca}_2[\text{Si}_{10}\text{N}_{18}\text{O}_4]:\text{Eu}^{2+}$.^[9]

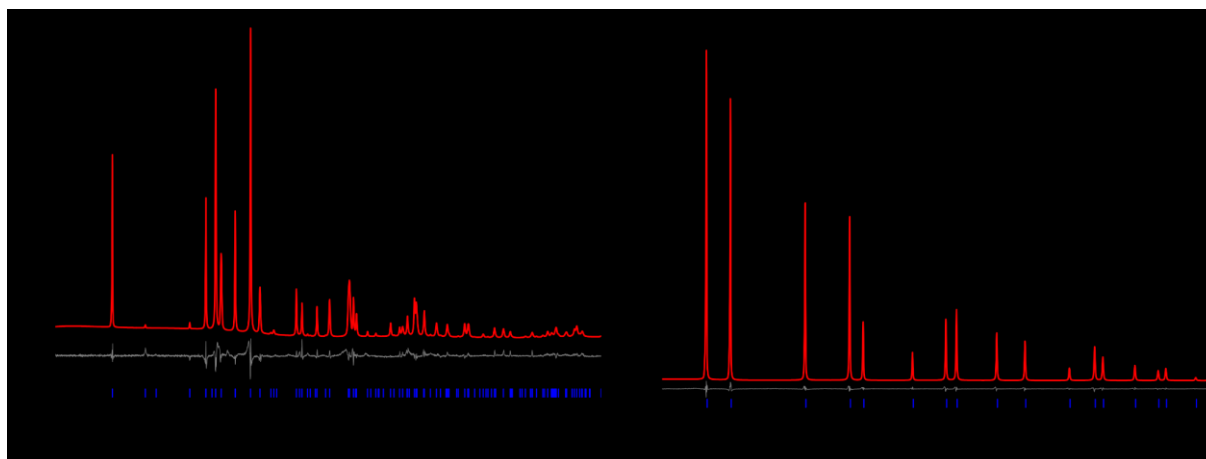


Figure C11. Rietveld refinement for (a) SrN and (b) CeN with respective observed (black) and calculated (red) powder X-ray diffraction patterns and the corresponding difference profile (gray). Vertical blue bars indicate the position of the Bragg reflections of the respective compounds based on the literature known compounds.^[10, 11]

Table C10. Details of the Rietveld refinements of SrN and CeN

Formula	SrN	CeN
formula weight / g·mol ⁻¹	101.623	154.12
crystal system	monoclinic	cubic
space group	<i>C2/m</i> (no. 12)	<i>Fm$\bar{3}m$</i> (no. 225)
lattice parameters / Å, °		
<i>a</i> =	13.4711(6)	
<i>b</i> =	3.8161(2)	4.9923(1)
<i>c</i> =	6.7343(3)	
β =	94.701(2)	90
<i>V</i> / Å ³	345.02(3)	124.42(1)
<i>Z</i>	8	4
density / g·cm ⁻³	3.91267	8.22702
diffractometer	STOE Stadi P	
radiation	Cu-Kα ₁ (λ = 1.5406 Å)	Mo-Kα ₁ (λ = 0.7093 Å)
monochromator	Ge(111)	
detector	Mythen 1K	
2θ range / °	5 ≤ 2θ ≤ 93	2 ≤ 2θ ≤ 60
data points	5875	3698
number of reflections	191	19
refined parameters	50	34
background function	shifted Chebyshev, 12 polynomials	
<i>R</i> values		
<i>R</i> _p =	0.0752	0.0485
<i>R</i> _{wp} =	0.1075	0.0730
<i>R</i> _{exp} =	0.0427	0.0419
<i>R</i> _{Bragg} =	0.0327	0.0051
<i>Goof</i> (χ ²)	2.5164	1.7411

Table C11. List of chemicals used for this work

Substance	Purity	Producer
LaN	99.9% (<i>REO</i>)	Alfa Aesar
Ce	99.9%	abcr
CeN	phase pure	synthesized (see Figure C11 and Table C10)
Ca ₃ N ₂	99%	Sigma Aldrich
Sr	99.99%	Sigma Aldrich
SrN	phase pure	synthesized (see Figure C11 and Table C10)
Ba ₂ N	99.7%	Materion
amorphous Si ₃ N ₄	SNA-00	Ube Industries
SiO ₂	0.035–0.070 nm, 60 Å	Acros Organics
Eu ₂ O ₃	99.99%	abcr

B. Supporting Information for Chapter 3

Table C12. Weighted starting materials for each $RE_{8-x}AE_x[Si_{10}N_{20-x}O_{2+x}]$ ($RE = La, Ce; AE = Ca, Sr, Ba; 0 \leq x \leq 2$) synthesis. Eu_2O_3 was used as a dopant in each of those synthesis

	LaN	CeN	Ca ₃ N ₂	SrN	Ba ₂ N	Si ₃ N ₄	SiO ₂
La ₇ Sr[Si ₁₀ N ₁₉ O ₃]	56.1 mg			37.3 mg		20.8 mg	4.7 mg
	0.367 mmol			0.367 mmol		0.149 mmol	0.079 mmol
La ₈ [Si ₁₀ N ₂₀ O ₂]	71.8 mg					24.7 mg	3.5 mg
	0.469 mmol					0.176 mmol	0.059 mmol
La ₆ Sr ₂ [Si ₁₀ N ₁₈ O ₄]	57.1 mg			88.6 mg		23.3 mg	7.5 mg
	0.374 mmol			0.872 mmol		0.166 mmol	0.125 mmol
La ₇ Ca[Si ₁₀ N ₁₉ O ₃]	66.6 mg		3.1 mg			24.7 mg	5.6 mg
	0.435 mmol		0.021 mmol			0.176 mmol	0.093 mmol
La ₆ Ca ₂ [Si ₁₀ N ₁₈ O ₄]	60.7 mg		6.5 mg			24.8 mg	8.0 mg
	0.397 mmol		0.044 mmol			0.177 mmol	0.132 mmol
La ₇ Ba[Si ₁₀ N ₁₉ O ₃]	62.8 mg				8.5 mg	23.3 mg	5.3 mg
	0.411 mmol				0.029 mmol	0.166 mmol	0.088 mmol
La ₆ Ba ₂ [Si ₁₀ N ₁₈ O ₄]	53.8 mg				16.9 mg	21.9 mg	7.1 mg
	0.352 mmol				0.059 mmol	0.156 mmol	0.117 mmol
Ce ₇ Sr[Si ₁₀ N ₁₉ O ₃]		64.9 mg		42.8 mg		23.9 mg	5.4 mg
		0.421 mmol		0.421 mmol		0.170 mmol	0.090 mmol
Ce ₈ [Si ₁₀ N ₂₀ O ₂]		71.9 mg				24.6 mg	3.5 mg
		0.467 mmol				0.175 mmol	0.058 mmol
Ce ₆ Sr ₂ [Si ₁₀ N ₁₈ O ₄]		57.3 mg		88.2 mg		23.2 mg	7.5 mg
		0.371 mmol		0.868 mmol		0.165 mmol	0.124 mmol
Ce ₇ Ca[Si ₁₀ N ₁₉ O ₃]		66.8 mg	3.1 mg			24.6 mg	5.6 mg
		0.433 mmol	0.021 mmol			0.175 mmol	0.093 mmol
Ce ₆ Ca ₂ [Si ₁₀ N ₁₈ O ₄]		60.9 mg	6.5 mg			24.7 mg	7.9 mg
		0.395 mmol	0.044 mmol			0.176 mmol	0.132 mmol
Ce ₇ Ba[Si ₁₀ N ₁₉ O ₃]		63.0 mg			8.4 mg	23.2 mg	5.3 mg
		0.409 mmol			0.029 mmol	0.165 mmol	0.088 mmol
Ce ₆ Ba ₂ [Si ₁₀ N ₁₈ O ₄]		54.0 mg			16.9 mg	21.9 mg	7.0 mg
		0.350 mmol			0.058 mmol	0.156 mmol	0.117 mmol

Table C13. Body colors and luminescence impressions of the synthesized compounds. “-“ refers to no luminescence or too weak for measurements

	Body Color	Luminescence
$\text{La}_7\text{Sr}[\text{Si}_{10}\text{N}_{19}\text{O}_3]:\text{Eu}^{2+}$	yellow orange	orange
$\text{La}_8[\text{Si}_{10}\text{N}_{20}\text{O}_2]:\text{Eu}^{2+}$	yellow	weak orange
$\text{La}_6\text{Sr}_2[\text{Si}_{10}\text{N}_{18}\text{O}_4]:\text{Eu}^{2+}$	light yellow	weak orange
$\text{La}_7\text{Ca}[\text{Si}_{10}\text{N}_{19}\text{O}_3]:\text{Eu}^{2+}$	yellow gray	-
$\text{La}_6\text{Ca}_2[\text{Si}_{10}\text{N}_{18}\text{O}_4]:\text{Eu}^{2+}$	yellow gray	-
$\text{La}_7\text{Ba}[\text{Si}_{10}\text{N}_{19}\text{O}_3]:\text{Eu}^{2+}$	yellow gray	-
$\text{La}_6\text{Ba}_2[\text{Si}_{10}\text{N}_{18}\text{O}_4]:\text{Eu}^{2+}$	beige gray	-
$\text{Ce}_7\text{Sr}[\text{Si}_{10}\text{N}_{19}\text{O}_3]:\text{Eu}^{2+}$	yellow orange	-
$\text{Ce}_8[\text{Si}_{10}\text{N}_{20}\text{O}_2]:\text{Eu}^{2+}$	dark red	orange
$\text{Ce}_6\text{Sr}_2[\text{Si}_{10}\text{N}_{18}\text{O}_4]:\text{Eu}^{2+}$	orange ocher	orange
$\text{Ce}_7\text{Ca}[\text{Si}_{10}\text{N}_{19}\text{O}_3]:\text{Eu}^{2+}$	reddish brown	orange
$\text{Ce}_6\text{Ca}_2[\text{Si}_{10}\text{N}_{18}\text{O}_4]:\text{Eu}^{2+}$	orange	orange
$\text{Ce}_7\text{Ba}[\text{Si}_{10}\text{N}_{19}\text{O}_3]:\text{Eu}^{2+}$	orange ocher	-
$\text{Ce}_6\text{Ba}_2[\text{Si}_{10}\text{N}_{18}\text{O}_4]:\text{Eu}^{2+}$	orange ocher	-

Table C14. Deposition Numbers of all reported compounds

	CSD-
La ₇ Sr[Si ₁₀ N ₁₉ O ₃]	2104245
La ₈ [Si ₁₀ N ₂₀ O ₂]	2141282
La ₆ Sr ₂ [Si ₁₀ N ₁₈ O ₄]	2141280
La ₇ Ca[Si ₁₀ N ₁₉ O ₃]	2141281
La ₆ Ca ₂ [Si ₁₀ N ₁₈ O ₄]	2141318
La ₇ Ba[Si ₁₀ N ₁₉ O ₃]	2141284
La ₆ Ba ₂ [Si ₁₀ N ₁₈ O ₄]	2141283
Ce ₇ Sr[Si ₁₀ N ₁₉ O ₃]	2141285
Ce ₈ [Si ₁₀ N ₂₀ O ₂]	2141287
Ce ₆ Sr ₂ [Si ₁₀ N ₁₈ O ₄]	2141319
Ce ₇ Ca[Si ₁₀ N ₁₉ O ₃]	2141288
Ce ₆ Ca ₂ [Si ₁₀ N ₁₈ O ₄]	2141289
Ce ₇ Ba[Si ₁₀ N ₁₉ O ₃]	2141290
Ce ₆ Ba ₂ [Si ₁₀ N ₁₈ O ₄]	2141320

References

- [1] T. Schlieper, W. Schnick, *Z. Anorg. Allg. Chem.* **1995**, *621*, 1535–1538.
- [2] K. Momma, F. Izumi, *J. Appl. Crystallogr.* **2011**, *44*, 1272–1276.
- [3] A. S. Wills, *VaList*, v. 4.0.7, University College London, UK, **2010**.
- [4] M. Amachraa, Z. Wang, C. Chen, S. Hariyani, H. Tang, J. Brgoch, S. P. Ong, *Chem. Mater.* **2020**, *32*, 6256–6265.
- [5] G. Blasse, A. Bril, *Philips Tech. Rev.* **1970**, *31*, 304–332.
- [6] G. Blasse, *Prog. Solid State Chem.* **1988**, *18*, 79–171.
- [7] S. Shionoya, W. M. Yen, *Phosphor Handbook*, CRC Press, New York, **1998**.
- [8] C. Maak, Dissertation, LMU Munich, **2019**.
- [9] OriginLab Corporation, *OriginPro*, Northampton, Massachusetts, USA, **2018**.
- [10] P. Etmayer, J. Waldhart, A. Vendl, *Monatsh. Chem.* **1979**, *110*, 1109–1112.
- [11] G. Auffermann, Y. Prots, R. Kniep, *Angew. Chem. Int. Ed.* **2001**, *40*, 547–549; *Angew. Chem.* **2001**, *113*, 565–567.

D. Supporting Information for Chapter 5

Table D1. Results (in atom%) of TEM-EDX point measurements for the single crystal of $\text{Ba}_{22.5+x}\text{La}_{55-x}[\text{Si}_{129}\text{N}_{240-x}\text{O}_x]\text{O}_3$ used for synchrotron data collection (standard deviations in parentheses)

Measurement	Ba	La	Si	N	O
1	7	14	29	45	5
2	7	13	32	41	6
3	7	12	31	42	8
4	7	14	32	41	5
5	7	15	34	39	4
6	7	19	28	42	4
average and standard deviation	7(1)	15(3)	31(2)	42(2)	5(2)
calculated for $\text{Ba}_{22.74}\text{La}_{54.84}\text{Si}_{129}\text{N}_{240}\text{O}_3$	5	12	29	53	1

Table D2. Results (in atom%) of TEM-EDX point measurements for the single crystal of $\text{Ba}_{25.5+x}\text{La}_{77-x}[\text{Si}_{170}\text{N}_{312-x}\text{O}_{9+x}]\text{O}_4$ used for synchrotron data collection (standard deviations in parentheses). Note that the spectra and especially the light atoms are affected by shading so that the ratio between light and heavy elements is systematically biased

Measurement	Ba	La	Ba/La	Si	N	O	N/O
1	11	30	0.37	25	31	3	10
2	16	43	0.37	24	17	1	17
3	12	32	0.38	27	26	2	13
4	16	44	0.36	25	15	1	15
average and standard deviation	14(2)	37(7)	0.38(9)	25(2)	22(8)	2(1)	14(3)
calculated for $\text{Ba}_{25.79}\text{La}_{76.74}\text{Si}_{170}\text{N}_{311.76}\text{O}_{13.24}$	4	13	0.31	29	52	2	26

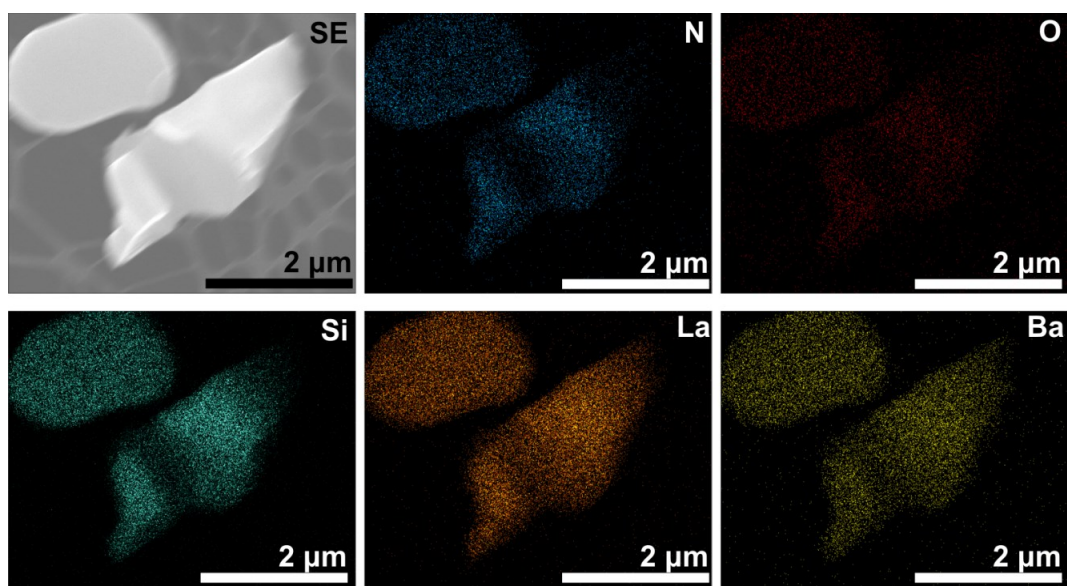


Figure D1. SEM-EDX maps of intergrown $\text{Ba}_{22.5+x}\text{La}_{55-x}[\text{Si}_{129}\text{N}_{240-x}\text{O}_x]\text{O}_3$ and $\text{Ba}_{25.5+x}\text{La}_{77-x}[\text{Si}_{170}\text{N}_{312-x}\text{O}_{9+x}]\text{O}_4$ crystallites show a homogeneous distribution of elements, which means that the two phases cannot be differentiated directly using EDX.

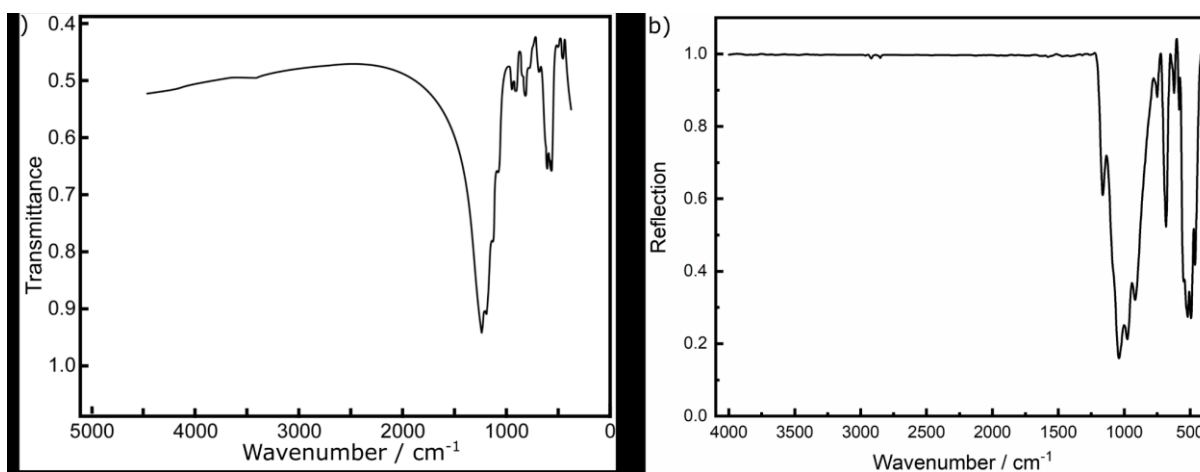


Figure D2. FTIR spectra of powder samples that consist of (a) $\text{Ba}_{22.5+x}\text{La}_{55-x}[\text{Si}_{129}\text{N}_{240-x}\text{O}_x]\text{O}_3$ and $\text{Ba}_{25.5+x}\text{La}_{77-x}[\text{Si}_{170}\text{N}_{312-x}\text{O}_{9+x}]\text{O}_4$ and (b) $\text{Sr}_{28.5+x}\text{La}_{75-x}[\text{Si}_{170}\text{N}_{312-x}\text{O}_{9+x}]\text{O}_4$. The absence of N–H (3100–3500 cm^{-1}) and O–H vibration modes (3200 and 3600 cm^{-1}) corroborates the absence of hydrogen in these phases.^[1]

Table D3. Details of the Rietveld refinement for $\text{Ba}_{22.5+x}\text{La}_{55-x}[\text{Si}_{129}\text{N}_{240-x}\text{O}_x]\text{O}_3$ ($x \approx 0.24$) and $\text{Ba}_{25.5+x}\text{La}_{77-x}[\text{Si}_{170}\text{N}_{312-x}\text{O}_{9+x}]\text{O}_4$ ($x \approx 0.24$) in a powder sample containing both phases based on their single-crystal data (standard deviations in parentheses). Only lattice parameters were refined; site occupancy factors as well as isotropic displacement parameters for all sites were taken from the single-crystal data

Formula		$\text{Ba}_{22.74}\text{La}_{54.84}\text{Si}_{129}\text{N}_{240}\text{O}_3$	$\text{Ba}_{25.79}\text{La}_{76.74}\text{Si}_{170}\text{N}_{311.76}\text{O}_{13.24}$
weight percent		31.6(4)	68.4(4)
formula mass / $\text{g}\cdot\text{mol}^{-1}$		17772.8	23554.5
crystal system			hexagonal
space group			$P\bar{6}$ (no.174)
lattice parameters / Å	$a =$	17.4923(4)	20.1381(2)
	$c =$	22.7027(7)	22.6425(4)
	$V / \text{Å}^3$	6015.9(3)	7952.3(2)
	Z		1
X-ray density / $\text{g}\cdot\text{cm}^{-3}$		4.90542	4.91818
diffractometer			Stoe StadiP
radiation			Mo- $K\alpha_1$ ($\lambda = 0.70930 \text{ Å}$)
monochromator			Ge(111)
	$F(000)$	7905	10484
	2θ range / °		$2.0 \leq \theta \leq 63.8$
	data points		4120
number of observed reflections		7273	9612
number of parameters			29
background function			shifted Chebyshev, 12 terms
R values	$R_p =$		0.0274
	$R_{wp} =$		0.0368
	$R_{exp} =$		0.0123
	$R_{Bragg} =$	0.0210	

Table D4. Result (in atom%) of TEM-EDX point measurements for the single crystal of $\text{Sr}_{28.5+x}\text{La}_{75-x}[\text{Si}_{170}\text{N}_{312-x}\text{O}_{9+x}]\text{O}_4$ used for synchrotron data collection (standard deviations in parentheses)

Measurement	Sr	La	Si	N	O
1	7	9	27	50	8
2	10	10	32	42	6
average and standard deviation	9(2)	9(1)	30(4)	46(5)	7(2)
calculated for $\text{Sr}_{24.79}\text{La}_{78.75}\text{Si}_{170}\text{N}_{315.71}\text{O}_{9.29}$	4	13	28	53	2

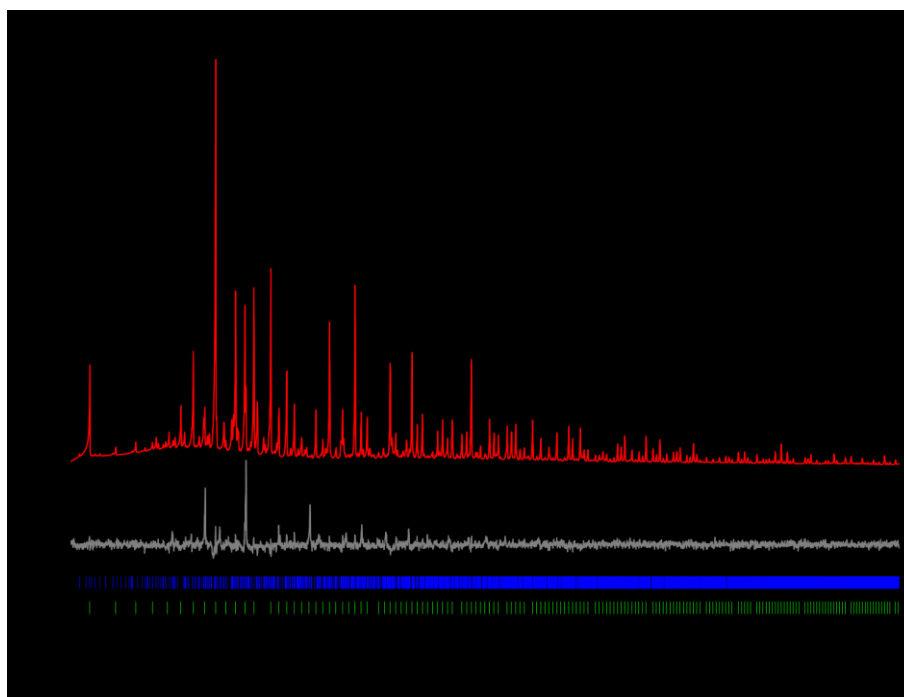


Figure D3. Rietveld refinement based on PXRD data ($\text{Mo-K}\alpha_1$, $\lambda = 0.70930 \text{ \AA}$) collected from a powder sample containing $\text{Sr}_{28.5+x}\text{La}_{75-x}[\text{Si}_{170}\text{N}_{312-x}\text{O}_{9+x}]\text{O}_4$ with $x \approx -3.71$ (approx. 28 wt%, vertical blue bars for indication of the position of its Bragg reflections) based on the structure model obtained by SCXRD data and $\text{La}_{13.68}\text{Sr}_{12.32}[\text{Si}_{60}\text{N}_{96}]\text{F}_{6.32}\text{O}_{5.68}$ (approx. 72 wt%, vertical green bars for indication of the position of its Bragg reflections). Additional reflections from an unknown phase are marked with asterisks. Observed (black) and calculated (red) powder X-ray diffraction patterns with corresponding difference profile (gray).

Table D5. Details of the Rietveld refinement for a sample containing $\text{Sr}_{28.5+x}\text{La}_{75-x}[\text{Si}_{170}\text{N}_{312-x}\text{O}_{9+x}]\text{O}_4$ ($x \approx -3.71$) and $\text{La}_{13.68}\text{Sr}_{12.32}[\text{Si}_{60}\text{N}_{96}]\text{F}_{6.32}\text{O}_{5.68}^{[2]}$ based on their respective single-crystal data (standard deviations in parentheses). Only lattice parameters were refined; site occupancy factors as well as isotropic displacement parameters for all sites were taken from the single-crystal data

Formula	$\text{Sr}_{24.79}\text{La}_{78.75}\text{Si}_{170}\text{N}_{315.71}\text{O}_{9.29}$	$\text{La}_{13.68}\text{Sr}_{12.32}[\text{Si}_{60}\text{N}_{96}]\text{F}_{6.32}\text{O}_{5.68}$
weight percent	27.6(9)	72.4(9)
formula mass / $\text{g}\cdot\text{mol}^{-1}$	22456.2	6208.12
crystal system	hexagonal	cubic
space group	$P\bar{6}$ (no.174)	$I\bar{4}3m$ (no.217)
lattice parameters / Å	$a =$	20.0487(12)
	$c =$	22.514(2)
$V / \text{Å}^3$	7837.1(1)	2365.29(10)
Z	1	1
X-ray density / $\text{g}\cdot\text{cm}^{-3}$	4.75778	4.35812
diffractometer	Stoe StadiP	
radiation	Mo- $K\alpha_1$ ($\lambda = 0.70930 \text{ Å}$)	
monochromator	Ge(111)	
$F(000)$	10098	2857
2θ range / °	$2.0 \leq \theta \leq 60.3$	
data points	3886	
number of observed reflections	8144	394
number of parameters	33	
background function	shifted Chebyshev, 12 terms	
R values	$R_p =$	0.0414
	$R_{wp} =$	0.0603
	$R_{exp} =$	0.0482
	$R_{Bragg} =$	0.0425
		0.0244

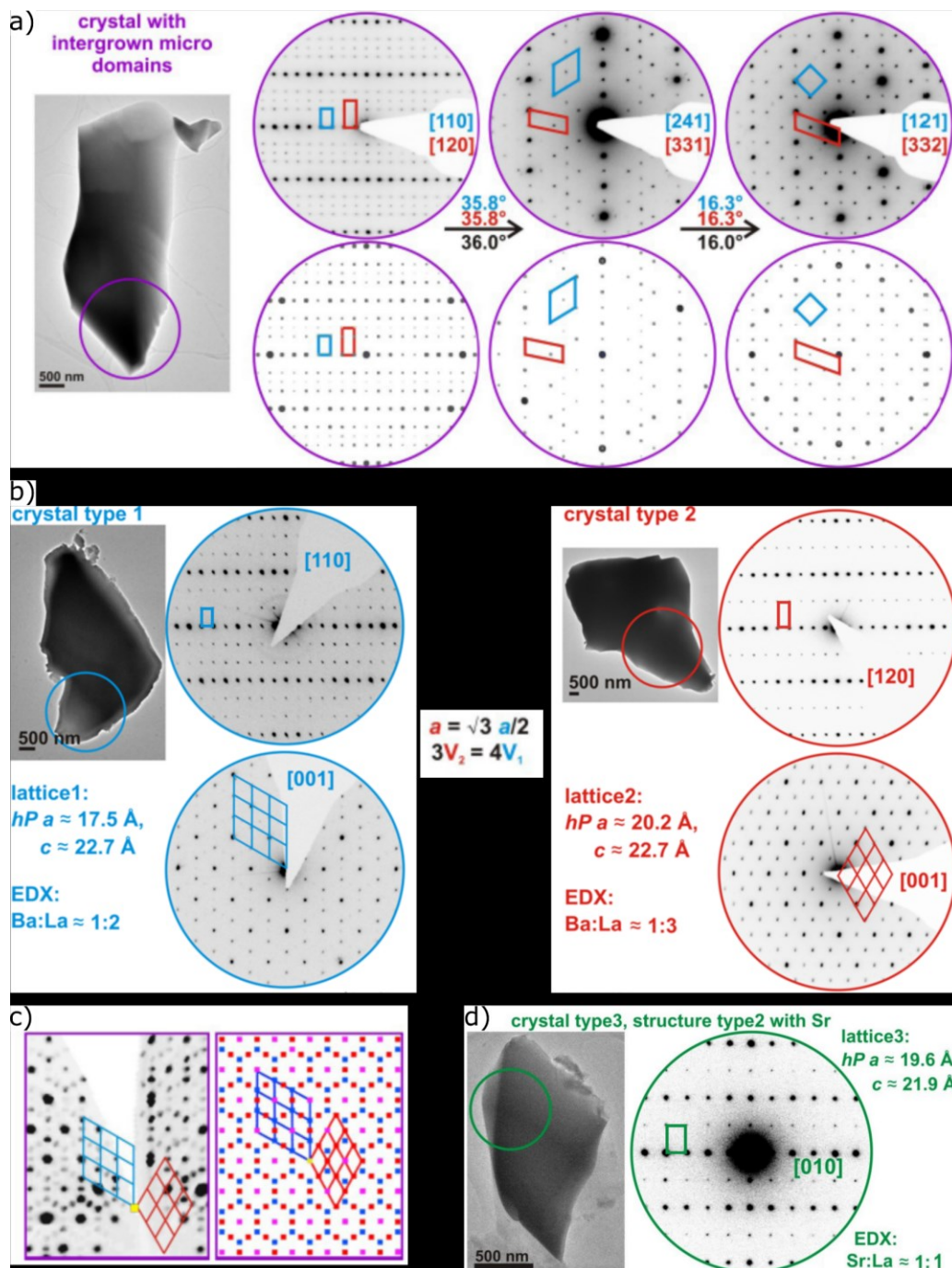


Figure D4. (a) Bright field (BF) image, SAED tilting series (top row) and corresponding superposition of the simulated SAED patterns (bottom row) of the lattice points based on structure models derived from synchrotron data of an intergrown crystallite with unit cells of two new, related hexagonal phases: type 1 (blue) corresponds to $\text{Ba}_{22.5+x}\text{La}_{55-x}[\text{Si}_{129}\text{N}_{240-x}\text{O}_x]\text{O}_3$ and type 2 (red) corresponds to $\text{Ba}_{25.5+x}\text{La}_{77-x}[\text{Si}_{170}\text{N}_{312-x}\text{O}_{9+x}]\text{O}_4$. (b) BF image of the individual pre-characterized single crystallites of the two new oxonitridosilicate oxides with approximate unit cell parameters, TEM-EDX element ratios and representative SAED patterns. The superposition of type 1 and type 2 patterns results in the patterns of intergrown crystals. (c) Comparison of reciprocal lattice section viewed along [001] of an intergrown crystal including a schematic pattern decomposition into the two lattice types. (d) BF image and SAED pattern of type 3 (green) corresponding to $\text{Sr}_{28.5+x}\text{La}_{75-x}[\text{Si}_{170}\text{N}_{312-x}\text{O}_{9+x}]\text{O}_4$ (similar to $\text{Ba}_{25.5+x}\text{La}_{77-x}[\text{Si}_{170}\text{N}_{312-x}\text{O}_{9+x}]\text{O}_4$) with approximate unit cell parameters and EDX element ratio.

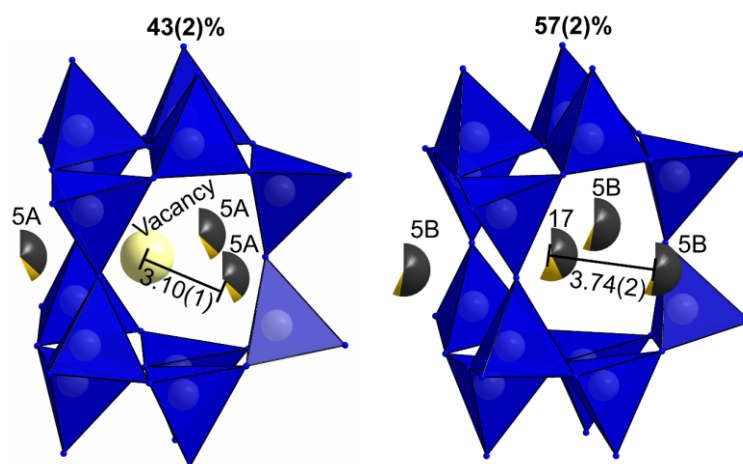


Figure D5. Vicinity of the position La/Ba17 ($s.o.f = 0.57(2)$) in $Ba_{22.5+x}La_{55-x}[Si_{129}N_{240-x}O_x]O_3$. If vacant, the neighboring cations (La/Ba5A, $s.o.f = 0.43(2)$) are located closer to the cage. If occupied, the neighboring cations (La/Ba5B, $s.o.f = 0.57(2)$) are in regular distance to its position. $[SiN_4]$ tetrahedra in blue, La yellow, Ba black, vacancy light yellow.

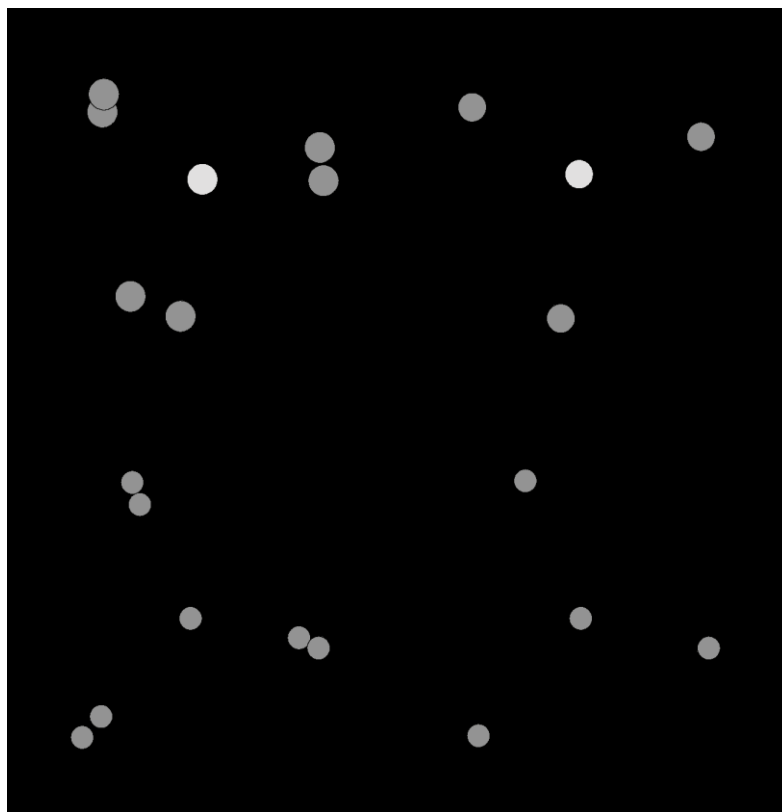


Figure D6. Difference Fourier maps of atoms in the vicinity of La/Ba17 in $Ba_{22.5+x}La_{55-x}[Si_{129}N_{240-x}O_x]O_3$: atomic positions from the refinement in Pm , taking sixfold twinning according to apparent Laue symmetry $6/mmm$ (isoline interval $1 e/\text{\AA}^3$, solid lines for positive and broken lines for negative densities) into account. Atom labels according to the final model refined in $P\bar{6}$. Left: After refinement with all positions of the model in $P\bar{6}$. Right: One split atom of each pair was removed while the other atom was assumed to be fully occupied; high residual densities are observed after “enforced” ordering.

Table D6. Bond valence sums (BVS) for the atoms in $\text{Ba}_{22.5+x}\text{La}_{55-x}[\text{Si}_{129}\text{N}_{240-x}\text{O}_x]\text{O}_3$ as calculated with VaList^[3] with the assumption that either only Ba or only La occupy the respective sites. Occupancy for Ba on site N calculated according to $\text{occ}[\text{Ba}_N] = [3 - \text{BVS}(\text{La}_N)] / [(\text{BVS}(\text{Ba}_N) - \text{BVS}(\text{La}_N)) - (2 - 3)] * 100$ and for La on site N according to $\text{occ}[\text{La}_N] = [2 - \text{BVS}(\text{Ba}_N)] / [(\text{BVS}(\text{La}_N) - \text{BVS}(\text{Ba}_N)) - (3 - 2)] * 100$ with $\text{BVS}(\text{Ba}_N)$ and $\text{BVS}(\text{La}_N)$ being the calculated bond valence sums of Ba or La on site N , respectively

Atom	BVS	Atom	BVS	Occupancy Ba / %	Occupancy La / %
Ba1A	2.25	La1A	1.28	87.5	12.5
Ba1B	3.03	La1B	1.72	55.5	44.5
Ba2A	4.14	La2A	2.35	23.3	76.7
Ba2B	3.23	La2B	1.84	48.5	51.5
Ba3	4.08	La3	2.32	24.7	75.3
Ba4	3.54	La4	2.02	38.9	61.1
Ba5A	2.12	La5A	1.21	94.0	6.0
Ba5B	1.80	La5B	1.06	100	0
Ba6	3.80	La6	2.16	31.9	68.1
Ba7	4.70	La7	2.67	11.0	89.0
Ba8	5.77	La8	3.28	0	100
Ba9	1.89	La9	1.13	100	0
Ba10	4.40	La10	2.50	17.2	82.8
Ba11	3.08	La11	1.81	52.4	47.6
Ba12	3.71	La12	2.25	30.4	69.6
Ba13	2.54	La13	1.45	74.3	25.7
Ba14	2.40	La14	1.37	80.2	19.8
Ba15	4.61	La15	2.62	12.7	87.3
Ba16	2.34	La16	1.33	82.9	17.1
Ba17	2.32	La17	1.32	84.0	16.0
Ba18	4.45	La18	2.53	16.1	83.9
Ba19	4.24	La19	2.41	20.8	79.2
Ba20	5.23	La20	2.98	0.7	99.3
Ba21	4.37	La21	2.49	17.7	82.3

Table D7. Bond valence sums (BVS) for the atoms in $\text{Ba}_{25.5+x}\text{La}_{77-x}[\text{Si}_{170}\text{N}_{312-x}\text{O}_{9+x}]\text{O}_4$ as calculated with ValList^[2] with the assumption that either only Ba or only La occupy the respective sites. Occupancy for Ba on site N calculated according to $\text{occ}[\text{Ba}_N] = [3 - \text{BVS}(\text{La}_N)] / [(\text{BVS}(\text{Ba}_N) - \text{BVS}(\text{La}_N)) - (2 - 3)] * 100$ and for La on site N according to $\text{occ}[\text{La}_N] = [2 - \text{BVS}(\text{Ba}_N)] / [(\text{BVS}(\text{La}_N) - \text{BVS}(\text{Ba}_N)) - (3 - 2)] * 100$ with $\text{BVS}(\text{Ba}_N)$ and $\text{BVS}(\text{La}_N)$ being the calculated bond valence sums of Ba or La on site N , respectively

Atom	BVS	Atom	BVS	Occupancy Ba / %	Occupancy La / %
Ba1	4.64	La1	3.24	0	100
Ba2	3.83	La2	2.71	13.7	86.3
Ba3	3.16	La3	2.25	39.3	60.7
Ba4	1.90	La4	1.38	100	0
Ba5	3.99	La5	2.85	7.0	93.0
Ba6	1.92	La6	1.37	100	0
Ba7	2.07	La7	1.50	95.5	4.5
Ba8	2.51	La8	1.76	70.9	29.1
Ba9A	2.39	La9A	1.69	77.1	22.9
Ba9B	2.37	La9B	1.72	77.6	22.4
Ba10	2.61	La10	1.84	65.5	34.5
Ba11	2.82	La11	1.97	55.7	44.3
Ba12	4.72	La12	3.39	0	100
Ba13	4.65	La13	3.30	0	100
Ba14	4.46	La14	3.20	0	100
Ba15	4.11	La15	2.97	1.4	98.6
Ba16	4.18	La16	2.98	0.9	99.1
Ba17	4.44	La17	3.14	0	100
Ba18	4.09	La18	2.88	5.4	94.6
Ba19	5.16	La19	3.68	0	100
Ba20	3.36	La20	2.41	30.3	69.7
Ba21	4.67	La21	3.25	0	100
Ba22	4.99	La22	3.60	0	100
Ba23	4.70	La23	3.29	0	100
Ba24	5.02	La24	3.59	0	100
Ba25	3.85	La25	2.72	13.1	86.9
Ba26	2.37	La26	1.37	81.5	18.5
Ba27	4.01	La27	2.28	26.4	73.6

Table D8. Bond valence sums (BVS) for the atoms in $\text{Sr}_{28.5+x}\text{La}_{75-x}[\text{Si}_{170}\text{N}_{312-x}\text{O}_{9+x}]\text{O}_4$ as calculated with VaList^[2] with the assumption that either only Sr or only La occupy the respective sites. Occupancy for Ba on site N calculated according to $\text{occ}[\text{Ba}N] = [3 - \text{BVS}(\text{La}N)] / [(\text{BVS}(\text{Ba}N) - \text{BVS}(\text{La}N)) - (2 - 3)] * 100$ and for La on site N according to $\text{occ}[\text{La}N] = [2 - \text{BVS}(\text{Ba}N)] / [(\text{BVS}(\text{La}N) - \text{BVS}(\text{Ba}N)) - (3 - 2)] * 100$ with $\text{BVS}(\text{Ba}N)$ and $\text{BVS}(\text{La}N)$ being the calculated bond valence sums of Ba or La on site N , respectively

Atom	BVS	Atom	BVS	Occupancy Ba / %	Occupancy La / %
Sr0	1.44	La0	1.57	100	0
Sr1	2.49	La1	2.71	37.2	62.8
Sr2	2.15	La2	2.37	81.0	19.0
Sr3	2.00	La3	2.18	99.8	0.2
Sr4	1.22	La4	1.36	100	0
Sr5	2.19	La5	2.39	76.3	23.8
Sr6	1.33	La6	1.47	100	0
Sr7	1.29	La7	1.43	100	0
Sr8	1.78	La8	1.92	100	0
Sr9B	1.76	La9B	1.94	100	0
Sr10A	1.87	La10A	2.03	100	0
Sr10B	1.81	La10B	1.96	100	0
Sr11	2.01	La11	2.18	99.3	0.7
Sr12	2.51	La12	2.73	34.6	65.4
Sr13	2.36	La13	2.57	54.4	45.6
Sr14	2.30	La14	2.50	62.5	37.5
Sr15	2.26	La15	2.46	67.5	32.5
Sr16	2.10	La16	2.28	87.8	12.2
Sr17	2.26	La17	2.45	67.9	32.1
Sr18	2.15	La18	2.33	81.7	18.3
Sr19	2.66	La19	2.90	13.2	86.8
Sr20	1.98	La20	2.15	100	0
Sr21	2.40	La21	2.62	48.7	51.3
Sr22	2.70	La21	2.95	6.7	93.3
Sr23	2.39	La23	2.61	11.4	88.6
Sr24	2.67	La24	2.92	36.8	63.2
Sr25	1.85	La25	2.01	100	0
Sr26	2.41	La26	2.62	48.1	51.9
Sr27	2.47	La27	2.68	40.5	59.5

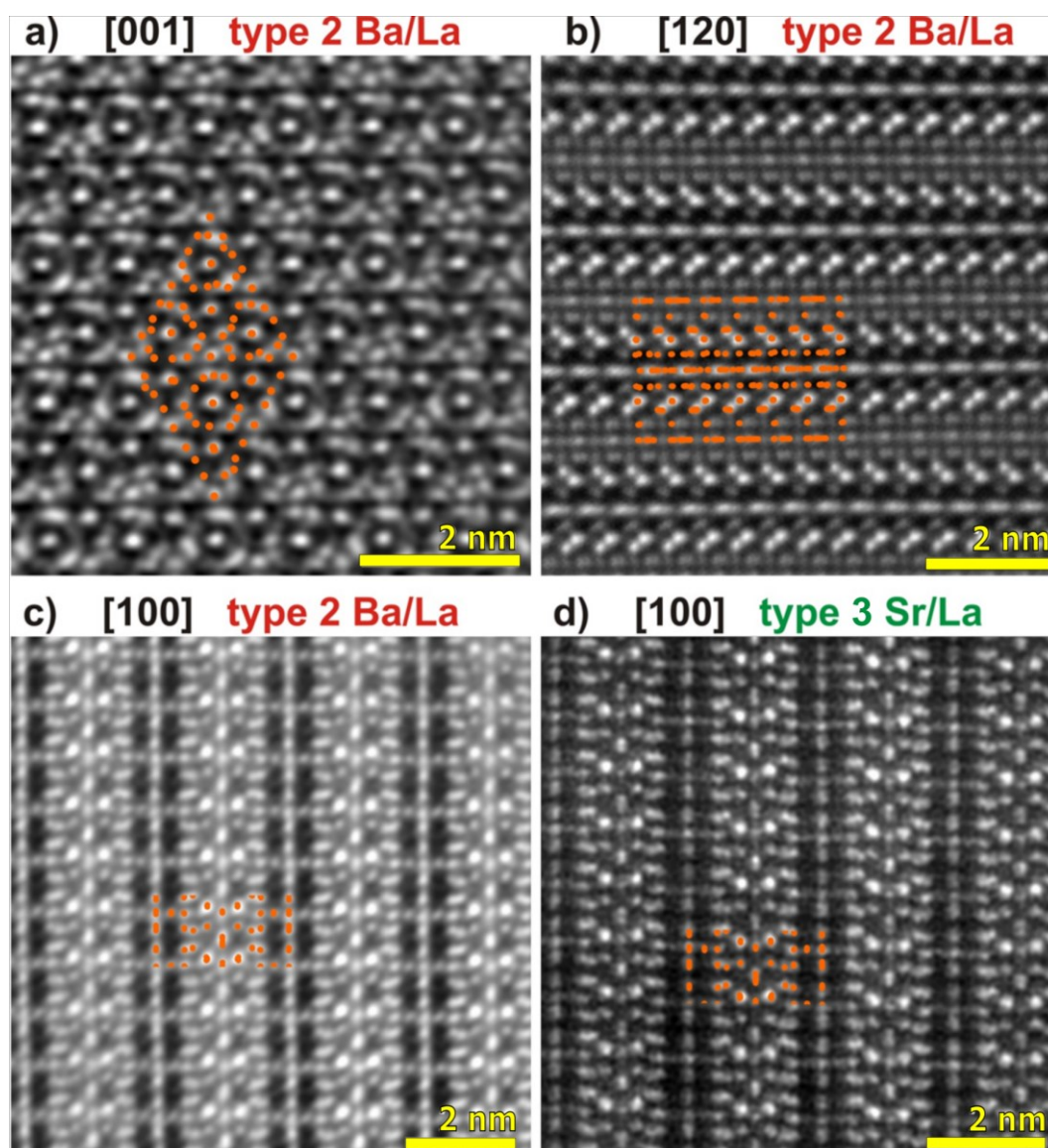


Figure D7. (a–c) Fourier-filtered Z-contrast STEM-HAADF (high-angle annular dark field) images of Ba/La oxonitridosilicate type 2 ($\text{Ba}_{25.5+x}\text{La}_{77-x}[\text{Si}_{170}\text{N}_{312-x}\text{O}_{9+x}]\text{O}_4$) along special directions showing the projection of the heavy atoms (highlighted with orange dots). The contrast distribution (metal cation positions) along [100] of (c) match the one of the isostructural La/Sr oxonitridosilicate $\text{Sr}_{28.5+x}\text{La}_{75-x}[\text{Si}_{170}\text{N}_{312-x}\text{O}_{9+x}]\text{O}_4$ (type 3) shown in (d).

8 Appendix

Table D9. Wyckoff positions, atomic coordinates, isotropic displacement parameters U_{eq} (in \AA^2) (U_{eq} is defined as one third of the trace of the orthogonalized U_{ij} tensor) and site occupancy factors of $\text{Ba}_{22.5+x}\text{La}_{55-x}[\text{Si}_{129}\text{N}_{240-x}\text{O}_x]\text{O}_3$; estimated standard deviations in parentheses. Unrefined s.o.f's are based on BVS calculations with minor corrections to achieve charge neutrality while s.o.f's with e.s.d.'s result from the refinement of the s.o.f's of the respective of split position pairs and nearby underoccupied sites

Atom	Wyckoff Position	x	y	z	U_{eq}	s.o.f.
La1A	3k	0.4702(2)	0.1547(3)	1/2	0.0208(9)	0.170(3)
Ba1A						0.694(13)
La1B	3k	0.4913(11)	0.207(2)	1/2	0.019(7)	0.069(8)
Ba1B						0.067(8)
La2A	3k	0.15797(14)	0.53113(17)	1/2	0.0176(7)	0.721(8)
Ba2A						0.1403(15)
La2B	3k	0.1895(11)	0.4987(10)	1/2	0.022(5)	0.081(5)
Ba2B						0.057(4)
La3	6l	0.01247(9)	0.33929(8)	0.28249(6)	0.0132(3)	0.8139
Ba3						0.1861
La4	3k	0.18016(12)	0.03107(12)	1/2	0.0149(4)	0.692
Ba4						0.313
Si1	6l	0.0181(4)	0.4708(4)	0.3892(4)	0.0179(14)	1
Si2	6l	0.0646(3)	0.3300(4)	0.4328(3)	0.0122(10)	1
Si3	6l	0.1666(3)	0.5132(3)	0.3533(3)	0.0082(11)	1
Si4	6l	0.5062(3)	0.1797(3)	0.3550(3)	0.0098(10)	1
Si5	6l	0.3171(4)	0.1272(4)	0.3722(3)	0.0116(11)	1
Si6	6l	0.0006(3)	0.1629(4)	0.3515(3)	0.0082(10)	1
N1	6l	0.2604(13)	0.0119(13)	0.3869(9)	0.015(4)	1
N2	6l	0.0923(12)	0.4290(12)	0.3999(9)	0.015(3)	1
N3	3k	0.021(2)	0.327(2)	1/2	0.026(6)	1
N4	6l	0.4878(19)	0.089(2)	0.3926(15)	0.041(6)	1
N5	6l	0.4083(12)	0.1751(12)	0.3311(10)	0.017(4)	1
N6	6l	0.0843(14)	0.1942(14)	0.3071(11)	0.024(4)	1
N7	6l	0.0773(14)	0.5208(13)	0.3255(11)	0.021(4)	1
La5A	3j	0.2030(7)	0.1262(6)	0	0.0143(16)	0.063(3)
Ba5A						0.367(17)
La5B	3j	0.2442(9)	0.1544(6)	0	0.0276(17)	0.0439(15)
Ba5B						0.525(18)
La6	2h	1/3	2/3	0.27377(11)	0.0114(4)	0.7472

D. Supporting Information for Chapter 5

Ba6						0.2528
La7						0.9572
Ba7	6 <i>l</i>	0.14059(8)	0.23689(8)	0.20997(6)	0.0123(2)	0.0428
La8	2 <i>i</i>	2/3	1/3	0.2703(2)	0.0536(12)	1
La9						0.0772
Ba9	6 <i>l</i>	0.34563(11)	0.32152(10)	0.11687(8)	0.0280(3)	0.9228
La10						0.8872
Ba10	6 <i>l</i>	0.43348(9)	0.21569(10)	0.22107(7)	0.0248(3)	0.1128
La11						0.5472
Ba11	3 <i>j</i>	0.56220(13)	0.08027(12)	0	0.0186(4)	0.4528
La12						0.7672
Ba12	3 <i>j</i>	0.25348(13)	0.40973(14)	0	0.0196(4)	0.2328
La13						0.3472
Ba13	1 <i>e</i>	2/3	1/3	0	0.0174(6)	0.6528
La14						0.2872
Ba14	3 <i>j</i>	0.00935(13)	0.32257(15)	0	0.0191(4)	0.7128
La15						0.9505
Ba15	2 <i>g</i>	0	0	0.27959(11)	0.0108(4)	0.0495
La16						0.2472
Ba16	1 <i>c</i>	1/3	2/3	0	0.0319(9)	0.7528
La17						0.141(5)
Ba17	1 <i>a</i>	0	0	0	0.034(2)	0.428(15)
La18						0.8972
Ba18	6 <i>l</i>	0.08666(9)	0.56327(8)	0.21705(7)	0.0158(3)	0.1028
Si7	6 <i>l</i>	0.1162(4)	0.3847(3)	0.1322(3)	0.0073(10)	1
Si8	6 <i>l</i>	0.1146(3)	0.0656(3)	0.1366(3)	0.0070(10)	1
Si9	6 <i>l</i>	0.2860(4)	0.0652(4)	0.1366(3)	0.0076(10)	1
Si10	6 <i>l</i>	0.2876(3)	0.5533(3)	0.1275(3)	0.0061(10)	1
Si11	6 <i>l</i>	0.4520(3)	0.0511(3)	0.0511(3)	0.0062(10)	1
Si12	6 <i>l</i>	0.6252(4)	0.2191(3)	0.1247(3)	0.0069(10)	1
Si13	6 <i>l</i>	0.5699(3)	0.1217(3)	0.2415(3)	0.0054(9)	1
Si14	6 <i>l</i>	0.1156(3)	0.5433(3)	0.0720(3)	0.0077(10)	1
Si15	6 <i>l</i>	0.4534(4)	0.2047(3)	0.0691(3)	0.0084(10)	1
Si16	6 <i>l</i>	0.2333(3)	0.4476(4)	0.2398(3)	0.0091(10)	1
Si17	6 <i>l</i>	0.2295(3)	0.1215(3)	0.2444(3)	0.0084(10)	1
Si18	6 <i>l</i>	0.3341(4)	0.3296(4)	0.2738(3)	0.0117(10)	1
Si19	6 <i>l</i>	0.0909(3)	0.2100(3)	0.0732(3)	0.0079(10)	1
O1	3 <i>j</i>	0.3410(17)	0.3433(18)	0	0.027(6)	1

8 Appendix

N8	6 <i>l</i>	0.0008(10)	0.3361(12)	0.1220(9)	0.009(3)	1
N9	3 <i>j</i>	0.096(3)	0.512(3)	0	0.043(10)	1
N10	3 <i>j</i>	0.072(2)	0.189(2)	0	0.024(6)	1
N11	6 <i>l</i>	0.3511(12)	0.1662(12)	0.1037(9)	0.012(4)	1
N12	6 <i>l</i>	0.2871(11)	0.3894(11)	0.2449(8)	0.012(3)	1
N13	2 <i>i</i>	2/3	1/3	0.1187(14)	0.011(5)	1
N14	6 <i>l</i>	0.1756(12)	0.0132(11)	0.1116(9)	0.012(3)	1
N15	6 <i>l</i>	0.1747(11)	0.4960(11)	0.1082(8)	0.009(3)	1
N16	6 <i>l</i>	0.1524(13)	0.1652(13)	0.1053(10)	0.018(4)	1
N17	6 <i>l</i>	0.2879(11)	0.2331(11)	0.2333(8)	0.012(3)	1
N18	6 <i>l</i>	0.1265(12)	0.0785(12)	0.2141(9)	0.014(3)	1
N19	6 <i>l</i>	0.4454(11)	0.3852(12)	0.2577(10)	0.017(4)	1
N20	6 <i>l</i>	0.1456(12)	0.3203(13)	0.0926(10)	0.018(4)	1
N21	6 <i>l</i>	0.0165(12)	0.5050(13)	0.1095(9)	0.013(3)	1
N22	6 <i>l</i>	0.2837(10)	0.0739(10)	0.2134(8)	0.006(3)	1
N23	2 <i>h</i>	1/3	2/3	0.1173(12)	0.002(5)	1
N24	6 <i>l</i>	0.5565(14)	0.3574(14)	0.1950(11)	0.025(5)	1
N25	6 <i>l</i>	0.3016(12)	0.5414(12)	0.2000(10)	0.015(3)	1
N26	2 <i>g</i>	0	0	0.1200(13)	0.005(5)	1
N27	6 <i>l</i>	0.3446(12)	0.5219(12)	0.0796(10)	0.017(4)	1
N28	6 <i>l</i>	0.5110(11)	0.3186(11)	0.0742(9)	0.012(3)	1
N29	3 <i>j</i>	0.446(3)	0.166(3)	0	0.042(9)	1
N30	6 <i>l</i>	0.568(2)	0.185(2)	0.2969(15)	0.042(6)	1
N31	6 <i>l</i>	0.5100(11)	0.1604(11)	0.1109(8)	0.009(3)	1
N32	6 <i>l</i>	0.1319(12)	0.3811(12)	0.2084(9)	0.014(3)	1
N33	6 <i>l</i>	0.4634(11)	0.0567(10)	0.2139(8)	0.006(3)	1
La19						0.8572
Ba19	6 <i>l</i>	0.46368(8)	0.34120(9)	0.38532(6)	0.0134(2)	0.1428
La20	6 <i>l</i>	0.18390(9)	0.19832(9)	0.38798(6)	0.0124(2)	1
La21						0.9072
Ba21	6 <i>l</i>	0.31059(9)	0.45003(8)	0.38280(7)	0.0149(3)	0.0928
Si20	3 <i>k</i>	0.3225(5)	0.2325(5)	1/2	0.0101(15)	1
Si21	2 <i>h</i>	1/3	2/3	0.4233(5)	0.0086(17)	1
Si22	2 <i>i</i>	2/3	1/3	0.4256(4)	0.0065(15)	1
Si23	3 <i>k</i>	0.2072(5)	0.3206(5)	1/2	0.0111(16)	1
Si24	2 <i>g</i>	0	0	0.4263(4)	0.0070(17)	1
Si25	3 <i>k</i>	0.0196(6)	0.5916(6)	1/2	0.0140(17)	1
N34	1 <i>d</i>	1/3	2/3	1/2	0.016(9)	1

D. Supporting Information for Chapter 5

N35	1 <i>b</i>	0	0	1/2	0.012(8)	1
N36	6 <i>l</i>	0.5595(12)	0.2738(12)	0.4005(9)	0.013(3)	1
N37	3 <i>k</i>	0.2201(18)	0.2317(18)	1/2	0.015(5)	1
N38	6 <i>l</i>	0.0964(15)	0.0093(14)	0.4009(11)	0.021(4)	1
N39	6 <i>l</i>	0.2307(12)	0.6005(12)	0.3982(10)	0.014(4)	1
N40	3 <i>k</i>	0.3057(18)	0.4185(18)	1/2	0.017(5)	1
N41	6 <i>l</i>	0.3198(10)	0.3201(11)	0.3482(9)	0.012(3)	1
N42	6 <i>l</i>	0.1561(12)	0.3152(11)	0.4361(9)	0.017(4)	1
N43	6 <i>l</i>	0.0353(13)	0.5465(13)	0.4379(11)	0.019(4)	1
N44	3 <i>k</i>	0.4145(14)	0.3365(16)	1/2	0.006(4)	1
N45	6 <i>l</i>	0.3212(11)	0.1784(11)	0.4362(9)	0.014(3)	1
N46	6 <i>l</i>	0.2222(17)	0.4867(16)	0.3050(13)	0.031(5)	1
N47	6 <i>l</i>	0.2283(11)	0.1049(11)	0.3213(9)	0.013(3)	1
N48	1 <i>f</i>	2/3	1/3	1/2	0.016(8)	1

8 Appendix

Table D10. Anisotropic displacement parameters (U_{ij} in \AA^2) of $\text{Ba}_{22.5+x}\text{La}_{55-x}[\text{Si}_{129}\text{N}_{240-x}\text{O}_x]\text{O}_3$. The anisotropic displacement factor is expressed as $\exp[-2\pi^2 (U_{11}h^2a^{*2} + U_{22}k^2b^{*2} + U_{33}l^2c^{*2} + U_{12}hka^*b^* + U_{13}hla^*c^* + U_{23}klb^*c^*)]$. Standard deviations are given in parentheses, sites with mixed occupancy were constrained to equal atomic displacement parameters

Atom	U_{11}	U_{22}	U_{33}	U_{12}	U_{13}	U_{23}
La/Ba1A	0.0229(13)	0.025(2)	0.0153(14)	0.0122(14)	0	0
La/Ba1B	0.010(7)	0.039(19)	0.003(8)	0.010(9)	0	0
La/Ba2A	0.0119(10)	0.0295(12)	0.0102(13)	0.0093(9)	0	0
La/Ba3	0.0173(6)	0.0104(5)	0.0110(7)	0.0062(5)	0.0017(4)	0.0015(4)
La/Ba4	0.0148(8)	0.0176(8)	0.0148(10)	0.0100(7)	0	0
Si1	0.011(3)	U_{11}	0.029(5)	0.004(2)	-0.001(2)	-0.003(2)
Si2	0.011(2)	0.010(2)	0.014(3)	0.005(2)	0.0005(19)	0.001(2)
Si3	0.006(2)	0.007(2)	0.009(3)	0.0012(19)	-0.0008(19)	-0.0007(18)
Si4	0.007(2)	0.006(2)	0.013(3)	0.0008(18)	-0.0039(19)	-0.003(2)
Si5	0.009(2)	0.011(2)	0.017(3)	0.007(2)	-0.003(2)	-0.002(2)
Si6	0.010(2)	0.006(2)	0.009(3)	0.0047(19)	0.0014(18)	0.0023(19)
La/Ba5A	0.021(4)	0.019(3)	0.011(3)	0.016(3)	0	0
La/Ba5B	0.048(5)	0.025(3)	0.018(2)	0.024(3)	0	0
La/Ba6	0.0084(5)	U_{11}	0.0176(12)	0.0042(3)	0	0
La/Ba7	0.0167(6)	0.0095(5)	0.0133(6)	0.0084(4)	-0.0022(4)	-0.0002(4)
La8	0.0120(7)	U_{11}	0.137(4)	0.0060(3)	0	0
La/Ba9	0.0313(8)	0.0193(7)	0.0217(9)	0.0040(6)	0.0045(6)	0.0023(5)
La/Ba10	0.0142(6)	0.0212(7)	0.0224(9)	-0.0036(5)	0.0012(5)	-0.0098(6)
La/Ba11	0.0191(8)	0.0127(8)	0.0135(11)	0.0001(7)	0	0
La/Ba12	0.0184(9)	0.0225(9)	0.0154(11)	0.0084(7)	0	0
La/Ba13	0.0204(9)	U_{11}	0.0114(17)	0.0102(4)	0	0
La/Ba14	0.0231(9)	0.0295(10)	0.0106(11)	0.0175(8)	0	0
La/Ba15	0.0091(5)	U_{11}	0.0142(12)	0.0045(3)	0	0
La/Ba16	0.0394(14)	U_{11}	0.017(2)	0.0197(7)	0	0
La/Ba17	0.037(3)	U_{11}	0.026(5)	0.0187(16)	0	0
La/Ba18	0.0160(6)	0.0098(5)	0.0177(7)	0.0036(5)	-0.0071(5)	-0.0034(4)
Si7	0.008(2)	0.003(2)	0.010(3)	0.0021(17)	-0.0001(19)	0.0022(18)
Si8	0.003(2)	0.005(2)	0.012(3)	0.0013(17)	0.0006(17)	0.0008(18)
Si9	0.005(2)	0.007(2)	0.010(3)	0.0033(18)	-0.0017(18)	0.0002(19)
Si10	0.006(2)	U_{11}	0.007(3)	0.0025(17)	-0.0003(18)	0.0006(17)
Si11	0.006(2)	0.004(2)	0.009(3)	0.0028(18)	-0.0007(18)	0.0012(18)
Si12	0.012(2)	0.002(2)	0.006(3)	0.0027(18)	-0.0002(19)	0.0020(18)
Si13	0.007(2)	U_{11}	0.005(3)	0.0049(18)	-0.0028(18)	-0.0040(18)

D. Supporting Information for Chapter 5

Si14	0.003(2)	0.005(2)	0.013(3)	0.0011(17)	-0.005(2)	-0.001(2)
Si15	0.004(2)	0.008(2)	0.008(3)	-0.0003(17)	-0.0028(19)	0.0008(19)
Si16	0.008(2)	0.010(2)	0.010(3)	0.0052(18)	-0.0007(18)	-0.0021(19)
Si17	0.011(2)	0.006(2)	0.010(3)	0.0058(19)	0.004(2)	0.0023(19)
Si18	0.011(2)	U_{11}	0.017(3)	0.008(2)	0.001(2)	-0.002(2)
Si19	0.008(2)	0.002(2)	0.014(3)	0.0024(17)	0.0043(18)	0.003(2)
La/Ba19	0.0109(5)	0.0118(5)	0.0178(7)	0.0058(5)	-0.0023(4)	-0.0038(5)
La20	0.0138(5)	0.0100(5)	0.0135(7)	0.0061(5)	-0.0021(4)	-0.0012(4)
La/Ba21	0.0144(6)	0.0132(5)	0.0197(8)	0.0090(5)	0.0007(5)	0.0019(5)
Si20	0.010(3)	0.007(3)	0.012(4)	0.004(3)	0	0
Si21	0.008(2)	0.008(2)	0.010(5)	0.0039(11)	0	0
Si22	0.009(2)	U_{11}	0.001(4)	0.0047(11)	0	0
Si23	0.015(4)	0.007(3)	0.015(5)	0.008(3)	0	0
Si24	0.009(2)	U_{11}	0.003(5)	0.0046(12)	0	0
Si25	0.015(4)	0.017(4)	0.013(5)	0.010(3)	0	0

8 Appendix

Table D11. Wyckoff positions, atomic coordinates, isotropic displacement parameters U_{eq} (in \AA^2) (U_{eq} is defined as one third of the trace of the orthogonalized U_{ij} tensor) and site occupancy factors of $\text{Ba}_{25.5+x}\text{La}_{77-x}[\text{Si}_{170}\text{N}_{312-x}\text{O}_{9+x}]\text{O}_4$; estimated standard deviations in parentheses. Unrefined s.o.f.'s are based on the comparison with the isostructural Sr compound and BVS calculations with minor corrections to achieve charge neutrality while s.o.f.'s with e.s.d.'s result from the refinement of the s.o.f.'s of the respective split position pairs and nearby underoccupied sites

Atom	Wyckoff Position	<i>x</i>	<i>y</i>	<i>z</i>	U_{eq}	s.o.f.
La1	2 <i>h</i>	1/3	2/3	0.27985(6)	0.0122(2)	1
La2	3 <i>j</i>	0.00888(8)	0.38183(8)	0	0.0220(2)	1
La3	3 <i>j</i>	0.13607(9)	0.14559(9)	0	0.0272(3)	1
La4	2 <i>g</i>	0	0	0.11050(7)	0.0223(3)	0.10
Ba4						0.90
La5	6 <i>l</i>	0.34346(5)	0.34773(5)	0.21274(4)	0.01899(16)	0.80
Ba5						0.20
La6	6 <i>l</i>	0.51236(6)	0.00191(5)	0.11330(4)	0.02378(18)	0.13
Ba6						0.87
La7	3 <i>j</i>	0.36692(8)	0.52311(8)	0	0.0261(3)	0.11
Ba7						0.89
La8	3 <i>j</i>	0.17820(7)	0.35178(7)	0	0.0181(2)	0.13
Ba8						0.87
La9A	3 <i>j</i>	0.52528(11)	0.35171(11)	0	0.0216(4)	0.1688(8)
Ba9A						0.565(3)
Ba9B	3 <i>j</i>	0.5034(3)	0.3713(3)	0	0.0216(4)	0.266(4)
Ba10	3 <i>j</i>	0.33491(11)	0.16399(13)	0	0.0438(5)	1
La11	1 <i>e</i>	2/3	1/3	0	0.0525(18)	0.213(3)
Ba11						0.319(4)
La12	6 <i>l</i>	0.33637(4)	0.16289(4)	0.27626(4)	0.01325(15)	1
La13	6 <i>l</i>	0.14567(4)	0.50059(4)	0.20848(3)	0.01195(14)	1
La14	6 <i>l</i>	0.01093(4)	0.15170(5)	0.21719(3)	0.01549(15)	1
La15	6 <i>l</i>	0.50718(5)	0.14802(5)	0.21236(4)	0.01727(15)	1
Si1	6 <i>l</i>	0.25537(19)	0.41279(18)	0.13536(16)	0.0091(6)	1
Si2	6 <i>l</i>	0.16007(19)	0.24055(19)	0.13770(16)	0.0093(6)	1
Si3	6 <i>l</i>	0.4120(2)	0.2562(2)	0.12884(17)	0.0119(6)	1
Si4	6 <i>l</i>	0.08358(19)	0.33876(19)	0.13376(15)	0.0092(6)	1
Si5	6 <i>l</i>	0.34141(19)	0.0058(2)	0.24122(15)	0.0096(6)	1
Si6	6 <i>l</i>	0.33881(19)	0.49765(19)	0.24388(15)	0.0087(6)	1
Si7	6 <i>l</i>	0.1732(2)	0.1580(2)	0.24111(15)	0.0097(6)	1
Si8	6 <i>l</i>	0.4905(2)	0.3314(2)	0.24370(17)	0.0138(7)	1
Si9	6 <i>l</i>	0.31521(19)	0.31566(19)	0.07086(15)	0.0103(6)	1
Si10	6 <i>l</i>	0.1815(2)	0.5010(2)	0.07429(15)	0.0097(6)	1
Si11	6 <i>l</i>	0.5040(2)	0.18188(19)	0.07199(15)	0.0098(6)	1

D. Supporting Information for Chapter 5

Si12	2g	0	0	0.2741(3)	0.0091(10)	1
Si13	6l	0.00161(18)	0.50266(18)	0.27000(17)	0.0096(6)	1
Si14	6l	0.0064(2)	0.1827(2)	0.07062(15)	0.0102(6)	1
Si15	6l	0.3449(2)	0.08596(19)	0.12757(15)	0.0094(6)	1
Si16	6l	0.3413(2)	0.5853(2)	0.13616(15)	0.0102(6)	1
Si17	6l	0.2416(2)	0.1508(2)	0.12525(15)	0.0095(6)	1
Si18	6l	0.5835(2)	0.33869(19)	0.13779(16)	0.0101(6)	1
O1	1a	0	0	0	0.069(13)	1
O2	3j	0.0075(10)	0.4936(9)	0	0.026(3)	1
N1	6l					0.56
O3	6l	0.0085(6)	0.5041(6)	0.3457(5)	0.018(2)	0.44
N2	6l	0.2601(6)	0.4984(6)	0.1092(4)	0.0097(18)	1
N3	3j	0.0411(10)	0.2119(10)	0	0.019(3)	1
N4	6l	0.3351(6)	0.1662(6)	0.1136(5)	0.013(2)	1
N5	2h	1/3	2/3	0.1191(8)	0.010(3)	1
N6	6l	0.3601(6)	0.0862(6)	0.2015(5)	0.013(2)	1
N7	2i	2/3	1/3	0.1221(8)	0.009(3)	1
N8	6l	0.4007(8)	0.3197(8)	0.0873(7)	0.027(3)	1
N9	6l	0.0727(6)	0.1685(6)	0.1111(5)	0.013(2)	1
N10	6l	0.3172(7)	0.0219(7)	0.3109(5)	0.017(2)	1
N11	6l	0.5824(7)	0.0774(7)	0.2431(5)	0.020(2)	1
N12	6l	0.0761(6)	0.5777(6)	0.2325(5)	0.0123(19)	1
N13						0.56
O4	2g	0	0	0.3481(8)	0.017(3)	0.44
N14	6l	0.2277(7)	0.1828(7)	0.3037(5)	0.015(2)	1
N15	6l	0.2241(7)	0.1293(7)	0.1977(5)	0.016(2)	1
N16	6l	0.1649(6)	0.3291(6)	0.1200(5)	0.013(2)	1
N17	3j	0.2818(12)	0.2945(12)	0	0.029(4)	1
N18	6l	0.3225(7)	0.3974(7)	0.1007(5)	0.018(2)	1
N19	6l	0.4105(7)	0.2686(7)	0.2034(6)	0.020(2)	1
N20	6l	0.2588(6)	0.0004(6)	0.1080(4)	0.0086(17)	1
N21	3j	0.5248(10)	0.2068(10)	0	0.021(3)	1
N22	6l	0.2639(6)	0.4182(6)	0.2109(5)	0.0103(19)	1
N23	6l	0.3452(6)	0.5784(6)	0.2119(5)	0.0120(19)	1
N24	6l	0.0838(6)	0.0760(6)	0.2489(5)	0.015(2)	1
N25	6l	0.4196(7)	0.0973(7)	0.0834(5)	0.017(2)	1
N26	6l	0.0765(7)	0.3453(7)	0.2107(5)	0.015(2)	1
N27	6l	0.4996(7)	0.2587(6)	0.1099(5)	0.013(2)	1
N28	6l	0.5735(6)	0.3393(6)	0.2142(5)	0.012(2)	1
N29	3j	0.1909(11)	0.5045(11)	0	0.023(4)	1
N30	6l	0.3233(6)	0.4915(6)	0.3203(5)	0.0123(19)	1
N31	6l	0.1824(6)	0.0814(6)	0.0761(5)	0.014(2)	1
N32	6l	0.2390(6)	0.2363(6)	0.1102(5)	0.013(2)	1

8 Appendix

N33	6l	0.1748(6)	0.5754(6)	0.1047(5)	0.0119(19)	1
N34	6l	0.1622(6)	0.2319(6)	0.2143(5)	0.0118(19)	1
N35	6l	0.0997(7)	0.4193(7)	0.0958(5)	0.017(2)	1
N36	6l	0.5756(7)	0.1727(7)	0.1082(5)	0.016(2)	1
N37	6l	0.4241(7)	0.0027(7)	0.2408(5)	0.017(2)	1
La16	6l	0.42797(5)	0.05735(6)	0.38529(4)	0.02069(17)	1
La17						1/2
Ba17	6l	0.16207(4)	0.33295(4)	0.28129(4)	0.01483(16)	1/2
La18						1/2
Ba18	3k	0.27684(6)	0.50292(6)	1/2	0.0142(2)	1/2
La19	3k	0.21990(6)	0.02922(6)	1/2	0.01350(19)	1
La20	3k	0.24719(8)	0.26185(11)	1/2	0.0348(4)	1
La21						0.75
Ba21	2i	2/3	1/3	0.28212(7)	0.0206(3)	0.25
La22	6l	0.13236(4)	0.08190(4)	0.37885(3)	0.01242(14)	1
La23	6l	0.43971(5)	0.37433(5)	0.38546(4)	0.01824(17)	1
La24	6l	0.13722(5)	0.55840(5)	0.38657(3)	0.01378(14)	1
Si19	2h	1/3	2/3	0.4263(3)	0.0118(11)	1
Si20	6l	0.3357(2)	0.17413(19)	0.42491(16)	0.0115(6)	1
Si21	6l	0.2507(2)	0.5036(2)	0.35117(15)	0.0101(6)	1
Si22	3k	0.0537(3)	0.5986(3)	1/2	0.0109(8)	1
Si23	6l	0.25842(19)	0.25369(19)	0.35514(16)	0.0104(6)	1
Si24	6l	0.24660(19)	0.0091(2)	0.35623(15)	0.0106(6)	1
Si25	3k	0.0607(3)	0.4495(3)	1/2	0.0132(9)	1
Si26	3k	0.5437(4)	0.0946(3)	1/2	0.0184(10)	1
Si27	6l	0.1312(2)	0.37075(19)	0.43390(15)	0.0113(6)	1
Si28	3k	0.0621(3)	0.0985(3)	1/2	0.0104(9)	1
Si29	6l	0.2982(2)	0.4118(2)	0.37092(16)	0.0130(6)	1
Si30	6l	0.0877(2)	0.2097(2)	0.39260(15)	0.0110(6)	1
N38	3k	0.1684(10)	0.3646(10)	1/2	0.019(3)	1
N39	1d	1/3	2/3	1/2	0.016(5)	1
N40	1b	0	0	1/2	0.010(4)	1
N41	6l	0.2101(6)	0.4110(6)	0.3844(5)	0.0116(19)	1
N42	6l	0.3019(6)	0.3456(6)	0.3259(5)	0.014(2)	1
N43						0.56
O5	6l	0.1962(7)	0.5198(7)	0.3055(5)	0.022(2)	0.44
N44	6l	0.0337(6)	0.1871(6)	0.3264(5)	0.0129(19)	1
N45	6l	0.1809(7)	0.2383(7)	0.3940(5)	0.018(2)	1
N46	3k	0.4462(10)	0.0387(10)	1/2	0.017(3)	1
N47	3k	0.3285(11)	0.1661(11)	1/2	0.025(4)	1
N48	6l	0.2959(7)	0.5725(7)	0.4029(5)	0.019(2)	1
N49	6l	0.0641(6)	0.2807(6)	0.4102(5)	0.0131(19)	1
N50	6l	0.3217(7)	0.2473(7)	0.4027(5)	0.017(2)	1

D. Supporting Information for Chapter 5

N51	3k	0.5915(9)	0.0433(9)	1/2	0.012(3)	1
N52	3k	0.1032(9)	0.5484(10)	1/2	0.016(3)	1
N53	6l	0.0904(7)	0.4273(7)	0.4346(5)	0.019(2)	1
N54	6l	0.0409(6)	0.1332(6)	0.4378(5)	0.0125(19)	1
N55	6l	0.3487(6)	0.4315(7)	0.4357(5)	0.016(2)	1
N56	6l	0.2643(7)	0.0876(7)	0.3956(5)	0.016(2)	1
N57						0.56
O6	3k	0.1513(10)	0.1138(9)	1/2	0.021(3)	0.44
N58	6l	0.4659(11)	0.2915(10)	0.3117(7)	0.045(4)	1
N59	6l	0.4204(7)	0.1846(8)	0.4011(6)	0.028(3)	1
N60	6l	0.5700(9)	0.1497(8)	0.4369(7)	0.037(3)	1
La25	3k					0.2433
Ba25	3k	0.4958(2)	0.2703(2)	1/2	0.0199(7)	0.09
Ba26	3k	0.7227(4)	0.4677(4)	1/2	0.0493(15)	1/3
La27	3k					0.2633
Ba27	3k	0.7950(3)	0.2756(2)	1/2	0.0194(7)	0.07
Si31	6l	0.7596(2)	0.2527(2)	0.35419(16)	0.0119(6)	1
Si32	6l	0.6224(6)	0.2492(6)	0.4323(5)	0.0147(19)	1/3
Si33	6l	0.7800(6)	0.3762(6)	0.3897(4)	0.0093(18)	1/3
N67	6l					0.706
O7	6l	0.5352(11)	0.1913(12)	0.3256(9)	0.069(5)	0.294
N68	6l	0.572(3)	0.286(2)	0.399(3)	0.069(5)	1/3
N69	6l	0.710(2)	0.2809(13)	0.402(3)	0.069(5)	1/3
N70	6l	0.730(3)	0.423(2)	0.386(3)	0.069(5)	1/3
N71	3k	0.640(5)	0.290(3)	1/2	0.069(5)	1/3

8 Appendix

Table D12. Anisotropic displacement parameters (U_{ij} in \AA^2) of $\text{Ba}_{25.5+x}\text{La}_{77-x}[\text{Si}_{170}\text{N}_{312-x}\text{O}_{9+x}]\text{O}_4$. The anisotropic displacement factor is expressed as $\exp[-2\pi^2 (U_{11}h^2a^{*2} + U_{22}k^2b^{*2} + U_{33}l^2c^{*2} + U_{12}hka^*b^* + U_{13}hla^*c^* + U_{23}klb^*c^*)]$. Standard deviations are given in parentheses, sites with mixed occupancy were constrained to equal atomic displacement parameters.

Atom	U_{11}	U_{22}	U_{33}	U_{12}	U_{13}	U_{23}
La1	0.0124(3)	U_{11}	0.0119(5)	0.00619(17)	0	0
La2	0.0256(6)	0.0283(6)	0.0153(5)	0.0157(5)	0	0
La3	0.0410(8)	0.0447(8)	0.0142(5)	0.0353(7)	0	0
La/Ba4	0.0237(5)	U_{11}	0.0195(7)	0.0119(2)	0	0
La/Ba5	0.0234(4)	0.0216(4)	0.0195(4)	0.0169(3)	-0.0071(3)	-0.0047(3)
La/Ba6	0.0310(5)	0.0205(4)	0.0204(4)	0.0132(4)	-0.0042(3)	-0.0015(3)
La/Ba7	0.0223(6)	0.0284(7)	0.0144(5)	0.0027(5)	0	0
La/Ba8	0.0229(6)	0.0167(5)	0.0130(5)	0.0085(5)	0	0
La/Ba9A	0.0258(9)	0.0205(8)	0.0132(6)	0.0075(6)	0	0
Ba9B	0.0258(9)	0.0205(8)	0.0132(6)	0.0075(6)	0	0
Ba10	0.0512(11)	0.0754(14)	0.0152(7)	0.0395(10)	0	0
La/Ba11	0.060(3)	U_{11}	0.037(3)	0.0301(14)	0	0
La12	0.0122(3)	0.0123(3)	0.0149(3)	0.0059(3)	0.0011(3)	0.0006(2)
La13	0.0147(3)	0.0102(3)	0.0101(3)	0.0055(3)	0.0007(3)	0.0003(2)
La14	0.0106(3)	0.0163(4)	0.0153(3)	0.0036(3)	0.0021(3)	0.0002(3)
La15	0.0135(4)	0.0174(4)	0.0198(4)	0.0068(3)	0.0054(3)	0.0053(3)
Si1	0.0097(14)	0.0061(14)	0.0118(15)	0.0042(11)	-0.0010(12)	-0.0001(11)
Si2	0.0084(14)	0.0089(14)	0.0109(15)	0.0045(12)	-0.0004(11)	-0.0013(11)
Si3	0.0088(14)	0.0090(14)	0.0175(16)	0.0043(12)	0.0016(13)	-0.0027(12)
Si4	0.0079(14)	0.0078(14)	0.0117(14)	0.0037(12)	0.0014(12)	-0.0003(11)
Si5	0.0086(14)	0.0095(14)	0.0103(14)	0.0041(12)	0.0012(11)	0.0002(12)
Si6	0.0070(13)	U_{11}	0.0112(14)	0.0027(11)	0.0009(11)	-0.0008(11)
Si7	0.0090(14)	0.0108(14)	0.0114(15)	0.0065(12)	0.0006(11)	0.0008(12)
Si8	0.0146(16)	0.0155(16)	0.0125(16)	0.0083(14)	0.0049(13)	0.0050(13)
Si9	0.0114(15)	0.0075(14)	0.0116(14)	0.0045(12)	0.0023(12)	0.0012(11)
Si10	0.0096(14)	0.0097(14)	0.0098(14)	0.0049(12)	0.0002(12)	0.0014(12)
Si11	0.0094(14)	0.0102(15)	0.0098(14)	0.0049(12)	0.0008(12)	0.0009(12)
Si12	0.0098(15)	U_{11}	0.008(2)	0.0049(7)	0	0
Si13	0.0075(13)	0.0096(14)	0.0124(15)	0.0047(12)	0.0007(11)	0.0009(11)
Si14	0.0099(14)	0.0097(14)	0.0092(13)	0.0035(12)	-0.0015(12)	-0.0007(12)
Si15	0.0078(14)	0.0087(14)	0.0114(14)	0.0039(12)	0.0012(12)	0.0004(12)
Si16	0.0087(14)	0.0129(15)	0.0093(14)	0.0057(12)	-0.0014(11)	-0.0007(12)

D. Supporting Information for Chapter 5

Si17	0.0110(14)	0.0094(14)	0.0093(14)	0.0061(12)	0.0013(12)	0.0002(12)
Si18	0.0100(15)	0.0089(14)	0.0113(15)	0.0048(12)	0.0015(12)	0.0007(12)
La16	0.0199(4)	0.0299(5)	0.0190(4)	0.0175(4)	0.0011(3)	0.0052(3)
La/Ba17	0.0161(3)	0.0145(4)	0.0136(4)	0.0074(3)	-0.0005(3)	0.0000(3)
La/Ba18	0.0144(5)	0.0131(5)	0.0124(5)	0.0049(4)	0	0
La19	0.0126(4)	0.0148(5)	0.0099(4)	0.0046(4)	0	0
La20	0.0197(6)	0.0548(10)	0.0104(5)	0.0040(6)	0	0
La/Ba21	0.0207(4)	U_{11}	0.0205(7)	0.0103(2)	0	0
La22	0.0118(3)	0.0107(3)	0.0152(3)	0.0060(3)	0.0009(3)	0.0006(3)
La23	0.0233(4)	0.0115(3)	0.0171(4)	0.0066(3)	-0.0031(3)	-0.0004(3)
La24	0.0153(3)	0.0141(3)	0.0138(3)	0.0088(3)	0.0019(3)	0.0002(3)
Si19	0.0138(16)	U_{11}	0.008(2)	0.0069(8)	0	0
Si20	0.0150(16)	0.0125(15)	0.0082(15)	0.0077(13)	0.0014(11)	-0.0001(11)
Si21	0.0112(14)	0.0108(14)	0.0097(14)	0.0065(12)	0.0010(12)	0.0000(12)
Si22	0.011(2)	U_{11}	0.012(2)	0.0064(18)	0	0
Si23	0.0098(14)	0.0091(14)	0.0121(14)	0.0046(12)	0.0014(12)	0.0016(11)
Si24	0.0102(14)	0.0099(14)	0.0110(14)	0.0046(12)	0.0026(12)	0.0015(12)
Si25	0.021(2)	0.010(2)	0.013(2)	0.0108(19)	0	0
Si26	0.026(3)	0.020(3)	0.013(2)	0.014(2)	0	0
Si27	0.0095(14)	U_{11}	0.0111(14)	0.0020(12)	0.0015(12)	0.0009(11)
Si28	0.012(2)	0.009(2)	0.009(2)	0.0048(17)	0	0
Si29	0.0157(16)	0.0119(15)	0.0116(15)	0.0071(13)	0.0002(12)	-0.0001(12)
La/Ba25	0.0173(16)	0.0271(19)	0.0158(16)	0.0114(15)	0	0
Ba26	0.049(4)	0.071(5)	0.051(3)	0.048(4)	0	0
La/Ba27	0.043(2)	0.0174(15)	0.0061(13)	0.0215(17)	0	0

8 Appendix

Table D13. Wyckoff positions, atomic coordinates, isotropic displacement parameters U_{eq} (in \AA^2) (U_{eq} is defined as one third of the trace of the orthogonalized U_{ij} tensor) and site occupancy factors of $\text{Sr}_{28.5+x}\text{La}_{75-x}[\text{Si}_{170}\text{N}_{312-x}\text{O}_{9+x}]\text{O}_4$; estimated standard deviations in parentheses. Unrefined s.o.f values of N and O are based on EDX, bond valence sum calculations and charge neutrality

Atom	Wyckoff Position	x	y	z	U_{eq}	s.o.f.
Sr0	1c	1/3	2/3	0	0.011(2)	0.79(3)
La1	2h	1/3	2/3	0.27887(10)	0.0082(4)	1
La2	3j	0.00338(13)	0.39178(14)	0	0.0151(4)	1
La3	3j	0.1417(2)	0.1535(2)	0	0.0307(7)	1
La4	2g	0	0	0.1085(2)	0.0303(16)	0.10(6)
Sr4						0.90(6)
La5	6l	0.33325(10)	0.34018(10)	0.21684(7)	0.0121(5)	0.79(3)
Sr5						0.21(3)
La6	6l	0.52341(17)	-0.00020(17)	0.12097(10)	0.0254(8)	0.14(3)
Sr6						0.86(3)
La7	3j	0.3659(2)	0.4981(2)	0	0.0252(12)	0.13(4)
Sr7						0.87(4)
La8	3j	0.16599(17)	0.34981(16)	0	0.0100(8)	0.14(4)
Sr8						0.86(4)
Sr9B	3j	0.50630(14)	0.37222(16)	0	0.0143(8)	0.42(4)
La9B						0.58(4)
S10A	3j	0.3152(3)	0.1250(3)	0	0.0142(13)	0.764(19)
S10B	3j	0.3702(12)	0.1827(13)	0	0.0142(13)	0.163(11)
Sr11	1e	2/3	1/3	0	0.0055(8)	1
La12	6l	0.33677(7)	0.16363(7)	0.27407(6)	0.0030(2)	1
La13	6l	0.14602(8)	0.49866(7)	0.20696(6)	0.0066(2)	1
La14	6l	0.01181(8)	0.15296(8)	0.21714(6)	0.0081(3)	1
La15	6l	0.51062(8)	0.15154(9)	0.21452(7)	0.0109(3)	1
Si1	6l	0.2548(3)	0.4132(3)	0.1363(2)	0.0002(2)	1
Si2	6l	0.1596(3)	0.2398(3)	0.1355(2)	0.0002(2)	1
Si3	6l	0.4117(3)	0.2580(3)	0.1233(2)	0.0002(2)	1
Si4	6l	0.0831(3)	0.3393(3)	0.1285(2)	0.0002(2)	1
Si5	6l	0.3421(3)	0.0073(3)	0.2380(2)	0.0002(2)	1
Si6	6l	0.3394(3)	0.4979(3)	0.2430(2)	0.0002(2)	1
Si7	6l	0.1734(3)	0.1578(3)	0.2385(2)	0.0002(2)	1
Si8	6l	0.4884(3)	0.3289(3)	0.2407(2)	0.0002(2)	1
Si9	6l	0.3145(3)	0.3203(3)	0.0694(2)	0.0002(2)	1

D. Supporting Information for Chapter 5

Si10	6l	0.1842(3)	0.5027(3)	0.0714(2)	0.0002(2)	1
Si11	6l	0.5061(3)	0.1816(3)	0.0706(2)	0.0002(2)	1
Si12	2g	0	0	0.2715(4)	0.0002(2)	1
Si13	6l	0.0011(3)	0.5037(3)	0.2669(3)	0.0002(2)	1
Si14	6l	0.0075(3)	0.1807(3)	0.0696(2)	0.0002(2)	1
Si15	6l	0.3453(3)	0.0873(3)	0.1244(2)	0.0002(2)	1
Si16	6l	0.3415(3)	0.5841(3)	0.1348(2)	0.0002(2)	1
Si17	6l	0.2413(3)	0.1518(3)	0.1216(2)	0.0002(2)	1
Si18	6l	0.5815(3)	0.3386(3)	0.1355(2)	0.0002(2)	1
O1	1a	0	0	0	0.0054(5)	1
O2	3j	0.0012(12)	0.5087(13)	0	0.0054(5)	1
N1						0.77
O3	6l	0.0101(10)	0.5060(10)	0.3407(8)	0.0054(5)	0.23
N2	6l	0.2579(11)	0.4985(11)	0.1134(8)	0.0054(5)	1
N3	3j	0.0458(16)	0.2081(16)	0	0.0054(5)	1
N4	6l	0.3334(10)	0.1657(10)	0.1066(9)	0.0054(5)	1
N5	2h	1/3	2/3	0.1177(14)	0.0054(5)	1
N6	6l	0.3622(11)	0.0864(11)	0.1992(8)	0.0054(5)	1
N7	2i	2/3	1/3	0.1167(14)	0.0054(5)	1
N8	6l	0.3987(11)	0.3213(11)	0.0812(8)	0.0054(5)	1
N9	6l	0.0718(11)	0.1652(11)	0.1087(8)	0.0054(5)	1
N10	6l	0.3164(11)	0.0213(11)	0.3053(8)	0.0054(5)	1
N11	6l	0.5841(11)	0.0816(11)	0.2418(8)	0.0054(5)	1
N12	6l	0.0756(11)	0.5774(11)	0.2298(8)	0.0054(5)	1
N13						0.77
O4	2g	0	0	0.3446(13)	0.0054(5)	0.23
N14	6l	0.2293(11)	0.1851(11)	0.3010(8)	0.0054(5)	1
N15	6l	0.2243(11)	0.1297(11)	0.1958(8)	0.0054(5)	1
N16	6l	0.1657(10)	0.3298(10)	0.1161(9)	0.0054(5)	1
N17	3j	0.2867(15)	0.3222(15)	0	0.0054(5)	1
N18	6l	0.3261(11)	0.4017(11)	0.1072(8)	0.0054(5)	1
N19	6l	0.4089(11)	0.2692(11)	0.1978(8)	0.0054(5)	1
N20	6l	0.2569(11)	0.0025(11)	0.1061(8)	0.0054(5)	1
N21	3j	0.5402(16)	0.2016(16)	0	0.0054(5)	1
N22	6l	0.2623(11)	0.4161(11)	0.2118(8)	0.0054(5)	1
N23	6l	0.3478(11)	0.5789(11)	0.2107(8)	0.0054(5)	1
N24	6l	0.0869(11)	0.0790(11)	0.2493(8)	0.0054(5)	1
N25	6l	0.4200(11)	0.1001(11)	0.0772(8)	0.0054(5)	1

8 Appendix

N26	6l	0.0759(11)	0.3456(11)	0.2041(8)	0.0054(5)	1
N27	6l	0.4977(11)	0.2598(11)	0.1028(8)	0.0054(5)	1
N28	6l	0.5706(11)	0.3341(11)	0.2097(8)	0.0054(5)	1
N29	3j	0.2126(15)	0.5104(15)	0	0.0054(5)	1
N30	6l	0.3261(11)	0.4948(11)	0.3198(8)	0.0054(5)	1
N31	6l	0.1804(11)	0.0810(11)	0.0709(8)	0.0054(5)	1
N32	6l	0.2395(11)	0.2369(11)	0.1073(8)	0.0054(5)	1
N33	6l	0.1744(11)	0.5763(11)	0.0994(8)	0.0054(5)	1
N34	6l	0.1654(11)	0.2329(11)	0.2105(8)	0.0054(5)	1
N35	6l	0.1009(11)	0.4169(11)	0.0882(8)	0.0054(5)	1
N36	6l	0.5739(11)	0.1699(11)	0.1111(8)	0.0054(5)	1
N37	6l	0.4242(11)	0.0051(11)	0.2411(8)	0.0054(5)	1
La16	6l	0.42767(9)	0.05707(10)	0.38417(7)	0.0125(3)	1
La17						0.59(3)
Sr17	6l	0.15817(9)	0.33104(9)	0.28066(7)	0.0071(5)	0.41(3)
La18						0.64(4)
Sr18	3k	0.27668(13)	0.50302(13)	1/2	0.0080(6)	0.36(4)
La19	3k	0.22006(10)	0.02778(10)	1/2	0.0039(3)	1
La20	3k	0.24911(15)	0.26028(16)	1/2	0.0236(6)	1
La21						0.73(5)
Sr21	2i	2/3	1/3	0.27902(11)	0.0090(8)	0.27(5)
La22	6l	0.13269(7)	0.08135(8)	0.37666(6)	0.0042(2)	1
La23	6l	0.43888(8)	0.37352(8)	0.38432(6)	0.0075(3)	1
La24	6l	0.13888(8)	0.55990(8)	0.38848(6)	0.0070(2)	1
Si19	2h	1/3	2/3	0.4264(4)	0.0002(2)	1
Si20	6l	0.3350(3)	0.1724(3)	0.4243(3)	0.0002(2)	1
Si21	6l	0.2503(3)	0.5030(3)	0.3508(2)	0.0002(2)	1
Si22	3k	0.0529(5)	0.5997(5)	1/2	0.0002(2)	1
Si23	6l	0.2581(3)	0.2537(3)	0.3555(2)	0.0002(2)	1
Si24	6l	0.2456(3)	0.0088(3)	0.3550(2)	0.0002(2)	1
Si25	3k	0.0599(5)	0.4499(5)	1/2	0.0002(2)	1
Si26	3k	0.5445(5)	0.0961(5)	1/2	0.0002(2)	1
Si27	6l	0.1304(3)	0.3706(3)	0.4337(2)	0.0002(2)	1
Si28	3k	0.0610(5)	0.0984(5)	1/2	0.0002(2)	1
Si29	6l	0.2976(3)	0.4118(3)	0.3706(2)	0.0002(2)	1
Si30	6l	0.0883(3)	0.2098(3)	0.3931(2)	0.0002(2)	1
N38	3k	0.1678(15)	0.3645(15)	1/2	0.0054(5)	1
N39	1d	1/3	2/3	1/2	0.0054(5)	1

D. Supporting Information for Chapter 5

N40	1b	0	0	1/2	0.0054(5)	1
N41	6l	0.2098(11)	0.4128(11)	0.3820(8)	0.0054(5)	1
N42	6l	0.3002(11)	0.3444(11)	0.3264(8)	0.0054(5)	1
N43	6l	0.1953(10)	0.5187(10)	0.3058(8)	0.0054(5)	0.77
O5						0.23
N44	6l	0.0344(11)	0.1879(11)	0.3261(8)	0.0054(5)	1
N45	6l	0.1807(11)	0.2372(11)	0.3955(8)	0.0054(5)	1
N46	3k	0.4475(15)	0.0401(15)	1/2	0.0054(5)	1
N47	3k	0.3298(15)	0.1655(15)	1/2	0.0054(5)	1
N48	6l	0.2897(11)	0.5738(11)	0.4026(8)	0.0054(5)	1
N49	6l	0.0643(11)	0.2798(11)	0.4097(8)	0.0054(5)	1
N50	6l	0.3206(11)	0.2475(11)	0.4047(8)	0.0054(5)	1
N51	3k	0.5922(15)	0.0437(16)	1/2	0.0054(5)	1
N52	3k	0.1027(15)	0.5492(16)	1/2	0.0054(5)	1
N53	6l	0.0878(11)	0.4272(11)	0.4346(8)	0.0054(5)	1
N54	6l	0.0394(11)	0.1314(11)	0.4377(8)	0.0054(5)	1
N55	6l	0.3488(11)	0.4329(11)	0.4345(8)	0.0054(5)	1
N56	6l	0.2626(11)	0.0878(11)	0.3942(8)	0.0054(5)	1
N57	3k	0.1486(15)	0.1149(15)	1/2	0.0054(5)	0.77
O6						0.23
N58	6l	0.4653(10)	0.2886(10)	0.3106(7)	0.0054(5)	1
N59	6l	0.4225(9)	0.1840(10)	0.4023(7)	0.0054(5)	1
N60	6l	0.5706(10)	0.1489(8)	0.4359(7)	0.0054(5)	1
La25	3k	0.4906(4)	0.2721(4)	1/2	0.009(2)	0.24(4)
Sr25						0.09(4)
La26	3k	0.7330(7)	0.4999(8)	1/2	0.022(4)	0.01(5)
Sr26						0.32(5)
La27	3k	0.8003(5)	0.2787(4)	1/2	0.004(2)	0.25(5)
Sr27						0.08(5)
Si31	6l	0.7600(3)	0.2539(3)	0.3546(2)	0.0002(2)	1
Si32	6l	0.6186(8)	0.2469(8)	0.4332(6)	0.0002(2)	1/3
Si33	6l	0.7735(8)	0.3758(9)	0.3918(6)	0.0002(2)	1/3
N67	6l	0.5418(9)	0.1948(10)	0.3276(7)	0.0054(5)	0.77
O7	6l	0.5418(9)	0.1948(10)	0.3276(7)	0.0054(5)	0.23
N68	6l	0.568(3)	0.287(2)	0.404(2)	0.0054(5)	1/3
N69	6l	0.7075(19)	0.2776(13)	0.406(3)	0.0054(5)	1/3
N70	6l	0.721(2)	0.4196(17)	0.385(2)	0.0054(5)	1/3
N71	3k	0.624(4)	0.287(3)	1/2	0.0054(5)	1/3

Table D14. Anisotropic displacement parameters (U_{ij} in \AA^2) of $\text{Sr}_{28.5+x}\text{La}_{75-x}[\text{Si}_{170}\text{N}_{312-x}\text{O}_{9+x}]\text{O}_4$. The anisotropic displacement factor is expressed as $\exp[-2\pi^2 (U_{11}h^2a^{*2} + U_{22}k^2b^{*2} + U_{33}l^2c^{*2} + U_{12}hka^*b^* + U_{13}hla^*c^* + U_{23}klb^*c^*)]$. Standard deviations are given in parentheses, sites with mixed occupancy were constrained to equal atomic displacement parameters

Atom	U_{11}	U_{22}	U_{33}	U_{12}	U_{13}	U_{23}
La1	0.0094(7)	0.0094(7)	0.0056(9)	0.0047(3)	0	0
La2	0.0107(9)	0.0208(11)	0.0081(8)	0.0034(8)	0	0
La3	0.060(2)	0.066(2)	0.0067(9)	0.0617(19)	0	0
La/Sr4	0.039(2)	0.039(2)	0.013(2)	0.0194(11)	0	0
La/Sr5	0.0195(9)	0.0178(9)	0.0090(7)	0.0169(7)	-0.0035(5)	-0.0022(5)
La/Sr6	0.0322(15)	0.0372(16)	0.0166(12)	0.0247(13)	0.0059(9)	0.0072(9)
La/Sr7	0.0209(19)	0.035(2)	0.0172(17)	0.0118(16)	0	0
La/Sr8	0.0173(16)	0.0073(13)	0.0042(12)	0.0053(11)	0	0
La/Sr9B	0.0063(11)	0.0235(15)	0.0069(11)	0.0028(10)	0	0
Sr10A/B	0.017(2)	0.027(2)	0.0028(17)	0.0141(17)	0	0
Sr11	0.0071(12)	0.0071(12)	0.0022(17)	0.0036(6)	0	0
La12	0.0016(5)	0.0008(5)	0.0067(5)	0.0008(4)	0.0009(4)	-0.0003(4)
La13	0.0107(6)	0.0022(5)	0.0051(5)	0.0018(5)	0.0020(4)	0.0002(4)
La14	0.0038(6)	0.0099(6)	0.0087(6)	0.0020(5)	0.0007(4)	0.0002(5)
La15	0.0068(6)	0.0103(7)	0.0165(7)	0.0050(5)	0.0069(5)	0.0067(5)
La16	0.0056(6)	0.0166(7)	0.0147(7)	0.0050(6)	0.0003(5)	0.0077(5)
La/Sr17	0.0070(8)	0.0075(8)	0.0056(8)	0.0027(6)	-0.0014(5)	-0.0016(5)
La/Sr18	0.0092(11)	0.0064(10)	0.0067(10)	0.0027(8)	0	0
La19	0.0021(7)	0.0032(7)	0.0017(7)	-0.0022(6)	0	0
La20	0.0177(11)	0.0276(13)	0.0052(9)	-0.0039(10)	0	0
La/Sr21	0.0099(10)	0.0099(10)	0.0071(12)	0.0050(5)	0	0
La22	0.0036(5)	0.0025(5)	0.0071(5)	0.0018(5)	0.0005(4)	0.0006(4)
La23	0.0092(6)	0.0047(6)	0.0094(6)	0.0041(5)	-0.0009(4)	0.0002(4)
La24	0.0082(6)	0.0061(6)	0.0085(5)	0.0048(5)	0.0030(4)	0.0026(4)

Table D15. Intervals of interatomic distances (in Å) for the anionic frameworks in the three compounds. Note that both values and e.s.d.'s are slightly biased as average positions of O/N were used despite the different size of neighboring metal atoms

	Layer 1 Si-N/O	Layer 1 O-La/Ba/Sr	Layer 2 Si-N/O	Layer 2 disordered unit Si-N/O
Ba _{22.5+x} La _{55-x} [Si ₁₂₉ N _{240-x} O _x]O ₃	1.66(3) – 1.81(2)	2.34(2) – 2.86(4)	1.63(2) – 1.81(2)	-
Ba _{25.5+x} La _{77-x} [Si ₁₇₀ N _{312-x} O _{9+x}]O ₄	1.68(2) – 1.81(1)	2.26(2) – 2.91(1)	1.64(2) – 1.83(1)	1.64(2) – 1.98(3)
Sr _{28.5+x} La _{75-x} [Si ₁₇₀ N _{312-x} O _{9+x}]O ₄	1.65(3) – 1.81(1)	2.37(3) – 2.97(3)	1.62(3) – 1.86(2)	1.68(2) – 1.94(7)

Table D16. Cation coordination polyhedra for Ba_{22.5+x}La_{55-x}[Si₁₂₉N_{240-x}O_x]O₃

Site	CN	Polyhedron Description	Interval of Distances / Å
La/Ba1A	7	irregular	2.77(3) – 3.18(2)
La/Ba1B	8	bicapped trigonal truncated pyramid	2.55(2) – 3.17(4)
La/Ba2A	7	irregular	2.62(2) – 2.78(2)
La/Ba2B	7	irregular	2.73(2) – 2.99(3)
La/Ba3	7	irregular	2.49(2) – 3.05(2)
La/Ba4	8	irregular	2.60(2) – 3.02(2)
La/Ba5A	9	irregular	2.75(2) – 3.33(3)
La/Ba5B	8	irregular	2.86(3) – 3.36(3)
La/Ba6	6	irregular	2.59(2) – 2.84(3)
La/Ba7	8	irregular	2.60(2) – 3.23(2)
La8	6	irregular	2.36(3) – 2.76(2)
La/Ba9	6	irregular	2.69(4) – 3.12(2)
La/Ba10	7	irregular	2.40(2) – 3.08(2)
La/Ba11	7	distorted pentagonal bipyramid	2.63(2) – 3.07(4)
La/Ba12	8	bicapped trigonal truncated pyramid	2.34(2) – 3.56(3)
La/Ba13	8	bicapped trigonal prism	2.69(3) – 3.10(2)
La/Ba14	5	distorted trigonal bipyramid	2.78(4) – 3.03(3)
La/Ba15	6	distorted square bipyramid	2.41(2) – 3.01(2)
La/Ba16	8	bicapped trigonal prism	2.66(3) – 3.19(2)
La/Ba17	5	trigonal bipyramid	2.72(3) – 2.89(3)
La/Ba18	5	irregular	2.56(2) – 2.69(2)
La/Ba19	7	irregular	2.50(2) – 3.08(3)
La20	7	irregular	2.44(2) – 2.95(2)
La/Ba21	9	irregular	2.48(2) – 2.89(2)

Table D17. Cation coordination polyhedra for $\text{Ba}_{25.5+x}\text{La}_{77-x}[\text{Si}_{170}\text{N}_{312-x}\text{O}_{9+x}]\text{O}_4$

Site	CN	Polyhedron Description	Interval of Distances / Å
La1	6	distorted square bipyramid	2.45(1) – 2.92(1)
La2	5	distorted square pyramid	2.27(2) – 2.69(1)
La3	7	distorted pentagonal bipyramid	2.59(1) – 2.97(2)
La/Ba4	4	trigonal Pyramid	2.50(2) – 2.95(1)
La/Ba5	7	irregular	2.56(1) – 3.18(1)
La/Ba6	6	irregular	2.61(3) – 3.12(1)
La/Ba7	8	irregular	2.75(1) – 3.19(1)
La/Ba8	5	distorted trigonal bipyramid	2.75(1) – 2.96(4)
La/Ba9A	8	irregular	2.85(1) – 3.00(1)
Ba9B	5	distorted square pyramid	2.67(2) – 2.95(1)
Ba10	7	irregular	2.57(1) – 3.30(2)
La/Ba11	5	trigonal pyramid	2.72(2) – 2.77(2)
La12	7	irregular	2.49(1) – 3.21(2)
La13	8	irregular	2.37(1) – 3.24(1)
La14	6	irregular	2.50(1) – 2.69(1)
La15	6	irregular	2.59(1) – 2.68(1)
La16	7	irregular	2.49(1) – 2.83(1)
La/Ba17	6	irregular	2.45(1) – 2.96(1)
La/Ba18	8	irregular	2.53(1) – 3.10(1)
La19	8	bicapped trigonal truncated pyramid	2.52(2) – 2.75(1)
La20	6	irregular	2.62(2) – 3.09(2)
La/Ba21	9	irregular	2.48(1) – 2.93(2)
La22	8	irregular	2.43(5) – 3.08(1)
La23	7	irregular	2.45(1) – 2.87(1)
La24	8	irregular	2.44(1) – 3.09(2)
La/Ba25	9	irregular	2.68(7) – 2.95(3)
Ba26	8	irregular	1.92(1) – 2.99(1)
La/Ba27	9	irregular	2.48(1) – 3.06(2)

Table D18. Cation coordination polyhedra for $\text{Sr}_{28.5+x}\text{La}_{75-x}[\text{Si}_{170}\text{N}_{312-x}\text{O}_{9+x}]\text{O}_4$

Site	CN	Polyhedron Description	Interval of Distances / Å
Sr0	5	trigonal bipyramid	2.65(3) – 2.84(3)
La1	6	distorted square bipyramid	2.46(2) – 2.94(2)
La2	5	distorted square pyramid	2.37(2) – 2.65(2)
La3	8	irregular	2.53(2) – 3.03(2)
La/Sr4	4	trigonal Pyramid	2.44(4) – 2.88(2)
La/Sr5	8	irregular	2.55(2) – 3.16(2)
La/Sr6	7	irregular	2.63(2) – 3.14(2)
La/Sr7	8	distorted pentagonal bipyramid	2.57(2) – 3.20(3)
La/Sr8	7	irregular	2.65(2) – 3.01(2)
La/Sr9B	8	irregular	2.57(2) – 3.18(2)
Sr10A	6	irregular	2.50(2) – 2.96(2)
Sr10B	6	irregular	2.48(2) – 3.13(3)
Sr11	5	trigonal bipyramid	2.59(3) – 2.63(3)
La12	7	irregular	2.48(2) – 3.10(2)
La13	8	irregular	2.39(2) – 3.08(2)
La14	6	irregular	2.52(2) – 2.69(2)
La15	6	irregular	2.57(2) – 2.70(2)
La16	7	irregular	2.55(2) – 2.86(2)
La/Sr17	6	irregular	2.47(2) – 2.91(2)
La/Sr18	6	irregular	2.53(3) – 2.89(2)
La19	8	bicapped trigonal truncated pyramid	2.53(3) – 2.76(3)
La20	7	irregular	2.58(3) – 3.23(4)
La/Sr21	9	irregular	2.49(2) – 2.88(2)
La22	9	irregular	2.43(9) – 3.13(6)
La23	7	irregular	2.49(2) – 2.86(2)
La24	8	irregular	2.49(2) – 2.98(2)
La/Sr25	9	irregular	2.54(4) – 3.09(2)
La/Sr26	6	irregular	2.16(7) – 2.99(4)
La/Sr27	9	irregular	2.42(2) – 2.94(3)

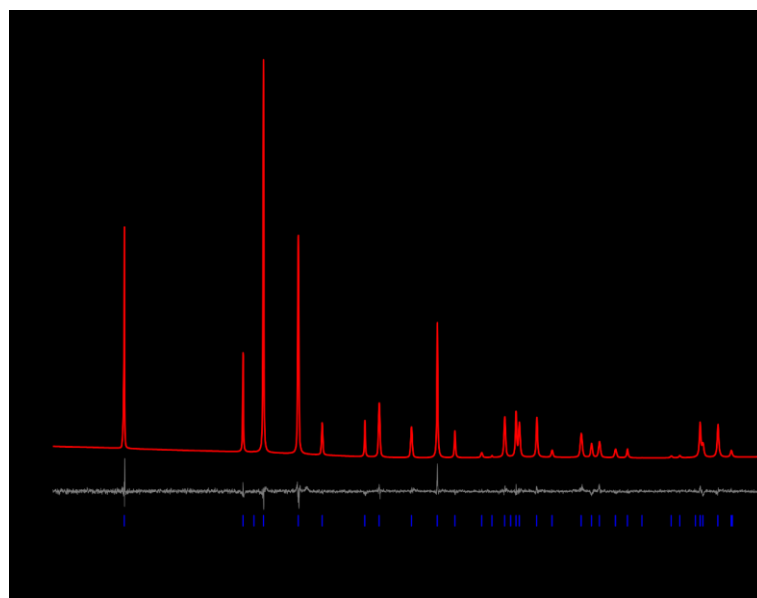


Figure D8. Rietveld refinement for Sr₂N with observed (black) and calculated (red) powder X-ray diffraction patterns and the resulting difference profile (gray). Vertical blue bars indicate the position of the Bragg reflections based on literature known Sr₂N.^[4]

Table D19. Details of the Rietveld refinement of Sr₂N

Formula		Sr ₂ N
formula weight / g·mol ⁻¹		189.2467
crystal system		trigonal
space group		$R\bar{3}m$ (no. 166)
lattice parameters / Å	<i>a</i> =	3.8567(1)
	<i>c</i> =	20.6879(5)
<i>V</i> / Å ³		266.49(1)
<i>Z</i>		3
density / g·cm ⁻³		3.53744
diffractometer		STOE Stadi P
radiation		Cu-Kα ₁ (λ = 1.5406 Å)
monochromator		Ge(111)
detector		Mythen 1K
2θ range / °		5.000 ≤ 2θ ≤ 93.380
data points		5893
total number of reflections		46
refined parameters		35
background function		shifted Chebyshev, 12 polynomials
<i>R</i> values	<i>R</i> _p =	0.0857
	<i>R</i> _{wp} =	0.1130
	<i>R</i> _{exp} =	0.1175
	<i>R</i> _{Bragg} =	0.0303
<i>Goof</i> (χ ²)		0.9617

Table D20. Details of the Rietveld refinement of both “ $\text{Sr}_{22.5+x}\text{La}_{55-x}[\text{Si}_{129}\text{N}_{240-x}\text{O}_x]\text{O}_3$ ” ($x \approx 0.24$) and $\text{Sr}_{28.5+x}\text{La}_{75-x}[\text{Si}_{170}\text{N}_{312-x}\text{O}_{9+x}]\text{O}_4$ ($x \approx -3.71$) in a powder sample containing both phases based on their single-crystal data (standard deviations in parentheses). Only lattice parameters were refined; site occupancy factors as well as isotropic displacement parameters for all sites were taken from the single-crystal data presented in the previous chapter

Formula	“ $\text{Sr}_{22.74}\text{La}_{54.84}\text{Si}_{129}\text{N}_{240}\text{O}_3$ ”	$\text{Sr}_{24.79}\text{La}_{78.75}\text{Si}_{170}\text{N}_{315.77}\text{O}_{9.29}$	
weight percent	23.9(5)	76.1(5)	
formula mass / $\text{g}\cdot\text{mol}^{-1}$	16642.4	22456.2	
crystal system		hexagonal	
space group		$P\bar{6}$ (no.174)	
lattice parameters / Å	$a =$	17.3770(9)	20.0439(1)
	$c =$	22.5063(19)	22.5187(2)
$V / \text{Å}^3$	5885.51(80)	7834.98(12)	
Z		1	
X-ray density / $\text{g}\cdot\text{cm}^{-3}$	4.69521	4.75906	
diffractometer		Stoe StadiP	
radiation		$\text{Cu-K}\alpha_1$ ($\lambda = 1.5406 \text{ Å}$)	
monochromator		Ge(111)	
detector		Mythen 1K	
$F(000)$	7496	10098	
2θ range / °		$5.000 \leq \theta \leq 122.285$	
data points		7820	
number of observed reflections	3150	4193	
number of parameters		35	
background function		shifted Chebyshev, 12 polynomials	
R values	$R_p =$	0.0251	
	$R_{wp} =$	0.0341	
	$R_{exp} =$	0.0179	
	$R_{Bragg} =$	0.0211	0.0268
$\text{Goof} (\chi^2)$		1.9063	

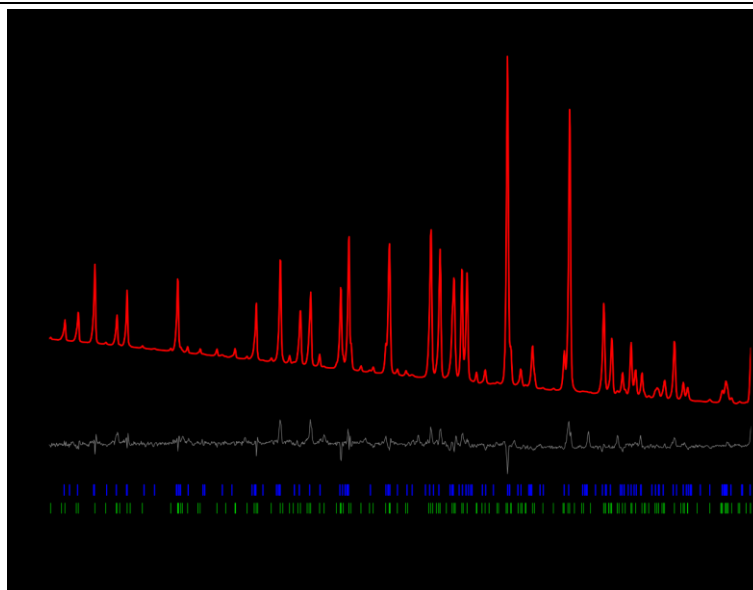


Figure D9. Extract of the Rietveld refinement based on PXRD data collected from a sample containing “ $\text{Sr}_{22.5+x}\text{La}_{55-x}[\text{Si}_{129}\text{N}_{240-x}\text{O}_x]\text{O}_3$ ” ($x \approx 0.24$, approx. 24 wt%) and $\text{Sr}_{28.5+x}\text{La}_{75-x}[\text{Si}_{170}\text{N}_{312-x}\text{O}_{9+x}]\text{O}_4$ ($x \approx -3.71$, approx. 76 wt%) based on the reported structure models. Observed (black) and calculated (red) powder X-ray diffraction patterns with corresponding difference profile (gray). Vertical blue or green bars indicate the position of the Bragg reflections of “ $\text{Sr}_{22.5+x}\text{La}_{55-x}[\text{Si}_{129}\text{N}_{240-x}\text{O}_x]\text{O}_3$ ” ($x \approx 0.24$) and $\text{Sr}_{28.5+x}\text{La}_{75-x}[\text{Si}_{170}\text{N}_{312-x}\text{O}_{9+x}]\text{O}_4$ ($x \approx -3.71$), respectively. Unidentified reflections marked with an asterisk. Reflections with fitting misfits but originating from the $\text{Sr}_{28.5+x}\text{La}_{75-x}[\text{Si}_{170}\text{N}_{312-x}\text{O}_{9+x}]\text{O}_4$ ($x \approx -3.71$) phase (matching vertical green bars) marked with \diamond .

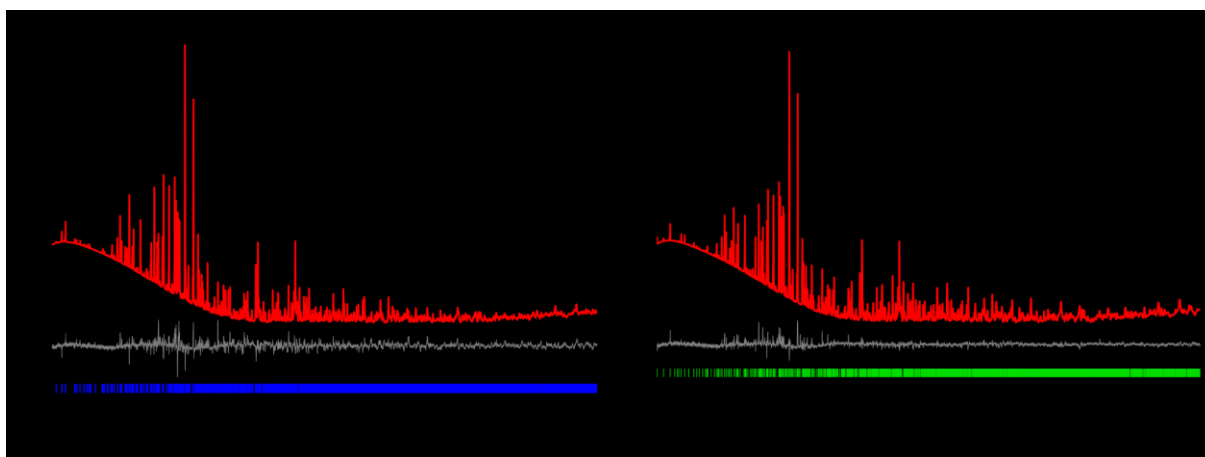


Figure D10. Rietveld refinement based on PXRD data collected from a sample containing both “ $\text{Sr}_{22.5+x}\text{La}_{55-x}[\text{Si}_{129}\text{N}_{240-x}\text{O}_x]\text{O}_3$ ” ($x \approx 0.24$, corresponding to $\text{Ba}_{22.5+x}\text{La}_{55-x}[\text{Si}_{129}\text{N}_{240-x}\text{O}_x]\text{O}_3$, in which Ba was substituted by Sr) and $\text{Sr}_{28.5+x}\text{La}_{75-x}[\text{Si}_{170}\text{N}_{312-x}\text{O}_{9+x}]\text{O}_4$ ($x \approx -3.71$) based on the reported structure models. Refinement solely based on (a) “ $\text{Sr}_{22.5+x}\text{La}_{55-x}[\text{Si}_{129}\text{N}_{240-x}\text{O}_x]\text{O}_3$ ” ($x \approx 0.24$) and (b) $\text{Sr}_{28.5+x}\text{La}_{75-x}[\text{Si}_{170}\text{N}_{312-x}\text{O}_{9+x}]\text{O}_4$ ($x \approx -3.71$). Observed (black) and calculated (red) powder X-ray diffraction patterns with corresponding difference profile (gray). Vertical blue or green bars indicate the position of the Bragg reflections of “ $\text{Sr}_{22.5+x}\text{La}_{55-x}[\text{Si}_{129}\text{N}_{240-x}\text{O}_x]\text{O}_3$ ” ($x \approx 0.24$) and $\text{Sr}_{28.5+x}\text{La}_{75-x}[\text{Si}_{170}\text{N}_{312-x}\text{O}_{9+x}]\text{O}_4$ ($x \approx -3.71$), respectively.

Table D21. Details of the Rietveld refinement of solely “ $\text{Sr}_{22.5+x}\text{La}_{55-x}[\text{Si}_{129}\text{N}_{240-x}\text{O}_x]\text{O}_3$ ” ($x \approx 0.24$) in a powder sample containing both “ $\text{Sr}_{22.5+x}\text{La}_{55-x}[\text{Si}_{129}\text{N}_{240-x}\text{O}_x]\text{O}_3$ ” ($x \approx 0.24$) and $\text{Sr}_{28.5+x}\text{La}_{75-x}[\text{Si}_{170}\text{N}_{312-x}\text{O}_{9+x}]\text{O}_4$ ($x \approx -3.71$) based on the single-crystal data (standard deviations in parentheses). Only lattice parameters were refined; site occupancy factors as well as isotropic displacement parameters for all sites were taken from the single-crystal data presented in the previous chapter

Formula	“ $\text{Sr}_{22.74}\text{La}_{54.84}\text{Si}_{129}\text{N}_{240}\text{O}_3$ ”
formula weight / $\text{g}\cdot\text{mol}^{-1}$	16642.4
crystal system	hexagonal
space group	$P\bar{6}$ (no.174)
lattice parameters / Å	$a =$
	$c =$
$V / \text{Å}^3$	5876.39(17)
Z	1
density / $\text{g}\cdot\text{cm}^{-3}$	4.7025
diffractometer	STOE Stadi P
radiation	$\text{Cu-K}\alpha_1$ ($\lambda = 1.5406 \text{ Å}$)
monochromator	Ge(111)
detector	Mythen 1K
2θ range / °	$5.000 \leq \theta \leq 122.285$
data points	7820
total number of reflections	3147
refined parameters	30
background function	shifted Chebyshev, 12 polynomials
R values	$R_p =$
	$R_{wp} =$
	$R_{exp} =$
	$R_{Bragg} =$
$\text{Goof} (\chi^2)$	3.4726

Table D22. Details of the Rietveld refinement of solely $\text{Sr}_{28.5+x}\text{La}_{75-x}[\text{Si}_{170}\text{N}_{312-x}\text{O}_{9+x}]\text{O}_4$ ($x \approx -3.71$) in a powder sample containing both “ $\text{Sr}_{22.5+x}\text{La}_{55-x}[\text{Si}_{129}\text{N}_{240-x}\text{O}_x]\text{O}_3$ ” ($x \approx 0.24$) and $\text{Sr}_{28.5+x}\text{La}_{75-x}[\text{Si}_{170}\text{N}_{312-x}\text{O}_{9+x}]\text{O}_4$ ($x \approx -3.71$) based on their single-crystal data (standard deviations in parentheses). Only lattice parameters were refined; site occupancy factors as well as isotropic displacement parameters for all sites were taken from the single-crystal data presented in the previous chapter

Formula		$\text{Sr}_{24.79}\text{La}_{78.75}\text{Si}_{170}\text{N}_{315.77}\text{O}_{9.29}$
formula weight / $\text{g}\cdot\text{mol}^{-1}$		22456.2
crystal system		hexagonal
space group		$P\bar{6}$ (no.174)
lattice parameters / Å	$a =$	20.0446(1)
	$c =$	22.5174(2)
$V / \text{Å}^3$		7835.07(13)
Z		1
density / $\text{g}\cdot\text{cm}^{-3}$		4.75901
diffractometer		STOE Stadi P
radiation		$\text{Cu-K}\alpha_1$ ($\lambda = 1.5406 \text{ Å}$)
monochromator		Ge(111)
detector		Mythen 1K
2θ range / °		$5.000 \leq \theta \leq 122.285$
data points		7820
total number of reflections		7820
refined parameters		30
background function		shifted Chebyshev, 12 polynomials
R values	$R_p =$	R0.0272
	$R_{wp} =$	0.0379
	$R_{exp} =$	0.0179
	$R_{Bragg} =$	0.0280
$\text{Goof} (\chi^2)$		2.1182

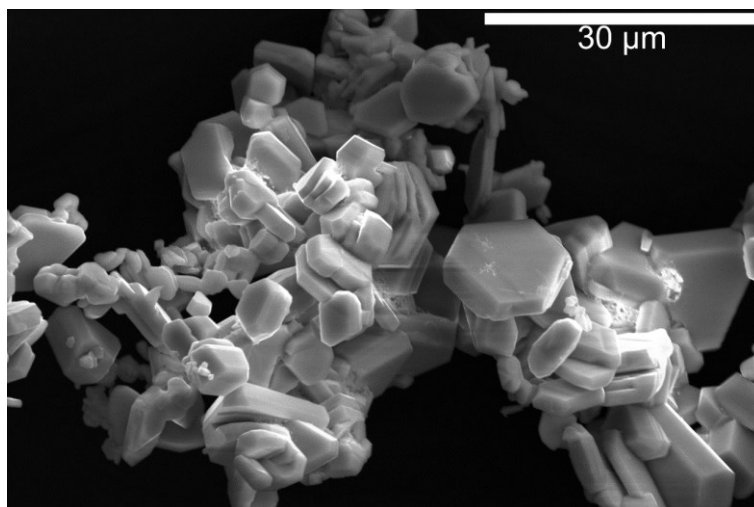


Figure D11. SEM image of the sample containing both “ $\text{Sr}_{22.5+x}\text{La}_{55-x}[\text{Si}_{129}\text{N}_{240-x}\text{O}_x]\text{O}_3$ ” ($x \approx 0.24$) and $\text{Sr}_{28.5+x}\text{La}_{75-x}[\text{Si}_{170}\text{N}_{312-x}\text{O}_{9+x}]\text{O}_4$ ($x \approx -3.71$).

Table D23. Results (in atom%) of SEM-EDX point measurements of a sample containing “ $\text{Sr}_{22.5+x}\text{La}_{55-x}[\text{Si}_{129}\text{N}_{240-x}\text{O}_x]\text{O}_3$ ” ($x \approx 0.24$) and $\text{Sr}_{28.5+x}\text{La}_{75-x}[\text{Si}_{170}\text{N}_{312-x}\text{O}_{9+x}]\text{O}_4$ ($x \approx -3.71$)

	Sr	La	Si	N	O
average and standard deviation	5(1)	11(1)	27(2)	52(2)	5(1)
calculated for “ $\text{Sr}_{22.5+x}\text{La}_{55-x}[\text{Si}_{129}\text{N}_{240-x}\text{O}_x]\text{O}_3$ ” ($x \approx 0.24$)	5	12	29	53	1
calculated for $\text{Sr}_{28.5+x}\text{La}_{75-x}[\text{Si}_{170}\text{N}_{312-x}\text{O}_{9+x}]\text{O}_4$ ($x \approx -3.71$)	4	13	29	52	2

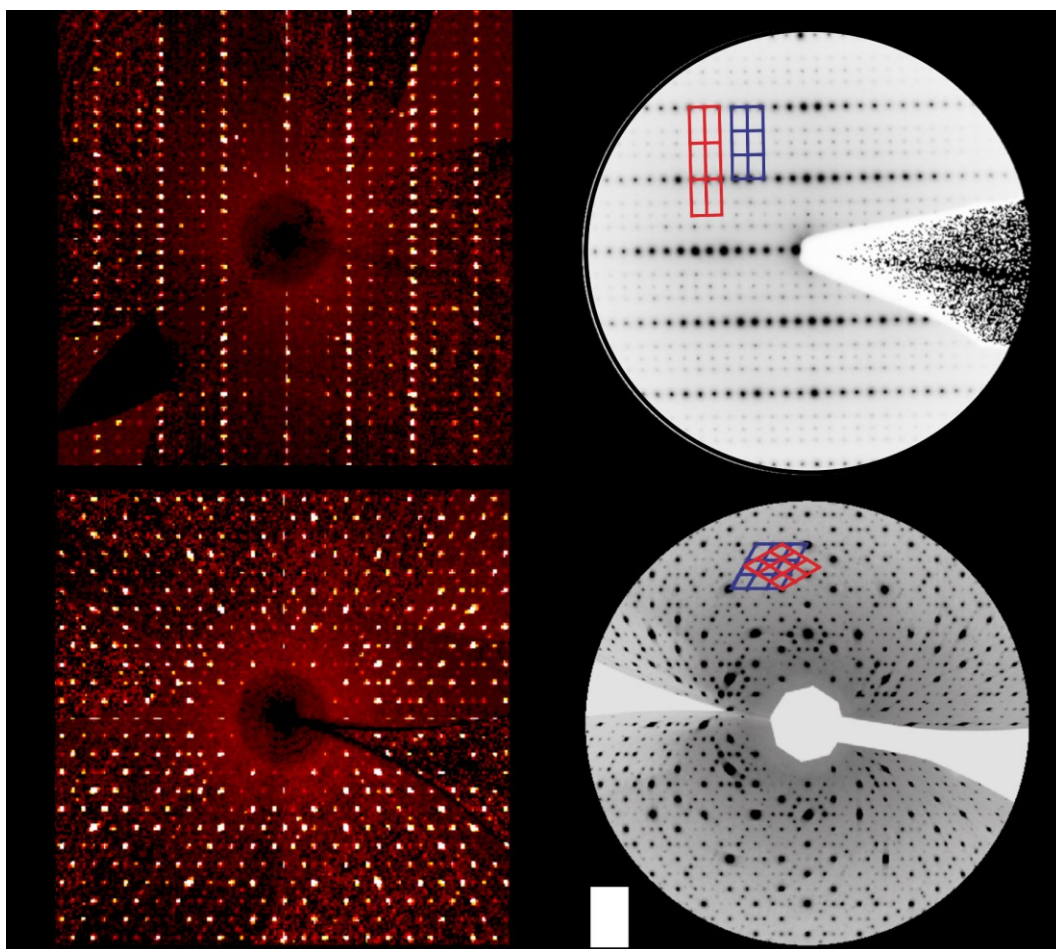


Figure D12. Comparison of reciprocal lattice sections. (a) Reciprocal lattice section along $[100]$ of “ $\text{Sr}_{22.5+x}\text{La}_{55-x}[\text{Si}_{129}\text{N}_{240-x}\text{O}_x]\text{O}_3$ ” ($x \approx 0.24$) with weak reflections of $\text{Sr}_{28.5+x}\text{La}_{75-x}[\text{Si}_{170}\text{N}_{312-x}\text{O}_{9+x}]\text{O}_4$ ($x \approx -3.71$) due to intergrowth. (b) SAED pattern along $[100]$ with lattice nodes of $\text{Ba}_{22.5+x}\text{La}_{55-x}[\text{Si}_{129}\text{N}_{240-x}\text{O}_x]\text{O}_3$ ($x \approx 0.24$) in blue and $\text{Ba}_{25.5+x}\text{La}_{77-x}[\text{Si}_{170}\text{N}_{312-x}\text{O}_{9+x}]\text{O}_4$ ($x \approx 0.24$) in red, respectively.^[5] (c) Reciprocal lattice section along $hk0$ of “ $\text{Sr}_{22.5+x}\text{La}_{55-x}[\text{Si}_{129}\text{N}_{240-x}\text{O}_x]\text{O}_3$ ” ($x \approx 0.24$) with weak reflections of $\text{Sr}_{28.5+x}\text{La}_{75-x}[\text{Si}_{170}\text{N}_{312-x}\text{O}_{9+x}]\text{O}_4$ ($x \approx -3.71$) due to intergrowth. (d) Reciprocal lattice sections $hk0$ with lattice nodes of $\text{Ba}_{22.5+x}\text{La}_{55-x}[\text{Si}_{129}\text{N}_{240-x}\text{O}_x]\text{O}_3$ ($x \approx 0.24$) in blue and $\text{Ba}_{25.5+x}\text{La}_{77-x}[\text{Si}_{170}\text{N}_{312-x}\text{O}_{9+x}]\text{O}_4$ ($x \approx 0.24$) in red, respectively.^[5]

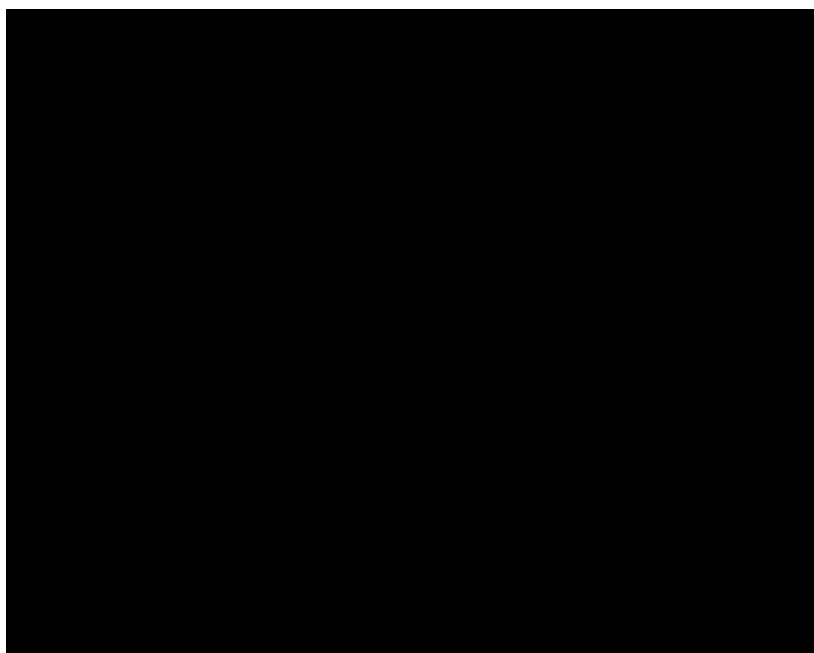


Figure D13. Temperature dependent relative integrated emission intensities of a sample containing both “ $\text{Sr}_{22.5+x}\text{La}_{55-x}[\text{Si}_{129}\text{N}_{240-x}\text{O}_x]\text{O}_3:\text{Eu}^{2+}$ ” ($x \approx 0.24$, 0.5 mol%) and $\text{Sr}_{28.5+x}\text{La}_{75-x}[\text{Si}_{170}\text{N}_{312-x}\text{O}_{9+x}]\text{O}_4:\text{Eu}^{2+}$ ($x \approx -3.71$, 0.5 mol%).

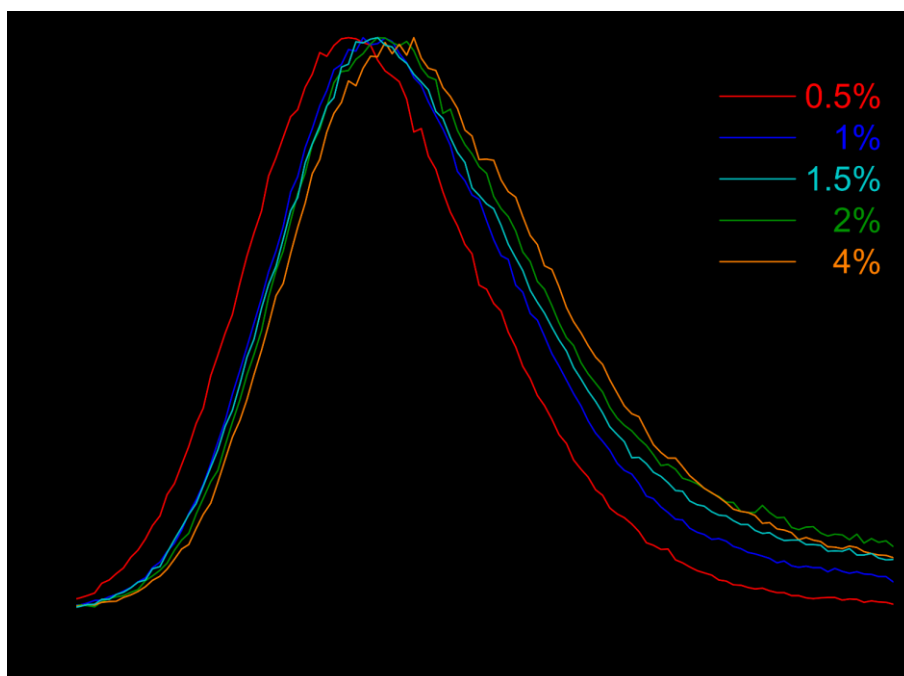


Figure D14. Normalized emission spectra ($\lambda_{\text{exc}} = 420 \text{ nm}$) of samples containing both “ $\text{Sr}_{22.5+x}\text{La}_{55-x}[\text{Si}_{129}\text{N}_{240-x}\text{O}_x]\text{O}_3:\text{Eu}^{2+}$ ” ($x \approx 0.24$) and $\text{Sr}_{28.5+x}\text{La}_{75-x}[\text{Si}_{170}\text{N}_{312-x}\text{O}_{9+x}]\text{O}_4:\text{Eu}^{2+}$ ($x \approx -3.71$) with varying doping concentrations.

Table D24. Comparison of emission maxima and full width at half-maximum for varying doping concentrations of samples containing both “ $\text{Sr}_{22.5+x}\text{La}_{55-x}[\text{Si}_{129}\text{N}_{240-x}\text{O}_x]\text{O}_3:\text{Eu}^{2+}$ ” ($x \approx 0.24$) and $\text{Sr}_{28.5+x}\text{La}_{75-x}[\text{Si}_{170}\text{N}_{312-x}\text{O}_{9+x}]\text{O}_4:\text{Eu}^{2+}$ ($x \approx -3.71$)

mol% Eu		0.2	0.5	1	1.5	2	4
λ_{em}	nm	600	600	604	606	608	618
$fwhm$	nm	73	76	78	78	82	84
	cm^{-1}	1991	2089	2083	2095	2153	2201

References

- [1] H. Günzler, H.-U. Gremlich, *IR-Spektroskopie: Eine Einführung*, Wiley-VCH, Weinheim, **2003**.
- [2] D. Durach, W. Schnick, *Z. Anorg. Allg. Chem.* **2016**, *642*, 101–106.
- [3] A. S. Wills, *VaList*, program available from www.ccp14.ac.uk, **2010**.
- [4] O. Reckeweg, F. J. DiSalvo, *Solid State Sci.* **2002**, *4*, 575–584.
- [5] L. Gamperl, L. Neudert, P. Schultz, D. Durach, W. Schnick, O. Oeckler, *Chem. Eur. J.* **2021**, *27*, 12835–12844.

9 Publications

9.1 List of Publications

9.1.1 Synthesis of $RE_{6-x}Ca_{1.5x}Si_{11}N_{20}O$ ($RE = Yb, Lu; x \approx 2.2$) with $Lu_{6-x}Ca_{1.5x}Si_{11}N_{20}O:Ce^{3+}$ Offering Interesting Spectral Properties for Yellow-Emitting Phosphors in 1pcLEDs

Lisa Gamperl, Georg Krach, Peter J. Schmidt, and Wolfgang Schnick

Eur. J. Inorg. Chem. **2019**, 47, 4985–4993

For this contribution, sample syntheses and formal analyses were performed by Lisa Gamperl and Georg Krach over the course of his Bachelor's thesis which was supervised by Lisa Gamperl and Wolfgang Schnick. Luminescence investigations were performed at the Lumileds Phosphor Center (LPC) Aachen. Evaluation of the measured spectra and values was done by Lisa Gamperl, whereby Peter J. Schmidt supported the interpretation of the luminescence data. Structure determination based on single crystal and powder X-ray diffraction data, lattice energy calculations, measurement, and interpretation of diffuse reflectance data, SEM-EDX measurements and interpretation, literature screening, image preparation, conceptualization and writing of the manuscript were performed by Lisa Gamperl. The revision process was conducted by Lisa Gamperl. Supervision of the research project was headed by Wolfgang Schnick. All authors contributed to the discussion of the results and revised the manuscript.

9.1.2 Missing Member in the $M^II M^III Si_4 N_7$ Compound Class: Carbothermal Reduction and Nitridation Synthesis Revealing Substitution of N by C and O in $CaLu[Si_4 N_{7-2x} C_x O_x]:Eu^{2+}/Ce^{3+}$ ($x \approx 0.3$)

Lisa Gamperl, Otto E. O. Zeman, Philipp Strobel, Peter J. Schmidt, and Wolfgang Schnick

Chem. Eur. J. **2022**, 28, e202104007– e202104014

Otto E. O. Zeman supported the evaluation of MAS solid-state NMR spectra. Luminescence measurements were performed by Philipp Strobel at LPC Aachen. Evaluation of the measured spectra and values was done by Lisa Gamperl with Philipp Strobel and Peter J. Schmidt supporting the interpretation of the luminescence data. Sample syntheses, elemental analyses, structure determination based on powder X-ray diffraction data, measurement, and interpretation of diffuse reflectance data, SEM-EDX measurements and interpretation, literature screening, visualization, conceptualization and writing of the

manuscript were performed by Lisa Gamperl. The revision process was conducted by Lisa Gamperl. Supervision of the research project was headed by Wolfgang Schnick. All authors contributed to the discussion of the results and revised the manuscript.

9.1.3 Synthesis and Luminescence Properties of Amber Emitting $\text{La}_7\text{Sr}[\text{Si}_{10}\text{N}_{19}\text{O}_3]:\text{Eu}^{2+}$ and Syntheses of the Substitutional Variants $\text{RE}_{8-x}\text{AE}_x[\text{Si}_{10}\text{N}_{20-x}\text{O}_{2+x}]:\text{Eu}^{2+}$ with $\text{RE} = \text{La}, \text{Ce}$; $\text{AE} = \text{Ca}, \text{Sr}, \text{Ba}$; $0 \leq x \leq 2$

Lisa Gamperl, Philipp Strobel, Peter J. Schmidt, and Wolfgang Schnick

Chem. Eur. J. **2022**, *28*, e202200760–e202200767

For this contribution, luminescence measurements were executed by Philipp Strobel at LPC Aachen. Interpretation of the measured spectra and values was conducted by Lisa Gamperl assisted by Philipp Strobel and Peter J. Schmidt. Sample syntheses, elemental analyses, structure determination based on single crystal and powder X-ray diffraction data, measurement, and interpretation of diffuse reflectance data, SEM-EDX measurements and interpretation, literature screening, image creation, conceptualization and writing of the manuscript were performed by Lisa Gamperl. The revision process was conducted by Lisa Gamperl. Supervision of the research project was headed by Wolfgang Schnick. All authors contributed to the discussion of the results and revised the manuscript.

9.1.4 Structure Elucidation of Complex Endotaxially Intergrown Lanthanum Barium Oxonitridosilicate Oxides by Combination of Microfocused Synchrotron Radiation and Transmission Electron Microscopy

Lisa Gamperl, Lukas Neudert, Peter Schultz, Dajana Durach, Wolfgang Schnick, and Oliver Oeckler

Chem. Eur. J. **2021**, *27*, 12835–12844

Sample syntheses and analytic measurements were performed by Dajana Durach. Investigations using TEM and subsequent data simulations were conducted by Lukas Neudert. The samples for investigations with microfocused synchrotron radiation were prepared by Lukas Neudert and Peter Schultz, while the measurements and the following structure elucidation based on the obtained single crystal diffraction data were conducted by Peter Schultz and Oliver Oeckler. The results were interpreted by Lisa Gamperl, Lukas Neudert, Peter Schultz, and Oliver Oeckler. Rietveld refinements based on powder X-ray diffraction data as well as interpretations of elemental analyses, bond valence sum

calculations, luminescence measurements, and diffuse reflectance and EDX data were performed by Lisa Gamperl. Literature screening, visualization, conceptualization, writing of the manuscript and the revision process were conducted by Lisa Gamperl. Supervision of the research project was headed by Wolfgang Schnick and Oliver Oeckler. All authors contributed to the discussion of the results and revised the manuscript.

9.2 Conference Contributions

1. 1000 Wege führen nach Rom, aber (noch) keiner zu „Ba[LiAl₃N₄]:Eu²⁺“

Lisa Gamperl, and Wolfgang Schnick

Talk

Schnick Group Seminar

Munich, Germany

06.06.2018

2. Erste Vertreter im System SE-Ca-Si-N-O (SE = Yb, Lu)

Lisa Gamperl, and Wolfgang Schnick

Talk

4. Obergurgl-Seminar Festkörperchemie

Obergurgl, Austria

29.01–01.02.2019

3. SE-EA-Nitridosilicate

Lisa Gamperl, and Wolfgang Schnick

Talk

Schnick Group Seminar

Munich, Germany

22.05.2019

4. Synthesis of $RE_{6-x}Ca_{1.5x}Si_{11}N_{20}O$ ($RE = Yb, Lu; x \approx 2.2$) with $Lu_{6-x}Ca_{1.5x}Si_{11}N_{20}O:Ce^{3+}$ as an Interesting New Yellow-Emitting Phosphor for 1pcLEDs

Georg Krach, Lisa Gamperl, and Wolfgang Schnick

Poster

Undergraduate Research Conference on Molecular Sciences (URCUP)

Kloster Irsee, Irsee, Germany

19.10.–20.10.2019

5. Leuchtstoffe auf Basis von *EA-SE*-Nitridosilicaten

Lisa Gamperl, and Wolfgang Schnick

Talk

Schnick Group Seminar

Munich, Germany

15.07.2020

6. Leuchtstoffe auf Basis von *EA-SE*-Nitridosilicaten – Ein Update

Lisa Gamperl, and Wolfgang Schnick

Talk

Schnick Group Seminar

Munich, Germany

26.05.2021

9.3 Deposited Crystallographic Data

The Crystallographic Information Files (CIF) of the investigated compounds are provided free of charge by the joint Cambridge Crystallographic Data Centre and Fachinformationszentrum Karlsruhe Access Structures service (<http://www.ccdc.cam.ac.uk/structures>) by quoting the corresponding deposition number.

Compound	CSD-
$\text{Yb}_{6-x}\text{Ca}_{1.5x}\text{Si}_{11}\text{N}_{20}\text{O}$ ($x \approx 2.2$)	1948717
$\text{CaLu}[\text{Si}_4\text{N}_{7-2x}\text{C}_x\text{O}_x]$ ($x \approx 0.3$)	2116432
$\text{La}_7\text{Sr}[\text{Si}_{10}\text{N}_{19}\text{O}_3]$	2104245
$\text{La}_8[\text{Si}_{10}\text{N}_{20}\text{O}_2]$	2141282
$\text{La}_6\text{Sr}_2[\text{Si}_{10}\text{N}_{18}\text{O}_4]$	2141280
$\text{La}_7\text{Ca}[\text{Si}_{10}\text{N}_{19}\text{O}_3]$	2141281
$\text{La}_6\text{Ca}_2[\text{Si}_{10}\text{N}_{18}\text{O}_4]$	2141318
$\text{La}_7\text{Ba}[\text{Si}_{10}\text{N}_{19}\text{O}_3]$	2141284
$\text{La}_6\text{Ba}_2[\text{Si}_{10}\text{N}_{18}\text{O}_4]$	2141283
$\text{Ce}_7\text{Sr}[\text{Si}_{10}\text{N}_{19}\text{O}_3]$	2141285
$\text{Ce}_8[\text{Si}_{10}\text{N}_{20}\text{O}_2]$	2141287
$\text{Ce}_6\text{Sr}_2[\text{Si}_{10}\text{N}_{18}\text{O}_4]$	2141319
$\text{Ce}_7\text{Ca}[\text{Si}_{10}\text{N}_{19}\text{O}_3]$	2141288
$\text{Ce}_6\text{Ca}_2[\text{Si}_{10}\text{N}_{18}\text{O}_4]$	2141289
$\text{Ce}_7\text{Ba}[\text{Si}_{10}\text{N}_{19}\text{O}_3]$	2141290
$\text{Ce}_6\text{Ba}_2[\text{Si}_{10}\text{N}_{18}\text{O}_4]$	2141320
$\text{Ba}_{22.5+x}\text{La}_{55-x}[\text{Si}_{129}\text{N}_{240-x}\text{O}_x]\text{O}_3$ ($x \approx 0.24$)	1958352
$\text{Ba}_{25.5+x}\text{La}_{77-x}[\text{Si}_{170}\text{N}_{312-x}\text{O}_{9+x}]\text{O}_4$ ($x \approx 0.24$)	1958355
$\text{Sr}_{28.5+x}\text{La}_{75-x}[\text{Si}_{170}\text{N}_{312-x}\text{O}_{9+x}]\text{O}_4$ ($x \approx -3.71$)	1864686